INFORMATION TO USERS

This manuscript has been reproduced from the microfilm master. UMI films the text directly from the original or copy submitted. Thus, some thesis and dissertation copies are in typewriter face, while others may be from any type of computer printer.

The quality of this reproduction is dependent upon the quality of the copy submitted. Broken or indistinct print, colored or poor quality illustrations and photographs, print bleedthrough, substandard margins, and improper alignment can adversely affect reproduction.

In the unlikely event that the author did not send UMI a complete manuscript and there are missing pages, these will be noted. Also, if unauthorized copyright material had to be removed, a note will indicate the deletion.

Oversize materials (e.g., maps, drawings, charts) are reproduced by sectioning the original, beginning at the upper left-hand corner and continuing from left to right in equal sections with small overlaps. Each original is also photographed in one exposure and is included in reduced form at the back of the book.

Photographs included in the original manuscript have been reproduced xerographically in this copy. Higher quality 6" x 9" black and white photographic prints are available for any photographs or illustrations appearing in this copy for an additional charge. Contact UMI directly to order.

Global Modeling of the Average Response of the Magnetosphere to Varying Solar Wind Conditions

by

Ronald Keith Elsen

A dissertation submitted in partial fulfillment of
the requirements for the degree of

Doctor of Philosophy

University of Washington

1996

Approved by ___*R. Wugler*_____

(Chairperson of Supervisory Committee)

Program Authorized
to Offer Degree____*Geophysics Program*_____

Date____*8/15/96*_____

UMI Number: 9704488

UMI
300 North Zeeb Road
Ann Arbor, MI 48103

In presenting this dissertation in partial fulfillment of the requirements for the Doctoral degree at the University of Washington, I agree that the Library shall make its copies freely available for inspection. I further agree that extensive copying of this dissertation is allowable only for scholarly purposes, consistent with "fair use" as prescribed in the U.S. Copyright Law. Requests for copying or reproduction of this dissertation may be referred to University Microfilms, 1490 Eisenhower Place, P.O. Box 975, Ann Arbor, MI 48106, to whom the author has granted "the right to reproduce and sell (a) copies of the manuscript in microform and/or (b) printed copies of the manuscript made from microform."

Signature _Ronald K Elen_

Date _8/15/96_

University of Washington

Abstract

Global Modeling of the Average Response of the Magnetosphere to Varying Solar Wind Conditions

by Ronald Keith Elsen

Chairperson of Supervisory Committee: Professor Robert M. Winglee
Geophysics Program

This dissertation quantifies the average configuration of the magnetosphere using global two- and three-dimensional numerical simulations. The plasma is approximated as a fluid, both with magnetohydrodynamics (MHD) and a modified fluid approximation that includes some particle effects. Model output is studied parametrically in terms of the controlling solar wind dynamic pressure and interplanetary magnetic field (IMF). Such quantitative studies are a new application of global models, which predict key features of the magnetosphere under a wide range of solar wind conditions. The mapping of magnetic field lines and field-aligned currents into the magnetotail from different auroral latitudes is investigated with a 2-D simulation in the noon-midnight meridian plane. The modified fluid approximation produces additional field-aligned currents present in observations, but absent in MHD simulations. While the instantaneous neutral line position during periods of southward IMF agrees with the near-Earth neutral line model, the average position of the neutral line in the simulations is much more distant, consistent with ensemble-averaged satellite data. The size and shape of the magnetopause is predicted using the magnetopause self-consistently generated by a 3-D global MHD simulation, which shows significant asymmetry between the noon-midnight meridian and equatorial planes. The average dawn-dusk magnetopause cross-section is nearly circular, but cross-sections in the tail are elongated in the Z direction on average. Databases of spacecraft magnetopause crossings are used to verify simulation results, which also agree well with two axisymmetric empirical magnetopause models when averaged over clock angle.

TABLE OF CONTENTS

LIST OF FIGURES

v

LIST OF TABLES

ACKNOWLEDGMENTS

I would like to thank my advisor, Dr. Robert Winglee, for teaching me the art and science of computer simulations. Robert provided the close supervision that I sorely needed during the first phase of my research and spent countless hours reading drafts of papers and teaching me how to interpret the simulation output. I also thank him for his thorough and fair criticism of my work and my work habits, as I have been able to become a better scientist in the process. I also thank him for the professional skills he fostered including giving many oral presentations and the emphasis on writing papers.

I also would like to thank my supervisory committee, Dr. George Parks, Dr. Robert Holzworth, Dr. John Sahr, and Dr. Ron Merrill, and the other professors of the Geophysics program for their encouragement, and the former two for serving on my Reading Committee. I thank George for facilitating my entry from industry into the Geophysics program and for providing the impetus for rapid graduation. I thank Bob for stimulating discussions (especially on ball lightning) and giving good and practical advice about the experience of graduate school. I would like to thank Ron for bridging the gap between space physics and geomagnetism. Finally, I would also like to thank Dr. J. Michael Brown for introducing me to the geophysics program and sparking my interest through his excellent teaching when I took his course back in 1988.

I thank my fellow graduate students and the post docs in the Space Physics group, Mark Wilber, Tony Goodson, Dr. Zhongwei Zhu, Ted Freeman, Dr. Ruth Skoug, Dr. Suvro Datta, Ben Barnum, Dr. Hua Hu, Dr. Ya-qi Li, Dr. Mitch Brittnacher, Kirsten Lorentzen, Frank Lind, Bill Schulz, Andrew Johnson, and Kerry McQuade for their good company, and their participation in our weekly Journal Club. I especially want to thank Mark for computer advice, as well as Ted, Tony, and him for many interesting discussions.

I would also like to thank my parents and the rest of my family for believing in my talents, and my mother for buying the Encyclopedia Brittanica long ago because, although expensive, she knew I would use it. I also believe the Denver Public Schools and The Colorado College provided a solid foundation upon which all of my further studies were built, and the reality is that very few individuals that lack that foundation will ever become scientists. I also thank my friends Keith and Julie Enevoldsen, and David Nielsen for philosophical conversations, both at college and later, that form the basis for valuing the pursuit of knowledge for its own sake.

Most of all I would like to thank my wife, Karin Leander Elsen, for her support, both financially and emotionally. I am grateful that she encouraged me to leave the safe nest of an industry job to pursue graduate studies. I continue to appreciate our nightly walks with Lucia Whippet.

Chapter 1

MODELING THE MAGNETOSPHERE

1.1 Introduction

1.1.1 The discovery of the solar wind

According to the theory originally outlined by *Parker* [1957a, 1958a, 1959], the corona, the hot outer atmosphere of the Sun that stretches out a few solar radii, expands outward at supersonic speeds and forms a "solar wind" that fills the solar system with the ionized gas called plasma. Similar to the way exhaust gases accelerate out of a rocket nozzle, this dynamic expansion maintains a radial mass flux against a large density gradient in the corona held in by the solar gravitational field. Parker's theory synthesized over a century of observations and speculation that challenged the prevailing view that the space surrounding the Earth was a vacuum populated only by dust grains and fragments shed by comets and asteroids and threaded by a magnetic field originating inside the Earth which stretched across interplanetary space.

Large perturbations to the geomagnetic field called geomagnetic storms were observed in the nineteenth century to have often been preceded a few days earlier by occasional energetic outbursts in the solar atmosphere known as "solar storms". A possible explanation was the "corpuscular hypothesis", originally proposed by *Carrington* [1860], which maintained that an enormous gas cloud released from the sun caused the geomagnetic storms through some unknown process when it struck the Earth. Traversing the 150 million km to Earth in a few days or less meant that these "high speed streams" of solar gas traveled at the incredible speeds of ~ 1000 km/sec. However, since strong geomagnetic storms and large solar storms were relatively rare occurrences, such high-speed streams were viewed as transient events. Streams of charged particles in these clouds were hypothesized by Becquerel, Birkeland, and others to be the cause of the aurora borealis or "northern lights" [cf. *Kivelson and*

2

Russell, 1995]. Geomagnetic storms were usually accompanied by strong auroral displays which might be caused by such charged particles following Earth's dipolar magnetic field lines and striking the atmosphere in polar regions.

Observations of comet tails led *Biermann* [1951, 1957] to conclude that solar corpuscular radiation was required to explain the formation of the portion of the tail that pointed almost radially away from the Sun. Hoffmeister in 1943 [cf. *Kivelson and Russell*, 1995] had found that these tails would typically lag behind the radial direction by about 5°, which allowed Biermann to estimate the speed of the corpuscular stream at $\sim$ 500 km/sec by comparison to orbital velocities [cf. *Kivelson and Russell*, 1995]. *Siedentopf* [1953] estimated that the average particle density in interplanetary space was as high as 600 per cm^3, estimated using the intensity and polarization of the zodiacal light in the ecliptic plane, assumed to be created by sunlight suffering Thomson scattering off free electrons. Furthermore, the persistence of the comet tails and the zodiacal light implied that such high-speed streams of corpuscles might be a permanent feature of interplanetary space. *Alfvén* [1957] suggested that these streams would carry a magnetic field with them derived from the Sun, and the magnetic field lines would drape around the head of the comet forming magnetic structures in this tail, which were often observed to disconnect from the comet and propagate at high speeds down the tail.

Unlike the much cooler and partially ionized plasma near the visible surface or photosphere of the Sun, the corona was discovered in 1938 by Edlén to be over a million degrees, as indicated by the multiple ionization of heavy ions, producing a condition which had misled solar spectroscopists for decades [cf. *Friedman*, 1986]. This led *Chapman* [1957] to propose that an extension of the corona filled interplanetary space with a tenuous but static plasma almost as hot as the corona due to its high thermal conductivity. In Parker's dynamic theory, however, most of the thermal energy of the coronal plasma is converted to bulk kinetic energy as it expands radially outward into the solar system reaching speeds similar to those estimated by Biermann. Furthermore, *Parker* [1962] estimated the density of the solar wind should be less than 30 per cm^3 on average to be consistent with the historical record of observed strengths of geomagnetic storms.

Exploration of the space plasma environment surrounding the Earth began with the launch of the first man-made satellites during the International Geophysical Year,

making it possible to test Parker's theory. The Van Allen radiation belts composed of particles with MeV energies were soon discovered [*Van Allen et al.*, 1958] with the Geiger counters on Explorers 1 and 3. The solar wind was briefly observed by Soviet spacecraft in 1960 and then unambiguously by Mariner 2 on its journey to Venus in 1962. Long-term measurements [*Neugebauer and Snyder*, 1966; *Hundhausen et al.*, 1967; *Bame et al.*, 1968] found the solar wind blows permanently with bulk speeds typically ranging between 250 to 800 km/sec (see Table 1.1), but is relatively cold (1 to 30 eV), both as predicted by Parker. It contains from 1 to 20 protons per cm^3 (Table 1.1), again similar to Parker's estimate, but much less than Siedentopf's estimate, which was too high due to interplanetary dust grains. Like solar plasma, the solar wind also contains a few percent doubly ionized helium particles and much smaller concentrations of heavier ions, which increase the mass density by about 20% on average. It also carries an interplanetary magnetic field (IMF), as predicted by Alfvén, with a magnitude ranging from 1 to 30 nT.

Being a fully ionized plasma, the solar wind also obeys the "frozen-in-field" condition [*Alfvén*, 1943; *Walén*, 1946] for convective motions in an infinitely conducting medium. This means the magnetic field is carried along with the solar wind as it expands through the solar system, and so can generally be traced back to regions of open magnetic field lines on the Sun. Although the plasma flows out radially, *Parker* [1958b, 1959] had also predicted that the rotation of the sun would twist the magnetic field into a spiral pattern, analogous to the pattern formed by a water sprinkler by radially flowing droplets. The magnetic field on average makes an angle of $\sim 50°$ with a line from the Earth to the Sun, known as the "garden hose angle", although this direction is observed to be quite variable. Consistent with the picture of the "Parker spiral", the IMF component perpendicular to the ecliptic plane is observed to be much smaller on average than the ecliptic plane components.

1.1.2 The magnetospheric cavity

When the solar wind encounters the Earth, the largest obstacle in its path is the terrestrial magnetic field. The geomagnetic field is generated in the Earth's core and can be approximated by a magnetic dipole that points from north to south, but is tilted by 11° relative to Earth's rotational axis. The frozen-in condition means that the solar wind plasma and the geomagnetic plasma will not easily mix. In an attempt

Table 1.1: Observed Solar Wind Properties.

Quantity	Units	Mean	Sigma	Extreme values
Proton density	cm^{-3}	6.6	7	1 to 100
Bulk velocity	km/sec	420	120	200 to 1000
Electron temperature	eV	13	4	1 to 100
Proton temperature	eV	11	8	1 to 50
Magnetic field	nT	7	3	1 to 30
IMF B_Z	nT	0	3.5	-30 to +30
Dynamic pressure	nPa	2.1	factor of 2	0.1 to 30

to understand geomagnetic storms, *Chapman and Ferraro* [1930, 1931] had predicted that the electrically conducting plasma in high-speed streams would sweep up the geomagnetic field as it approached the Earth and temporarily confine it into a cavity which would form around the obstacle of the terrestrial magnetic field (Figure 1.1). The permanence of solar streams implied by Biermann's and Siedentopf's results led *Dungey* [1954] to predict the permanence of the cavity, which was named the "magnetosphere" by *Gold* [1959].

The boundary of the magnetospheric cavity, the magnetopause, separates the tenuous plasma residing in the geomagnetic field from the denser solar wind plasma and the IMF. Figure 1.2 shows the general configuration of the magnetosphere (to be discussed shortly) that has been inferred from numerous observations by space-borne magnetometers and plasma instruments in the last four decades. The shape of the magnetospheric cavity is comet-like with the nose or "subsolar point" pointing toward the Sun, measuring on average some 70,000 km or a bit more than 10 Earth radii (R_E). The average distance perpendicular to the Earth-Sun direction is $\sim 15R_E$. The dynamic pressure of the solar wind confines the magnetic field on this "dayside" portion of the magnetosphere into roughly a hemispherical shape, but one that is slightly flared out on the flanks. The magnetosphere extends more than a million km ($> 200R_E$) on the "nightside", however, with an elongated magnetotail composed of magnetic field lines stretched out through an interaction with the solar wind.

Three-dimensional dynamic computer simulations of the magnetosphere based on
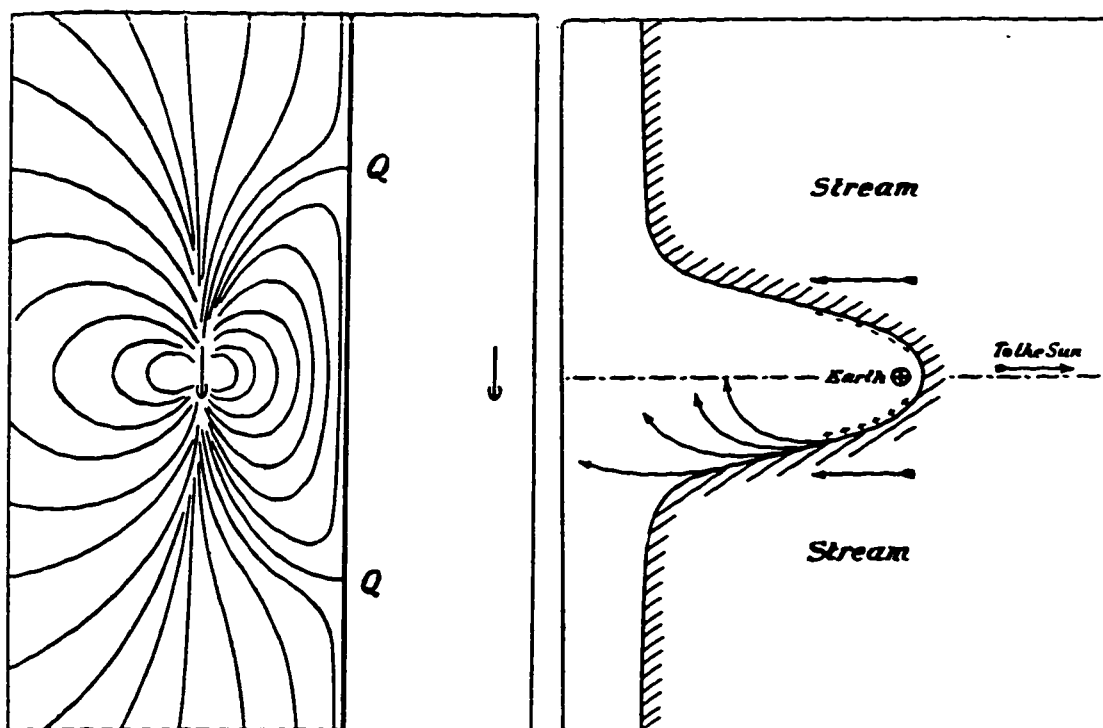
Figure 1.1: The formation of the magnetosphere, the geomagnetic cavity in the solar wind, as originally envisioned by *Chapman and Ferraro* [1931]. Left panel shows advancing plane of infinitely conducting solar wind sweeping up geomagnetic field and excluding it from the solar wind region (left). This ideal solution for the magnetic field shielded by a conducting plane was first obtained by *Maxwell* [1873] by adding an image dipole (right arrow) to the actual dipole (left arrow). Neutral magnetic points labeled Q correspond to the magnetic cusp (Section 1.2.5). Right panel shows how passage of solar wind around the geomagnetic field will lead to formation of a cavity. This simple model provides a way to estimate the standoff distance to the magnetopause at the subsolar point, where solar wind dynamic pressure is balanced by magnetic pressure from the compressed geomagnetic field (Sections 1.2.3, 1.2.4). [From *Chapman and Bartels*, 1940.]
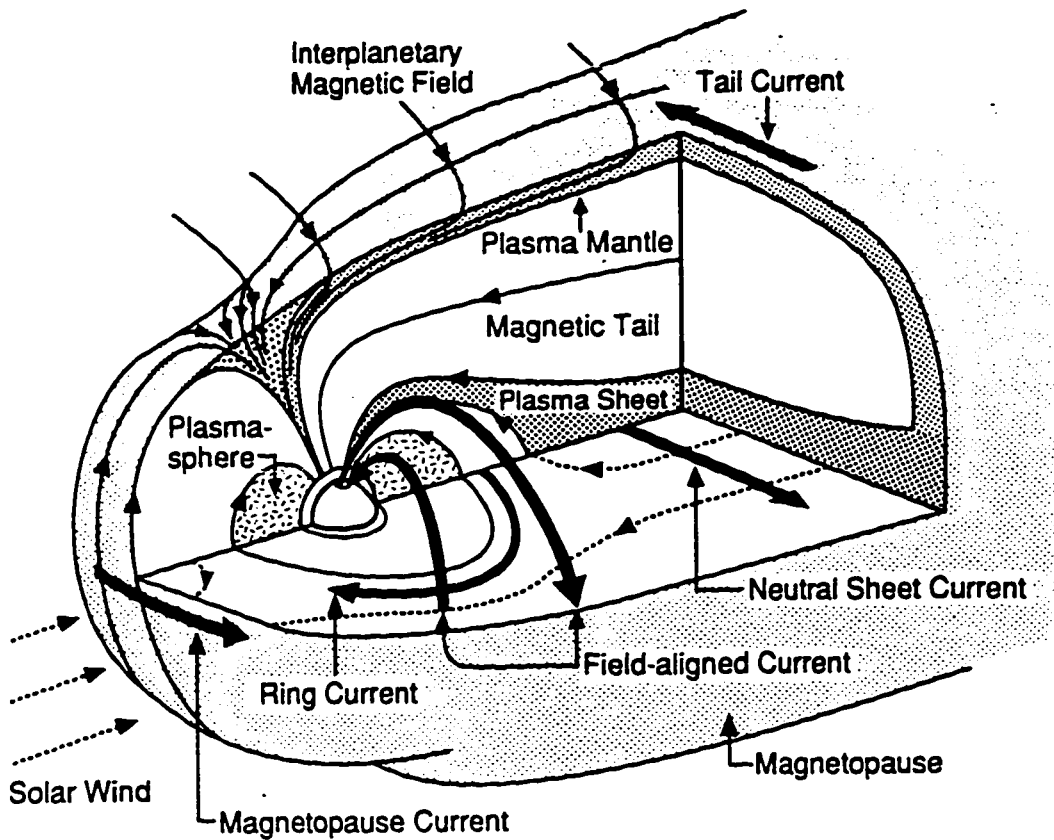
Figure 1.2: This idealized view of the magnetosphere has been developed over the last four decades through exploration by numerous spacecraft of the various regions of the magnetosphere. The magnetospheric cavity forms through the interaction of the Earth's magnetic field with the solar wind and faces into the outward flowing solar wind, much like a comet. The nose (or subsolar point) lies on average about 70 thousand kilometers from the Earth and the extended magnetic tail (or magnetotail) stretches well past the orbit of the Moon. Three-dimensional computer simulations are able to predict the size and shape of the magnetopause, the outer surface of the magnetosphere. Although the magnetotail is approximately cylindrical, these simulations show an asymmetry in the shape which depends on the orientation of the interplanetary magnetic field (IMF) carried from the Sun by the solar wind. See text for description of electrical current systems and plasma structures in other regions of the magnetosphere. [From *Kivelson and Russell*, 1995.]

this interaction between the solar wind and the geomagnetic field were pioneered more than a decade ago [*Lebouef et al.*, 1981]. A magnetospheric configuration very much like that pictured in Figure 1.2 is self-consistently generated in these "global simulations", which have matured in the last decade. Until now, however, global modeling has been used mostly been limited to qualitatively studying the magnetic topology and dynamics of the magnetosphere arising in the simulations for different idealized solar wind conditions. This dissertation is concerned with quantitative modeling of the magnetosphere using global simulations and its comparison with empirical descriptions of the magnetosphere derived from data collected with spacecraft. Both the quantitative study and the thorough comparison with data are new application of global models. In particular, these simulations predict the 3-D shape and size of the magnetospheric cavity, delineated by the magnetopause, which can be directly related to the properties of the solar wind. Although the magnetotail is approximately cylindrical, the simulations show that the magnetopause generally deviates from an axisymmetric shape to a degree that depends on the IMF.

1.2 The Configuration of the Magnetosphere

1.2.1 Particles in the magnetosphere

The upper portion of the atmosphere is partially ionized, principally through the absorption of solar extreme ultraviolet radiation and X-rays above $\sim$ 90 km, forming the electrically conducting ionosphere [*Chapman*, 1931]. Unlike the tenuous plasma of the magnetosphere, which is virtually collisionless, the collision frequencies in the ionosphere increase drastically with depth as densities increase by many orders of magnitude as one gets closer to the Earth [*Johnson*, 1961]. Coulomb collisions as well as collisions with much more numerous neutral atmospheric species produces an electrical resistivity in this weakly ionized plasma [*Nicolet*, 1953; *Chapman*, 1956]. The ionosphere stretches out to several Earth radii at the magnetic equator with densities of $10^2 - 10^4$ per cm^3 forming a plasmasphere [*Storey*, 1953]. Dipole magnetic field lines outline this torus of cold ($\sim$ 1 eV) plasma, which corotates with the Earth's magnetic field, and was found to fade away at 3 to 5 R_E, often with a sharp boundary called the plasmapause [*Carpenter*, 1963; *Chappell et al.*, 1970].

Charged particles in the geomagnetic field will execute a trajectory determined by

the Lorentz equation, causing many particles to be "trapped" and drift azimuthally around the Earth, especially in the more dipolar inner magnetosphere [Singer, 1957]. The drift speed and direction in this inhomogeneous geomagnetic field depends on the particle energy and charge, so the different drifts of electrons and protons produces an electrical current [Hamlin et al., 1961; Northrop, 1963]. Other particles are only partially trapped since they cannot drift all the way around the Earth without hitting the magnetopause boundary [Roederer, 1969]. The region of trapped and semi-trapped particles extends out to the dayside magnetopause, but with lower energies than the radiation belts ($\sim$ 1 to 200 keV) and much lower densities (0.1 to 1 cm^{-3}). Despite their low density, their high drift speeds are sufficient to create an enormous "ring current", which can carry millions of amps of electrical current concentrated between 3 and 7 R_E [Frank, 1967]. This is one of several large scale current systems external to the Earth which are responsible for the perturbations to the geomagnetic field, observed not only during magnetic storms but at magnetically quieter times as well.

Some magnetospheric particles following magnetic field lines will reach the atmosphere and suffer collisions with neutral and ionized air molecules above $\sim$ 100 km. Such particle "precipitation" is responsible for the production of visible light seen in the aurora, and is also another source of ionospheric ionization. Auroral precipitation is especially intense in the "auroral oval", a roughly ring-shaped region around each geomagnetic pole [Feldstein, 1963], which can be viewed in its entirety from space [Anger et al., 1973; Rogers et al., 1974; Frank et al., 1981]. Ions above the collisional altitudes in the ionosphere can travel freely up magnetic field lines into the magnetosphere and become a source of magnetospheric plasma, characteristically marked by singly ionized oxygen and helium, which are absent in solar wind plasma [Waite et al., 1985; Moore et al., 1986; Chappell et al., 1987].

1.2.2 Upstream of the magnetosphere

Since the magnetized solar wind usually travels many times faster with respect to the Earth than the propagation speed of any compressional wave in this medium, a standing shock wave, or bow shock, forms upstream of the magnetosphere. The solar wind plasma is essentially collisionless, with a mean free path of $\sim 10^8$ km [cf. Parks, 1991], preventing the formation of a collisional shock wave, as occurs in a ordinary gas flowing supersonically. A bow shock caused by electromagnetic forces in the solar

wind plasma was predicted independently by *Axford* [1962] and *Kellogg* [1962], and observed by OGO 1 in 1964 [cf. *Kivelson and Russell*, 1995]. The average subsolar distance to the bow shock is 14-15 R_E, about 30% larger than the magnetopause distance, and the average distance perpendicular to the Earth-Sun line is $\sim 25 R_E$ [*Fairfield*, 1971; *Formisano*, 1979].

Pressure perturbations in the plasma produce the "ion acoustic wave", which has typical speeds of about 60 km/sec in the solar wind, giving a "sonic Mach number" that usually falls between 5 and 10 [*Feldman et al.*, 1977]. The speed of the hydromagnetic Alfvén wave [*Alfvén*, 1942] averages about 40 km/sec, giving an "Alfvénic Mach number" that usually falls between 4 and 20 [*Feldman et al.*, 1977]. The square of these Mach numbers can also be interpreted as the ratio of the bulk kinetic energy density (proportional to v^2) to the thermal or magnetic energy density (proportional to the speeds of these waves squared). Since these Mach numbers have similar magnitudes, the plasma beta of the solar wind, a ratio of the thermal to magnetic energy densities, is usually close to one. This ratio also indicates that both magnetic and gasdynamic forces are important in determining flow patterns in a reference frame traveling outward from the Sun at the average speed of the solar wind plasma, but they are not important in determining the overall outward pattern of radial expansion. The fastest compressional mode in this medium is the magnetosonic wave, a coupling of the Alfvén and acoustic modes, which usually has speeds from 50 to 140 km/sec, with an average magnetosonic Mach number near 6 [*Feldman et al.*, 1977].

The relatively cold solar wind plasma is suddenly slowed at the bow shock and much of its bulk kinetic energy is converted to thermal energy ($\leq$ 1 keV). This shocked and thermalized plasma flows around the magnetospheric cavity, in a region called the magnetosheath [*Dessler*, 1964], which is also observed to be very turbulent [*Hundhausen et al.*, 1967; *Bame et al.*, 1968]. The thermal conversion is almost total at the stagnation point just outside the subsolar point where the bulk plasma flow virtually ceases. The flow is largely tangential down the flanks of the magnetosheath [*Hundhausen et al.*, 1969], where the magnetosheath plasma close to the magnetopause accelerates back to solar wind speeds as its thermal energy is again converted to bulk kinetic energy [*Olbert*, 1968]. The magnetosheath has somewhat higher plasma densities and magnetic field strengths than the solar wind plasma due to shock compression and slower flow velocities [*Howe and Binsack*, 1972]. The field

lines of the IMF are distorted as they are draped around the magnetosphere, but are still connected to the undisturbed magnetic field lines outside the bow shock that continue to flow at the solar wind speed [*Fairfield*, 1967, 1976]. Magnetosheath plasma is weakly magnetized, which permits magnetic forces to be neglected and flow to be determined by gasdynamics [*Spreiter et al.*, 1968]. Gasdynamics generally does a very good job describing the flow of the magnetosheath plasma around the magnetosphere, which is treated as a solid object [*Spreiter et al.*, 1966, 1969; *Dryer and Heckman*, 1967], but such axisymmetric modeling cannot predict two effects. When the IMF is roughly perpendicular to the Earth-Sun line, plasma flow up the field is predicted to cause a density depletion [*Zwan and Wolf*, 1976] that has been observed just outside the magnetopause for northward IMF [*Crooker et al.*, 1979]. Also, magnetic tension due to curvature of the retarded portions of the field lines inside the bow shock may assist the acceleration of magnetosheath plasma along the flanks, where flow speeds sometimes rise slightly above the incident solar wind speed [*Chen et al.*, 1993].

1.2.3 The balance of forces

The magnetospheric cavity is thus produced by the force that the shocked magnetosheath plasma exerts on the magnetopause. The geomagnetic field is compressed until its internal magnetic and plasma pressure equals this outside pressure, the condition which determines the equilibrium position to the dayside magnetopause called the "standoff distance". The plasma pressure in the magnetosheath is overwhelmingly supplied by the solar wind dynamic pressure (or more correctly the momentum density flux, *Landau and Lifshitz* [1987]) which averages 2 nanopascals (nPa) [*Fairfield*, 1979b; *Sibeck et al.*, 1991]. The solar wind thermal pressure and magnetic pressures are almost always much smaller and can essentially be ignored in the pressure balance (when the sonic and Alfvénic Mach numbers are both much greater than one) [*Spreiter et al.*, 1968]. The plasma pressure of the rarefied outer magnetosphere, typically with densities of a few tenths of a particle per cm^3, usually contributes less than 10% as much as magnetic pressure to this pressure balance [*Paschmann et al.*, 1986], despite being very hot with energetic particles populations ranging from a keV to several MeV.

The average distance to the subsolar point is 10-11 R_E, as determined from statistical studies of observations [*Fairfield*, 1971], but is occasionally seen at geosyn-

chronous orbits $(6.6R_E)$ when dynamic pressure is very high [*Rufenach et al.*, 1989]. However, most of the time the subsolar distance ranges between 8 and 14 R_E, with most of this variation accounted for by changes in solar wind dynamic pressure [*Fairfield*, 1971; *Holzer and Slavin*, 1978]. This distance can be roughly estimated using a one-dimensional analysis based on the Chapman-Ferraro model [*Martyn*, 1951], which balances solar wind dynamic pressure P_D with the magnetic pressure $B^2/2\mu_0$ of the geomagnetic field, assuming solar wind flow perpendicular to the dipole axis. For a dipole field, $B_{eq}(r) = 31,000nT(R_E/r)^3$ is the magnitude of the dipole field at a radial distance r on the magnetic equator. This gives a dipole strength of $\sim$ 30 nT near 10 R_E.

The solar wind dynamic pressure near the subsolar point is supplied largely by the protons and is well approximated by $P_D \approx nm_pV_{SW}^2$, where n is the solar wind density, m_p is the proton mass, and V_{SW} is the solar wind velocity. This one-dimensional analysis predicts subsolar distances around 9 R_E if average solar wind values are used, which is somewhat less than the observed values. A more careful analysis which allows for the curvature of the surface and other effects is able to match observed values quite well [*Schield*, 1969; *Tsyganenko and Sibeck*, 1994]. The magnetopause position is sensitive to changes in the dynamic pressure and will readjust to a new equilibrium position quickly with the speed of hydromagnetic waves (a timescale of a few minutes) [*Dessler and Parker*, 1959].

Mercury, Jupiter, Saturn, Uranus and Neptune also have strong magnetic fields and have now been observed by interplanetary probes to possess magnetospheres, but with somewhat different configurations. Jupiter's magnetic moment [*Ness et al.*, 1979a, 1979b] is some 20 thousand times greater than the Earth's, resulting in an enormous Jovian magnetosphere larger than the Sun [*Bridge et al.*, 1979a, 1979b; *Krimigis et al.*, 1979a, 1979b] that may have a tail that stretches past the orbit of Saturn [*Wolfe*, 1976; *Intriligator et al.*, 1979]. Large centrifugal forces, due to the 10-hour rotation period of Jupiter and significant amounts of internal plasma due partly to volcanic eruptions on the moon Io, greatly change the balance of forces that determines the magnetopause surface. This internal plasma pressure makes the size of the Jovian magnetosphere much more variable than at Earth, producing a "spongy" magnetopause [*Lepping*, 1995]. The magnetic moments of Uranus and Neptune are highly tilted with respect to their rotational axes and displaced from the center of the

planet [*Ness et al., 1986, 1989*, so that their magnetospheres may undergo drastic reconfiguration on a daily basis [*Bridge et al.*, 1986; *Belcher et al.*, 1989; *Krimigis et al.*, 1986, 1989; *Voigt et al.*, 1987]. For planets with weak magnetic fields, such as Venus or Mars, the solid body of the planet itself is the primary obstacle to the solar wind. Magnetosheath pressure is balanced largely by gas pressure of the highly ionized atmosphere of Venus, forming a surface termed the ionopause, whose currents shield the planet from the IMF [*Luhmann*, 1995].

1.2.4 The magnetopause

The magnetopause separates the magnetospheric plasma and the geomagnetic field from the magnetosheath plasma and the IMF. The magnetic field magnitude typically is observed to decrease from about 50 to 100 nanotesla (nT) just inside the dayside magnetosphere to maybe 10 or 20 nT in the magnetosheath outside, and generally changes its direction as well. Ampère's law requires an electric current to flow on the surface of the magnetosphere to maintain these strong magnetic field gradients [*Chapman and Ferraro*, 1931, 1933]. This "Chapman-Ferraro current" shields the geomagnetic field from the magnetosheath, almost cancelling it outside in the magnetosheath and roughly doubling it just inside a planar conducting boundary [*Maxwell*, 1873; *Chapman and Ferraro*, 1931]. When curvature of the magnetopause is considered, the total field is predicted to increase somewhat more strongly than this, by a factor of about 2.4-2.5 at the subsolar point [*Mead and Beard*, 1964; *Schield*, 1969], with an upper limit of 3 for a spherical magnetopause [*Stern*, 1995]. This characteristic magnetic signature provided the earliest evidence of a magnetospheric boundary [*Sonnett et al.*, 1960; *Heppner et al.*, 1963; *Coleman*, 1964], which was first unambiguously crossed by Explorer 12 in 1961 [*Cahill and Amazeen*, 1963]. Magnetic field measurements from this magnetopause crossing are shown in Figure 1.3.

The Chapman-Ferraro current must be supplied by charged particles. These particles will also gyrate in magnetic field at the magnetopause, creating a characteristic boundary layer thickness that is observed to be on average 800 km or about 10 ion gyroradii [*Berchem and Russell*, 1982; *Russell*, 1995], but the inferred current layer is often much thinner than the total boundary thickness. Plasma instruments also see sudden changes during the many seconds to few minutes it takes them to cross from the relatively dense and cold magnetosheath to the hot rarefied plasma of the
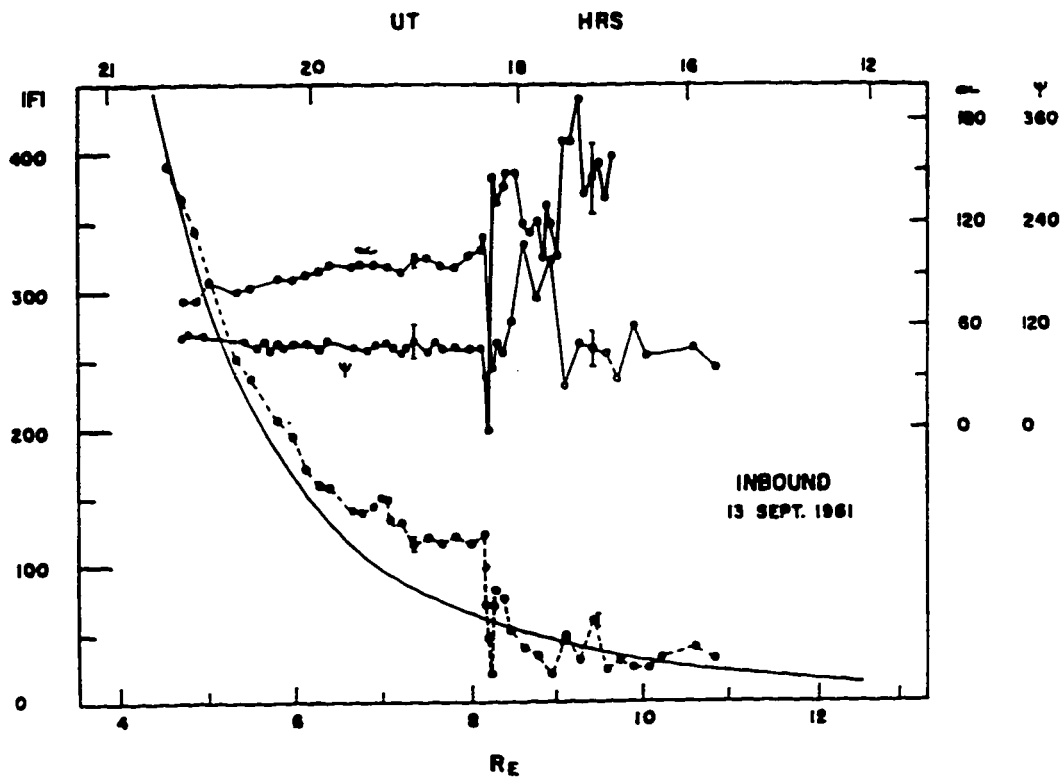
Figure 1.3: Magnetic field data from spacecraft exploring the outer magnetosphere provided evidence for the existence of the magnetopause early in the space age. The first unambiguous crossing of the magnetopause by Explorer 12, inferred from traces of three magnetic field measurements by an on-board magnetometer plotted against radial distance from the Earth. The smooth line shows the magnetic field magnetic magnitude from a pure dipole magnetic field. The sharp decrease near 8 R_E marks the magnetopause, inside of which the field magnitude is characteristically doubled from the ideal dipole values. [From *Cahill and Amazeen*, 1963.]

14

magnetosphere. Such magnetopause crossings indicate that the total magnetopause boundary layer contains considerable fine structure in which many plasma populations are present in different regions. This fine structure results from a mixture of magnetosheath and magnetospheric plasma and also other microphysical processes operating at the magnetopause to produce multiple internal boundary and current layers.

Figure 1.4 shows an example of such a crossing near the subsolar point during magnetically quiet conditions, taken from *Song et al.* [1993]. The dense and cold plasma (N and T) of the magnetosheath gives way over a period of 10 minutes to a tenuous and hot plasma in the magnetosphere. The plasma velocity (V) is low (much less than solar wind speeds) on both sides of the magnetopause, as would be expected for a crossing near the stagnation point (Section 1.2.2). Plasma pressure (P) is much greater in the magnetosheath and is resisted by the magnetic pressure of the strong magnetic field ($B_T^2/2\mu_0$) of the magnetosphere. Besides being much weaker the magnetic field in the magnetosheath is turbulent compared to the uniform magnetospheric field. The magnetopause boundary can be seen to contain additional fine structure.

A spacecraft (typically traveling 1 to 2 km/sec) often will experience multiple crossings of the boundary for a period of about an hour as the magnetopause repeatedly sweeps back and forth past the spacecraft. This indicates that boundary is traveling much faster and possibly oscillating from surface waves, much like a flag rippling in the wind, as originally proposed by *Kaufmann and Konradi* [1969]. These oscillations are generally stronger in the tail, displacing the surface on the order of 1 R_E with wavelengths considerably longer. By analyzing surface normals they can be inferred to generally propagate tailward [*Aubry et al.*, 1971; *Ledley*, 1971].

1.2.5 Magnetospheric topology and magnetic reconnection

Before the magnetotail was discovered, the magnetosphere was originally envisioned to be relatively small and egg-shaped, closed behind by the thermal pressure of the solar wind, shielding the newly discovered radiation belts from the solar wind [*Beard*, 1960; *Johnson*, 1960]. In this configuration all of the geomagnetic field lines close on themselves producing a "closed" magnetosphere. A viscous interaction was proposed by *Axford and Hines* [1961] to operate across such a closed boundary, allowing the
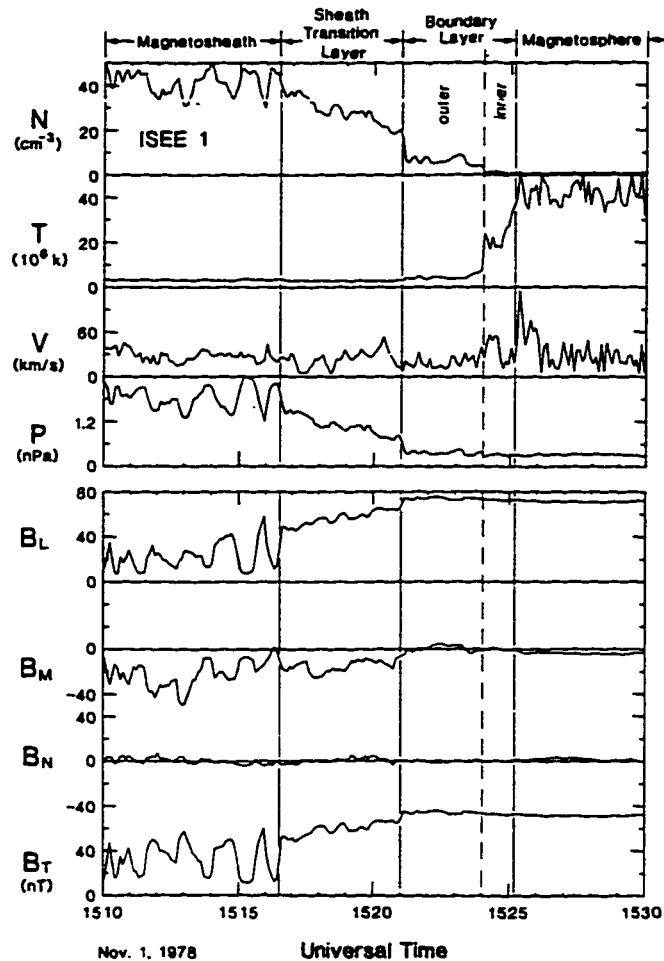
Figure 1.4: Plasma measurements (above) and magnetic field measurements (below) plotted against time from a magnetopause crossing by the ISEE-1 spacecraft near the subsolar point. The proton number density (N), ion temperature (T), bulk ion velocity (V), and plasma pressure (P) were measured by the Fast Plasma Experiment from Los Alamos, while the three magnetic field components (B_L, B_M, B_N) and their magnitude (B_T) were provided by the triaxial fluxgate magnetometer from UCLA. The magnetic field components are expressed in boundary normal coordinates (L, M, N) where L is along the direction of the nominal magnetospheric field, N is normal to the nominal magnetopause surface, and M completes a right handed coordinate system. Unlike this crossing, which occurred during magnetically quiet conditions (with northward IMF, Section 1.2.5), interpreting magnetic and plasma data from other crossings is not always easy, so that proper identification of the magnetopause is still something of an art. [From *Song et al.*, 1993.]

transport of mass, momentum, and energy from the solar wind across the magnetopause (Figure 1.5). This process may help produce the magnetotail (as shortly described) of highly stretched magnetic field lines that are still closed at large distances from the Earth. The microphysics of this macroscopic interaction are still uncertain, but could involve drift of particles across magnetic field lines, the mixing of particles due to their gyroradii (magnetosheath ions generally are largest), and any locally created electromagnetic wave fields. Current estimates suggest that less than 10% of the total energy coupled into the magnetosphere by the solar wind is supplied by the viscous interaction [*Mozer*, 1984].

Alternatively, if some magnetic flux penetrates the magnetopause, the magnetosphere is said to be "open". For example, magnetic field lines may be dragged out by a solar wind interaction, as suggested by *Piddington* [1960], and map out into the solar wind without returning to the surface of the Earth, in much the same way the IMF opens out into interplanetary space from the corona. *Dungey* [1961] explained how an open magnetosphere may arise when the frozen-in condition that creates such an effective barrier to the solar wind breaks down at the magnetopause when the IMF is anti-parallel to the geomagnetic field. Geomagnetic field lines run from the southern to the northern hemisphere, so this condition occurs when the IMF points southward. The magnetic field may diffuse through the plasmas and connect IMF to geomagnetic field lines, according to the picture of "magnetic reconnection". This microphysical process can be studied from both the fluid and particle viewpoint, but it is thought to have macrophysical effects that couples significant amounts of solar wind mass, momentum, and energy into the magnetosphere. Reconnection also represents a fundamental change in the magnetic topology of the magnetosphere, transforming closed geomagnetic field lines into open lines connected to the solar wind (see Figure 1.6a).

In the original steady-state fluid theory of reconnection, highly magnetized plasma flows in toward the current sheet separating anti-parallel magnetic fields [*Parker*, 1957b; *Sweet*, 1958] and weakly magnetized plasma flows away from an assumed neutral point in the magnetic field which produces an "X" in the local magnetic field topology (Figure 1.7a) that is assumed to lie on the current sheet. The 2-D picture is imagined to extend to a third dimension, producing an "X line" which is surrounded by a diffusion region where the magnetic field is annihilated and incoming magnetic energy is converted to plasma energy through ohmic heating. The tangential electric
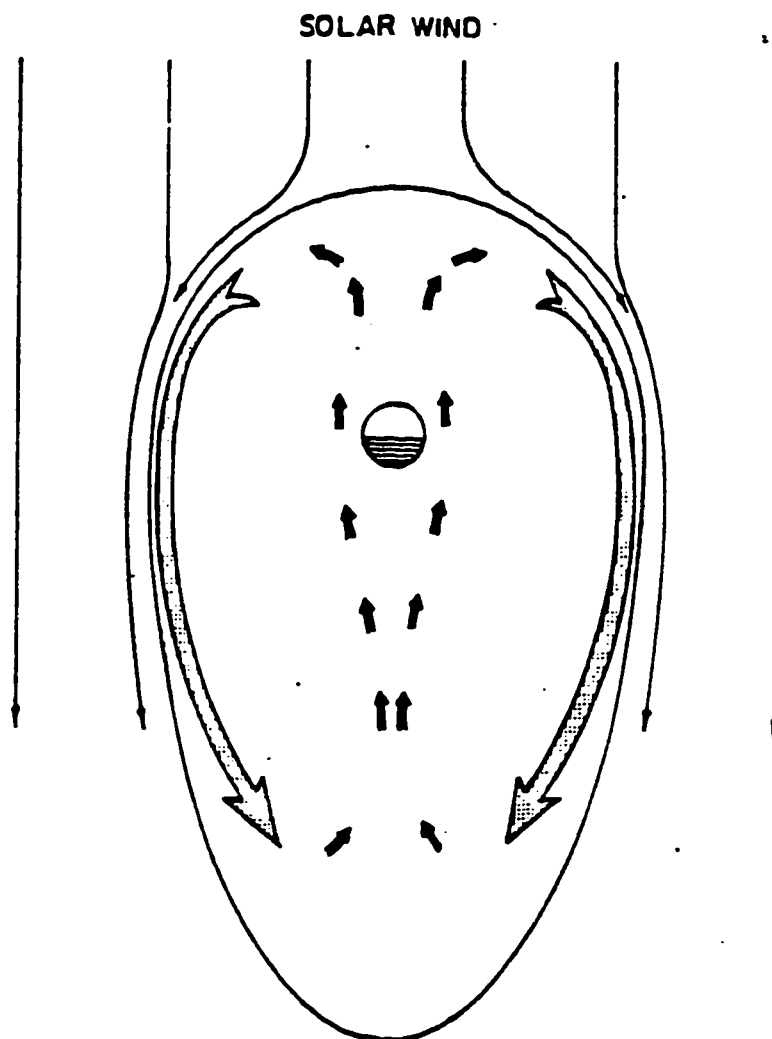
Figure 1.5: The viscous coupling mechanism proposed by *Axford and Hines* [1961] to transport of mass, momentum, and energy from the solar wind across the magnetospheric boundary. The diagram shows plasma flow in the equatorial plane, both in the solar wind and within a closed magnetosphere. Tailward flows near the flanks are due to coupling of solar wind momentum across the boundary, a process that leads to a return flow in the center toward the Earth. [From *Axford and Hines*, 1961.]

(a) **Interplanetary Field Southward**

(b) **Interplanetary Field Northward**
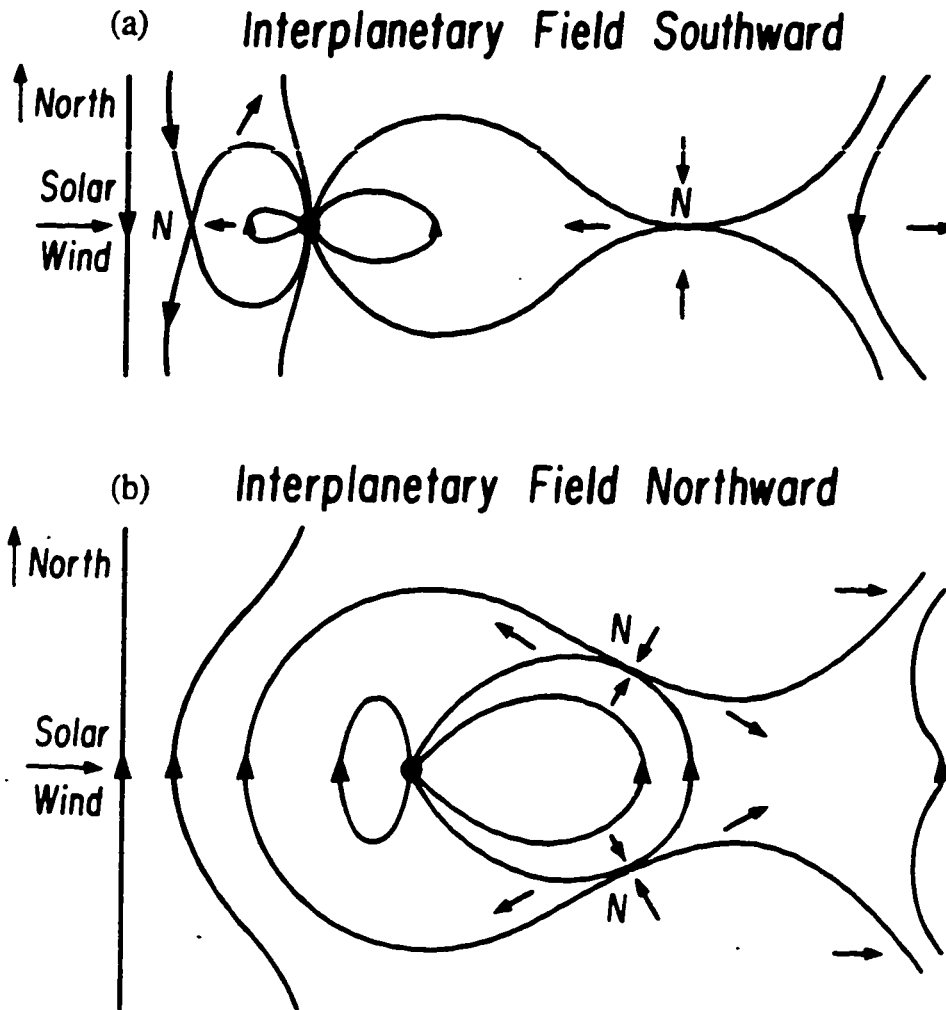
Figure 1.6: The magnetic topology of the magnetosphere in the noon-midnight meridian plane, according to the solar wind coupling mechanism proposed by *Dungey* [1961]. (a) Magnetic reconnection at the magnetopause occurs near the subsolar point when IMF is southward, directed opposite to geomagnetic field lines at the magnetopause. This mechanism connects the IMF lines in the solar wind to previously closed geomagnetic field lines, which are then dragged into the magnetotail. The oppositely aligned magnetic field lines in the magnetotail may then undergo further magnetic reconnection transorming open field lines back to a closed topology. (b) When IMF points northward reconnection may occur tailward of the magnetic cusp, as proposed by *Dungey* [1963]. An IMF field line connecting to a magnetotail field line is transformed into a closed field line on the dayside, while newly created lines unconnected to the Earth are expelled out the magnetotail eventually joining the solar wind. [Both from *Dungey*, 1963.]

field component, however, must be continuous throughout the plane of Figure 1.7a and across this boundary, as required by Maxwell's equations. While the convective electric field far from the diffusion region goes to zero in the diffusion region it is assumed to be replaced by a resistive electric field. The effective resistivity in this collisionless plasma may be "anomalous resistivity" produced by other microphysical processes such as wave-particle interactions which substitute for the classical resistivity produced by Coulomb collisions.

Equating the resistive and convective electric field along with Ampère's law determine the width of the diffusion region, through which all magnetic field must diffuse before being reconnected and flowing away, giving a timescale for the diffusion process. A steady state also requires total pressure throughout the system be constant and determines that the outflow speed is close to the Alfvén velocity. The outflow speed and diffusion region timescale thus effectively limit the inflow speed of the plasma. The ratio of inflow to outflow speeds in this Parker-Sweet model of reconnection is found to be inversely proportional to the square root of the magnetic Reynolds number R_M of the plasma far from the reconnection site. R_M can be enormous for space plasmas, so the inflow velocity and hence the reconnection rate can be severely limited, which led *Parker* [1963] to question this model's viability as a mechanism for energizing the magnetosphere (and also solar flares).

A refinement of this theory by *Petschek* [1964] used a more realistic geometry and also introduced standing shock waves across which plasma flows may be accelerated without going through the diffusion region. The actual reconnection process still occurs in the diffusion region, but this can be shrunk so that very little plasma actually travels through it. This effectively removes the bottleneck in the Parker-Sweet model in which all accelerated plasma was required to flow through the diffusion region. The plasma still flows out of the system at close to the Alfvén velocity. The inflow velocity is allowed to be much larger, however, with a $(\log R_{MA})^{-1}$ dependence which virtually makes the maximum reconnection rate independent of the magnetic Reynolds number. *Sonnerup* [1970] further refined this "rapid reconnection" model by introducing another pair of shocks, which allows an inflow speed near the Alfvén velocity. *Priest and Forbes* [1986] found that the *ad hoc* Petschek and Sonnerup solutions [felt by some to be rather artificial, cf. *Vasyliunas*, 1975] were special cases of a general solution to the steady-state MHD reconnection problem, putting these theories on
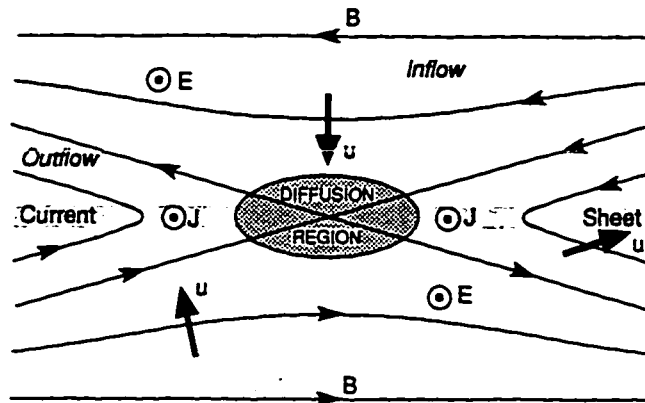
Figure 1.7a: An idealized view of the magnetic reconnection process at an X line on a current sheet separates the oppositely aligned magnetic field lines. Plasma and magnetic field flow in from the top and bottom into a diffusion region where magnetic field lines are reconnected, which flow out to the left and right at the Alfvén speed. This symmetric situation represents reconnection that occurs in the magnetotail. [From *Kivelson and Russell*, 1995]
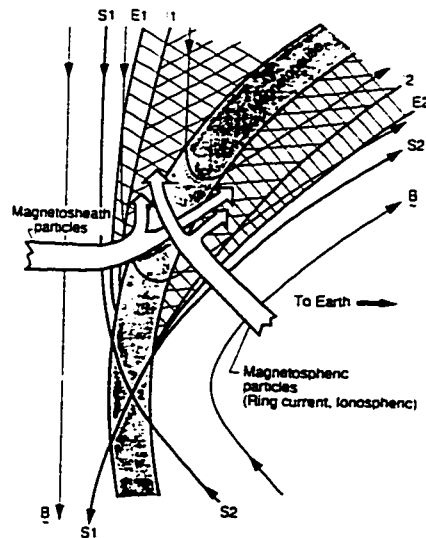
Figure 1.7b: The magnetic reconnection process at the magnetopause. Unlike (a), a strong asymmetry exists in both the plasma and magnetic field on each side of the magnetopause current sheet. This diagram represents the reconnection process that occurs near the subsolar point when IMF is southward. Dense, weakly magnetized plasma of the magnetosheath flows in from the left, while a tenuous, strongly magnetized plasma from the magnetosphere flow in from the right. Reconnected field lines flow out of the X line on the top and bottom. [From *Gosling et al.*, 1990.]

a more solid mathematical foundation. These developments meant that the Dungey [1961] mechanism could be an effective mechanism for transporting mass, momentum and energy into the magnetosphere. The reconnection rate is determined more by external plasma conditions rather than being limited by a bottleneck at the reconnection site. Although fundamentally based on microphysics, magnetic reconnection now becomes a macrophysical process which can be simulated by global models.

The ideal mathematical conditions of these MHD solutions are often not realized in the magnetosphere. Flow at the magnetopause is very asymmetric, especially on the dayside, bounded on one side by the dense, less magnetized magnetosheath and the other by the tenuous, more magnetized magnetosphere, as shown in Figure 1.7b. Reconnection produces an open magnetopause boundary which can be inferred in spacecraft measurements by the presence of a non-zero magnetic field component normal to the magnetopause boundary. This and other physical signatures of magnetic reconnection at the magnetopause are reviewed by *Sonnerup* [1984]. (The normal magnetic field component B_N in Figure 1.4 can be seen to be negligible near the boundary, consistent with the boundary expected for a closed magnetosphere and a lack of vigorous reconnection at the magnetopause during magnetically quiet times.)

Finally, the IMF orientation is always changing, so that reconnection in the magnetosphere is a temporal process, instead of steady state, which will have an effect on magnetosphere dynamics. Reconnection may not proceed at a uniform rate on the magnetopause, but instead observed to occur in bursts that often last about 10 minutes or so [*Russell and Elphic*, 1978]. These "flux transfer events" or FTE's can be observed with spacecraft due to their characteristic magnetic signature, and are believed to send bundles of magnetic flux to the tail with diameters of about 1 R_E from the dayside into the tail.

The magnetopause boundary is effective but not perfect; something like 1% of the solar wind plasma may cross this boundary, becoming an important source of magnetospheric plasma [cf. *Kivelson and Russell*, 1995]. Besides plasma that enters through processes associated with reconnection or the viscous interaction, some of the magnetosheath plasma can enter directly through a throat at high latitudes near magnetic noon called the "polar cusp". The cusp position can be identified at lower altitudes by high fluxes of low energy particles (< 500 eV), with both the cusp position and the "injection" rate highly dependent on the IMF conditions [*Burch*,

1968; *Frank and Ackerson*, 1971]. Mathematically, a neutral point where the magnetic field vanishes is required to exist in each hemisphere by the topology of magnetic field lines if they are to be totally confined inside a smooth surface [*Grad and Hu*, 1966]. While the magnetosphere may be open, a cusp is still expected from which magnetic field lines fan out, connecting it to the rest of the magnetopause. These regions of very weak magnetic field have been measured with satellites [*Russell et al.*, 1971] for both northward and southward IMF, and are located near the magnetopause above and somewhat sunward of the magnetic poles.

1.2.6   The magnetotail

The magnetotail is composed of magnetic field lines from the polar areas of each hemisphere, highly stretched out through the interaction with the solar wind [*Ness et al.*, 1964; *Ness*, 1965, 1969; *Mihalov et al.*, 1968; *Behannon*, 1968, 1970]. Spacecraft measurements show the tail on average has a roughly cylindrical shape with a radius of 20 to 30 R_E that slowly increases with distance down the tail [*Howe and Binsack*, 1972]. Most of the tail is filled with two "lobes" of oppositely directed magnetic field aligned with the flow direction of the solar wind. The area where the open field lines of each lobe map to the surface of the Earth is called the polar cap, and is generally believed to fill most of the area inside the auroral oval. The lobes have very uniform magnetic fields with a low level of turbulence, and also have the lowest plasma densities (~ 0.01 per cm^3) observed anywhere in the magnetosphere. The temperature ($\sim 300 eV$) is similar to the magnetosheath with very few particles over 5 keV, indicating lobe plasma may originate by diffusion from the magnetosheath, but the presence of singly ionized oxygen indicates an ionospheric source also [*Eastman et al.*, 1984]. Observation of low energy particles of solar wind origin in the lobes also provides strong evidence that the lobe magnetic field actually are connected to the solar wind and indeed open [*Anderson and Lin*, 1969; *Mizera and Fennel*, 1978]. The magnetotail may extend downstream over several thousand R_E, as evidenced by intermittent plasma and magnetometer observations of the magnetotail near 1000 R_E by Pioneer 7 [*Ness et al.*, 1967; *Wolfe et al.*, 1967] and near 500 R_E by Pioneer 8 [*Mariani and Ness*, 1969; *Intriligator et al.*, 1969], followed by plasma observations again near 3100 R_E by Pioneer 7 [*Intriligator et al.*, 1979]. The disturbed plasma environments that characterize these observations have been interpreted as a "geo-

magnetic wake" by *Siscoe et al.* [1970], but the two-lobe structure of the magnetotail has been seen by ISEE 3 at 240 R_E [*Tsurutani et al.* [1984].

The lobes are surrounded by denser plasma populations. At high latitudes between the lobes and the magnetosheath lies the mantle which has high densities, but similar temperatures, when compared to the lobes just inside [*Rosenbauer et al.*, 1975]. A plasma sheet usually several R_E thick lies between these lobes populated by a hot plasma of a few keV with higher densities from 0.1 to 1 per cm^3 [*Bame et al.*, 1967]. Unlike the open field lines of the lobes which will not permit plasma to build up, the plasma sheet is usually imagined to lie on closed field lines [cf. *Kivelson and Russell*, 1995]. The plasma sheet thus maps to the areas equatorward of the polar cap, and may be the source of many of the particles producing auroral precipitation on the nightside. Oxygen ions form a significant fraction of this plasma, especially during magnetically disturbed times. The outer portion of the plasma sheet, adjacent to the lobes, is the plasma sheet boundary layer (PSBL), which not only has lower densities and temperatures than the inner portion called the "central plasma sheet", but also often has high velocity ion streams (several hundred km/sec) toward and away from the Earth as well [*Eastman et al.*, 1984].

The viscous coupling mechanism of *Axford and Hines* [1961] is generally pictured to be stronger near the equatorial plane where magnetic field lines are roughly perpendicular to the magnetosheath flow and weaker near the meridian plane where flow will be roughly parallel (Figure 1.5). This viscous coupling is a possible mechanism for creating a plasma boundary layer observed just inside the magnetopause near the equatorial plane called the "low latitude boundary layer", but other mechanisms have also been suggested, including reconnection. The LLBL may stretch great distances down the tail, filling in the gaps between the plasma sheet which extends to the equatorial magnetopause and the mantle at higher latitudes. Thus, in a cross-section through the tail these denser plasma populations surrounding the barren lobes will have the appearance of the Greek letter theta (Θ), as illustrated in Figure 1.8.

Equatorward of the auroral oval the magnetic field lines are generally not severely stretched. The geomagnetic field is mostly dipolar out to about 6 R_E, but gradually transitions on the nightside to the tail field, which becomes dominant past about 10 R_E. Past about 20 R_E the field becomes totally tail-like, with the average observed lobe field of 20 to 30 nT falling off very slowly with distance from the Earth. The

24
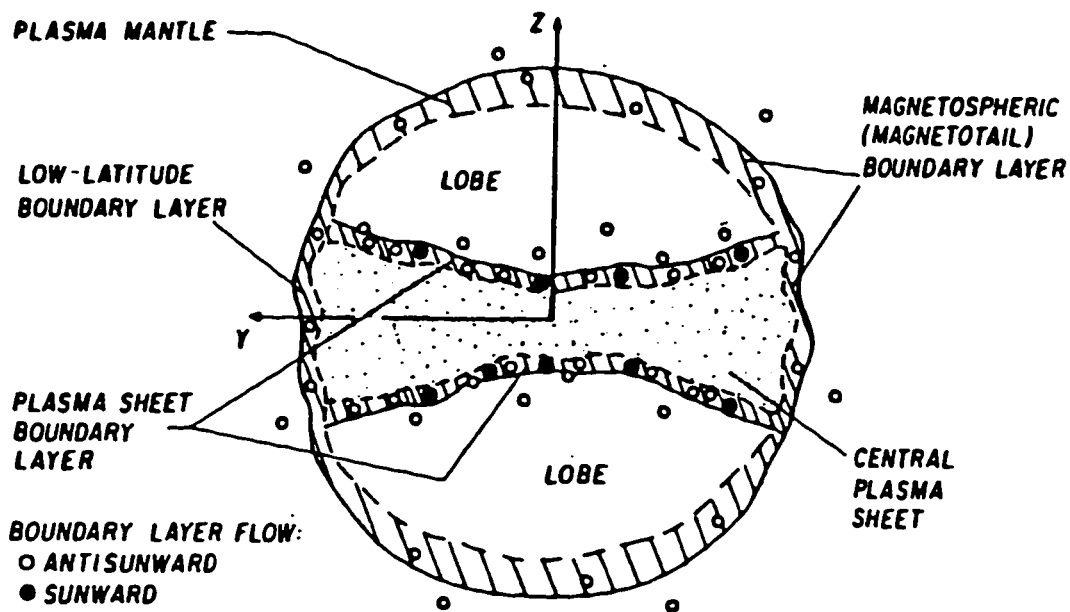
Figure 1.8: Cross-sectional geometry of the magnetotail whose plasma populations have the appearance of the Greek letter theta (Θ). The barren lobes are surrounded by dense plasma of the plasma mantle, plasma sheet, and low latitude boundary layer. The magnetopause and cross-tail current also outline a theta. [From *Eastman et al.*, 1984.]

oppositely directed field lines of the lobes require a large sheet of electrical current, the "cross-tail current", which flows in the dawn-to-dusk direction near the equatorial plane [Axford et al., 1965]. At the center of the current sheet the magnetic field can be imagined ideally to vanish at a "neutral sheet". In fact, a small amount of normal magnetic flux usually connects the two hemispheres so that the magnetic field magnitude typically falls to minimum of a few nT [Fairfield and Ness, 1970; Fairfield, 1968, 1986].

Reconnection and the viscous interactions are also believed to contribute flux to the magnetotail. Magnetic field lines opened by reconnection will be dragged onto the nightside through magnetic tension resulting from the connection with the solar wind (Figure 1.6a). These lines will travel primarily over the magnetic poles [Dungey, 1961]. Momentum imparted to plasma on closed magnetic field lines by the viscous mechanism will also stretch them, but this is believed to operate mostly along the equatorial flanks [Axford and Hines, 1961]. Surface waves may also increase the drag of the solar wind on the magnetosphere, and help increase tail flux.

If the magnetic field does drop to zero somewhere in the tail, the antiparallel magnetic field lines may also undergo magnetic reconnection (Figure 1.6a) as at the magnetopause, along an X line, also called a neutral line [Dungey, 1961; Russell and McPherron, 1972; Schindler, 1974]. This will transform two open field lines into one that is closed and another that is not connected to the Earth at all, but rather connected to the solar wind on each end. The reconnection process will remove magnetic flux from the magnetotail lobes. Inflow velocity and magnetic field magnitude of the magnetotail lobes would be expected to be approximately symmetric, and thus the idealized situation in Figure 1.7a should represent the magnetic reconnection process in the magnetotail much better than at the magnetopause. Closed flux tubes on the nightside are also thought to convect toward the Earth and can transport flux back to the dayside, where it can replenish flux lost to the tail by reconnection and other processes [Coroniti and Kennel, 1973; Holzer and Slavin, 1978].

This convection in the tail is driven by a dawn-to-dusk electric field that can also be traced back to the solar wind interaction with the magnetosphere. A collisionless plasma will drift in the direction given by $\mathbf{E} \times \mathbf{B}$ in a homogeneous magnetic field, which on the nightside for closed (upwardly directed) field lines past the dipolar region is generally in the Earthward direction. This drift produces a convection pattern in

the equatorial plane which is directly linked with the magnetic reconnection and viscous processes that drive it. One can just as well imagine the electric field being created by the convection pattern, given by $\mathbf{E} = -\mathbf{v} \times \mathbf{B}$ when it obeys the frozen-in-field condition. By controlling the amount of magnetic flux in the tail, magnetic reconnection and the resulting convection patterns can also produce changes in the size and shape of the magnetopause.

1.2.7 Magnetospheric current systems

The cross-tail current in the magnetotail splits near the magnetopause with roughly half going around each lobe. Thus in a cross section of the tail the current also resembles a theta (Figure 1.8), much like the plasma populations, but the current layers are generally observed to be much thinner (several hundred km) than the relatively thick plasma layers (a few R_E). The mantle reaches further in from the magnetopause while the plasma sheet reaches further out from the cross-tail current sheet. The magnetopause current, shown in Figure 1.2, is thus comprised of two merged components: (1) the Chapman-Ferraro current confined to the magnetopause which circulates around the cusp and would be present even if there were no magnetotail, and (2) the cross-tail closure (or return) currents [Axford et al., 1965].

Field-aligned (or Birkeland) currents are also observed to flow from the magnetosphere down into the auroral regions where they are closed through the resistive ionosphere and flow back out into the magnetosphere. Such currents were hypothesized early in the century by Birkeland to drive ionospheric currents observed to create large magnetic perturbations on the ground associated with auroral activity, but were not observed until 1966 with magnetometers on satellites [Zmuda et al., 1966; Zmuda and Armstrong, 1974; Arnoldy, 1974].

The field-aligned currents can themselves be broken up into several constituent parts, each of which presumably maps to a different place in the magnetosphere. Statistical studies by Iijima and Potemra [1976a, 1976b, 1978] show two currents systems are generally present, as shown in Figure 1.9. Region 1 currents are on the poleward edge and are downward on the dawn side of the oval and are upward on the dusk side. Region 2 currents lie in the equatorward portion of the oval and are oppositely directed. There are also currents systems located inside the oval and near the cusp [Potemra, 1994].
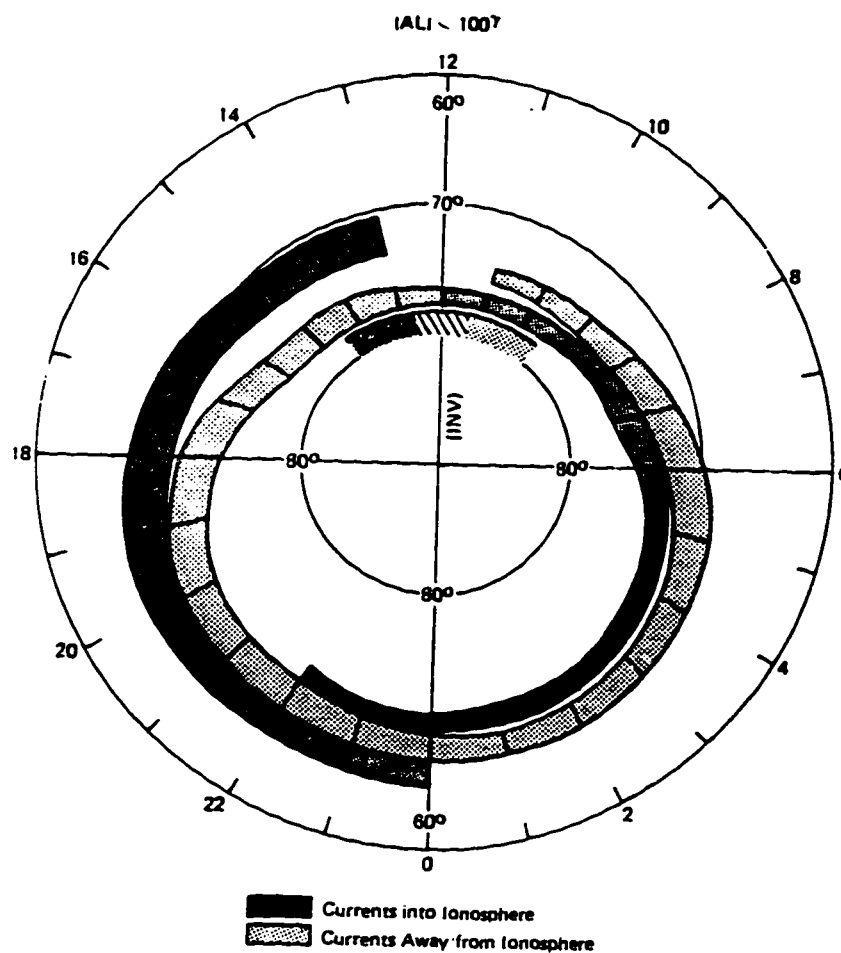
Figure 1.9: The average field-aligned current pattern in the ionosphere during magnetically quiet times. The figure is centered around the geomagnetic pole, with noon at the top of figure, midnight at the bottom. These patterns represent the statistical positions of field-aligned current sheets inferred from magnetometer measurements made during satellite passes over the polar regions. The poleward (equatorward) portions of the current on both the dawn (right side) and dusk (left side) flanks are designated Region 1 (Region 2) currents. Cusp currents, also called Region 0, are also present poleward of Region 1. [From *Iijima and Potemra*, 1978.]

This dissertation is concerned with studying the large scale configuration of the magnetosphere, as just described, and its dependence on the solar wind. Global magnetospheric simulations self-consistently produce many of these features, but as of yet are not quantitatively related to solar wind conditions. The dissertation will present a new application of global modeling which is used to construct self-consistent quantitative models of the magnetosphere.

1.3 Changes in the Magnetospheric Configuration

The magnetosphere thus contains four large scale current systems outside of the ionosphere: the ring, cross tail, magnetopause, and field-aligned currents, as shown in Figure 1.2. The overall magnetic field configuration of the magnetosphere at any time is determined by the superposition of the internal geomagnetic field with the magnetic field generated by such external current systems. The magnetosphere is not static, however, but constantly changes its configuration. This self-consistently requires changes to the external current systems, which might be considered to define "magnetospheric activity" in the most general sense.

1.3.1 Factors influencing magnetospheric configuration

Solar wind conditions are constantly changing, so that the magnetosphere is always changing also. Increased dynamic pressure compresses the magnetosphere everywhere, reducing not only the subsolar distance but also the radius of the magnetotail (Figure 1.10a). This essentially uniform compression mostly changes the size of the magnetosphere, but does not greatly alter its shape. The north-south component of the IMF called IMF B_Z also has a direct effect on the overall configuration of the magnetosphere. Not only do they both strongly influence the shape and size of the magnetopause through direct effects, but they also cause magnetospheric activity (described shortly) which leads to large scale reconfiguration of the magnetosphere.

Large scale, persistent magnetic reconnection on the dayside magnetopause is believed to occur when IMF B_Z is southward or negative for long periods. Such reconnection is believed to drag enough magnetic flux to the nightside to significantly reconfigure the magnetosphere in a process called flux erosion. This process enlarges or "flares" the magnetotail which now contains more flux while the subsolar distance
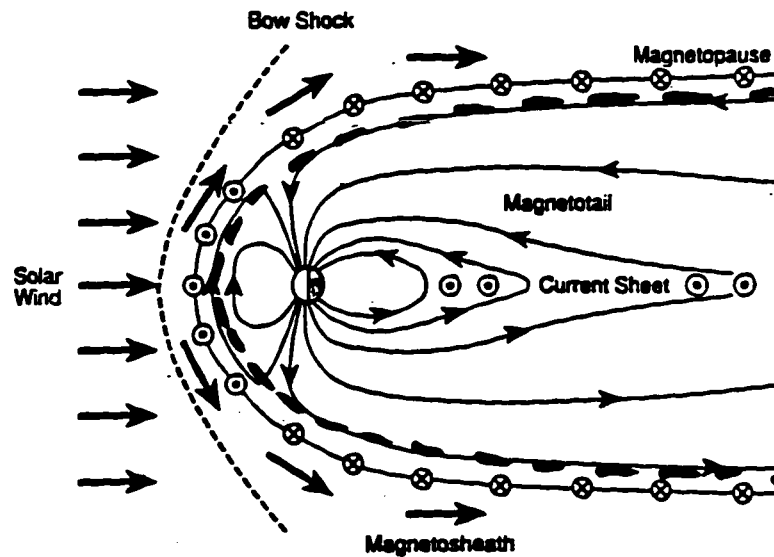
Figure 1.10a: Changes in the size and shape of the magnetopause induced by the solar wind. Figures represent cross-sections of the magnetosphere in the noon-midnight meridian plane. Compression from increased solar wind dynamic pressure. The dashed line represents new equilibrium position of magnetopause for increased solar wind dynamic pressure, with both the subsolar and flank distances decreasing.
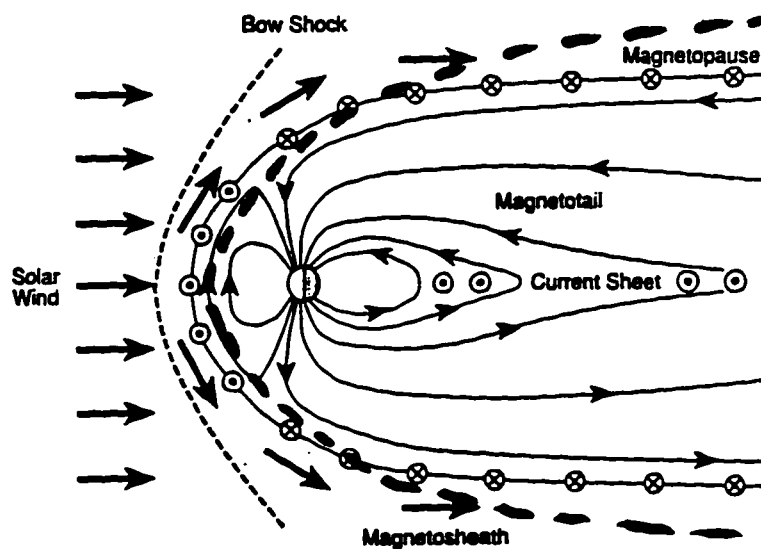
Figure 1.10b: Flaring induced by enhancement of negative IMF B_Z. The new equilibrium position has decreased subsolar distance but increased flank distances. [Adapted from *Kivelson and Russell*, 1995.]

will decrease since there is less magnetic flux on the dayside to resist magnetosheath pressure (Figure 1.10b). The resulting change of shape blunts the magnetopause, and exposes the widened flanks to more magnetosheath pressure, which would be expected to alter the magnetospheric interaction with the solar wind.

Dungey [1963] predicted that reconnection at the magnetopause may also occur when IMF is northward, but in this case would occur tailward of the cusp where the draped IMF lines would be anti-parallel to the magnetopause field (see Figure 1.6b). This process undoes the effects of subsolar reconnection by transforming open field lines that stretch into the tail and making them close on the dayside, thereby increasing the flux on the dayside.

The dawn-to-dusk electric field in the tail will be strongly influenced by B_Z, which should change the magnetospheric convection patterns. This will influence the rate at which magnetic flux is convected to the dayside and possibly result in a change to the size and shape of the magnetosphere. Convection patterns in the ionosphere, which are believed to mirror those in the magnetosphere, are observed to turn over on a timescale of about 1 to 2 hours, the time it takes a magnetic field line frozen to the plasma to be dragged across the polar cap ($\sim$ 2000 km) at several hundred m/sec. *Coroniti and Kennel* [1973] showed that the timescale for changes in magnetospheric convection is essentially determined by the resistivity of the ionosphere, and estimated it at one hour, compatible with observations. Thus, convection is just as important as reconnection in explaining changes to the magnetopause size and shape, since the net effect of both combined processes is what determines these changes.

Since reconnected flux is convected over the poles, the flaring of the tail would be expected to occur mostly near the noon-midnight meridian plane. If this additional flux was not redistributed, the effect of flaring near the equatorial plane might be minimal and the the tail may no longer be roughly circular in cross-section, as is usually assumed. Thus, magnetotail flaring may possibly create a strong asymmetry in average shape of the magnetosphere. As previously mentioned, the viscous coupling mechanism of *Axford and Hines* [1961] is generally pictured to be stronger near the equatorial plane and weaker near the meridian plane, providing another mechanism to generate this type of asymmetry. The magnetic cusp will also produce an asymmetry between the magnetopause shape in the meridian and equatorial planes, if the magnetopause is indented by magnetosheath pressure in this area of weak magnetic

pressure. Through all of these mechanisms, we therefore expect an asymmetry between the noon-midnight meridian and equatorial planes with the degree strongly influenced by B_Z.

The rotation of the Earth causes the dipole direction to constantly change, so that it rarely is exactly perpendicular to the Sun-Earth line. Since the magnetotail is aligned with the solar wind flow direction, but the inner magnetosphere is centered around the dipole axis, these two portions of the magnetosphere are "hinged" together. Tilt of the geomagnetic dipole should produce further asymmetry in the northern and southern hemispheres through this hinging, and also pushes one cusp sunward and the other tailward. Changing tilt means the shape of the magnetosphere is reconfigured on a daily basis, even in the absence of solar wind changes. The other components of the IMF, B_X and B_Y, also probably have a direct influence on the shape of the magnetopause, since they will control the location of reconnection at the magnetopause and may preferentially cause flux to be distributed differently between hemispheres. Despite these effects on shape, dipole tilt and IMF B_X and B_Y are believed to have a weaker affect on activity than B_Z as has been ascertained by numerous statistical studies.

In Chapter 4 we investigate the effect of some of these factors on the 3-D shape of the magnetosphere.

1.3.2 Geomagnetic storms and magnetospheric substorms

Two types of intense magnetospheric activity, the geomagnetic storm and the magnetospheric substorm, involve large scale reconfiguration of the magnetosphere. Geomagnetic storms cause the most intense perturbations to the geomagnetic field, occurring several times per year. The strongest are often caused by strong interplanetary shock waves originating at the Sun. Such shocks can travel at > 1000 km/sec, considerably faster than the average solar wind speed. They can strongly compress the magnetosphere and enhance the magnetopause currents during the initial phase. The ring current is also strongly enhanced on slower timescales, and is responsible for the main phase. The magnetic signatures from both of these enhanced current systems can be detected on the ground by magnetometers [see review by *Gonzalez et al.*, 1994].

There are also the smaller but more common "magnetospheric substorms", which

occur on almost a daily basis, creating the characteristic auroral displays in the auroral oval, but often at moderate or weak levels. They typically occur in rapid succession during a geomagnetic storm, giving them their name [*Akasofu*, 1964]. Much of the activity can be described by large changes in the cross-tail current system and field-aligned currents which are closed by large currents in the ionosphere in the auroral oval. Again these changes can be detected on the ground, but the signatures are more intense in the auroral zones, rather than worldwide as in geomagnetic storms. In one popular model of the substorm, large scale reconnection occurs in the tail at a "near Earth neutral line" and releases magnetic energy that has been stored in the tail. Reconnection reconfigures the open magnetic field lines in the tail, producing equal numbers of closed field lines and those disconnected from the Earth. A closed field line points northward near the equatorial plane, and is said to have a "positive B_Z". When created the disconnected line will point southward or have "negative B_Z". Satellite measurements of negative B_Z indicate that reconnection may indeed occur in the magnetotail.

Global magnetospheric activity is believed to be adequately represented by the K_p index [*Chapman and Bartels*, 1940], which is produced by combining records of the perturbations observed in mid-latitude magnetic field measurements. Both geomagnetic storms and magnetospheric substorms are known to be strongly influenced by a high solar wind dynamic pressure P_D, which appears to be essential for the geomagnetic storm. However, the north-south component of the interplanetary magnetic field, IMF B_Z, is also important [*Gonzalez et al.*, 1994]. Numerous case studies since the 1960's using data collected from ground-based and spacecraft-borne instruments have established that the P_D and IMF B_Z are also especially significant for substorm production. Substorm activity tends to be high when IMF B_Z is negative and low when it is northward, but the relationship is not simple and not yet fully understood. There is also more substorm activity when the dynamic pressure is high, but again no simple pattern has yet been found. Nevertheless these correlations suggest there may be a quantitative relationship between K_p and solar wind conditions. A number of other variables are also probably involved in determining K_p, but P_D and IMF B_Z are probably the most significant.

The magnetosphere is highly dynamic, as we have just seen, and quantitative models for this ever changing system have yet to be developed. Changes such as

those just described will also be self-consistently reflected in the current systems generated in a global simulation, driven by the dynamic pressure and IMF B_Z input into the simulations. Although the effects of dynamic pressure can be estimated well by scaling, the net result of all of the effects due to B_Z (reconnection, convection patterns, internal current systems) are very difficult to calculate analytically. These changes will easily be handled by the global simulation, however, and can be directly related to the solar wind values. This dissertation will investigate how magnetospheric activity and changes in the configuration associated with substorms depend on solar wind conditions.

1.4 Empirical Descriptions of Magnetosphere

We have seen that the average configuration of the magnetosphere and the shape of the magnetopause and their dependence on solar wind conditions is a global problem. Another way to study the global configuration is to use large numbers of observations gathered by many spacecraft. Statistical studies of such data have allowed a good empirical description of many regions of the magnetosphere to be developed in recent years, both in the form of large data sets and descriptive models derived from them. The magnetotail has been explored by many spacecraft and large databases containing many tens of thousands of magnetometer measurements have been assembled. While a general picture of the magnetotail was developed within a few years, it is very dynamic and can be drastically reconfigured by reconnection, especially during storms and substorms [*Fairfield and Ness*, 1970].

The average configuration of the magnetospheric magnetic field is described by several semi-empirical models [*Olson and Pfitzer*, 1974; *Mead and Fairfield*, 1975; *Tsyganenko and Usmanov*, 1982; *Tsyganenko*, 1987; *Tsyganenko*, 1989; *Tsyganenko*, 1995a], which fit the parameters of a limited physical description to measurements producing a more realistic description than that given by earlier physical models, some of which even lack a magnetotail [e.g., *Mead and Beard*, 1964]. For example, the T89 magnetic field model of *Tsyganenko* [1989] is derived from least squares fits to tens of thousands of magnetic field measurements and provides a useful description of the magnetosphere that can predict the average magnetic field at any given point within $\sim 50\%$ out to 70 R_E in the tail. Such models have been used in numerous studies, from mapping auroral zones out to the magnetotail [*Elphinstone et al.*, 1991] to studying

particle kinetics in this global magnetic field [*Ashour-Abdalla et al.*, 1993]. The model depends on the K_p index and not directly on solar wind parameters. The model assumes a closed configuration although it is produced from measurements during both northward and southward IMF. The model also lacks a magnetopause and the tail is stretched much more than observations suggest [*Stern and Tsyganenko*, 1992; *Tsyganenko*, 1995b]. The more recent T95 model of *Tsyganenko* [1995a] addresses these shortcomings and, for example, does include a magnetopause surface, but it has a prescribed shape and is not self-consistently produced. Although simple to use and fairly realistic, the lack of physics means such models cannot be used to independently study the magnetospheric configuration, but rather their use must be limited to applications using the derived model configuration.

Thousands of magnetopause crossings have also been collected in the last 30 years [*Fairfield*, 1971; *Formisano et al.*, 1979; *Song et al.*, 1988; *Sibeck et al.*, 1991]. Another global model derived from empirical data is the magnetopause model of *Roelof and Sibeck* [1993], derived from correlating about a thousand observations of magnetopause crossings with solar wind measurements. Given the solar wind conditions, this model can predict the position of the magnetopause within $\sim 1R_E$ on the dayside and $\sim 2R_E$ on the nightside. This is useful, for example, in determining if a spacecraft will be inside or outside the magnetopause at a given time. Such a magnetopause boundary can also be used as the inner boundary for the gasdynamic simulations that have successfully modeled the flow of the shocked solar wind in the magnetosheath [*Spreiter et al.*, 1969; *Stahara et al.*, 1989] or as the outer boundary of a magnetospheric model, e.g. the aforementioned T95 model [*Tsyganenko*, 1995a]. Such models are necessary to predict "space weather" [*Maynard*, 1995] , the immediate environment in near-Earth space, which directly affects radio communications through coupling to the ionosphere and electrical power systems on the ground through induced currents. This forecasting is hoped to be accomplished in real time using the solar wind parameters typically measured an hour upstream of the Earth. The lack of physics in the empirical models, however, will severely limit the detail of the forecast.

This empirical description of the magnetosphere represented by these and other models is far from complete, however, since data sampling has been severely limited by the numbers and orbits of these spacecraft. While an average description of some

magnetospheric region can often be determined in the least squares sense, it is much more difficult to determine how this description depends on solar wind parameters. Typically only about half of the measurements in a data set are accompanied by simultaneous solar wind measurements, which are required for magnetospheric behavior or structures to be correlated with the controlling solar wind parameters. Such constraints prevent basic aspects of the magnetospheric configuration, such as the aforementioned asymmetry of the magnetopause, from being resolved by such empirical models at present, requiring the models instead to assume axisymmetry. Numerous other processes and variations operating on vastly different size and timescales, such as magnetospheric substorms, the ring current, the ever changing tilt of the geodipole, coupling with the ionosphere, etc., create perturbations to the magnetosphere that vastly complicate the global picture, often making such determinations very difficult, if not impossible. The physics of the interaction of the solar wind with the magnetosphere is usually lacking in these empirical models, creating a fundamental limitation. Despite these limitations this empirical description of the magnetosphere provides a framework to guide the global modeling, which gains credibility if it can reproduce empirical results.

1.5 Self-Consistent Models of the Magnetosphere

Self-consistent descriptions of the magnetosphere embodied in global models can provide another solution to the global problem. They necessarily are based to some degree on the physics that describes the interaction of the solar wind with the Earth's magnetosphere, a fundamental advantage over the empirical approach. They also automatically provide a global solution to a global problem, which is difficult if using only localized measurements.

1.5.1 Global magnetospheric simulations

Global simulations of the magnetosphere using a fluid description of the plasma are computationally feasible using the magnetohydrodynamics or MHD equations. In MHD the plasma is assumed to be quasi-neutral, i.e. the electron and proton densities are assumed to be equal everywhere, and the displacement current is ignored in Maxwell's equations. As shown in the next chapter, these assumptions lead to many

simplifications, but they also fundamentally restrict the physics making it impossible to describe microphysical processes. Equal proton and electron densities means this is a "single fluid" description of the plasma with a single independent density, temperature, etc., at each point in space, which cuts the number of fluid variables in half. More importantly, these assumptions greatly increase the time and length scales that can be resolved in the fluid making computation vastly easier.

Lebouef et al. [1978] and *Lyon et al.* [1980, 1981] constructed the first 2-D global simulations of the magnetosphere, and were able to produce a bow shock, a magnetospheric cavity, and magnetosheath flow. Global model development rapidly followed the call for a three-dimensional analysis of magnetospheric magnetic fields by several authors [*Akasofu et al.*, 1978; *Fairfield*, 1979a; *Coroniti et al.*, 1980], who recognized a need for analysis to escape the noon-midnight meridian plane of *Dungey* [1961] and the equatorial plane of *Axford and Hines* [1961]. The 2-D simulations were immediately followed by the 3-D global simulations of three groups [*Lebouef et al.*, 1981; *Brecht et al.*, 1981, 1982; *Wu et al.*, 1981, 1983].

In global MHD simulations of the magnetosphere a solar wind plasma is blown into a simulation box containing a magnetic dipole which interacts with the flowing solar wind as the simulation is allowed to evolve in time. Internal physical boundaries, such as the bow shock or magnetopause, are self-consistently calculated based on the physics involved, and a magnetospheric cavity is generated surrounded by flow in the magnetosheath (see Figure 1.11). Magnetic reconnection is very apparent in these simulations, producing magnetic field topology with both open and closed configurations, with reconnection occurring both at the dayside magnetopause and in the tail. Viscous processes can also be present, so global simulations can be used to study the solar wind-magnetosphere interaction. The resulting magnetospheric configuration is very sensitive to the solar wind conditions, especially the orientation of the introduced IMF. An inner model boundary representing the ionosphere was introduced [*Wu et al.*, 1983; *Ogino and Walker*, 1984], and then coupled with a separate ionospheric model by *Fedder and Lyon* [1987]. Many of these early global magnetospheric simulations are reviewed by *Brecht* [1985], and the differences in methodology discussed. The mechanics of global MHD simulations are described further in Chapter 2.

Global simulations have successfully produced many other qualitative features of
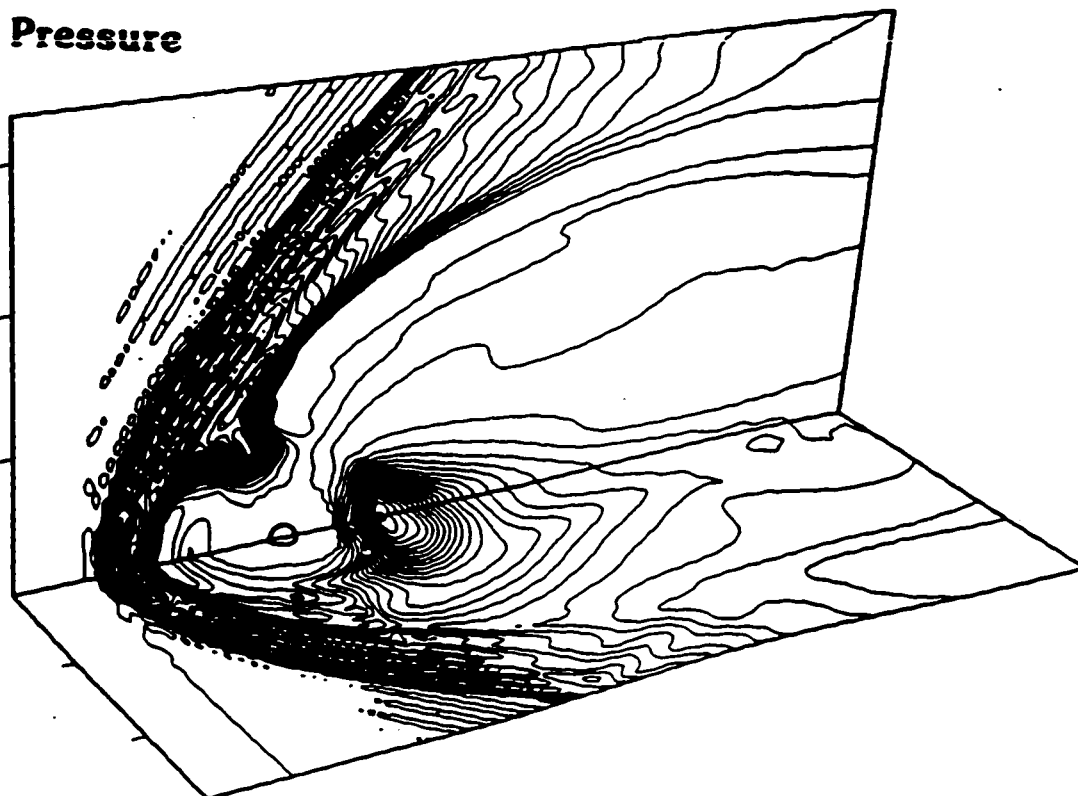
Pressure

Figure 1.11: Plasma pressure contours clearly outline the bow shock and magnetopause, which are formed self-consistently in global magnetospheric simulations. This 3-D MHD simulation of *Watanabe and Sato* [1990] employs a quarter space using symmetry boundary conditions across the equatorial (horizontal) and noon-midnight meridian (vertical) planes. Uniform low pressure in the solar wind, which blows in from the left, gives way across the bow shock to high pressure plasma of the magnetosheath, then across the magnetopause to low uniform pressure in the magnetospheric lobes. High pressure of the plasma sheet is seen tailward of the Earth, especially in the equatorial plane. High pressure also fills an indentation at the magnetic cusp. The magnetospheric configuration produced by the model can be studied looking also at density, velocity, magnetic field, electric current, etc.

the global magnetosphere, described in Section 1.2. These include (1) the structures of the magnetotail, i.e. cross-tail current sheet, plasma sheet, lobes, and mantle; (2) additional aspects of the magnetic topology, such as the cusp, neutral lines, and the draping of magnetic field lines in the magnetosheath, and (3) field-aligned currents concentrated in an oval at auroral latitudes qualitatively displaying many of the statistical patterns compiled by observers. The qualitative configuration produced by global models, especially the dependence of the magnetic topology on IMF orientation (Figure 1.12) and the generation of field-aligned currents (Figure 1.13), has been extensively studied with several models for over a decade now with more mature global models, an application we call "case studies". The models used to perform these case studies include: (1) the "Wu" model [*Wu*, 1983, 1984, 1985], (2) the "Ogino and Walker" model [*Ogino and Walker*, 1984; *Ogino et al.*, 1985, 1986, 1989, 1990, 1992, 1994, 1996; *Ogino*, 1986; *Walker and Ogino*, 1988, 1989, 1996; *Walker et al.*, 1987, 1989, 1993; *Chen et al.*, 1993], (3) the "Fedder and Lyon" model [*Fedder and Lyon*, 1987, 1995; *Fedder et al.*, 1991, 1995a; *Slinker et al.*, 1995; *Chen et al.*, 1995], (4) the "Watanabe and Sato" model [*Watanabe and Sato*, 1990; *Watanabe et al.*, 1992; *Kageyama et al.*, 1992; *Usadi et al.*, 1993], (5) the "Raeder" model [*Raeder*, 1994; *Raeder et al.*, 1995; *Berchem et al.*, 1995a, 1995b], and (6) the "Winglee" model [*Winglee*, 1995].

1.5.2 New applications of global magnetospheric modeling

In the last few years two other applications of global fluid models have emerged. In "event studies" the idealized solar wind input is replaced with that actually measured by an interplanetary monitor during a specific period which is used to drive the simulation with three of these models [*Frank et al.*, 1995; *Fedder et al.*, 1995b; *Winglee et al.*, 1996]. Unlike these idealized steady-state mathematical models of magnetic reconnection discussed in Section 1.2.5, temporal and spatial variations in the reconnection rate produced by a varying solar wind interacting with a dynamically changing magnetopause are automatically handled by a 3-D global simulation. The resulting time-dependent magnetospheric configuration is studied in order to understand an event of interest and can provide information about regions not observed during the event. Measurements taken by other spacecraft located at various places within the magnetosphere can be directly compared to synthetic data from the
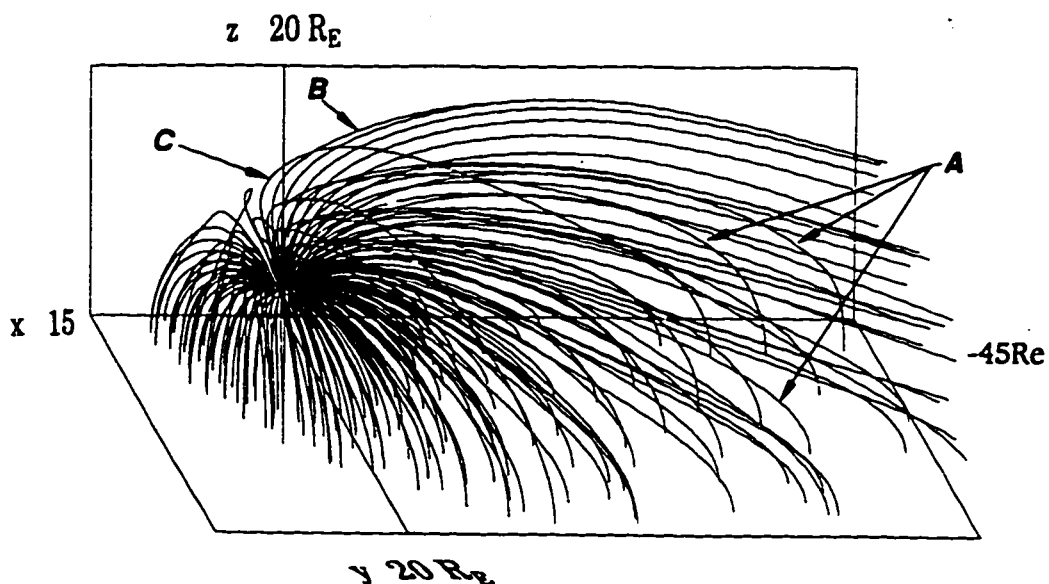
Figure 1.12: Magnetic field lines traced from the northern polar cap of the Earth in a global MHD magnetospheric simulation by *Ogino et al.* [1992] for northward IMF and are seen to fill up the magnetospheric cavity. These field lines indicate a closed magnetic topology of the magnetosphere for this symmetric case, in which all lines intersect the equatorial plane and will close in the southern polar cap. The limit of the footpoints of these field lines in the equatorial plane marks the approximate position of the magnetopause. The cusp lies near the point dividing dayside lines from magnetotail lines. Reconnection just tailward of this point is occurring (C) and has just created a new field line on the dayside.

12

18
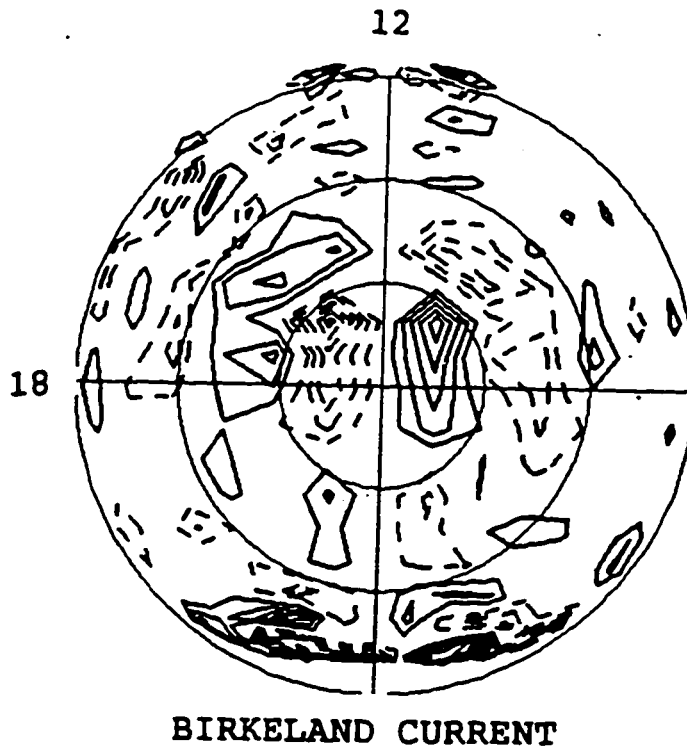
BIRKELAND CURRENT

Figure 1.13: The pattern of mapped field-aligned (or Birkeland) currents in the iono-
sphere generated in the global MHD magnetospheric simulation of *Fedder and Lyon*
[1995], presented as in Figure 1.9 with noon at the top. Solid (dashed) lines indicate
currents away from (toward) the ionosphere. Strong Region 1 currents are present,
in addition to oppositely directed Region 0 currents, while the most equatorward
current system (Region 2) is relatively weak. There is a general correspondence with
the average empirical pattern determined by *Iijima and Potemra* [1978.]

corresponding time and location of the simulation. Comparisons can also be made with ground or ionospheric measurements as well, if the simulation parameters are mapped down to these altitudes.

Large scale kinetics (LSK) examines particle motion in the magnetic and electric field produced by the global model, and is able to determine some kinetic effects such as transport of particles from one region to another or the composition of the plasma pressure tensor [*Walker and Ashour-Abdalla*, 1995]. Studies of particle orbits in a prescribed magnetospheric magnetic field have progressed from simple physical models [*Williams and Mead*, 1965; *Taylor and Hones*, 1965; *Roederer*, 1969] to the more realistic empirical models [*Ashour-Abdalla et al.*, 1993]. These studies are now using a snapshot of the global magnetospheric field at an instant in time [*Richard et al.*, 1994], but soon may be done using a magnetospheric configuration evolving in time [*Walker and Ashour-Abdalla*, 1995].

The resulting magnetospheric configuration, which depends directly on the solar wind input, can also be parametrically studied by running a large number of simulations so the direct dependence of the magnetospheric configuration upon solar wind parameters can be quantified. This is a new application of global MHD simulations, which we may call "quantitative studies" or "parametric studies". A literature search shows that the direct quantitative determination of any magnetospheric structure with a range of solar wind conditions has not been previously attempted. Large scale magnetospheric structures such as the magnetopause can be studied and quantified. The quantitative effect of additional variables on the magnetospheric configuration, e.g. dipole tilt, can potentially be addressed as well.

The comparison with empirical models and averaged spacecraft data also has relatively little precedent, consisting at present of only a few published studies using four of the global models [*Walker and Ogino*, 1988; *Walker et al.*, 1989; *Kaymaz et al.*, 1995; *Khurana et al.*, 1996; *Elsen and Winglee*, 1996a (presented in Chapter 3)]. *Walker and Ogino* [1988] studied how the pattern of field-aligned currents mapped to the ionosphere changes with IMF orientation and compared these results to current patterns inferred from spacecraft passes over the polar cap. *Walker et al.* [1989] studied how the shape of the curved neutral sheet in the tail changes with dipole tilt; the neutral sheet generated by a global code at different dipole tilt angles was compared to the empirical models of *Fairfield* [1980] and *Gosling et al.* [1986]. *Kay-*

42

maz et al. [1995] compared averages of magnetic field measurements by IMP 8 in the magnetotail with those generated by a 3-D global MHD model. *Khurana et al.* [1996] compared the ionospheric electric potential from the empirical model of *Heppner and Maynard* [1987] with that generated by a 3-D global MHD model. The empirical comparisons in the first four studies, however, are still essentially qualitative in nature, while the empirical comparisons performed for this dissertation (and the latter study) are much more quantitative in nature.

1.6 Scope of Research

This dissertation describes 2-D and 3-D global simulations of the magnetosphere that quantitatively determine the average state of the magnetosphere as a function of solar wind conditions. These studies are essentially self-contained and so the specific motivation for each study is contained within the chapter along with any background material necessary to understand it. Predicted variations of magnetospheric regions are then compared to various empirical descriptions of the magnetosphere. This second phase is critically important, since it allows us to test and calibrate the simulations and also to establish credibility for the results.

Chapter 2 contains more technical material on the MHD equations and the mechanics of global simulations. Chapter 3 is a 2-D study which uses a modified MHD formulation to study the magnetic field and field-aligned currents in the noon-midnight meridian. A new methodology of time averaging the simulation output is introduced which produces more representative measurements, which may provide a better comparison to empirical data than a snapshot at a single time. Comparisons are made with an empirical magnetic field model to study mapping and the position of the neutral line is compared to ensemble averages of satellite data.

Chapter 4 studies the 3-D shape of the magnetopause generated by a 3-D global MHD simulation. The global model output is again studied in a new way, this time by generating a mathematically simple magnetopause model that predicts how the average three-dimensional shape of the magnetopause depends on the solar wind dynamic pressure and IMF B_Z. Extensive comparisons are made with empirical magnetopause models and good agreement is found. The asymmetry between the noon-midnight and equatorial planes is also studied and quantified, which the empirical models cannot provide. Chapter 5 summarizes the results, presents ideas on how they can be

refined, and suggests several similar "quantitative studies" of the magnetosphere for future work.

Chapter 2

MHD AND GLOBAL SIMULATION METHODOLOGY

This chapter develops the MHD equations used in the global simulations from the two-fluid equations. The limitations of the MHD approximation are discussed, along with the conditions that permit certain terms in the equations to be ignored. The methodology used in the global simulations is described in detail and previous results from global simulations are briefly discussed.

2.1 Macroscopic Fluid Equations

2.1.1 Conservation laws

By integrating the plasma kinetic equation for each plasma species over velocity space, macroscopic fluid equations can be derived [cf. *Parks*, 1991]. The zeroth moment gives a continuity equation for each species

$$\frac{\partial n_\alpha}{\partial t} + \nabla \cdot (n_\alpha \mathbf{V}_\alpha) = s_\alpha, \tag{2.1}$$

where n_α is the number density and $\mathbf{V}_\alpha$ is the mean velocity for species α. Sources and sinks are represented by s_α, but this term is only significant in the ionosphere, so we set it to zero. Multiplying by and integrating over velocity gives a momentum equation

$$m_\alpha n_\alpha \frac{\partial \mathbf{V}_\alpha}{\partial t} + m_\alpha n_\alpha (\mathbf{V}_\alpha \cdot \nabla) \mathbf{V}_\alpha = -\nabla \cdot \overset{\leftrightarrow}{\mathbf{P}}_\alpha + q_\alpha n_\alpha (\mathbf{E} + \mathbf{V}_\alpha \times \mathbf{B}) + \mathbf{K}_\alpha, \tag{2.2}$$

where m_α is the mass and q_α is the electric charge for species α, $\mathbf{E}$ and $\mathbf{B}$ are the macroscopic (spatially averaged) electric and magnetic fields, $\mathbf{K}_\alpha$ represents the effects of particle collisions, and $\overset{\leftrightarrow}{\mathbf{P}}_\alpha$ is the pressure tensor of each species given by

$$\overset{\leftrightarrow}{\mathbf{P}}_\alpha = n_\alpha m_\alpha \int (\mathbf{v} - \mathbf{V}_\alpha)(\mathbf{v} - \mathbf{V}_\alpha) f_\alpha \, d\mathbf{v}, \tag{2.3}$$

where f_α is the distribution function for that species and the integral is performed over all velocities $\mathbf{v}$. The second moment integration gives an energy relation for

each species (not shown) [cf. *Boyd and Sanderson*, 1969]. When we assume a fully ionized plasma with only protons and electrons, these equations provide a "two-fluid" description.

We obtain a single fluid description by combining the two-fluid equations. Multiplying the continuity equations for each species by m_α and adding them together gives a conservation of mass relation

$$\partial \rho_m / \partial t + \nabla \cdot (\rho_m \mathbf{V}) = 0, \tag{2.4}$$

where $\rho_m = m_i n_i + m_e n_e$ is the mass density of the fluid and $\mathbf{V} = (m_i n_i \mathbf{V}_i + m_e n_e \mathbf{V}_e)/\rho_m$ is the center of mass fluid velocity. The net charge density is $\rho_q = q_i n_i + q_e n_e = e(n_i - n_e)$ and the current density is $\mathbf{J} = q_i n_i \mathbf{V}_i + q_e n_e \mathbf{V}_e = e(n_i \mathbf{V}_i - n_e \mathbf{V}_e)$, where e is the elementary unit of charge. Multiplying the continuity equations by q_α and adding gives a conservation of charge relation

$$\partial \rho_q / \partial t + \nabla \cdot \mathbf{J} = 0. \tag{2.5}$$

Adding the momentum equations gives the single-fluid equation of motion:

$$\rho_m \frac{\partial \mathbf{V}}{\partial t} + \rho_m (\mathbf{V} \cdot \nabla) \mathbf{V} = -\nabla \cdot \overset{\leftrightarrow}{\mathbf{P}} + \rho_q \mathbf{E} + \mathbf{J} \times \mathbf{B}. \tag{2.6}$$

The collision terms have cancelled out since $\mathbf{K}_i = -\mathbf{K}_e$ as required by Newton's third law. The pressure tensor $\overset{\leftrightarrow}{\mathbf{P}} = \overset{\leftrightarrow}{\mathbf{P}}_i^{CM} + \overset{\leftrightarrow}{\mathbf{P}}_e^{CM}$, where each pressure component is calculated in the center of mass frame, i.e. relative to the mean fluid velocity $\mathbf{V}$. An electric body force $\rho_q \mathbf{E}$ and a magnetic body force $\mathbf{J} \times \mathbf{B}$ result from the Lorentz force.

This equation can be more generally put into "conservative form":

$$\frac{\partial}{\partial t} (\mathbf{p} + \mathbf{g}) + \nabla \cdot \left(\overset{\leftrightarrow}{\mathbf{\Pi}} + \overset{\leftrightarrow}{\mathbf{T}} \right) = 0. \tag{2.7}$$

Here $\mathbf{p} = \rho \mathbf{V}$ is the fluid momentum, $\mathbf{g} = \mathbf{E} \times \mathbf{B}/\mu_0 c^2$ is the momentum carried by the electromagnetic field, $\overset{\leftrightarrow}{\mathbf{\Pi}}$ is the fluid momentum flux density tensor given by $\Pi_{jk} = \rho V_j V_k + P_{jk}$ and $\overset{\leftrightarrow}{\mathbf{T}}$ is the Maxwell or electromagnetic stress tensor given by $T_{jk} = \epsilon_0(E^2 \delta_{jk}/2 - E_j E_k) + (B^2 \delta_{jk}/2 - B_j B_k)/\mu_0$, where δ_{jk} is the Kronecker delta. This equation just says that the rate of change in the total momentum (fluid plus

electromagnetic) in a volume equals the rate at which momentum is transferred across the boundaries by the fluid and electromagnetic field.

This method also gives an energy conservation relation in its most general form:

$$\frac{\partial}{\partial t}\left(\frac{\rho V^2}{2} + U + u_{EM}\right) + \nabla \cdot \left[\left(\frac{\rho V^2}{2} + U\right)\mathbf{V} + \overset{\leftrightarrow}{\mathbf{P}} \cdot \mathbf{V} + \mathbf{S} + \mathbf{Q}\right] = 0. \qquad (2.8)$$

Here $U = P_{jj}/2$ is the fluid internal energy density and $u_{EM} = (\epsilon_0 E^2/2 + B^2/2\mu_0)$ is the electromagnetic energy density. The Poynting vector $\mathbf{S} = \mathbf{E} \times \mathbf{B}/\mu_0$ gives the transport rate of electromagnetic energy. Additional heat flux is represented by $\mathbf{Q}$, which in general can be due to a number of dissipative processes, e.g. viscosity, thermal conduction, diffusion, and electrical resistivity, which all increase the entropy density of the fluid and are represented by scalar coefficients. The left hand term represents the rate of change of the total energy density (bulk kinetic, internal, and electromagnetic) in a volume, while the right hand term gives the flux of energy out of this volume. The additional term $\overset{\leftrightarrow}{\mathbf{P}} \cdot \mathbf{V}$ represents the flux of work done by pressure forces on the fluid [*Landau and Lifshitz*, 1987].

Poynting's theorem in its differential form, $\partial u_{EM}/\partial t + \nabla \cdot \mathbf{S} = \mathbf{J} \cdot \mathbf{E}$, can be used to simplify this equation. The increase in fluid energy is represented by Joule heating, $\mathbf{J} \cdot \mathbf{E}$, which includes both adiabatic (reversible) heating as well energy dissipation due to electrical resistivity, an irreversible process we may call ohmic heating. While other dissipative processes such as viscosity and thermal conduction are often included in ordinary fluid mechanics, we shall neglect them, since this is usually a good approximation in a collisionless plasma. Compression of collisionless plasma is usually nearly adiabatic, with the major exception of collisionless shock waves, which are thermodynamically irreversible and produce large increases in entropy. Introducing $\varepsilon = \rho V^2/2 + U$ to represent the total fluid energy density, we have:

$$\frac{\partial \varepsilon}{\partial t} + \nabla \cdot (\varepsilon \mathbf{V} + \overset{\leftrightarrow}{\mathbf{P}} \cdot \mathbf{V}) = \mathbf{J} \cdot \mathbf{E}. \qquad (2.9)$$

2.1.2 Closing the fluid equations

The moment equations described are not closed, i.e. there are more variables than equations, a problem cannot be remedied by taking higher order moments [cf. *Boyd and Sanderson*, 1969]. The equations must be closed by assuming relations among

the existing variables, e.g. a relation for the electric field in Ohm's law. Multiplying the momentum equations by q_α/m_α and subtracting them gives a "generalized Ohm's law",

$$\frac{\partial \mathbf{J}}{\partial t} + \nabla \cdot (\mathbf{VJ} + \mathbf{JV} + \rho_q \mathbf{VV}) = \left(\frac{e^2 n_i}{m_i} + \frac{e^2 n_e}{m_e}\right)\mathbf{E} +$$

$$\frac{e^2 n_i}{m_i}\mathbf{V}_i \times \mathbf{B} + \frac{e^2 n_e}{m_e}\mathbf{V}_e \times \mathbf{B} + \frac{e}{m_e}\nabla \cdot \overset{\leftrightarrow}{\mathbf{P}}_e - \frac{e}{m_i}\nabla \cdot \overset{\leftrightarrow}{\mathbf{P}}_i + \left(\frac{e}{m_e} + \frac{e}{m_i}\right)\mathbf{K}_1, \quad (2.10)$$

which can be simplified as follows. The $\mathbf{V}_\alpha \times \mathbf{B}$ terms can be expressed in terms of their average and their difference, i.e. the bulk velocity $\mathbf{V}$ and the current $\mathbf{J}$. Furthermore, $m_i \gg m_e$ allows us to drop several terms. The terms on the left hand side, the "inertial term" involving $\partial \mathbf{J}/\partial t$ and the three "quadratic terms" are negligible for low frequencies, i.e. when $\omega \approx V/L \ll \omega_{pe}V/c$ [cf. *Boyd and Sanderson*, 1969] or equivalently over large distances $L \gg c/\omega_p$. This "electron inertial length" $c/\omega_{pe} \leq 50$ km everywhere in the magnetosphere since the electron plasma frequency $f_{pe} \geq 10^3$ Hz (for $n \geq .01$ cm^{-3}). Thus neglecting these terms is justified in a global magnetospheric simulation, where we require $L \geq 1000$ km for the simulation to be computationally feasible. The collision term is assumed proportional to the difference in velocities and hence proportional to the current, i.e. $-\eta \mathbf{J}$. This is an accurate approximation for a collisional plasma described by a perturbed Maxwellian distribution function, but may not necessarily be true for a collisionless plasma [cf. *Boyd and Sanderson*, 1969]. For a collisional plasma η is the reciprocal of the classical or Spitzer conductivity, $\eta = 1/\sigma = \nu m_e/ne^2$, resulting from the collision frequency ν. This leaves five terms in the Ohm's law:

$$\mathbf{E} + \mathbf{V} \times \mathbf{B} + \eta \mathbf{J} = \frac{m_i}{\rho_m e}\mathbf{J} \times \mathbf{B} + \frac{m_i}{\rho_m e}\nabla \cdot \mathbf{P}_e. \quad (2.11)$$

These one-fluid equations are combined with two of Maxwell's equations:

$$\nabla \times \mathbf{E} = -\frac{\partial \mathbf{B}}{\partial t} \quad \text{and} \quad \nabla \times \mathbf{B} = \mu_0 \left(\mathbf{J} + \epsilon_0 \frac{\partial \mathbf{E}}{\partial t}\right), \quad (2.12)$$

where μ_0 and ϵ_0 are the permeability and permittivity of free space, respectively. The divergence free condition $\nabla \cdot \mathbf{B} = 0$ is not an independent equation, since it can be derived from Faraday's law, but is retained as an initial condition. Poisson's equation

$\nabla \cdot \mathbf{E} = \rho_q / \epsilon_0$ is also not independent and is not used in one-fluid equations. We thus have 14 variables $(\mathbf{E}, \mathbf{B}, \mathbf{V}, \mathbf{J}, \rho_q, \rho_m)$ and 14 equations if we assume that pressure can be represented by a single (scalar) quantity $P = P_i + P_e$, as is customary.

The symmetric pressure tensor has six independent quantities, whose calculation would require 5 more independent equations. Fluid pressure is usually assumed to be isotropic $P_{jk} = P\delta_{jk}$, which holds in a collisional plasma for timescales $\tau \gg 1/\nu$ [cf. *Boyd and Sanderson*, 1969]. This assumption is mathematically convenient, but often not justified in a space plasma which may have very large collision timescales. Fortunately, the magnetic field in a collisionless plasma will produce gyromotion which will restrict particle motion perpendicular to the magnetic field, making the fluid description valid over a perpendicular length scale $L_\perp \gg \rho_i$. Particles are free to travel parallel to the magnetic field, however, so that the pressure tensor can be written in terms of only two pressures, $P_\perp$ and $P_{\parallel}$, the components perpendicular and parallel to the magnetic field, respectively [cf. *Boyd and Sanderson*, 1969]. Closure requires two energy relations, so the distribution of thermal energy between $P_\perp$ and $P_{\parallel}$ must be somewhat arbitrarily imposed [*Hesse and Birn*, 1992], if they are assumed to be coupled.

Therefore, we shall henceforth treat pressure as isotropic, recognizing this assumption has only limited validity in space simulations. This scalar pressure P simplifies the pressure force to $-\nabla P$. The internal fluid energy density U becomes $P/(\gamma - 1)$, which from classical (collisional) thermodynamics is also $U = Nnk_BT/2$, where N is the number of degrees of freedom. The total fluid energy density becomes $\epsilon = \rho v^2/2 + P/(\gamma - 1)$.

2.1.3 Further simplifications

Unfortunately these equations still need further simplification to become tractable for simulations, which require large length and time scales, L and τ. This "MHD approximation" is achieved by assuming quasi-neutrality, i.e. $n_i \approx n_e = n$ and by neglecting the displacement current in Ampère's law (discussed in Section 2.2). Quasi-neutrality is a good approximation for length scales much longer than the Debye length, the distance in which charges are electrically screened out in the plasma:

$$L^2 \gg \lambda_D^2 = \frac{\epsilon_0 k_B T}{ne^2} = \frac{k_B T}{m_e \omega_{pe}^2}, \qquad (2.13)$$

where k_B is Boltzmann's constant, T is the plasma temperature (assuming $T_i = T_e$), and ω_{pe} is the plasma frequency. This criterion is easily met in the magnetosphere and solar wind where everywhere $\lambda_D \leq 1$ km [cf. *Kivelson and Russell*, 1995], but $L \geq 1000$ km.

Often the two left hand terms still remaining in the generalized Ohm's law (Eq. 2.11) can be neglected. The "Hall term" involving $\mathbf{J} \times \mathbf{B}$ can be ignored when the current is small enough compared to the bulk velocity, i.e.

$$\mathbf{V} \times \mathbf{B} \approx VB \gg \frac{m_i}{\rho_m e}\mathbf{J} \times \mathbf{B} \approx \frac{JB}{ne}, \qquad \text{or } J \ll neV. \qquad (2.14)$$

The pressure gradient term is negligible when temperatures are low enough, i.e.

$$\mathbf{V} \times \mathbf{B} \approx VB \gg \frac{m_i}{\rho_m e}\nabla P_e \approx \frac{m_i}{nm_i e}\frac{nk_B T_e}{L} \approx \frac{k_B T}{eL}, \qquad \text{or } k_B T \ll LeVB. \qquad (2.15)$$

Neglecting the Hall term and the pressure gradient terms are not always justified in the magnetosphere. For example, in some parts of the tail current sheet $J \approx 1 - 6 \times 10^{-9}$ A/m² [*Tsyganenko*, 1990], the same magnitude as neV using $n = 0.4$ cm⁻³ and $V = 100$ km/sec, typical values in the plasma sheet. Likewise, the thermal energy in the hot plasma sheet ($k_B T \approx 1 - 5$ keV) can be similar to the electrostatic potential energy difference across the length scale of the current sheet $LeVB$ for $L = 1R_E$, $V = 100$ km/sec, and $B = 5$ nT.

However, neglecting these terms leaves $\mathbf{E} + \mathbf{V} \times \mathbf{B} - \eta\mathbf{J} = 0$, the simpler form of Ohm's law that is usually used in MHD, and which has a mathematical form that necessarily makes the electric field orthogonal to $\mathbf{B}$. The Hall and pressure gradient terms that we have just shown are often significant in some regions of the magnetosphere will give a separation of electrons and ions, which produces an additional ambipolar electric field that may have a non-zero electric field component parallel to the magnetic field, $E_{\parallel}$. This can produce additional field-aligned currents absent in MHD and may also have a significant effect on the global magnetospheric configuration. We shall come back to these terms in Chapter 3 where we use a modified fluid approximation developed by *Winglee* [1994] to perform global 2-D simulations.

Finite Larmor radius effects will come into play if the length scale is on the order of a gyroradius or smaller (see above), so the gridspacing must be chosen such that $L \gg \rho_{ci} = m_i v_i/eB$, where v_i is the ion velocity perpendicular to the magnetic field in

order for the MHD approximation to be valid. In the magnetosphere the largest ion gyroradius might be found near the neutral sheet with a magnitude of several hundred km or $\sim 0.1 R_E$, for a keV plasma when $B \leq 5$ nT, which serves as a practical lower limit to the gridspacing in global simulations.

Poisson's equation does not become identically $\nabla \cdot \mathbf{E} = 0$ under quasi-neutrality, because $(n_i - n_e)$ is allowed to have small perturbed values. The electrostatic field calculated by a one-fluid simulation will not be divergence-free and so this small density perturbation can be estimated through $\Delta n = n_i - n_e = \nabla \cdot \mathbf{E}/\epsilon_0 e$ [cf. *Krall and Trivelpiece*, 1986].

2.2 The MHD Approximation

Quasi-neutrality by itself does not produce the MHD approximation, which requires also that the displacement current be ignored in the Ampère-Maxwell law. High-frequency electromagnetic waves, whose generation explicitly requires the displacement current are not allowed in MHD, so that electromagnetic waves are restricted to low frequency hydromagnetic waves. Fluid velocities are required to be much less than the speed of light when the displacement current is neglected [cf. *Parks*, 1991]. This also means that the energy carried by the electromagnetic field is overwhelmingly magnetic ($B^2/2\mu_0$) and electrical energy ($\epsilon_0 E^2/2$) can be ignored. Similarly, the momentum of the electromagnetic field $\mathbf{g}$ is also negligible compared to the fluid momentum $\mathbf{p}$ [*Landau et al.*, 1984], which simplifies the momentum equation. The electric force is also negligible in the momentum equation [*Boyd and Sanderson*, 1969], since

$$\frac{\rho_q \mathbf{E}}{\mathbf{J} \times \mathbf{B}} \approx \frac{(\epsilon_0 E/L)E}{(B/\mu_0 L)B} = \frac{E^2 \epsilon_0 \mu_0}{B^2} = \frac{V^2 B^2}{B^2} \frac{1}{c^2} = \frac{V^2}{c^2} \ll 1. \qquad (2.16)$$

The Maxwell stress tensor retains only the magnetic terms, so the electromagnetic force has only two significant components. These are the magnetic pressure force $-\nabla(B^2/2\mu_0)$ and the magnetic tension or curvature force $(\mathbf{B} \cdot \nabla)\mathbf{B}/\mu_0$, which combined give the $\mathbf{J} \times \mathbf{B}$ force (missing the contribution from the displacement current).

2.2.1 The MHD equations

The MHD equations with both of these assumptions incorporated become:

$$\frac{\partial \rho}{\partial t} + \nabla \cdot (\rho \mathbf{V}) = 0 \tag{2.17}$$

$$\frac{\partial (\rho \mathbf{V})}{\partial t} + \nabla \cdot (\rho \mathbf{V}\mathbf{V}) = -\nabla p + \mathbf{J} \times \mathbf{B} + \mathbf{f} \tag{2.18}$$

$$\frac{\partial \varepsilon}{\partial t} + \nabla \cdot [(\varepsilon + P)\mathbf{V}] = \mathbf{J} \cdot \mathbf{E} + \mathbf{f} \cdot \mathbf{V} \tag{2.19}$$

$$\frac{\partial \mathbf{B}}{\partial t} = -\nabla \times \mathbf{E} = \nabla \times (\mathbf{V} \times \mathbf{B}) + \nabla \times (\nu_m \nabla \times \mathbf{B}) \tag{2.20}$$

$$\nabla \cdot \mathbf{B} = 0 \tag{2.21}$$

$$\mathbf{J} = \frac{\nabla \times \mathbf{B}}{\mu_0} \tag{2.22}$$

$$\mathbf{E} + \mathbf{V} \times \mathbf{B} = \eta \mathbf{J} \tag{2.23}$$

Here ρ is the fluid mass density (since we shall no longer deal with net charge density), γ is the polytropic index, η is the electrical resistivity, and $\nu_m = 1/(\mu_0 \sigma)$ is the magnetic diffusivity. The MHD equations listed above express the conservation of mass, momentum, and energy in the MHD fluid. The continuity equation (Eq. 2.17) is not altered from ordinary fluid dynamics. The equation of motion (Eq. 2.18) is very similar to the Euler equation of fluid dynamics, except that a magnetic body force ($\mathbf{J} \times \mathbf{B}$) has been added. Gravitational or other conservative body forces represented by a scalar potential, $\mathbf{f} = \rho \nabla \psi$ can easily be added, but often can be neglected, as in our magnetospheric simulations. The energy equation (Eq. 2.19) also contains Joule heating ($\mathbf{J} \cdot \mathbf{E}$) as a source, but otherwise looks like the isentropic energy conservation relation for an ideal (inviscid) fluid [Landau and Lifshitz, 1987]. If additional body forces are included, an energy term $\mathbf{f} \cdot \mathbf{V}$ must be present in the energy equation to account for work done on the fluid by these forces. Sometimes a simpler energy relation, such as the adiabatic or isothermal condition, is assumed instead of the energy conservation equation, reducing the number of free thermodynamic variables by one.

2.2.2 Closure of MHD equations

These fluid equations are joined with three of Maxwell's equations, as in two-fluid theory. Faraday's equation (Eq. 2.20) gives the electromagnetic induction. Current is not independently calculated by $\sum n_\alpha q_\alpha V_\alpha$, as in two-fluid theory, but rather determined through Ampère's law in (Eq. 2.22), where the displacement current has been dropped. No continuity equation is needed for charge, since $\nabla \cdot \mathbf{J} = 0$ because $\mathbf{J}$ has zero divergence from its solenoidal form guaranteed by Ampère's equation. This also means that currents are automatically closed in MHD and current closure does not have to be enforced, as in two-fluid theory. Closure of equations is achieved in the case of MHD by assuming a simplified form Ohm's law, which gives a relation for $\mathbf{E}$.

The resistivity η is usually given by a uniform value over the simulation or sometimes determined through an assumed relation, e.g. $\eta \propto J^2$. In a 3-D system the polytropic index $\gamma = (N + 2)/N = 5/3$, which is generally used in simulations, although measurements show that γ often differs from this ideal value. Nevertheless, both η and γ are prescribed because they cannot be independently calculated with MHD. Pressure P and fluid energy ε are not both independent, and one of them can be expressed in terms of the other variables. For a 3-D situation there are 15 variables ($\mathbf{V}$, $\mathbf{B}$, $\mathbf{E}$, $\mathbf{J}$, ρ, e, p) and 2 (prescribed) coefficients (η, γ) given in (2.17) - (2.23). However, $\mathbf{E}$, $\mathbf{J}$, and P can be expressed in terms of $\mathbf{V}, \mathbf{B}, \rho$, and ε, which reduces the number of independent variables and equations to 8.

2.2.3 Ohm's law and dissipation

The simplest form of Ohm's law (Eq. 2.23) permits only a "convective electric field" ($-\mathbf{V} \times \mathbf{B}$) if resistivity is set to zero. Electrical conductivity is then infinite, giving "ideal MHD", where the magnetic field is frozen into the plasma. A non-zero η allows diffusion of the magnetic field. Resistivity can be ignored when the convective timescale is much less than the diffusive timescale. The ratio of these timescales defines the Lundquist or magnetic Reynolds number

$$R_M = \frac{\nabla \times (\mathbf{V} \times \mathbf{B})}{\nu_m \nabla^2 \mathbf{B}} \approx \frac{VB/L}{\nu_m B/L^2} = \frac{VL}{\nu_m} = \mu_0 \sigma VL \qquad (2.24)$$

Because the magnetic field specifies a direction at every point in the plasma, the description of electrical resistivity, even in the simplified MHD approximation,

requires several parameters [*Landau et al.*, 1984]. In a uniform, isotropic medium resistivity is gauged by a single scalar dissipative parameter (η). Assuming conductivity is independent of the magnetic field implies that the mean free path of the current carriers is much greater than the gyroradius, or equivalently the collision frequency is much greater than the gyrofrequency, conditions that often are not satisfied by tenuous space plasmas. Plasma resistivity ordinarily is due to Coulomb collisions, but in a collisionless plasma is derived from other microphysical processes such as wave-particle interactions, which provides a substitute for Coulomb collisions. Such microphysical processes may be approximated in MHD by imposing an "anomalous resistivity", which cannot be self-consistently generated in MHD because the necessary physics is missing. The additional terms in Ohm's law, however, are used in the study of Chapter 3 to estimate an effective plasma resistivity η, which otherwise must be imposed somewhat arbitrarily.

2.3 General Methodology for Global Simulations

In general fluid simulations, the variables that describe the fluid are specified at each gridpoint that fills a simulation box. The spacing between these gridpoints determines the spatial resolution of the simulation, so the value of a fluid variable can be thought of as an average over the portion of space represented by the gridpoint. The simulations used for this dissertation were all done on uniformly spaced Cartesian grids. The desired fluid equations are solved numerically as an initial value problem (and can subsequently be driven by boundary conditions, as in our simulations), using finite differencing methods. As implied by its name, finite differencing replaces spatial derivatives with an algebraic difference taken across gridspaces and thus converts differential equations into algebraic equations, which are then straightforward to solve. These methods generally only operate on internal grid points where derivatives are clearly defined, so that gridpoints on any inner or outer boundary must be determined by other means. When these boundary conditions are also specified, this set of typically hyperbolic partial differential equations is allowed to evolve in time, using a finite time step to approximate time derivatives.

First we describe more general properties of the simulations, followed by more specific details of the simulations used for this dissertation in Section 2.4 . In global fluid simulations of the magnetosphere, the initial state consists of a stationary ge-

omagnetic dipole surrounded by plasma that generally is at rest (Figure 2.1). The inner boundary ideally would be a conducting sphere of radius 1 R_E, but in practice is usually set at a radius of 3 to 5 R_E for computational reasons described below. The outer boundary conditions are the faces of the simulation box, whose X axis is customarily aligned with the solar wind flow direction with the magnetic dipole is located in the $X - Z$ plane. The X axis also points toward the sun, Y points in the dusk direction, and Z points northward in this geocentric solar magnetospheric (GSM) coordinate system [*Russell*, 1971]. The magnetic dipole axis is aligned with the Z axis when there is no dipole tilt and constrained to be in the X_Z plane when tilt is non-zero. The solar wind plasma and IMF properties are fixed on the sunward face, so that the solar wind blows down the length of the box as the simulation evolves.

At the beginning of the simulation, the entering solar wind plasma immediately begins to form a shock wave when it collides with the stationary plasma filling the box. This shock wave progresses down the box and after some time the solar wind encounters the dipole, first setting up a standing bow shock and later a magneto-spheric cavity (Figure 2.2). The other faces ideally would be those at infinity, which is usually approximated by a uniform fluid value or a uniform gradient at a suitably large distance from the dipole. If the simulation box is too small these outer boundaries will interfere with the simulation, for example, by allowing fluid to reflect off the boundaries. This problem is alleviated by covering more space, but this requires more gridpoints or greater gridspacing, making a tradeoff that must be decided by considering computational limitations.

2.3.1 *Algorithms and numerical stability*

The numerical algorithm used for the simulations performed for this dissertation is the "Two-step Lax-Wendroff" method, which has been extensively used in many global magnetospheric simulations [*Ogino and Walker*, 1984; *Ogino et al.*, 1985, 1986, 1989, 1990; *Ogino*, 1986; *Walker and Ogino*, 1988, 1989; *Walker et al.*, 1987, 1989; *Winglee*, 1994, 1995; *Winglee et al.*, 1996]. Two-step Lax-Wendroff [*Lax and Wendroff*, 1960] is a general purpose method recommended for sets of hyberbolic partial differential equations that are cast as initial value problems in flux conservative form [*Richtmyer and Morton*, 1967; *Sod*, 1978; *Press et al.*, 1986]. The MHD equations are easily put
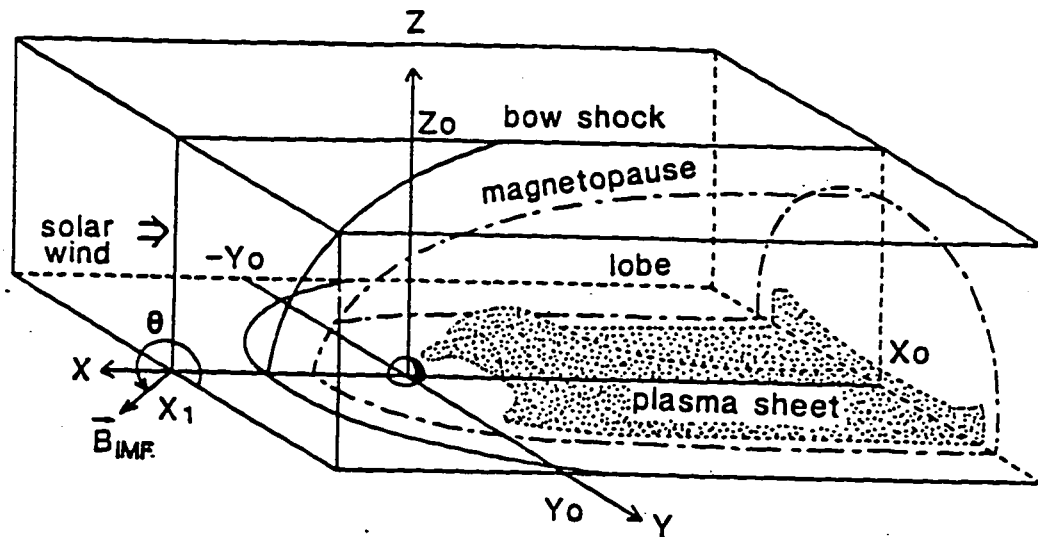
Figure 2.1: The global magnetospheric simulation box is a 3-D gridspace on which the MHD (or other fluid) equations are solved by finite differencing methods. A dipole magnetic field aligned with the Z axis is centered at the position of the Earth, which is surrounded by an inner boundary usually set at about 3 R_E. The solar wind plasma blows in from the left, traveling in the negative X direction, carrying the IMF, which generally can have any orientation. The MHD values of the solar wind are used as boundary conditions on the front face of the box (on left), while free or symmetry boundary conditions are used on the other faces. The bottom face is the equatorial $(X - Y)$ plane in this example, while the noon-midnight meridian plane $(X - Z)$ plane lies at the center of the box. The approximate position of magnetospheric structures, such as the bow shock, magnetopause, and plasma sheet, which are self-consistently generated within the box, are indicated. [From Ogino et al., 1986.]
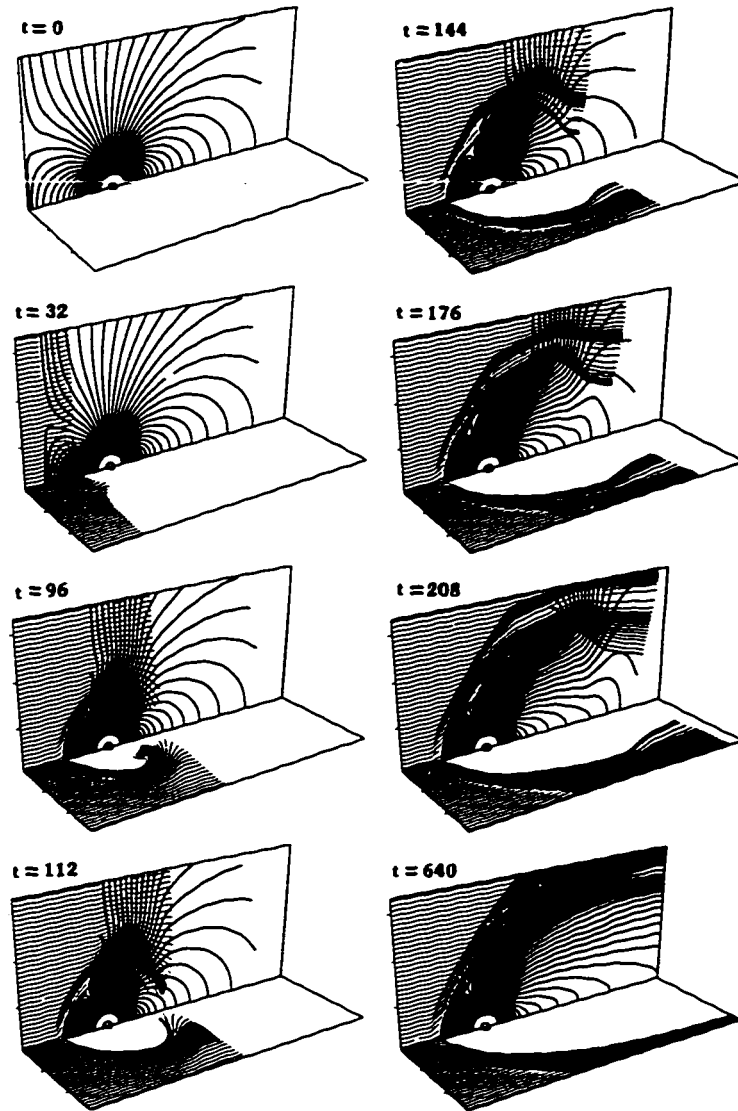
Figure 2.2: Time sequence showing the formation of a magnetospheric cavity during the evolution of the global MHD magnetospheric simulation of *Watanabe and Sato* [1990]. Magnetic field lines (heavy lines) are shown in the noon-midnight meridian plane and plasma flow streamlines (light lines) are shown in both the noon-midnight and equatorial planes. Solar wind enters from the left at time $t = 0$, and compresses of the geomagnetic field into a cavity by end of this sequence, which introduces no IMF. Solar wind plasma flows in straight along streamlines, and does not penetrate the magnetopause (white space in equatorial plane), but is deflected around it in the magnetosheath which eventually reaches the back of the box. Initially the plasma in the portion of box displayed is at rest and the geomagnetic field is given by the superposition of a dipole and an image dipole, as described in Figure 1.1, so it has no component perpendicular to the solar wind flow direction at the front of the box.

into this form,

$$\frac{\partial \mathbf{u}}{\partial t} + \nabla \cdot \mathbf{F(u)} = S(\mathbf{u}), \qquad (2.25)$$

where u is the conserved independent variable, **F** is the conserved flux function, and S is a source term, which is generally desired to be as small as possible [*Press et al.*, 1986].

The first step of the Lax-Wendroff method is to estimate fluid values u at half gridspaces $x_{j+1/2}$ and a half timestep in the future $t_{n+1/2}$ using the existing fluid values on the grid u_n^j and the existing fluxes of this fluid variable F_n^j,

$$u_{j+1/2}^{n+1/2} = \frac{1}{2}\left(u_{j+1}^n + u_j^n\right) - \frac{\Delta t}{2\Delta x}\left(F_{j+1}^n - F_j^n\right) \qquad (2.26)$$

The first term on the left is just a spatial average, shown here only for one dimension, but easily generalized to two or three dimensions, while the second term gives the change due to fluxes in and out of the grid cell. The fluxes at the half timestep and half gridspace $F_{j+1/2}n + 1/2$ are calculated with these updated fluid quantities, which are used in the second step to calculate the fluid quantities on the gridspace after a whole timestep

$$u_j^{n+1} = u_j^n - \frac{\Delta t}{\Delta x}\left(F_{j+1/2}^{n+1/2} - F_{j-1/2}^{n+1/2}\right) \qquad (2.27)$$

The intermediate fluid values $u_{j+1/2}^{n+1/2}$ are then discarded. Since the second step used fluxes centered on the half gridspace ($j \pm 1/2$) and centered in the total time interval ($n+1/2$), a more accurate estimate of the final fluid values u_j^{n+1} results. This method has second-order accuracy in time and space, i.e. the errors are on the order of the square of the finite differencing gridspace and timestep, since the first order errors cancel out [*Press et al.*, 1986].

The most challenging aspect of finding approximate solutions to these types of equations is avoiding numerical instability, which is achieved in Lax-based schemes [*Lax*, 1954] by the addition of spatial averaging in the first step. The price paid for this stability is a numerical error in the simulations over the length scale of a gridspace due to this spatial averaging. This error is called numerical diffusiveness or numerical viscosity, because it is numerically equivalent to introducing a diffusion term in each of the equations. The Lax-Wendroff method overcomes these stability problems fairly well, being numerically robust with a good level of accuracy. It is also

58

easy to program, requires relatively little memory, and is computationally efficient, but has also relatively little diffusiveness for a Lax-based scheme [*Press et al.*, 1986].

The limit of stability for this method (and many other numerical methods as well) is the Courant-Friedrichs-Lewy stability criterion [*Courant et al.*, 1928],

$$\frac{|v|\,\Delta t}{\Delta x} \leq 1, \tag{2.28}$$

where v is a wave mode velocity, Δt is the finite differencing timestep, and Δx is the finite differencing spatial step (or gridspace) [*Press et al.*, 1986]. Physically, this "Courant condition" just says that all wave modes permitted by the equations must be resolved in space and time as they propagate across the grid. If this condition is violated at some location in the simulation, short wavelength waves will be unstable at this point, grow exponentially and quickly contaminate the simulation. In practice this becomes $\Delta t = S\Delta t/|v_{max}|$, where v_{max} is the maximum wavespeed anywhere in the simulation and S is a step-size coefficient, $0 < S < 1$.

For many problems, such as those involving shock waves, as in our simulations, the numerical viscosity of the Lax-Wendroff method alone is inadequate to prevent instability. These nonlinear equations can produce a "nonlinear instability" when fluid quantities have large gradients, which again are most effectively damped out at the shortest wavelength by using "artificial viscosity" [*von Neumann and Richtmyer*, 1950] and other smoothing methods. This additional artificial viscosity has the same numerical form as the numerical diffusion inherent in the Lax-Wendroff algorithm, and in practice is very apparent in the simulations, blurring the simulation features, such as shock waves and current sheets, so they have a minimum thickness of 3 to 5 gridspaces. Other smoothing methods, e.g. Lapidus smoothing [*Lapidus*, 1967] or "flux correction" smoothing [*Boris and Book*, 1973], can also be used in the simulations in combination with artificial diffusion. The advantage of the Lapidus method is that it applies more smoothing at large velocity gradients, exactly where it is most needed, but has very little effect on other portions of the simulation. Unlike diffusion, however, this smoothing operation does not have a simple physical interpretation.

Numerical and artificial diffusion produces an equivalent magnetic diffusivity in the induction equation, which is physically equivalent to a finite electrical conductivity. Smoothing also produces an artificial viscosity in the momentum equation that has the same effect as a physical fluid viscosity. Thus, numerical and artificial

diffusion mimics that produced by physical processes, e.g. providing resistivity that allows magnetic reconnection to occur and viscosity that transports momentum, and so can successfully simulate macroscopic processes of microphysical origin that are believed to have a strong effect on the global magnetospheric configuration (Chapter 1). Artificial mass diffusion also occurs in the continuity equation, while fluid energy diffusion occurs in the energy equation, but these side effects do not produce any desirable behavior in the simulations.

Other numerical methods can be used that are not as diffusive and produce sharper boundaries, but they have other drawbacks, generally requiring more computer memory or computational steps. For example, the global simulation of *Watanabe and Sato* [1990] (shown in Figures 1.11 and 2.2) used a fourth-order Runge-Kutta-Gill method [*Press et al.*, 1986], which is less diffusive than the traditional Lax-Wendroff method. They claim that no mass, momentum or energy are observed to cross the magnetopause in their simulation. This method uses four computational steps rather than two, so it requires twice as much data storage as Lax-Wendroff, which in practice means that for a given memory allocation only half as many gridpoints can be used to define the system. Furthermore, the more complicated algorithm will also be slower, decreasing the amount of physical time that can be simulated for a given amount of CPU time.

2.4 Specifics of Global Magnetospheric Simulations

We now discuss more specific aspects of the simulations performed for this dissertation, with these comments pertaining to the 3-D simulations unless otherwise specified. First we consider the size of the simulation box. The dipole position must be far enough from the front of the box so that the bow shock can stand freely upstream, so $X_{front} \geq 15R_E$. Since the bow shock is so blunt, even a very wide box, say $\sim 60R_E$, will not capture all of it. Fluid entering the box must be allowed to leave, so the simulation must be wide enough to allow the high speed flow of the magnetosheath, in practice $\geq 20 - 24R_E$. The tail length is less critical - short tail simulations have been successfully performed (e.g., $\sim 24R_E$ in *Walker et al.* [1987] and also in the development of the simulations used in this dissertation), but while numerically stable they may not be physically realistic. The longer the tail the more realistic the tail dynamics will be, because the interference from back of the simula-

tion box will be minimized. This usually involves making the tail from $60 - 120R_E$ in most recent simulations, e.g. *Watanabe and Sato* [1990], *Walker and Ogino* [1993], *Berchem et al.* [1995a], and *Winglee et al.* [1996]. A few simulations with extremely long tails ($\geq 300R_E$) have been recently performed [*Fedder and Lyon*, 1995; *Raeder et al.*, 1995], but unless dynamics are being studied very deep in the tail this extreme length shows little difference from a simulation with a tail length of 100 R_E [*Berchem et al.*, 1995a].

The simulation box is set up to exploit symmetry when the noon-midnight meridian plane of the magnetosphere is collocated with an $X-Z$ plane in the simulation box and the equatorial plane is collocated with an $X - Y$ plane. A symmetry boundary condition can be used at the noon-midnight meridian plane when the dawn hemisphere is a mirror image of the dusk hemisphere. A necessary, but not sufficient condition for this symmetry to occur, is when IMF B_Y is set to zero. Symmetry also requires that the incoming plasma velocity has only an X component and the transverse components are set to zero, unlike the real situation which generally has small V_Y and V_Z components. Furthermore, IMF B_X must be set to zero to have symmetry, again contrary to the observed solar wind which generally has an IMF B_X component. Likewise, the northern and southern hemispheres may be mirror images of each other across the equatorial plane when the dipole tilt is zero. If there is no dipole tilt and the IMF has only a Z component, again with the other necessary ideal conditions, then symmetry exists at both planes and only one quadrant needs to be simulated, as in Figure 1.11. This requires only a fourth as many gridpoints or alternatively allows four times as many gridpoints to define the quadrant. The 3-D simulations performed in Chapter 4 exploited this symmetry.

An Earth-centered dipole magnetic field $\mathbf{B}^{dip}$ is most conveniently expressed in Cartesian coordinates [*Russell*, 1971] for our simulations:

$$B_X^{dip} = \frac{3XZB_E}{(X^2 + Y^2 + Z^2)^{5/2}},$$

(2.29)

$$B_Y^{dip} = \frac{3YZB_E}{(X^2 + Y^2 + Z^2)^{5/2}},$$

(2.30)

$$B_Z^{dip} = \frac{(2Z^2 - X^2 - Y^2)B_E}{(X^2 + Y^2 + Z^2)^{5/2}},$$

(2.31)

where X, Y, and Z are the dimensionless distance components from the center of the Earth expressed in R_E, and B_E is the magnetic field on the surface of the Earth at the magnetic equator. These expressions are for an untilted dipole, which will point in the Z direction. A tilted dipole is easily handled through a rotation of coordinates.

2.4.1 Inner boundary conditions

We now discuss the inner boundary conditions, which are usually set at a radius $r \geq 3R_E$ out of computational necessity. The finite differencing time step Δt is inversely proportional to the maximum wavespeed in the simulation box, which in a global magnetospheric simulation turns out to be the Alfvén velocity $(B/\sqrt{\mu_0\rho})$ in the highly magnetized inner region, which is filled with the high density plasma of the plasmasphere (out to $3 - 5R_E$). The Alfvén speed decreases rapidly with $B \sim r^{-3}$ for a plasmaspheric density that changes slowly with r, so if the simulations have an inner boundary $r \geq 3R_E$, the time step (for a fixed density and gridspacing) is at least 30 times larger than if the boundary were set at 1 R_E. Gridspacing is typically larger than 0.5 R_E, a choice which will generally result in large finite differencing errors near the Earth where there are large magnetic gradients. Minimizing these finite differencing errors could involve finer gridspacing (say 0.1 R_E) near the Earth, but this then gives an even smaller time step (proportional to Δx) and also could result in more gridpoints near the Earth than in the rest of the simulation box [since gridspace density is proportional to $(\Delta x)^{-3}$]. Surrounding the Earth by a finer grid and using physically realistic values for the magnetic field and plasma easily results in a simulation that is not computationally feasible.

Fortunately, this computationally convenient choice of inner boundary $(r \geq 3R_E)$ is physically justified in several ways and gives conditions that determine the MHD boundary conditions. The MHD equations are not simulated inside this boundary, but rather this region is approximated by a static dipole magnetic field and a plasma with a fixed density and pressure that is either static or corotates with the Earth like the plasmasphere. Three things need to be achieved by the inner boundary: (1) currents must close somewhere outside the Earth as in the ionosphere, (2) the plasma density and temperature (and hence the pressure) must be set, and (3) the dawn-dusk electric field must be shielded out at low latitudes and plasma velocities limited. We treat each in turn.

At $3-5R_E$ the magnetic field is still overwhelmingly dipolar and the external field only constitutes a small fraction of the total field. The mapping of magnetic field lines inside this radius will not be significantly affected by external magnetic field, so its absence in this region does not produce significant mapping errors. Currents automatically close everywhere in MHD, since $\nabla \cdot \mathbf{J} = 0$ identically, but must be excluded from the Earth as achieved by the highly conducting ionosphere and the underlying electrically insulating neutral atmosphere. Field-aligned currents close in the ionosphere, so this is simulated by treating the inner boundary as an electrically conducting shell which will prevent currents from crossing the boundary. This gives conditions for setting the boundary conditions for the perturbed portion of the magnetic field, since the background dipole field is fixed. Zeroing out the perturbed magnetic field tangential to the boundary is equivalent to infinite conductivity at the boundary, which induces a surface current that shields out the perturbed magnetic field from the interior. The normal component must be continuous from Maxwell's equations for any surface, so setting this term to zero prevents perturbed flux from entering inside the boundary. Even if ideal MHD is used, however, finite differencing methods will create a numerical resistivity which is particularly large near the inner boundary where there are large gradients in the magnetic field. This resistivity permits currents to close in a shell of finite thickness out from the boundary rather than only at the surface of the boundary. A further refinement to global models determines the inner boundary conditions by coupling with a separate ionospheric model [*Fedder and Lyon*, 1987] and is discussed in Chapter 5.

The plasmaspheric density is several orders of magnitude higher than in the outer magnetosphere, but within the plasmasphere the density often is fairly uniform over a distance of a few R_E. This higher plasma density means the Alfvén speed is significantly lower due to the presence of the plasmasphere, which helps the simulation significantly by permitting larger time steps. This higher density also provides mass loading of the magnetic field lines and for a given momentum density gives a lower bulk plasma speed. Our simulations generally use a density profile near this boundary, which falls off as r^{-3} to r^{-6}, a choice which makes the Alfvén speed increase less near the inner boundary and permits larger time steps. The thermodynamic state of the plasma at the inner boundary is determined by setting two variables, e.g. the density and temperature, which then determines thermal pressure of the plasma. The

simulations generally use number densities from 100 to 1000 per cm^3 and temperatures near 1 eV, as in the cold plasma of the real plasmasphere. This ignores the pressure contribution from the less numerous energetic particles, which can be accounted for by increasing the average plasma temperature without increasing the number density. This method is employed in the simulations of Chapter 4, which utilizes an enhanced pressurization near the inner boundary.

Another important property of the plasmasphere is its electric shielding, which can be accomplished by setting the plasma velocity at the inner boundary to zero. Inside the plasmapause the electric field is mostly corotational, while far outside it is in the dawn-to-dusk direction. If the dawn-dusk electric field suddenly increases, charges will build up near the plasmapause over a period of a few hours to shield out the electric field from the inner magnetosphere [Kelley, 1989]. The corotational speed at $3R_E$ is actually near 1 km/sec, much less than the plasma flow speeds in the outer magnetosphere which are generally many tens of km/sec and sometimes several hundred km/sec. Magnetospheric forcing near the inner boundary can produce speeds in the simulation of tens of km/sec, which greatly exceed the corotational velocity. Mass loading near the inner boundary helps slow these speeds, but by itself is generally inadequate to constrain plasma velocities. The velocity at the boundary can be set to the corotational speed, but this is really mostly just a refinement to the main purpose of this boundary condition, i.e. shielding out the electric field and keeping velocities low near the boundary of the simulation.

2.5 Conclusion

This chapter has shown how the MHD equations relate to the general two-fluid equations for plasma. The limitations and conditions for validity of MHD has been discussed, as well as the methodology used to perform global magnetospheric simulations. The possible importance of several terms that are conventionally neglected in MHD, e.g. in Ohm's law, has been demonstrated, and will be pursued further in the next chapter. Both MHD and these modified fluid equations will be used to perform global magnetospheric simulations in the following chapters.

Chapter 3

MAPPING AND CURRENTS IN THE
NOON-MIDNIGHT MERIDIAN

3.1 Introduction

3.1.1 Outline of chapter

In this chapter, a 2-D magnetospheric simulation in the noon-midnight meridian plane is performed using a modified fluid approximation. This fluid formulation is based on keeping the Hall term and electron pressure gradient term in the Ohm's law, which were shown in Chapter 2 to often be significant in the magnetosphere. This modified fluid approximation incorporates additional field-aligned currents not included in MHD but which are shown to be a vital component to the auroral current system in the noon and midnight sectors. A representative static magnetospheric configuration is prepared by time-averaging the dynamic magnetic field generated by the global model. Time-averaging provides a new way to study the output of this global magnetospheric model and permits meaningful comparisons with ensemble-averaged satellite data and empirical magnetospheric models.

The model produces a cyclical substorm while the IMF is southward, with a growth phase, an expansion phase, and a recovery phase. The resulting time-averaged configurations are studied parametrically using two series of runs that vary the solar wind dynamic ram pressure and the southward component of the interplanetary magnetic field, respectively. Although the time-dependent position of the X line can be as small as 13 R_E, the average position of the X line exceeds 42 R_E in all the cases studied. The auroral currents map to magnetic latitudes near 70° at midnight and move equatorward and intensify both for increased dynamic pressure and IMF B_Z. These static magnetic configurations are compared with the T89M empirical magnetospheric magnetic field model of *Tsyganenko* [1989]. The peak tail current shows a variation similar to that in the T89M model but is about 30% less. Reducing the tail magnetic field of T89M to 70% of its original value gives more realistic values

for B_Z in the near-Earth tail and improves equatorial mapping of closed field lines in the tail. Increased activity causes a fixed point in the tail to map to a position more equatorward in the ionosphere within the simulations but to a position more poleward in T89M. The results of this chapter have been published in *Elsen and Winglee* [1996a].

3.1.2 Motivation for study

Recent MHD global magnetospheric simulations [e.g., *Walker et al.*, 1993; *Ogino et al.*, 1994; *Fedder and Lyon*, 1995; *Raeder et al.*, 1995; *Watanabe and Sato*, 1990; *Usadi et al.*, 1993] have been mostly case studies, usually for some specified IMF conditions. These models have successfully produced the overall morphology of the magnetosphere and provide strong support for the near-Earth neutral line substorm model [*Hones*, 1984; *Kan*, 1990]. Some of these three-dimensional (3-D) MHD simulations have incorporated a resistive ionosphere and have produced field-aligned currents, which are mostly confined to the dawn and dusk sectors and are relatively weak near midnight [e.g., *Ogino*, 1986; *Fedder and Lyon*, 1987; *Hesse and Birn*, 1991]. However, there is a need to relate the results of these global models to not only a specific observation, as in a case study, but also to large groups of observations to determine the average behavior of the magnetosphere as a function of solar wind conditions. The problem is that even a single case study requires considerable computational resources and that unless the dynamic configuration approaches some kind of equilibrium, one only has a "snapshot" of the magnetosphere at a particular time.

Semiempirical magnetosphere models fitted to large databases of satellite measurements, as exemplified by the models of *Tsyganenko* [1987, 1989], provide an average value of the global magnetic field. Although these models are static, they indicate changes in the magnetospheric magnetic field with the K_p index. By time-averaging a dynamic model over a considerable period of time, i.e., an hour or more, the resulting average global magnetospheric configuration can be compared more easily with time-averaged measurements and thereby provide a link between static configurations and global dynamics. For example, a 3-hour average of the fluid model can be prepared and then compared with data sorted by the K_p index or to hourly averaged satellite data of the kind used to fit the semiempirical models.

A modified fluid approximation has been developed by *Winglee* [1994]. It has been

used for a 2-D global simulation in the noon-midnight meridian plane [*Winglee*, 1994], as well as 3-D simulations [*Winglee*, 1995; *Winglee et al.*, 1996]. This methodology, called magnetoplasma dynamics (MPD), incorporates to a limited degree some of the particle effects not present in standard MHD. The fluid resistivity needed to drive magnetic reconnection is calculated rather than arbitrarily imposed. Besides the convective electric field, the modified fluid approximation allows for an ambipolar electric field in the plane of the plasma flow and magnetic field, which is particularly strong at the boundary layers of the magnetopause and magnetotail current sheets, where differential penetration of incoming electrons and ions is large. In addition to the MHD current system, this electric field along with a modified Ohm's law then produces field-aligned currents which divert some of the magnetopause and magnetotail currents into the dayside and nightside auroral sectors. This diversion also produces an effective resistivity in the magnetopause and magnetotail current sheets, enabling reconnection to occur without the need for an anomalous resistivity.

Dynamic pressure has been used as a predictor of both magnetopause location and magnetospheric activity since the 1960s, and IMF B_Z since the early 1970s [*Aubry et al.*, 1970; *Fairfield*, 1971; *Holzer and Slavin*, 1978; *Petrinec et al.*, 1991; *Roelof and Sibeck*, 1993]. We produced a wide range of magnetospheric activity and configurations by varying just these two parameters in our simulations.

The simulation performed for this chapter is two dimensional (2-D), yet most recent simulations are 3-D. To date, 3-D simulations have only provided a limited number of isolated case studies, while the present study is a systematic study of the magnetospheric response to a large range of solar wind conditions. Two-dimensional studies have the disadvantage that they may not exhibit the proper geometry, and the results must be viewed with caution [*Lyon et al.*, 1986]. However, most of the flows in the noon-midnight meridian plane are restricted to remain in the plane, particularly for southward IMF. The magnetic fields in the tail and at the magnetopause scale to the right magnitudes and are very similar to 3-D results [*Winglee*, 1995]. We also find that converting the latitudes of high-latitude field lines and auroral currents to their equivalent 3-D latitudes results in fairly realistic mapping of these field lines and currents. The 2-D results more often than not compare favorably with empirical models, ensemble-averaged data, and 3-D models. We do find some notable exceptions, such as the magnetopause shape where the ratio of polar to subsolar distance

is significantly higher than in 3-D, but demonstrate in general that 2-D is a better approximation in the noon-midnight meridian than might be expected.

Three-dimensional simulations are presented in the next chapter. Based on these results and other work performed with 3-D codes, we do not see substantial differences between the present 2-D results and features in the noon-midnight meridian derived from 3-D results, except where noted. It is vitally important to establish the accuracy of the modeling against the known average behavior of the magnetosphere. The time-averaging methodology developed in this paper represents one of the first such comparisons of global model results with both averaged satellite measurements and a semiempirical global model.

3.1.3 Scope of this chapter

The MPD model and other methodology used for the present parametric study are described in Section 3.2. The dynamic behavior of a representative MPD run during southward IMF is discussed in Section 3.3, showing a moderately strong substorm with distinct growth, expansion, and recovery phases. A comparison with the corresponding time-averaged static configuration is made in Section 3.4. This time-averaged MPD configuration is tested in Section 3.5 by comparison with T89M, an updated version of T89, the semiempirical magnetic field model by *Tsyganenko* [1989]. Parametric studies of the location of the neutral point and auroral MPD currents are presented in Sections 3.6 and 3.7. Conclusions are presented in Section 3.8.

3.2 Magnetoplasmadynamics (MPD)

3.2.1 The modified fluid approximation

The modified fluid equations that form the basis for the 2-D magnetospheric model are derived by *Winglee* [1994] and are briefly described here. The derivation starts with the more general form of Ohm's law derived in Chapter 2, in which the Hall term and the electron pressure gradient term have been retained, but now m_i/ρ_m has been approximated by $1/n$ and P_e is a scalar rather than a tensor.

$$\mathbf{E} + \mathbf{V} \times \mathbf{B} \approx \eta \mathbf{J} + \frac{\mathbf{J} \times \mathbf{B}}{en} - \frac{\nabla P_e}{en} \tag{3.1}$$

As described in Chapter 2, these terms can produce an additional ambipolar electric field that will produce additional currents (and their associated magnetic field). Such currents are shown to be present in particle simulations, also performed by Winglee [1994], but are absent from MHD. This new class of currents are called "surface currents" and distinguished from the "body currents" of MHD.

The MPD formulation accounts roughly for some effects seen in the particle simulations, and which are also expected from the more general Ohm's law from two-fluid theory, hence the name "modified fluid approximation". Mathematically, MPD is a perturbed MHD, with the same length and time scales as MHD, which is necessary to keep the simulations computationally feasible. (A full two-fluid treatment must resolve much shorter length and time scales, including high-frequency Langmuir oscillations, and so cannot be used for a global magnetospheric simulation, since it would far exceed the practical limits for computation.)

To obtain an explicit solution the Ohm's law is first decomposed into body and surface components, denoted by subscripts b and s, respectively.

$$\mathbf{E}_b + \mathbf{V} \times \mathbf{B}_b = \eta \mathbf{J}_b + \frac{\mathbf{J}_s \times \mathbf{B}_b}{en} \tag{3.2}$$

$$\mathbf{E}_s + \mathbf{V} \times \mathbf{B}_s = \frac{\mathbf{J}_b \times \mathbf{B}_b}{en} - \frac{\nabla P_e}{en} \tag{3.3}$$

For a 2-D system, equation 3.2 contains components perpendicular to the noon-midnight meridian plane, and except for the final Hall term is identical to the MHD Ohm's law. If this Hall term is equated to $\eta_{eff}\mathbf{J}_b$ and the ordinary resistive term neglected, since $\eta_{classical}$ is very small for a collisionless plasma, the effective plasma resistivity is given by

$$\eta_{eff} = \frac{|\mathbf{J}_s \times \mathbf{B}_b|}{en |\mathbf{J}_b|} \tag{3.4}$$

The components within the noon-midnight plane are used in equation 3.3, and are perturbative terms totally absent from MHD. Since this is a perturbation, the $\mathbf{J}_s \times \mathbf{B}_s$ term is second order and therefore neglected, while $\mathbf{J}_b \times \mathbf{B}_s$ is zero since the vectors are parallel by definition.

An expression is needed for the electrostatic field $\mathbf{E}_s$, which is assumed to be given by a potential that depends on the energy of the plasma

$$\mathbf{E}_s \approx \frac{1}{en} \nabla(\rho V^2 + P). \tag{3.5}$$

By further assuming that $\nabla P \approx \mathbf{J} \times \mathbf{B}$ and making some other simplifications, an explicit representation for the surface magnetic field and currents is produced in terms of known MHD quantities:

$$\mathbf{B}_s = \frac{(\mathbf{V} \cdot \mathbf{B}_b)\mathbf{J}_b}{en(V^2 + \mid \mathbf{V} \cdot \mathbf{V_A} \mid)} \tag{3.6}$$

$$\mathbf{J}_s = \frac{\nabla \times \mathbf{B}_s}{\mu_0} \tag{3.7}$$

This also gives a revised Ohm's law:

$$\mathbf{E}_b + \mathbf{V} \times \mathbf{B}_b = \chi \frac{\mathbf{J}_s \times \mathbf{B}_b}{en} + \eta_a \mathbf{J}_b, \tag{3.8}$$

where χ is the MPD resistive parameter and η_a is an anomalous MHD resistivity, either or both of which may be used for a simulation. The addition of $\mid \mathbf{V} \cdot \mathbf{V_A} \mid$ in the denominator of (3.6), where V_A is the local Alfvén velocity, is to avoid numerical problems near gridpoints where V is very small, but otherwise this has little effect on the simulations. These three equations are then used with equations (2-17) through (2-22) to perform the simulation. The strictly MPD simulations performed for this study set $\chi \approx 1$ and $\eta_a = 0$. The scale length at which the surface currents are a significant fraction of body currents is shown to be $L \approx c/\omega_{pi}$, where ω_{pi} is the ion plasma frequency. This means the surface currents are strong in thin structures such as current sheets and relatively insignificant at most other locations.

3.2.2 The global model

These MPD equations are solved using a two-step Lax-Wendroff method with artificial diffusion and additional flux correction smoothing [Boris and Book, 1973]. The Earth's dipole is aligned with the Z direction, giving north-south symmetry. The simulation grid is 375 × 125, with the grid spacing equivalent to 2000 km. The simulation box ranges from 34 R_E on the dayside to -78 R_E on the nightside, and from 0 to 37 R_E in the Z direction. The incoming solar wind is blown in with a specified velocity, southward IMF, density, and temperature. The resulting activity in the magnetosphere is then studied parametrically as a function of the solar wind dynamic pressure p and IMF B_Z.

The model must use a 2-D magnetic dipole that falls off as r^{-2} in order to have zero divergence of $\mathbf{B}$ in the simulation plane. The strength of the dipole was chosen so that the magnetopause was generated near 10 R_E. The inner model boundary is set at 3.0 R_E and has infinite conductivity and tangential flow. The radius of the inner boundary is similar to that seen in most 3-D global simulations [e.g., *Fedder and Lyon*, 1995]. An increased plasma density that falls off as r^{-3} limits the Alfvén speed and hence prevents the finite differencing time step from being too small at low radial distances. The Alfvén speed at the inner radius is set to 1300 km/s, close to that observed in the ionosphere and our 3-D simulations. The model currents close at this inner boundary with the magnetic field inside an unperturbed dipole field. Auroral currents are strong near the inner boundary but map much too poleward using this 2-D dipole field. Instead, the equivalent latitude that these points would map to with a 3-D dipole field inside the inner boundary was estimated and found to correspond roughly with the statistical auroral oval.

Incoming solar wind velocity is kept constant at 450 km/s in all the simulation runs, a speed slightly higher than average solar wind value. The solar wind dynamic pressure is varied by changing the solar wind particle density from 1.2 to 20 per cm^3, which is slightly more than the 2σ range of observed solar wind number densities [*Feldman et al.*, 1977]. An unmagnetized fluid is blown at the dipole for the equivalent of 3 hours to achieve a fluid equilibrium. Incoming solar wind IMF with only a B_Z component is then ramped up linearly for a period of 40 min and held constant for a period of 160 min. For each case, a time-averaged magnetic field and current configuration is computed by linearly averaging each magnetic field component from 50 uniformly spaced snapshots from the final 200 min of the run.

Northward IMF cannot be run for an extended period of 3 hours in our 2-D model, owing to the pileup of the magnetic field lines at the magnetopause, limiting this study to southward IMF B_Z. Two sequences of the MPD model were executed: (1) a "pressure" sequence with variable dynamic pressure and constant IMF B_Z and (2) a "B_Z" sequence with variable IMF B_Z and constant dynamic pressure. These solar wind parameters were stepped by a factor of 2 to cover a large range of observed solar wind conditions and hence magnetospheric activity. The scaled dynamic pressure levels in the pressure sequence varied from 0.56 to 9.0 nPa, which corresponds roughly to the 2σ range of measured values [*Roelof and Sibeck*, 1993].

IMF B_Z ranged from -0.35 to -4.2 nT, from close to the mean value (0 nT) down to a little past the 1σ value for southward IMF B_Z of -3.5 nT [*Roelof and Sibeck*, 1993].

3.3 Dynamic Behavior of the MPD Model

Magnetic field lines, calculated with a stream function, are shown for the entire simulation box in Figure 3.1 for the final hour of a 200-min MPD run with a moderately strong southward IMF B_Z of -2.8 nT and moderate dynamic pressure p of 2.2 nPa. These solar wind input values produce a fairly high level of magnetospheric activity (to be shortly defined). Figure 3.1a depicts a time 140 min after IMF has entered the simulation box.

There is an X line in the tail at $X_{gsm} = -39 \ R_E$, which had formed earlier in the middle tail at 28 R_E. The neutral point continues to move outward, while the tail current sheet continues to thin (Figures 3.1b and 3.1c). Another neutral line has formed in Figure 3.1d but now is much closer to the Earth at 13 R_E, forming a true plasmoid (with locally closed magnetic field lines). This new X line soon moves tailward and reaches 32 R_E by the end of the simulation (Figure 3.1f), with the magnetic configuration approaching that seen an hour earlier in Figure 3.1a.

Closeups of the corresponding MPD currents that map into the auroral zone are shown in Figure 3.2 by combining an arrow plot with stream function contours. The arrow lengths are scaled to the square root of the current magnitude for a larger dynamic range. The contours of the stream function for the auroral current indicate the mapping of the currents as well as magnitude. On the dayside, these MPD currents are downward at the cusp and upward on each side of the cusp. The upward currents equatorward of the cusp map to a large circulatory feature near the subsolar magnetopause, while the poleward current maps to the outer edge of the plasma mantle.

The nightside currents mapped to the Earth are concentrated in a fairly narrow range of latitude around 70°, consistent with the typical position of the auroral oval. The poleward edge of the auroral current is upward and has the sense of region 1 current on the dusk side of the auroral oval, while the equatorward edge of this current is directed downward. These auroral currents are seen to intensify and move equatorward and then poleward, respectively, in association with the formation and subsequent tailward motion of the near-Earth neutral line seen in Figure 3.1. The
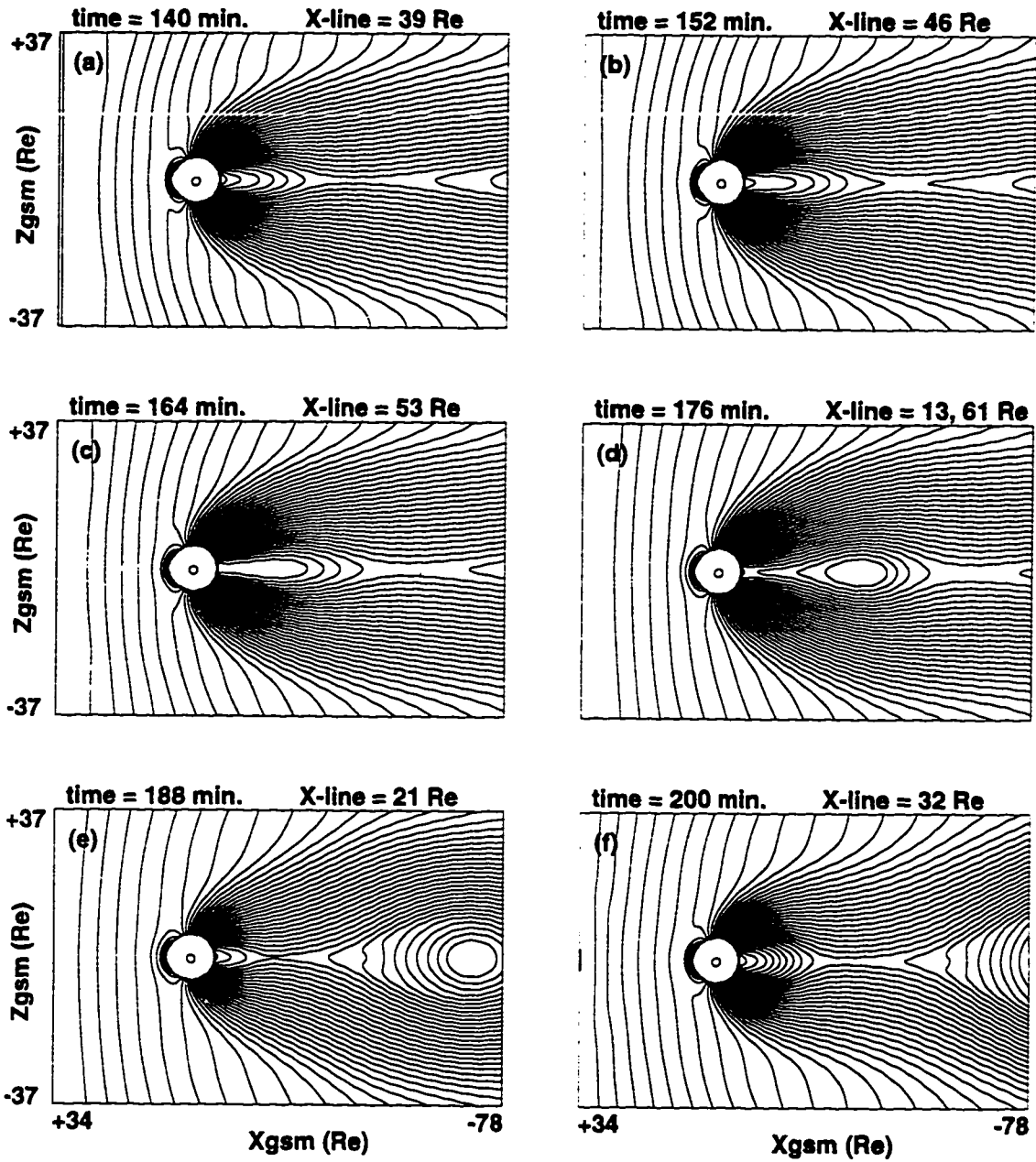
Figure 3.1: Snapshots of magnetic field lines as indicated by a stream function in the noon-midnight meridian plane at six times during an hour-long substorm cycle ending a 200-min MPD simulation. To enhance the plots, the magnetic field was zeroed out inside the larger circle at 6 R_E and reflected around the simulation symmetry line (at $Z = 0$). The small inner circle is the Earth.

140 minutes - substorm growth phase

16

(a)

Zgsm (Re)

peak auroral
current latitude
72°

0

176 minutes - just after substorm onset

16

(b)

Zgsm (Re)

69°

0

196 minutes - end of expansive phase

16

(c)

Zgsm (Re)

74°

0

+12   -12

Xgsm (Re)
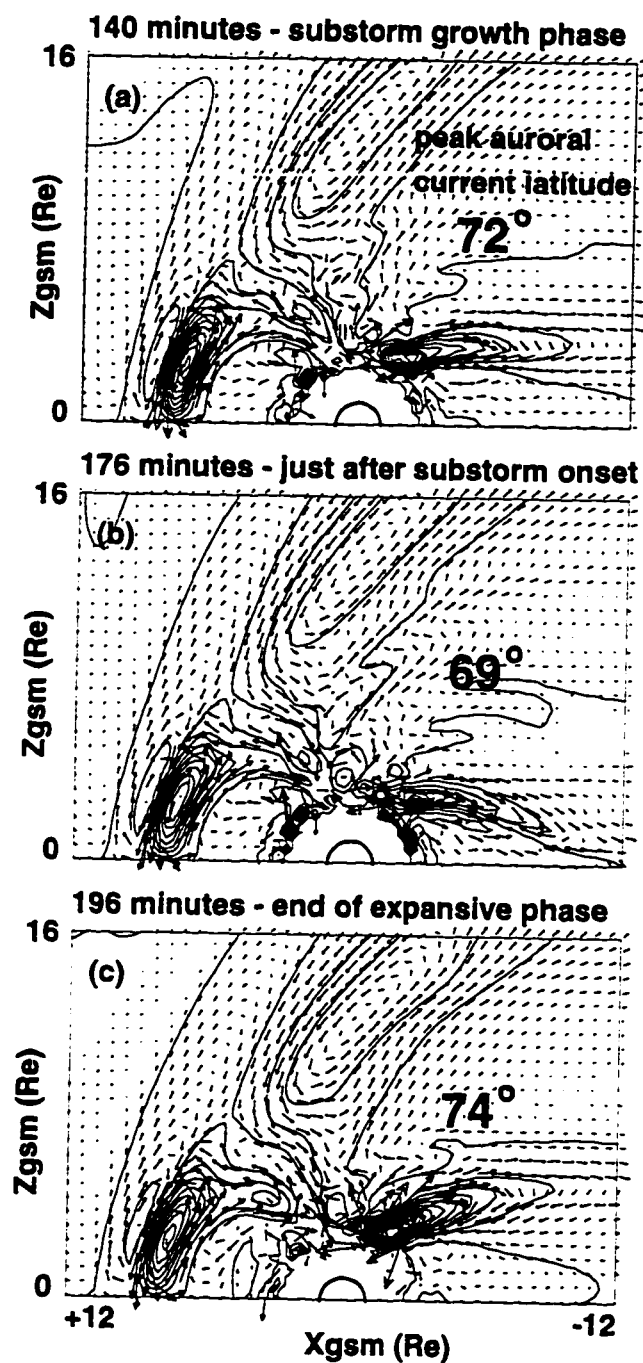
Figure 3.2: A closeup of auroral currents in the noon-midnight meridian plane at three times in the same hour-long substorm cycle shown in Figure 3.1. Auroral current is indicated in two ways, an arrow plot of current vectors superimposed on a stream function plot of the current. The perturbed currents close at the inner boundary of the model, a conducting ionosphere at 3 R_E. The small inner circle is the Earth.

global magnetospheric configuration varies cyclically, roughly reproducing the events of Figures 3.1 and 3.2 after an hour or more.

Time histories of quantities characterizing the auroral and magnetospheric currents are shown in Figure 3.3. The positions of magnetic neutral points on the Sun-Earth line ($B_Z = 0$) in Figure 3.3a show the traces of both the initial and the second X line. After moving earthward or remaining stationary for a short time, both are ejected tailward at a steady velocity of about 100 km/s. The formation of our second X line is delayed about an hour until the first X line has reached 55 R_E.

Peak cross-tail (MHD) currents are shown in Figure 3.3b and are well correlated with the tailward motion of the X line. The solid line shows the maximum value of current along the nightside X axis, while the dotted line shows the value at 18 R_E. The largest currents are seen when the plasmoid is ejected, rather than during the earlier disconnection event. The current begins growing just 8 min before the formation of the second X line and rises rapidly by a factor of more than 3 in 28 min, and is followed by a sharp decline. The current at 18 R_E shows an even sharper rise and fall, dropping by a factor of 10 in 8 min.

The time history of the central auroral latitude, i.e., the latitude separating the upward and downward MPD currents on the nightside, is plotted in Figure 3.3c. Turning the IMF southward drives the auroral latitude equatorward from the quiescent value near 80° to a minimum below 70° at the time the first X line is ejected tailward. The latitude then increases, but decreases again when the second X line forms, and reaches a minimum of 68° when plasmoid ejection commences.

The strong modulation of the cross-tail currents by a factor of 3 produced by the MPD model also drives similar modulations in the auroral currents, as shown by the integrated upward auroral current on the nightside versus time in Figure 3.3d. Auroral current starts at very low values but begins to increase by the time of the first X line formation. It continues to grow in a ragged fashion for an hour, then declines slowly until the second X line forms, and finally rapidly increases threefold in magnitude. The rise time of 28 min is the same as for the cross-tail current, but the times for the minimum and maximum auroral current are delayed 12 min relative to the cross-tail current.

This sequence of events after tail disconnection is generally consistent with the phenomenology of a magnetospheric substorm, i.e., it displays five of the twelve (ob-
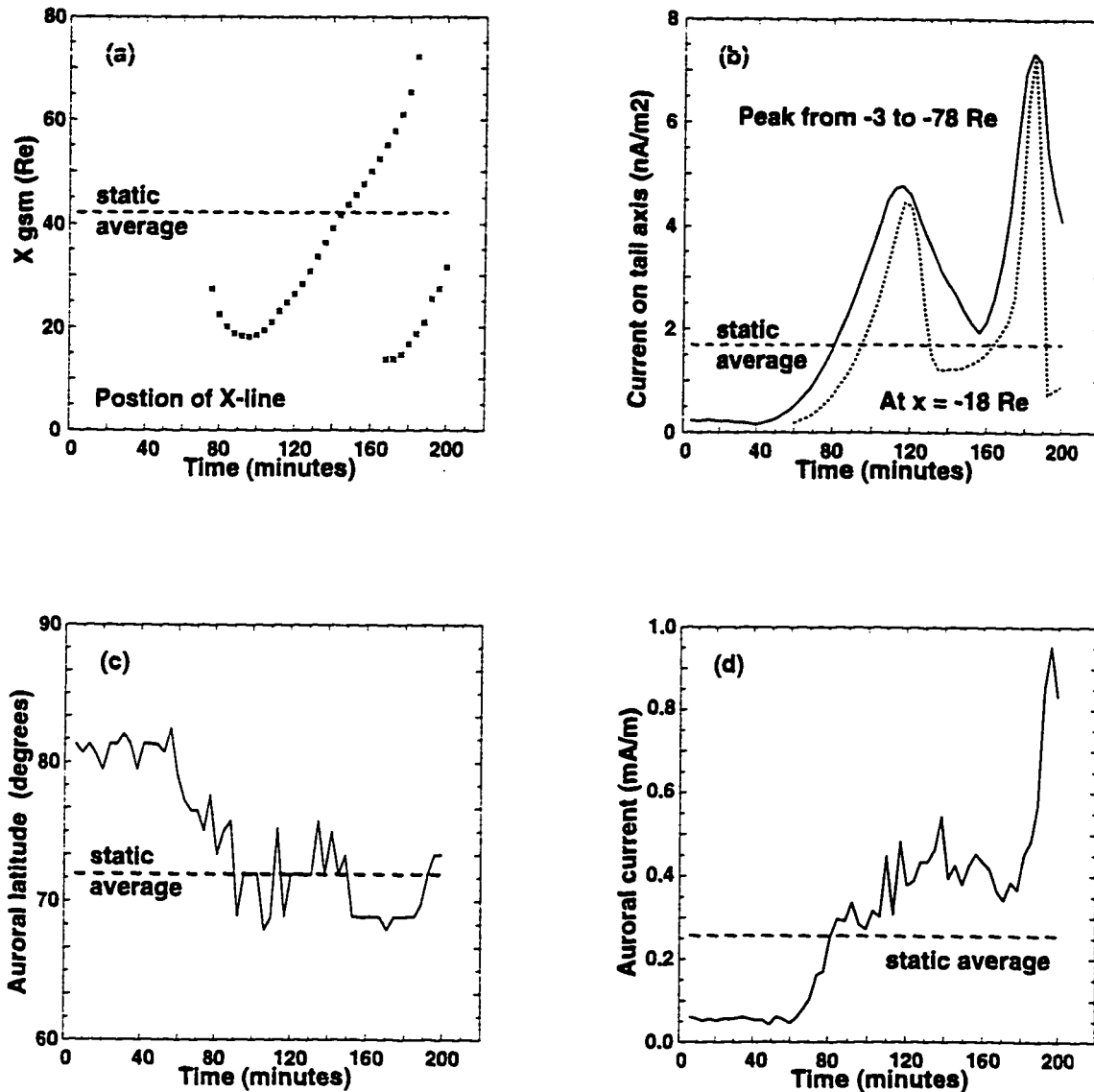
Figure 3.3: Time histories of four dynamic quantities during the entire 3 hours of the MPD simulation shown in Figures 3.1 and 3.3, with the time-averaged value of each quantity shown by a dashed horizontal line. (a) The position of X lines in the tail. (b) The peak cross-tail current along the tail axis (solid line) and the value at $X = -18 R_E$ (dotted line). (c) The mapped latitude of the center of nightside auroral current. (d) The integrated upward nightside auroral current.

served) ionospheric and magnetospheric signatures of a substorm listed by *Kan* [1990]. The most obvious features are the ones similar to the near-Earth neutral line substorm model [*Hones*, 1984], i.e., the creation of an X line near the Earth, the formation and ejection of a plasmoid down the tail, and the generation of field-aligned currents in the tail. As previously described, producing field-aligned currents in the noon-midnight plane is unique to the MPD model. There are also some ionospheric substorm signatures, such as the equatorward and poleward motions of auroral currents associated with modulations in current magnitude.

Each cycle of activity roughly corresponds to a magnetospheric substorm, but the first period of activity involving tail disconnection does not produce a true plasmoid and might be considered to represent pseudo-breakup. From 140 to 168 min, auroral currents decreased but mapped to increasingly lower latitudes. Although the peak cross-tail current along the entire axis decreased and then increased during this interval, the current at 18 R_E began to increase by 140 min and increased during this entire 30-min interval, as shown by the dotted curve in Figure 3.3b. This is consistent with current sheet thinning in the near-Earth region and allows us to identify the time period from 140 to 168 min as a growth phase. Substorm onset can be identified as occurring at 168 min, if we use the creation of the neutral line at 13 R_E as the criterion, or about 8 min later, if we wait for a significant increase in auroral current, corresponding to the brightening of the first auroral arc. From 168 to 196 min, auroral currents move poleward and increase in magnitude, so we can label this the expansion phase. Finally, with tail current peaking at 184 min and auroral currents peaking 12 min later at 196 min, we can identify the beginning of the recovery phase. The X line has reached 32 R_E by 200 min so there is no longer a neutral line near the Earth (less than about 20 to 30 R_E).

Although the scaled strength of the auroral (MPD) currents are shown to be considerably less than the measured field-aligned currents in Section 3.7, the modulation of the auroral currents displays the magnetospheric activity of model (Figures 3.3c and 3.3d), in concert with the X line motion and cross-tail current modulation. Furthermore, the effective (local) resistivity of the plasma is determined from these currents, as discussed by *Winglee* [1994], and is important in driving the substorm cycle. This cycle is characterized by the time required after the disconnection of the magnetotail for the plasmoid to form along with the associated buildup and relax-

ation of the tail current sheet and surges of auroral (MPD) currents to and from the ionosphere. Thus a small local parameter based on mesoscale physics is driving the global behavior seen in the model rather than being arbitrarily imposed.

These events representing magnetospheric activity occurred sooner for stronger IMF B_Z and/or dynamic pressure. All cases studied, except that with the weakest IMF B_Z (-0.35 nT), had formed a near-Earth neutral line within 3 hours after IMF introduction. More than half of the simulations, those with IMF B_Z stronger than -1.4 nT and/or pressure greater than 2.2 nPa, had formed a true plasmoid by the end of the simulation. The strongest IMF B_Z case of -4.2 nT (not shown) had expelled most of the plasmoid by 3 hours, and the current sheet was starting to thin again, indicating repetition on a timescale of roughly an hour for the most active cases. Thus the magnetospheric activity as gauged by the repetition frequency of the X line formation and the associated modulation and magnitude of both tail (MHD) currents and auroral (MPD) currents was strongly tied to the strength of the solar wind dynamic pressure and IMF B_Z.

3.4 The Equivalent Static Magnetosphere

An "equivalent static magnetosphere" was prepared using the method of linear averaging previously described in Section 3.2 and is shown in Figure 3.4a. The magnetic field lines are calculated with a stream function and show a much simpler magnetic configuration. The dynamic behavior of plasmoid formation and ejection is averaged out, because at any given point a plasmoid produces alternate swings in B_Z that cancel out in the time average. The averaged X line position is 42 R_E, significantly more tailward than the actual formation distances of 27 and 13 R_E (Figure 3.3a). The heavy line on the dayside marks the center of the magnetopause current layer and also corresponds to the division between open and closed magnetic field lines. The overlaid contours on the nightside mark the regions with strong MHD currents (J_Y) perpendicular to the simulation plane. The solid line shows where the tail current sheet is intense, while the dashed line outlines intense regions of return current. The MPD plasma mantle currents are embedded within this contour, and the outer edge of the return current shows the approximate outer edge of the nightside magnetopause.

Numerical errors in front of the subsolar magnetopause where the field is very weak cause some distortion of the field lines, and the hooks in some of the high-
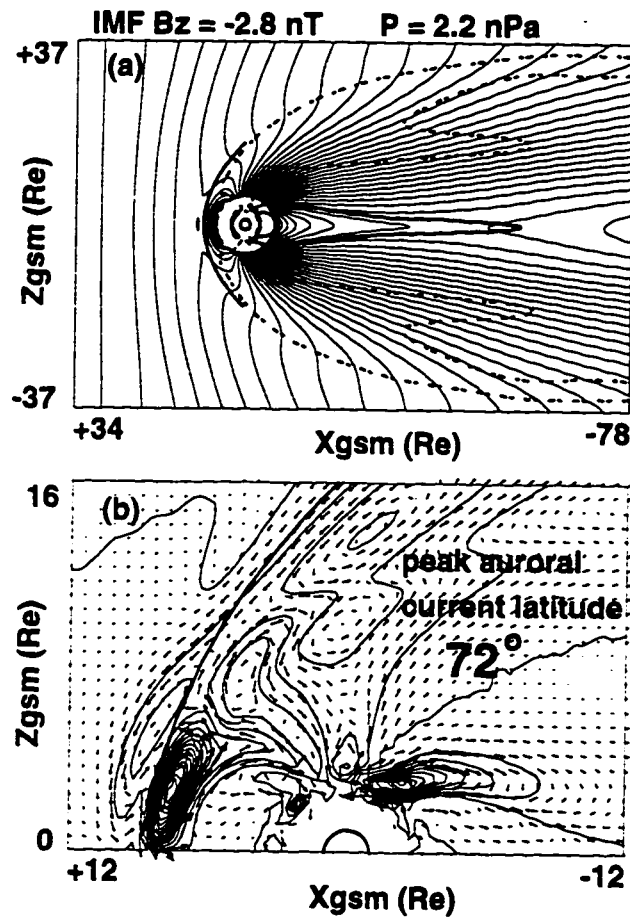
Figure 3.4: (a) The static time-averaged configuration produced by averaging the magnetic field in Figure 3.2 over the 3 hours of the MPD simulation. The magnetic field is shown as in Figure 3.2 with overlying current structures added. The bold solid line on the dayside is the calculated elliptical magnetopause passing through the center of the Chapman-Ferraro current layer at the subsolar point. The solid line on the nightside outlines the cross-tail current sheet, while the dashed line shows the current from the nightside magnetopause and plasma mantle. (b) A closeup of the static time-averaged auroral currents, as in Figure 3.2, with the magnetopause surface again indicated by the bold line.

latitude magnetic field lines are accentuated by this averaging process. The prongs seen in this negative (return) current contour deep in the tail are also an artifact of the averaging process and indicate two long-term positions of the magnetopause. The inner prong lies approximately at the magnetopause position before the disconnection event, while the outer prong shows the return current at later times blurred out to some degree. The outer portion of the return current profile shows the approximate position of the outer edge of the nightside magnetopause during the portion of the simulation with active reconnection and attendant magnetospheric activity.

Figure 3.4b shows a closeup of the auroral currents in the time-averaged static configuration. Both the peak cross-tail current and the integrated auroral current of the averaged configuration are considerably less than the corresponding peak substorm values, by factors of more than 3 (cf. Figures 3.3b and 3.3d). The auroral latitude of the static configuration is 72°, near the value at the beginning of the growth phase (Figure 3.3c). The circulatory MPD current on the dayside is mostly located inside the center of the MHD current layer (heavy curve), but a substantial amount of MPD current threads its surface.

Figure 3.5 shows three more static average MPD configurations constructed from our studies. This sequence displays increasing levels of magnetospheric activity (Figures 3.5a, 3.5c, and 3.5e) along with the corresponding closeups of auroral MPD current (Figures 3.5b, 3.5d, and 3.5f). The first jump in magnetospheric activity, from Figure 3.5a to 3.5c, is produced by quadrupling the dynamic pressure while leaving B_Z unchanged. The lobe magnetic field is stronger, as indicated by closer spacing of magnetic flux lines in the tail, but the total number of flux lines in the tail is relatively unchanged. The second jump in activity, from Figure 3.5c to 3.5e, is produced by leaving dynamic pressure set at the higher level and tripling the strength of the southward IMF B_Z. The number of flux lines in the tail now shows a significant increase, indicative of a higher average rate of magnetic reconnection at the subsolar point, which leads to the transport of magnetic flux from the dayside to the nightside. Although there is more flux on the nightside, the magnetic field in Figure 3.5e, as shown by the spacing of the lobe field lines, is not much stronger than that in Figure 3.5c, because the flux is spread out in a thicker tail. When the distance to the flanks of the magnetosphere is larger for a given subsolar distance (Figure 3.5e), the magnetopause is termed "flared," while the opposite situation is
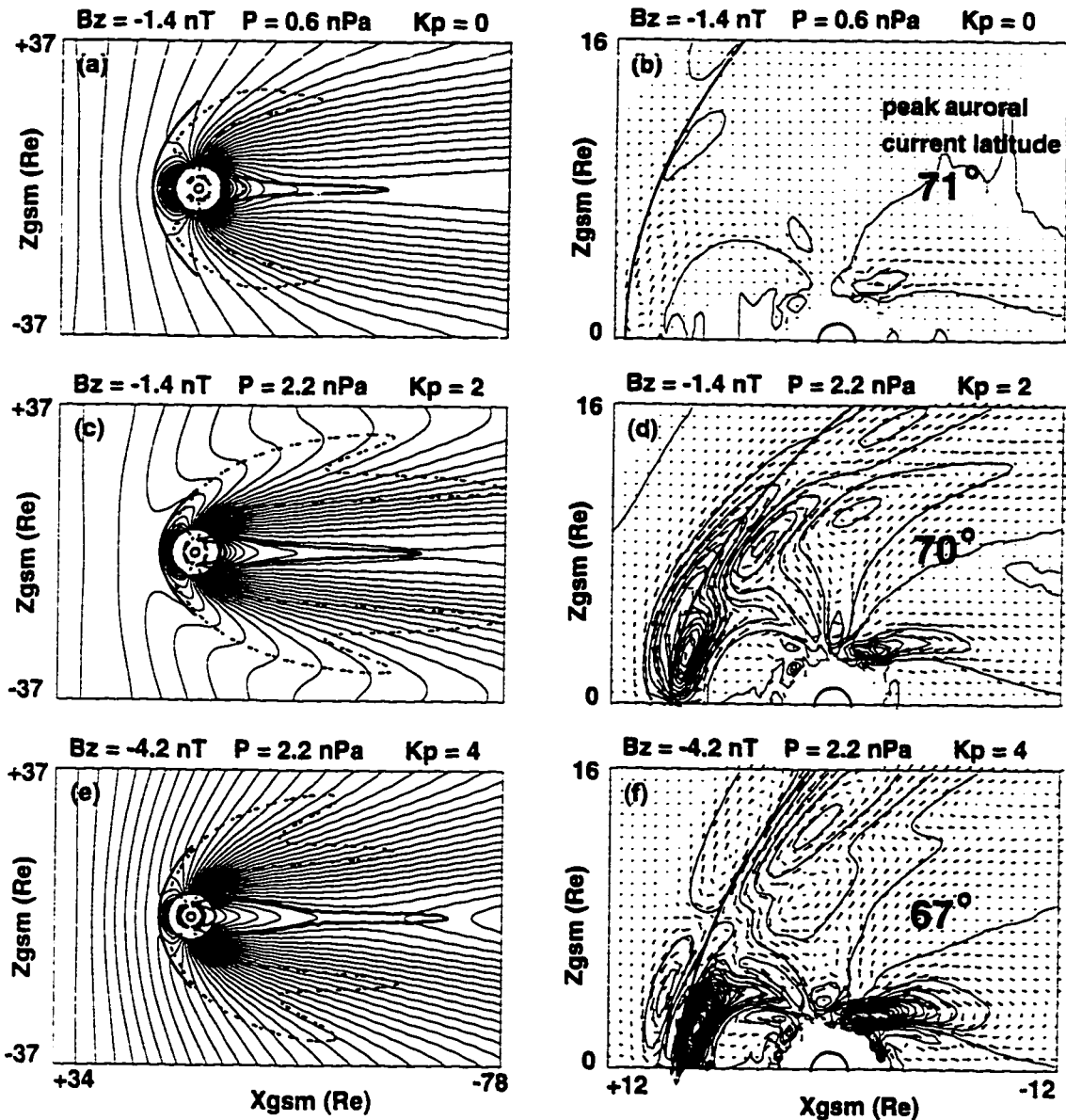
Figure 3.5: Increasing magnetospheric activity. (a) and (b) show the time-averaged magnetic configuration and a closeup of the associated auroral MPD currents for the lowest pressure case of the MPD pressure sequence. (c) and (d) show the same when solar wind dynamic pressure is increased by a factor of 4, while (e) and (f) show when IMF B_Z is increased by a factor of 3 over the second case.

termed "compressed" (Figure 3.5c).

The magnetopause surface passing through the center of the Chapman-Ferraro current layer is shown on the dayside, similar to that in Figure 3.4, while the outer edge of the return current is a good indicator of the magnetopause position on the nightside. Together these outline an approximate shape for the magnetopause which exhibits the same trends just described for nightside magnetic flux. We see that the flanks, now as indicated by the current layers rather than magnetic field lines, are again compressed by the pressure jump (Figures 3.5a to 3.5c), then flared (Figures 3.5c to 3.5e) by the stronger B_Z, all while subsolar distance decreases.

These qualitative trends for increased pressure and IMF B_Z, i.e., compression and flaring, are in good agreement with recent empirical models of the magnetopause [*Sibeck et al.*, 1991; *Roelof and Sibeck*, 1993; *Sibeck*, 1995; *Petrinec et al.*, 1991; *Petrinec and Russell*, 1993, 1995]. There are, however, some very significant quantitative differences between our 2-D simulations and the empirical models and our 3-D simulations [*Winglee*, 1995]. First, the flank distance to the magnetopause in this 2-D simulation is greater than in the 3-D simulations, because magnetic flux is forced to be draped over the poles rather than convecting around the equatorial flanks. The ratio of the polar to subsolar distance varies around 1.5 in both the empirical models and our 3-D simulations but has an average value between 1.8 and 2.0 in our 2-D simulations.

The subsolar distances also do not scale the same as the empirical models and 3-D models. This is due to the use of a 2-D dipole in the simulation, which falls off as r^{-2}. We do see some qualitative similarities to the empirical models, such as power law scaling for dynamic pressure that produces roughly self-similar magnetopause shapes with a fairly constant flank to subsolar ratio at all pressures. The subsolar distance decreases monotonically with B_Z, roughly consistent with the linear decrease seen in the empirical models, but the average gradient is about twice that in the 3-D and empirical models.

The average X line position ranges from 42 to 60 R_E and will be discussed more in Section 3.6. The associated auroral MPD currents in Figures 3.5b, 3.5d, and 3.5f grow significantly on both the dayside and nightside for these increases in IMF B_Z and p, while the center of the auroral currents moves equatorward, again consistent with the general phenomenology of substorms. These currents are discussed further

in Section 3.7. The cross-tail current and return current through the plasma mantle also increase with both IMF B_z and p. All three current systems are good indicators of a general level of magnetospheric activity. Cross-tail current is examined more in Section 3.5 and used as the starting point for a comparison with the empirical T89M magnetic field model.

3.5 Comparisons with the T89M Model

3.5.1 The T89 magnetospheric magnetic field model

The T89 magnetospheric magnetic field model of *Tsyganenko* [1989] is briefly described here before analyzing the tail currents in more detail. The model gives the average magnetic field out to a distance of 70 R_E in the tail for different values of the K_p index and dipole tilt angles. This is an average (static) field description that matches time-dependent observed values to within about 50% on average. The T89 magnetic field is modular, combining an internal field model with an external field model described by three modules that give the magnetic field contribution from the ring current, the cross-tail current, and the magnetopause current, all of which are described by 34 parameters. This empirical model is based on least squares fitting of these parameters to over 36,000 data points in a large data base that is constructed from measurements taken within the magnetosphere at radial distances between 4 and 70 R_E by a large number of spacecraft. The data base is sorted by six bins of the K_p index, so that the separate least squares fits provides an average magnetic field description for each bin. (This was increased to 7 bins in the T89M model, which also has 2 more model parameters and a somewhat larger data base.) The criterion for least squares fitting was simply minimizing the magnitude of the vector difference between the measured and model magnetic field.

The magnetic field measurements used to construct the data base are averaged in the manner used by Mead and Fairfield [1975], in which space is divided into a Cartesian lattice of cubes 1 R_E on a side in the GSM coordinate system. All of the magnetic field measurements taken by a satellite during the traversal through one of these cubes, which typically might take up to about an hour, are linearly averaged. The average magnetic field, average spacecraft position, and dipole tilt for the traversal then becomes a single data point to be used for fitting and it is

correlated with the 3-hour K_p index during this interval.

The ring and tail current modules contain mathematical functions that are physically realistic, although not strictly derived from physics. The curl of the ring current module produce a torus of current centered around the magnetic dipole axis, while the tail current module produces a cross-tail current sheet of finite thickness. This current sheet is hinged in the X direction by dipole tilt and also limited and warped in the dawn-dusk direction, in agreement with observations [Fairfield, 1980]. The magnetopause module, however, is much less realistic and is really just a general polynomial that accounts for everything other than the ring and tail current fields, i.e. primarily the magnetopause current fields, but also to some extent the fields from field-aligned currents. While the magnetopause polynomial estimates the contribution from magnetopause currents at specified points within the magnetosphere, it does not have a representation for the magnetopause surface.

3.5.2 Cross-tail current

Returning to the analysis of the cross-tail currents, the average cross-tail current along the tail axis is plotted in Figure 3.6 for the two parametric simulation sequences. In Figure 3.6a, the pressure is kept constant at 2.2 nPa, while the magnitude of southward IMF increases from -0.35 to -4.2 nT, from weak to moderate southward values. This gives the variation of the average tail current for changes only in IMF B_Z with a typical dynamic pressure. The cross-tail current is a good overall indicator of magnetospheric activity, being well correlated with X line dynamics and auroral currents, as we have seen. The peak values increase for stronger values of IMF by a factor of almost 4, while the IMF strengthens by 12. The position of the peak value moves toward the Earth, while the profile grows sharper. There is some intersection of the curves, i.e., J_Y does not always increase at every X for an increase in IMF strength. Conversely, in Figure 3.6b, the IMF B_Z was kept constant at -1.4 nT while dynamic pressure varied from 0.56 to 9.0 nPa, corresponding roughly to the 2σ variation in the solar wind dynamic pressure [Sibeck et al., 1991]. In this sequence, each increase in the pressure produces an increase in J_Y at all values of X in the tail, in contrast to the previous case. The position of the peak current shows no consistent trend toward or away from the Earth, while the peak value increases by almost 3 for a dynamic pressure increase by 16.
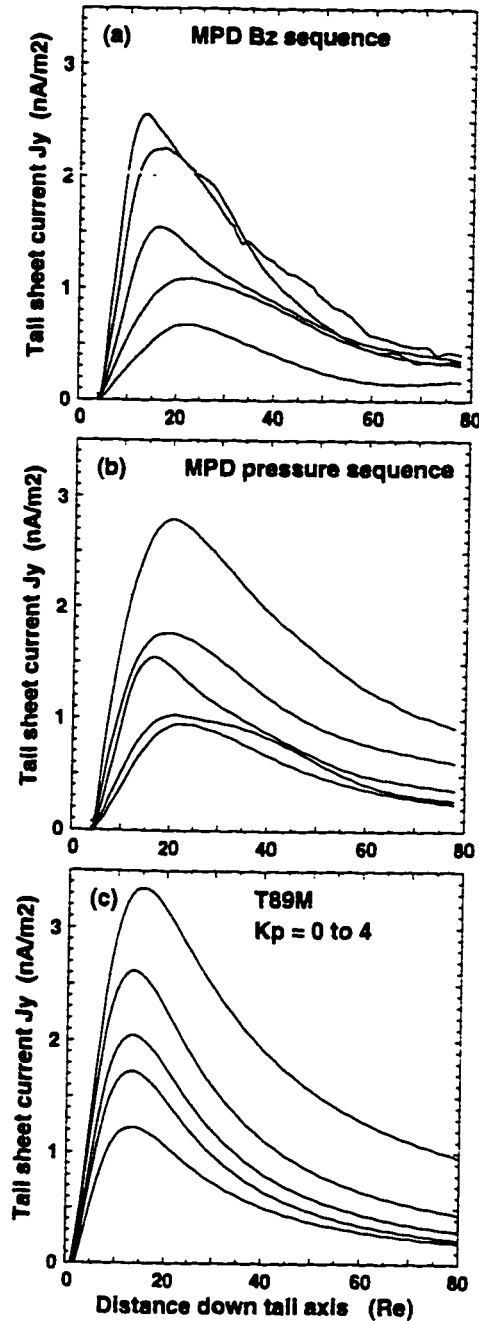
Figure 3.6: Comparing the static average cross-tail current J_Y along the tail axis. (a) The current profiles for five MPD simulations with increasing southward IMF B_Z and constant solar wind dynamic pressure. (b) The same for five MPD simulations with increasing dynamic pressure and constant IMF B_Z. Increasing magnitude of the solar wind input corresponds to increased peak current values. (c) The tail-current profiles calculated with T89M for $K_p = 0$, 1, 2, 3, and 4 with no dipole tilt and with the contribution from the ring current deleted.

The average tail current sheet profiles as a function of X in the pressure sequence have a shape quite similar to those in the T89M model. Figure 3.6c shows the current profiles derived from the T89M model along the Sun-Earth line for zero dipole tilt at the five lowest levels of activity as given by the K_p index. These are $K_p = 0$, 0^+; $K_p = 1^-$, 1, 1^+; $K_p = 2^-$, 2, 2^+; $K_p = 3^-$, 3, 3^+; and $K_p = 4^-$, 4, 4^+, which we shall simply now call $K_p = 0, 1, 2, 3$, and 4, respectively. Since the equivalent of a ring current is missing in a 2-D fluid model and the ring current magnetic field in T89M has a totally different scale and shape than the tail magnetic field, the ring current field has been deleted from the T89M tail fields when calculating J_Y current profiles in the tail to facilitate comparison.

The value of J_Y in T89M increases at all values of X, i.e., none of the curves intersect, for this range of K_p, similar to the MPD pressure sequence in Figure 3.6b. The position of the peak current, however, moves slightly tailward as activity increases, in contrast to the B_Z sequence, which moved earthward, and the pressure sequence, which moved back and forth with no clear trend. Despite these differences, the general shape of the family of curves given by T89M is very similar to those in both the pressure and B_Z sequences, as can seen by inspection, but the magnitudes are about 40% higher. The relative increase in T89M peak tail current as the level of activity increases from 0 to 4 by a factor of about 3 is also similar to the MPD simulation results. This difference is cross-tail current magnitudes is related to previously documented discrepancies in the T89 model.

3.5.3 Stretching of the magnetotail

Although the parameters in the Tsyganenko models (T87, T89, and their derivatives) are least squares fitted to large data sets of satellite measurements, the T89 model has recently been found to have significant discrepancies in particular regions of the magnetosphere [*Huang et al.*, 1990; *Huang et al.*, 1991; *Donovan et al.*, 1992; *Stern and Tsyganenko*, 1992; *Peredo et al.*, 1993; *Huang and Frank*, 1994]. When compared with ISEE 1 data measurements for low K_p (less than or equal to 2), the B_Z component near the plasma sheet ($Z = \pm 2\ R_E$, $Y = \pm 10\ R_E$) for near-Earth distances ($X = -10$ to $-22\ R_E$) was found to be consistently too low by a factor of about 2. This indicates that the tail current is too strong and is canceling out too much of the dipole field.

The dashed outline in Figure 3.7 contains the great majority of the ISEE 1 data points for such conditions, drawn from Figure 1 of *Stern and Tsyganenko* [1992]. The B_Z component along the tail axis is plotted for $K_p = 0$, 1, and 2 using the T89M model and is seen to lie below the box containing most of the ISEE data points. The T89M model, although fitted to a larger data set than T89, still exhibits similar behavior, i.e., the tail magnetic field is excessively stretched in this region. To reduce the stretching, we tried multiplying magnetic field modules of the Tsyganenko models by scalar factors, a procedure similar to that used by *Pulkkinen* [1991] and *Pulkkinen et al.* [1991]. Those studies, however, constructed a time-dependent magnetospheric configuration that matched dynamic measurements during a substorm, while this exercise is attempting to reproduce a static configuration that better matches ensemble-averaged data in a critical region. If the tail magnetic field with negative B_Z is weakened by multiplying it by a factor of 0.70, the total value of B_Z is increased in the near-Earth region, by a factor of as much as 3 in some places. The resulting curves for this reduced tail T89M are plotted in Figure 3.7 with heavy lines and lie in the middle of the box of data points. Thus the reduced tail T89M gives more realistic values of B_Z and is not excessively stretched in the equatorial region. When the average MPD B_Z values for low activity levels are plotted (dashed lines), we see that they also predict realistic values for B_Z in this region, about 5 nT at 16 R_E, right in the center of the ISEE data.

As demonstrated by *Winglee* [1995], our 3-D code produced a quiet, closed configuration for a dynamic pressure of 1 nPa and northward IMF B_Z of 3.6 nT. Magnetic field lines drawn from a latitude of 70° reach out to about 15 R_E on the nightside. Similar lines traced using T89M with $K_p = 0$ reach out to about 55 R_E in the tail, a symptom of the excessive tail stretching. When reduced tail T89M is used, the same lines reach only to 14 R_E, within a few R_E of the 3-D simulation, indicating that the tail may be stretched about the right amount.

Although this modification to T89M has improved the accuracy of B_Z in the near-Earth tail, it has made another problem with T89M worse. *Pulkkinen et al.* [1995] have shown that T89 (and hence T89M) significantly underestimates the strength of the magnetic field in the lobes. Reducing the tail current of T89M will further decrease the lobe magnetic field. The problem with the lobe fields can be seen in Figure 3.8, which shows the magnitude of the magnetic field along a vertical cut at

Kp <= 2

- - - - - MPD low activity

——— T89M

━━━ Reduced Tail T89M

Box contains most
ISEE data points

Bz (nT)

24

18

12

6

0

10   14   18   22   26

Distance down tail axis (Re)
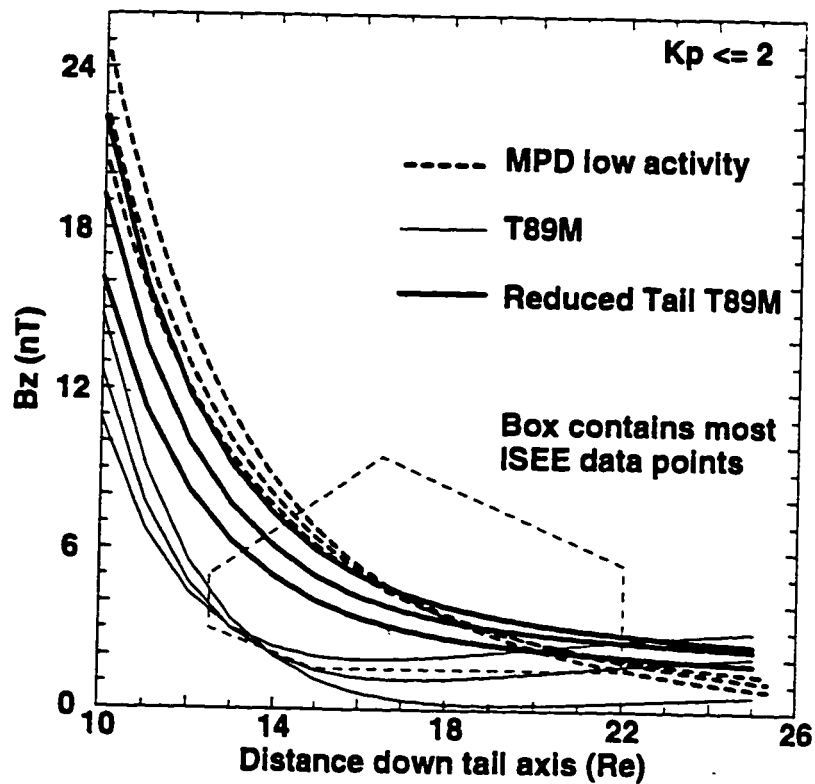
Figure 3.7: A comparison of B_Z values in the tail of three models versus time-averaged satellite measurements of B_Z during quiet times. The dashed outline contains the great majority of the ISEE 1 data points from Figure 1 of *Stern and Tsyganenko* [1992]. The light solid lines show the values from T89M for $K_p = 0$, 1, and 2, while the bold solid lines show the equivalent values obtained by multiplying the tail magnetic field by a factor of 0.70. The bold dashed lines indicate the scaled values of B_Z from the time-averaged configurations for the three lowest activity runs of the MPD pressure sequence.

$X = -40\ R_E$ for the MPD and T89M models. The MPD field magnitude (solid line) reaches a peak value over 20 nT at about $Z = 12\ R_E$, but then drops off as it approaches the magnetopause, and finally drops to very low values outside the magnetopause (past $\sim$30 R_E). Case studies using our 3-D code have similar profiles and peak values (not shown).

The magnetic field magnitude along the same vertical cut in T89M for $K_p = 3$ (dashed line) quickly reaches 10 nT just a few R_E above the tail axis, but at the center of the lobe, say, 10 to 15 R_E, has a magnitude not much more than half that of the MPD simulation. Instead of leveling off or peaking, as might be expected, it continues to grow with Z, reaching above 20 nT when it is outside the magnetopause. The growth in field magnitude at large values of Z is due to the magnetopause polynomial portion of the T89M magnetic field, used to contain the T89M magnetic field within a cavity.

We can also gauge the strength of the lobe magnetic field by the integrated tail current profile along the X axis, although this is an underestimate in T89M at large values of Z. The J_Y profiles along the tail axis of both the simulations and T89M (Figure 3.6) decrease rapidly with distance, suggesting small integrated values deep in the tail. The integrated tail current in T89M for $K_p \leq 3$ is $\sim$30 mA/m near the Earth ($\sim$12 R_E), drops to $\sim$5 mA/m at 50 R_E, and keeps dropping with distance [cf. *Pulkkinen et al.*, 1995]. The drop in current density seen in the simulations, however, is compensated by a broadening of the current sheet and actually causes the integrated current to level off by the end of the simulation box. The peak integrated tail current in the MPD simulation (not shown) near the Earth (12 R_E) is about 30 mA/m, drops to 22 mA/m at 30 R_E, but levels off at about 15 mA/m (78 R_E). Values inferred from observations by *Slavin et al.* [1985] give about 33 mA/m at 30 R_E, leveling off at about 15 mA/m tailward of 120 R_E. The integrated tail current of MPD matches T89M fairly well near the Earth, but matches observations well in the deep tail, being slightly underestimated in the middle tail.

3.5.4 Magnetic field line mapping in the magnetotail

The MPD model, despite being 2-D, predicts magnetic field values in the far tail better than T89M, both the B_Z component in the equatorial plane and the B_X component that dominates the lobe. The magnetic field strength of the case shown in Figure 3.4
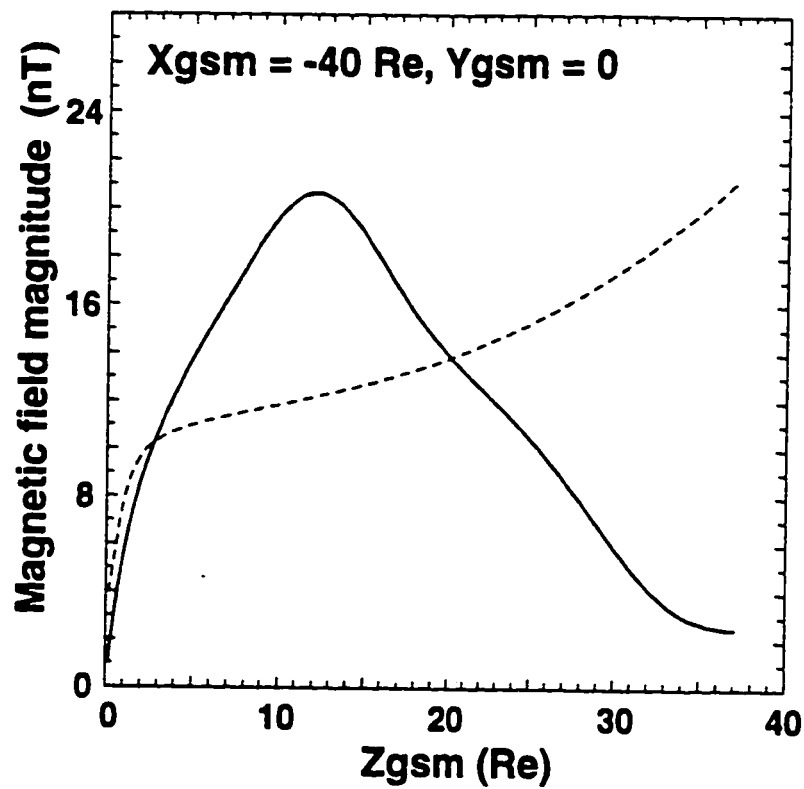
Figure 3.8: The magnetic field magnitude along a vertical cut from $X = -40\ R_E$ on the tail axis for several magnetospheric configurations. The solid line shows the MPD case of Figure 3.4, while the dashed line shows the same using T89M with $K_p = 3$.

scales to 53 nT just inside the subsolar magnetopause, on the low end of typically observed values. Hence we have fairly realistic (even if slightly underestimated) values for the magnetic field everywhere in the magnetotail outside the region dominated by the dipole and the ring current. The magnitude of B_Z in the equatorial plane and B_X in the lobe both strongly affect the mapping of high-latitude field lines. This leads us to find a significant qualitative difference in this mapping as magnetospheric activity increases when MPD is compared with T89M.

We examined the distance that magnetic field lines in the noon-midnight meridian lie above the equatorial plane at various positions down the magnetotail. Figure 3.9a shows this vertical distance at 60 R_E plotted as a function of the colatitude of the field line for five K_p levels of the T89M model. The horizontal line corresponds to a fixed point deep in the tail ($X = -60\ R_E$, $Y = 0$, and $Z = 20\ R_E$). The five solid squares show the mapped colatitude at the Earth's surface of the field line that passes through this fixed point for the different K_p levels. This colatitude decreases as the magnetospheric activity increases, i.e., a fixed point in the tail maps to higher latitudes as K_p increases. This trend in the T89M mapping of high-latitude field lines is contrary to that given by *Pulkkinen* [1991], who simulated the increased stretching of the magnetotail during the substorm growth phase by enhancing the tail current of T89, reflecting a time-dependent increase in magnetospheric activity. When the T89 tail current was multiplied by a factor of 1.3 for a fixed K_p, tail lines became more stretched near the equatorial plane, while the lobe lines were compressed. This modification gives field lines that map to lower latitudes when magnetospheric activity increases.

Figure 3.9b shows the mapping of high-latitude magnetic field lines for the three cases illustrated in Figure 3.5, with increasing levels of magnetospheric activity labeled 1, 2, and 3. The first jump in dynamic pressure by a factor of 4 pushes the curve to the right by a few degrees, while the second jump when IMF B_Z was additionally tripled also pushes the curve to the right by a similar amount. The B_Z sequence produced about twice as much equatorward motion overall as the pressure sequence, but this trend of equatorward mapping for increased magnetospheric activity is quite general. Similar behavior is seen in the mapping of high-latitude field lines in our 3-D models as well, especially for changes in IMF B_Z. A fixed point in the tail maps increasingly equatorward as magnetospheric activity increases, similar to *Pulkkinen*
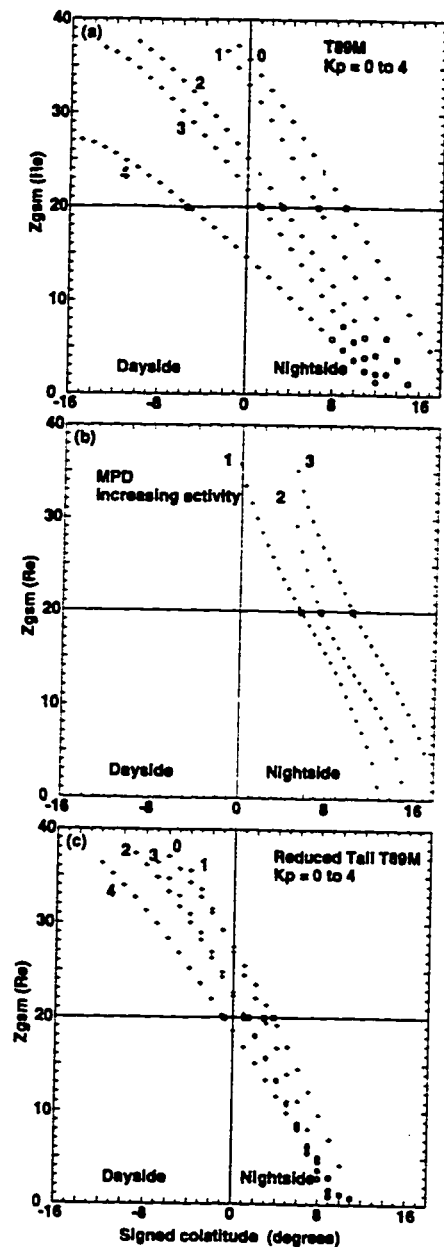
Figure 3.9: A comparison of magnetic field line mapping for high-latitude magnetic field lines in the tail. (a) The colatitude at the Earth's surface of these field lines in the noon-midnight meridian plane, with positive values on the nightside. Each cross or circle gives the Z value where the field line intersects the $X = -60\,R_E$ plane. The mapping was done for the five lowest K_p levels of the T89M model. The solid squares indicate the colatitude where a field line passing through $X = -60$, $Z = 20\,R_E$ will strike the Earth's surface. (b) The mapping of field lines from the three MPD cases shown in Figure 3.5. (c) The same mapping as (a) using reduced tail T89M.

[1991] but opposite what is seen in Figure 3.9a when K_p was increased in the T89M model.

This change in mapping is what one would expect from substorm phenomenology, so we shall call this "regular mapping." Since the mapping of tail field lines that originate from high latitudes in T89M moves in the opposite direction with increasing activity, we shall call this "reversed mapping." While ionospheric footpoints clearly move equatorward when magnetospheric activity rises, the motion of field lines in the tail is not well understood and there is no standard to gauge it against, except the global simulations and empirical models themselves. We have seen, however, that the magnetic field values in the tail of the simulation are fairly realistic, while the T89M model is excessively stretched and has weak lobes.

Reversed mapping is significantly reduced in reduced tail T89M, but not quite canceled out (Figure 3.9c). The mapping for K_p of 1 is actually slightly equatorward of that for 0, and 3 is also slightly equatorward of 2, but the overall trend is still poleward. The poleward motion of 15° seen in T89M as K_p increases from 0 to 4 reduces to about 4° (bold points). Further decreasing the tail current, to 50% of its original value, actually causes overall equatorward motion by about 2° (not shown). While reductions in tail current cause all mapped positions on the tail axis to move earthward (less stretching), it also flares the lines in the lobe, the opposite of effects produced by *Pulkkinen* [1991]. This causes the slope to the traces seen in Figure 3.9a to become steeper, so that poleward changes seen on the tail axis are weaker (or even equatorward) at high values of Z. The reversal of the mapping trend occurs because the lowest K_p cases move the most poleward and overtake the higher K_p cases. Increasing the magnetopause polynomial in T89M can also reverse the mapping in much the same fashion by pushing lower K_p cases more poleward. While this increases the undervalued lobe field strength somewhat, it also causes significant problems, such as large changes in the subsolar magnetopause distance (over 1 R_E).

The closed magnetospheric cavity of the T89M model is increasingly compressed as the K_p index rises, while the MPD magnetospheric flanks can compress or flare when pressure or B_Z is increased, respectively. Increasing either of these solar wind parameters, however, raises magnetospheric activity (e.g., increases tail current), so the T89M model lacks a degree of freedom that our model has. In fact, the magnetopause surfaces of the T89M model for increasing K_p (not shown) match the

magnetopause surfaces of *Sibeck et al.* [1991] for increases in dynamic pressure fairly well. This indicates that the effect of p is much stronger on the magnetospheric configurations of T89M, while the effect of B_Z has been canceled out to some extent, presumably by averaging cases of both positive and negative IMF B_Z in each K_p bin.

Although the resulting field departs from a least squares fit to the satellite data set, the changes to T89M are of the same magnitude as that used in the studies by *Pulkkinen* [1991] and *Pulkkinen et al.* [1991]. Reduced tail T89M successfully produces mapping for a less stretched tail that is similar to the mapping of equatorial field lines in 3-D codes, especially when magnetospheric activity is low. While the lobe magnetic field is further underestimated, changes to other areas of the model are relatively minor. The subsolar magnetopause shifts by only about 0.1 R_E, the cusp latitude changes by less than 1°, and low-latitude lines do not change much because they are dominated by the dipole field.

3.6 Average X Line Position and Resistive MHD

Despite the violent plasmoid formation and ejection in the dynamic sequence of Figure 3.1, all that remains after time-averaging is a single X line located at 60 R_E, as seen in Figure 3.4a. The average X line position was found to vary more in the B_Z sequence than in the pressure sequence. For the strongest southward IMF of -4.2 nT, the X line came in to 42 R_E, while for the weakest IMF of -0.35 nT, there was no X line at all (the simulation box goes out to 78 R_E). Average X line position decreased monotonically as IMF B_Z was strengthened and shifted large distances (over 36 R_E), suggesting that B_Z is very important for predicting the average X line position. For changes in only the solar wind dynamic pressure, however, the X line position ranged from 42 to 60 R_E and did not vary monotonically, suggesting that dynamic pressure is much less important as a predictor for X line position. Most significant, the average X line position was 42 R_E or deeper in the tail for all the MPD simulation cases studied.

Satellite magnetometer data have been averaged over periods ranging from a few minutes up to 3 hours for statistical studies of magnetic field [cf. *Behannon* 1970; *Mihalov et al.*, 1968]. These studies show that the average value of B_Z in the equatorial plane of the magnetotail is more likely to be negative on short timescales of a few minutes, compared with timescales of a few hours. *Behannon* [1970] found that about

25% of the tail measurements from 20 to 70 R_E within 8 R_E of the neutral sheet with unrestricted Y_{gsm} had negative B_Z when averaged over 1 hour. *Fairfield* [1986] also found that a significant fraction of the B_Z measurements (2.5-min averages) near the noon-midnight meridian ($-9\,R_E \leq Y_{gsm} \leq +7\,R_E$) in the plasma sheet were negative ($|Z_{gsm}| \leq 3R_E$). When conditions were mildly disturbed ($AE > 50$ nT), 29% of the measurements between 10 and 20 R_E and 15% between 20 and 40 R_E were negative. Alternatively, all of the data at a particular position can be averaged to produce a long-term average value [cf. *Fairfield*, 1986]. When all the measurements were averaged over the sectors, i.e., with no timescale, B_Z was always positive out to 40 R_E. *Fairfield* [1986] does not, however, provide averages of B_Z in the midtail on longer timescales (e.g., 1 to 3 hours) that can be directly compared with our simulation results.

Although we had transient negative values of B_Z due to X line formation near the Earth as close as 13 R_E, similar to the measurements given by *Fairfield* [1986], when the configuration is time-averaged, there are significant qualitative differences in the magnetospheric configuration which agree with long-term averages of data. The presence of a positive value of B_Z out to 40 R_E in our 3-hour averages is similar to the positive overall (long term) averages given by *Fairfield* [1986]. The tendency of our code to produce positive B_Z on a timescale as short as 3 hours is related to the ease with which substorm recovery is achieved in a 2-D simulation. Preliminary results with 3-D codes suggest that B_Z may be negative in midtail regions near the noon-midnight meridian for periods longer than 1 hour, owing to continuous convection of magnetic flux around the flanks. This may be consistent with some negative B_Z measurements in 1-hour averages seen in the magnetotail by *Behannon* [1970].

We ran several resistive MHD simulations with otherwise identical input conditions to investigate the time history and average position of the X line compared with MPD. The MHD behavior was generally consistent with the findings of *Lyon et al.* [1986], who studied the effect of resistivity on the magnetotail dynamics of a 2-D MHD global magnetosphere model. A uniform magnetic Reynolds number of 5600 produced dynamics and time histories (not shown) with the same qualitative behavior as the MPD run described in Figures 3.1 to 3.4. Cross-tail currents were somewhat weaker and there was less modulation in current intensity, but plasmoid formation and ejection were much the same, except on a slightly slower timescale. The average

X line position (43 R_E) was close to the MPD value, but the subsolar distance to the magnetopause was about 1 R_E larger, indicating a lower average reconnection rate at the subsolar point. Despite these differences, the similarity in global behavior means the equivalent magnetic Reynolds number for the entire MPD configuration is near 5600, although the resistivity and hence the magnetic Reynolds number are determined locally.

Another highly resistive MHD run (also not shown) with a magnetic Reynolds number of 1100 displayed radically different behavior after the X line formed, giving an average X line position of only 27 R_E. Although the X line initially formed at 28 R_E and then moved earthward, much like the other simulations, the subsequent tailward motion of the X line was considerably slower. By 200 min the X line had only reached 33 R_E, and a second X line nearer the Earth (and a true plasmoid) had never formed. Instead of cyclical modulation of the cross-tail current, the current rises after disconnection and then drops and flattens out. Negative B_Z beyond 27 R_E over a 3-hour period means this more resistive configuration is less like the long-term average produced by *Fairfield* [1986], the MPD configurations, or the less resistive MHD configurations. While a high anomalous resistivity may produce a higher reconnection rate, most critically in the magnetotail for southward IMF, it also prevents the tail from recovering through continuous dissipation of energy [cf. *Lyon et al.*, 1986].

The X line time history in both Figure 3.3a and our less resistive MHD case is qualitatively quite similar to the X line motion of the 3-D MHD magnetotail simulation shown in Figure 4 of *Birn and Hones* [1981]. That less resistive MHD simulation had higher velocities for plasmoid ejection, and subsequent X line reformation occurred very quickly. If time-averaged, this less resistive configuration would also have an average X line position significantly earthward of 40 R_E and also would repeat on a timescale much less than 1 hour. We find that the effective resistivity that modulates tail and auroral currents on a substorm timescale (1 to 3 hours) in our 2-D simulations also produces a higher value for the average position of the X line, consistent with long-term averages of observations. Higher (lower) resistivity lengthens (shortens) the timescale for magnetospheric activity, but in either case produces X line positions that are inconsistent with observations, i.e., too close to the Earth.

The MPD prescription can have a high reconnection rate at the subsolar point and at certain locations in the magnetotail, owing to a high local value of the effective re-

sistivity, while having a relatively low effective resistivity in other areas. MPD drives a substorm with strong current modulation, permits the tail to recover, the plasmoid to be ejected, and gives a relatively high value of the average X line location consistent with observations. Matching substorm timescales with the simulations provides another means of assuring that the overall resistivity of the global configuration is approximately correct.

3.7 Current Magnitudes and Variation

Although field-aligned currents can have a peak magnitude from 1 to 20 $\mu A/m^2$ in an auroral arc [*Lyons and Williams*, 1984; *Fukunishi et al.*, 1993], they are considerably weaker at several Earth radii. Field-aligned currents measured by satellites at about 3 R_E have average densities up to about 0.05 to 0.10 $\mu A/m^2$. The average field-aligned current density, calculated from Plate 2 of *Winglee et al.* [1988], is 0.053 $\mu A/m^2$ over a width of 2100 km and can be taken as typical during moderately active times. The integrated current across this structure is 110 mA/m.

The largest time-averaged current density in the auroral zone close to 3 R_E in the simulations scales to about 0.5 nA/m^2, smaller by a factor of 100 than the observed current density values. The instantaneous current density values can be as large as 1.2 nA/m^2, still smaller by a factor of 50. The integrated nightside auroral current, calculated using the difference in the scaled stream function, is about 1.4 mA/m for the time-averaged case, again less than the observed integrated current by a factor of about 80. Thus the auroral currents in the present simulation are smaller than the observed field-aligned currents by a factor of 50 to 100. This discrepancy in magnitude is probably due to the limited latitudinal resolution of the fluid model, which is about 2000 km. This distance is comparable to the typical width of field-aligned currents seen by polar-orbiting spacecraft at 3 R_E [*Winglee et al.*, 1988]. Since the strength of the surface currents is expected to be inversely proportional to the square of the grid spacing [*Winglee*, 1994], the present work underestimates the strength of these currents. However, global simulation with grid spacing of a few hundred kilometers is presently beyond computational capability.

The strongest B_Y perturbations, which are ignored in the simulations, rise at most to a few percent of the magnetopause magnetic field and only significantly affect the mapping of field lines in the vicinity of neutral points. The MPD field-aligned currents

close in the plane of the simulation, while MHD field-aligned currents largely close azimuthally. The MPD currents constitute the entire field-aligned current system in our 2-D model, but in our 3-D model the MPD currents are only one component of the total field-aligned current system. Our 3-D model does produce the typical dawn and dusk patterns of region 1 current [*Winglee*, 1995], but it also produces additional currents strong at the cusp and at midnight, similar to those in our 2-D model. These additional, non-MHD currents look much like those reported by *Potemra* [1994], who has broken down the typical observed field-aligned current patterns into constituent elements. In addition to the well-known region 1 and 2 currents, field-aligned currents are observed near the cusp and at the midnight portion of the auroral oval. Such current patterns are missing from MHD simulations, such as those of *Ogino* [1986] and *Fedder and Lyon* [1995]. In fact, in a dawn-dusk symmetric situation, which occurs when IMF $B_Y = 0$, MHD field-aligned currents are explicitly required to be zero in the noon-midnight meridian from symmetry arguments, contrary to observations [*Potemra*, 1994, and references therein; *Kamide*, 1991; *Friis-Christensen and Lassen*, 1991].

The average auroral latitude (Figures 3.5b, 3.5d, and 3.5f) moves equatorward by $\sim7°$ (from 77° to 70°) for the B_Z sequence but only $\sim2°$ for the pressure sequence. While these latitudes are somewhat higher than the statistical auroral oval at the midnight meridian (64° to 72°) [*Feldstein*, 1973], field-aligned currents centered on the auroral oval are produced in our 3-D code [*Winglee*, 1995]. The change in latitudes, however, seen in the 2-D MPD simulations is similar to observations. Furthermore, the time-dependent latitude of the nightside auroral currents (Figure 3.2) varied by a similar amount ($\sim8°$) after tail disconnection (Figure 3.3).

The cusp maps to a latitude near 76° for all cases of the pressure sequence, varying by only about a degree. This latitude is close to but a few degrees less than that in our 3-D model ($\sim80°$ to 82°), which matches observed cusp latitudes well [cf. *Potemra*, 1994]. This invariance of cusp latitude with the dynamic pressure is related to the approximately self-similar scaling of the magnetopause shape in the simulation. The cusp latitude, however, moves strongly equatorward for the B_Z sequence, but the movement is much stronger than in our 3-D model, by a factor of at least 3. We find that B_Z governs both nightside auroral latitude and cusp latitude more strongly than p in our 2-D model. While the predicted auroral and cusp latitudes are not as

accurate as those in our 3-D simulations, converting latitudes with a 3-D dipole can give fairly realistic values. More important, both the time-dependent variation and the parametric variation due to p and B_Z have been shown to be qualitatively right.

3.8 Conclusions

The MPD model is a fundamentally new fluid treatment that can incorporate some particle kinetic effects not included in MHD. This modified fluid algorithm can produce auroral currents near noon and midnight consistent with observations, something the standard MHD codes have difficulty doing. While these current densities are smaller than what is inferred from observations, high grid resolution may fully resolve these currents. These currents map to the ionosphere much like the observed field-aligned currents, and their mapped latitude varies much as expected with the phases of the simulated substorm, which repeats itself on a timescale of a little more than an hour for the most active cases studied. Following disconnection, the simulation exhibited growth and expansion phases, each lasting about 30 min. This was followed by a recovery, with the IMF still pointing southward; thus northward IMF was not required to produce a substorm recovery. This realistic timing of substorm phenomena (1) makes the time-averaging over a 3-hour simulation period meaningful and (2) facilitates comparison with a static semiempirical model based on the same timescale (3-hour K_p index).

Resistive MHD can produce a similar timescale for such a sequence of events when the resistivity is low enough, with modulation in the cross-tail current, although field-aligned currents are absent from the noon-midnight meridian plane. The reconnection rates at the subsolar point and in the tail, however, are lower than in MPD, which can have regions of high effective resistivity. Stronger reconnection can be driven in the tail with a higher anomalous resistivity, but this makes it difficult to produce a recovery of the tail due to continuing ohmic dissipation, giving an average position of the X line much nearer the Earth. In a highly resistive MHD case, the average X line position was 27 R_E, which is less similar to the long term averages of *Fairfield* [1986], who predicts that the long-term average position of the X line lies beyond 40 R_E. Because our MPD model predicts positive average values of B_Z out to 42 R_E in all cases studied, accompanied by transient negative values of B_Z as close as 13 R_E, we have connected the results of fluid simulations with ensemble-averaged satellite

data in a meaningful way.

The observed magnetic fields in the tail are well represented by 2-D simulations. The equatorial value of B_Z matches observations, as do both the lobe magnetic field and the integrated tail current. Comparisons with a limited number of 3-D simulations show similar results. This is because these fields are produced self-consistently by convection of plasma and magnetic field in the noon-midnight meridian in regions where the dipole field is very weak. The average profile of the tail current is similar in shape but has somewhat lower magnitudes than that given by the T89M model. The peak current also showed similar growth by a factor of 3 as magnetospheric activity increased. Reduced tail T89M produces B_Z values that agree better with ISEE observations but unfortunately produces a weaker lobe magnetic field, which is already known to be underestimated by T89M. The mapping of high latitude field lines to the ionosphere from a fixed point in the tail maps to higher latitudes as K_p increases in T89M, while MPD maps equatorward. This reversed mapping in T89M is due to both the excessively stretched tail and the weak magnetic field in the lobes. While magnetopause shape exhibits some qualitative trends (flaring and compression) seen in recent empirical models, as does subsolar distance, there can be significant quantitative differences.

The methodology used in this study provides a new (and sometimes easier) way to study the global properties of the simulation, i.e., preparing a time-averaged static representation of the time-dependent configuration. We have seen that the time-averaged values of some quantities, such as the position of the X line, are very different from the instantaneous values. Presently most fluid simulations are compared at a specific time step with observations. If the observations are instantaneous, that comparison is valid; but when data are averaged, averaging the model measurements provides a better comparison. The 2-D model also facilitated parametric study of simulation results, for example, with two solar wind parameters in the present study, as opposed to studying a limited number of 3-D case studies. Both the time-averaging methodology and their parametric variation can be easily extended to 3-D to produce time-averaged, static magnetospheric configurations which can be connected with observations and empirical models in a meaningful way. A global set of such synthesized data providing uniform coverage and consistent variation of the parameters permits discovery of magnetospheric relationships, some of which may be more difficult to

discover by data analysis of real observations due to nonuniform coverage and other nonideal conditions.

Chapter 4

THE THREE-DIMENSIONAL SHAPE OF THE MAGNETOPAUSE

4.1 Introduction

4.1.1 Outline of chapter

In this chapter the results from 3-D global MHD simulations of the magnetosphere are presented, focusing on the shape and size of the magnetopause. A predictive model of the magnetopause is constructed from these simulations over a range in solar wind dynamic pressure and the north-south component of the interplanetary magnetic field (IMF B_Z). The magnetopause is identified in the simulations using electric current intensity, thermal pressure, and magnetic field line mapping. The magnetopause is fitted by least squares to an ellipse in each plane, and a fully 3-D magnetopause surface is constructed by assuming an elliptical cross-section at intermediate clock angles. There is considerable flaring of the magnetopause dependent on B_Z in the noon-midnight meridian plane due to reconnection, but virtually no flaring in the equatorial plane.

Despite this asymmetry, when averaged over clock angle, the model shows a general agreement with recent (axisymmetric) empirical magnetopause models and predicts observed magnetopause crossings with about the same accuracy as the empirical models. Unlike these empirical models, our model can directly investigate asymmetries between the meridian and equatorial planes. The subsolar distance, directly measured from the simulations, varies linearly with B_Z for both northward and southward IMF, as do distances to the magnetopause on the flanks. Magnetospheric plasma pressure causes these distances to scale with dynamic pressure by a power law whose exponent is a bit less than $-1/6$ on the dayside, but little deviation from this ideal Chapman-Ferraro value is seen in the magnetotail. These uniform changes with B_Z lead to approximate conservation of (1) magnetopause shape in the dayside equatorial plane, (2) projected area in the dayside meridian plane, and (3) magne-

topause cross-sectional area in the dawn-dusk plane. The dawn-dusk magnetopause cross-section is nearly circular on average, but cross-sections in the tail are elongated in the Z direction on average. The results of this chapter are contained in *Elsen and Winglee* [1996b].

4.1.2 Motivation for study

When large numbers of observed magnetopause crossings are correlated with solar wind and terrestrial conditions, much of the transient variation cancels out and the average position for a given set of conditions can be determined. The two solar wind variables most important for determining the average magnetopause position are believed to be the dynamic pressure (momentum density flux) of the solar wind and the northward/southward component of the interplanetary magnetic field (IMF B_Z) [*Fairfield*, 1991, 1995; *Sibeck et al.*, 1991; *Roelof and Sibeck*, 1993]. The average shape of the magnetopause as a function of these variables has recently been determined by two groups [*Sibeck et al.*, 1991; *Roelof and Sibeck*, 1993, 1994, 1995; *Petrinec et al.*, 1991; *Petrinec and Russell*, 1993a, 1993b, 1995a, 1996a, 1996c]. Both of these models have root mean square (rms) errors near one earth radius (R_E) on the dayside and 2 R_E on the nightside.

These models are in substantial quantitative agreement where they are well constrained by a large number of observations; significant differences between the models occurring at low dynamic pressures and IMF B_Z strongly northward or southward are due mostly to the small number of observations for these conditions [*Sibeck*, 1995]. While subsolar distance and magnetopause shape change continuously in both models with southward IMF, these quantities are constant for northward IMF in the dayside magnetopause model of *Petrinec and Russell* [1995a]. These quantities vary continuously in the model of *Roelof and Sibeck* [1993], however, pointing to a significant qualitative difference between these models for northward IMF.

In the seventies, the effect of IMF B_Z on magnetopause size and shape was realized, with this change attributed to flux erosion, the large-scale transfer of magnetic flux from the dayside to the nightside [*Aubry et al.*, 1970, 1971; *Meng*, 1970; *Fairfield*, 1971, 1979; *Coroniti and Kennel*, 1972; *Burch*, 1974; *Maezawa*, 1974; *Holzer and Slavin*, 1978; *Formisano et al.*, 1979]. In this scheme, persistent southward IMF is expected to lead to flaring of the magnetopause, i.e., the flank distances to the

magnetopause increase near the meridian plane while the subsolar distance decreases and the equatorial distances change little. This changes the shape of the magnetopause, especially in the meridian plane, so that self-similar scaling of the dayside magnetopause with dynamic pressure [*Sibeck et al.*, 1991] also breaks down. Magnetic reconnection behind the cusp may also operate when IMF is northward, giving rise to an opposite process where magnetic flux is transferred from the nightside to the dayside. Convection will return magnetic flux to the dayside, so the movement of the dayside magnetopause will depend on the net flux transfer due to both reconnection and convection [*Coroniti and Kennel*, 1973; *Holzer and Slavin*, 1978]. The resulting changes to the magnetopause may be markedly different in the noon-midnight and equatorial planes, creating an asymmetry in magnetopause shape dependent on B_Z that may be especially strong on the nightside.

Virtually any magnetopause model can be scaled by the dynamic pressure, but the inclusion of flaring due to IMF B_Z is much more difficult. Currently, the only models that can successfully predict the position of the magnetopause for IMF B_Z in addition to P_D are the aforementioned empirically based models [*Roelof and Sibeck*, 1993, hereafter called RS93; and the updated hybrid dayside and nightside models of *Petrinec and Russell*, 1995a, 1996a, hereafter called PR95 and PR96, respectively]. Flaring due to IMF B_Z is present in these axisymmetric models, but only in an average sense, with no difference between the meridian and equatorial planes. These magnetopause data bases date back to early statistical studies of magnetopause position [*Fairfield*, 1971; *Holzer and Slavin*, 1978; *Formisano et al.*, 1979]. Their limited size, however, makes it difficult to investigate the expected differences in magnetopause shape between the equatorial and noon-midnight meridian planes due to flaring, as well as other influences on the average magnetopause shape [*Roelof and Sibeck*, 1993].

One way around the limitations of the empirical models is to use 3-D global MHD models of the magnetosphere as the foundation for a magnetopause model. Although global MHD modeling of the Earth's magnetosphere [e.g., *Fedder and Lyon*, 1987, 1995; *Fedder et al.*, 1995; *Ogino*, 1986; *Walker et al.*, 1993; *Ogino et al.*, 1994; *Raeder et al.*, 1995; *Watanabe and Sato*, 1990; *Usadi et al.*, 1993] produces the overall morphology of the magnetosphere, the simulations to date have usually been limited to case studies, and have not been used to quantitatively determine the average shape and position of the magnetopause. Global models self-consistently produce a

magnetopause for any given solar wind input, permitting direct incorporation of not only IMF B_Z, but other variables such as IMF B_Y or dipole tilt, if desired. A steady-state solution will show the average position for steady solar wind conditions, and any resulting asymmetry between the noon-midnight meridian and equatorial planes is easily studied.

A predictive magnetopause model is developed in this chapter by using about 30 3-D global fluid simulations that cover a significant range of solar wind dynamic pressures and IMF B_Z. The magnetopause positions are then measured for each of these simulated cases. We approximate the magnetopause from the simulations by fitting ellipses in both the meridian and equatorial planes. Differences between these planes can be significant, especially in the magnetotail when IMF is southward. Interpolating between the two planes using the clock angle of the observation point produces a three-dimensional, non-axisymmetric model of the magnetopause surface that directly shows the effects of flaring due to IMF B_Z.

4.1.3 Scope of this chapter

Observational evidence for asymmetry is summarized briefly in Section 4.2. The global magnetospheric model is described in Section 4.3. The magnetopause from the simulations is described in Section 4.4 along with methods used for measurement. Fitting these measurements to ellipses is described in Section 4.5. The 3-D shape of our magnetopause and how this shape varies with B_Z is described in Section 4.6. Families of ellipses representing magnetopause cross-sections for the various dynamic pressures and IMF B_Z are presented in Section 4.7 and compared with empirical model curves. We test the model in Section 4.8 by calculating a predicted magnetopause position for observed magnetopause crossings paired with simultaneous solar wind data, and find that our model and the recent empirical models all have about the same accuracy as measured by the root mean square of the errors. The variation of magnetopause size and shape with dynamic pressure and IMF B_Z are presented in Sections 4.9 and 4.10, respectively, and more comparisons are made with the empirical models. The asymmetry of our model is explored in more detail in Section 4.11. Conclusions are presented in Section 4.12.

4.2 Observational Evidence for Asymmetry

There are some indications of asymmetry from empirical studies which do not assume symmetry. Fits of magnetopause crossing data to conic sections near the equatorial plane [*Fairfield*, 1971; *Holzer and Slavin*, 1978] found that the subsolar point differs by $\sim 1R_E$ for average northward and southward IMF conditions, consistent with the flux erosion estimates of *Aubry et al.* [1970]. This change in the subsolar distance produces relatively little change of average magnetopause shape in the equatorial plane, as indicated by the ratio of the flank distance (at $X = 0$ in the geocentric solar magnetospheric (GSM) coordinate system) to the subsolar distance, which stays near 1.4 for all solar wind conditions [*Holzer and Slavin*, 1978]. In fits near the meridian plane *Formisano et al.* [1979] found that the polar distance to the magnetopause was larger for southward IMF, indicating a significant change in average shape of the dayside magnetopause in this plane. *Formisano et al.* [1979] also found larger polar distances for increased solar wind density using data normalized to dynamic pressure, and attributed this difference to higher internal plasma pressures from the penetration of solar wind plasma in the "entry layer". Since solar wind dynamic pressure (and density) has been found to vary with solar cycle [*Fairfield*, 1979, 1995], the average asymmetry of the magnetopause may also vary with the solar cycle.

Such distance variations produce magnetopause cross-sections in the dawn-dusk plane that are more elongated in the Z direction for southward IMF than northward IMF. Despite this possible change of shape with IMF B_Z, when the data is averaged over IMF B_Z, the average magnetopause shape has been shown to be nearly circular near the dawn-dusk plane [*Stahara et al.*, 1989; *Formisano et al.*, 1979]. While these empirical studies indicate that there is little net asymmetry near the dawn-dusk plane, separate fittings to ellipses using crossing points near the equatorial and meridian planes [*Sibeck et al.*, 1991] indicate that on average the dayside is oblate (or flattened), i.e., the mean equatorial distance exceeds the mean meridian plane distance. Such dayside asymmetry has recently also been inferred from analysis of ISEE observations [*Petrinec and Russell*, 1995b, 1996b] and detected in observations using high-latitude magnetopause crossings by HAWKEYE [*Zhou and Russell*, 1995].

The smaller number of observations tailward of $\sim 20R_E$ and their higher scatter means that the shape of the magnetotail is less well constrained than the dayside magnetopause. The magnetotail is often assumed to be axisymmetric on average

[e.g., *Howe and Binsack*, 1972], an assumption supported by *Hammond et al.* [1994], who found a nearly circular cross-section at 25 R_E when dipole tilt was small. Particle data from IMP 7 and 8 led *Meng et al.* [1981] to infer a moderate flaring in the middle tail (30-40 R_E), while *Ohtani and Kokubun* [1990] inferred the opposite asymmetry (a moderate flattening) in the same region using high-latitude magnetic data from IMP 8. These and other studies indicate that the degree of possible asymmetry in the middle tail (out to $\sim 40R_E$) is probably not more than $\sim 20 - 25\%$ on average [cf. Table 1 of *Sibeck et al.*, 1986]. Observations in the deep tail have led some investigators [*Behannon*, 1970; *Tsurutani et al.*, 1984] to speculate that the magnetotail becomes more strongly flared with distance, while theory and observations lead others to predict severe flattening very deep in the tail [*Michel and Dessler*, 1970; *Sibeck et al.*, 1986 and references therein; *Fairfield*, 1992].

The magnetic cusp will also produce an asymmetry between the meridian and equatorial planes. The cusp is seen as a distinct indentation in early 3-D magnetopause surfaces calculated by balancing solar wind dynamic pressure against the magnetic pressure of a vacuum dipole field [e.g., *Mead and Beard*, 1964; *Midgely and Davis*, 1963]. The magnitude of this dayside asymmetry (up to 1 R_E), however, is much smaller than that due to magnetotail flaring by IMF B_Z (often 5-10 R_E, as we shall see). Tilt of the geomagnetic dipole and IMF B_Y should produce further asymmetry in the northern/southern and dawn/dusk hemispheres, respectively. The expected asymmetry due to tilt ($\sim 1 - 2R_E$ sunward of $X = -30R_E$) [*Hammond et al.*, 1994; *Sotirelis*, 1995], is much smaller than that due to flaring. IMF B_Y shifts the cusp position and twists the magnetotail, and so may redistribute any asymmetry due to flaring from IMF B_Z.

4.3 The Three-Dimensional Global MHD Magnetospheric Simulations

4.3.1 The 3-D global model

The 3-D global fluid model comprising the foundation of this work use the standard MHD equations in the conservative form derived in Chapter 2. This model has also been used for the other 3-D studies of the magnetosphere, but with the MPD modified fluid approximation [*Winglee*, 1995; *Winglee et al.*, 1996]. The MPD perturbation is neglected in this chapter, because it was found to have very little effect on the

size and shape of the magnetopause, which is essentially determined by the MHD pressure balance. In the simulations performed for this chapter, the fluid equations in the ideal MHD limit are used, obtained in the model by setting the both the anomalous resistivity η_a and MPD resistive parameter χ in Equation 3.8 to zero.

The MHD equations were solved as an initial value problem using the two-step Lax-Wendroff method, much the same as in the simulations of Chapter 3, except (1) the simulation was now in three dimensions rather than two, and (2) additional smoothing was provided by Lapidus smoothing [*Lapidus*, 1967] instead of flux correction smoothing. The Cartesian grid spacing was uniform and set at 0.84 R_E in all three dimensions. Incoming solar wind was blown at a magnetic dipole, and nearly steady-state solutions were produced for about 30 combinations of steady dynamic pressure (P_D) and IMF B_Z. The Earth's magnetic dipole had no tilt and the IMF had no B_Y or B_X component in these simulations. The symmetry of the magnetic field under these conditions means that only one quadrant of the magnetosphere need be simulated. The simulation box reached to 90 R_E in the tail, 28 R_E on the dayside, and 41 R_E in the equatorial and meridian planes. The inner boundary was set at 4.2 R_E; the ionosphere was approximated by a conducting shell and the plasma velocity was zeroed out at the boundary.

The density and temperature of the plasma at the inner boundary were modified to approximate the effects of the ring current, which is virtually absent in MHD simulations [*Pulkkinen et al.*, 1995]. The ring current was mimicked by increasing the plasma pressure at the inner boundary of the simulation, equivalent to a mixture of cold and hot plasma populations of the plasmasphere and ring current regions. Without the ring current, MHD simulations underestimate the subsolar distance by about 1 R_E. Our artificial ring current significantly increases the subsolar distance producing a value of 10.3 Re for average solar wind conditions (2.0 nPa pressure and 0 IMF B_Z), which is consistent with observations. Our results are consistent with the estimates of *Schield* [1969] that the total disappearance of the quiet-time ring current would cause a 10% decrease in subsolar distance. *Petrinec and Russell* [1993a], however, found relatively little effect from the ring current (as gauged by Dst) on the average subsolar distance inferred with their model.

An example of two of the 3-D magnetospheric simulations used for this study is shown in Figure 4.1a (for northward IMF), and Figure 4.1b (for southward IMF).

Thermal pressure (contours) and electric current (arrows) are shown in perspective in the noon-midnight plane, equatorial plane, and cross-tail planes. The inner boundary near 4 R_E is clearly seen in the pressure contours, along with the bow shock near the front of the closeup portion of the simulation box. The magnetospheric lobes are seen to have a uniform low pressure and a pressure indentation can be seen near the cusp. Higher pressure in the plasma sheet is seen near the equatorial plane, where the large duskward cross-tail current is also seen. Large current arrows show the approximate position of the magnetopause with the high thermal pressures of the magnetosheath between the bow shock and magnetopause. The magnetotail for southward IMF is more flared than the northward case, as expected, indicated by the larger lobe cross-section at $X = -15R_E$.

Figure 4.2a and 4.2b show the same simulations from a different angle. Thermal pressure contours are the same, but arrows show the plasma bulk flow or convection velocity. The solar wind plasma enters from the left and is deflected around the magnetopause in the magnetosheath, as can be discerned in the flow vectors. The flaring of the magnetotail by southward IMF is clearly seen in the noon-midnight meridian when the lobe and magnetosheath flow in (b) is compared to (a). Convection on the nightside for northward IMF is tailward in most of the noon-midnight plane, and earthward between this plane and the magnetosheath. When IMF is southward a strong earthward flow onto the dayside is seen in the equatorial plane. Flows further down the tail are tailward with the bifurcation occurring near the neutral line shown in Figure 4.3c. While much of the flow in the noon-midnight plane is still tailward, some earthward convection is seen just above the equatorial plane tailward of the flow bifurcation. The three-dimensional convection patterns are much more complicated still.

The dynamic pressures in our simulated cases ranged from 0.5 to 4.0 nPa and IMF B_Z ranged from -5.0 to +5.0 nT. Observed solar wind values from both magnetopause data bases fall within these bounds about 65% of the time. The average observed solar wind dynamic pressure is near 2.0 nPa and the standard deviation (σ) is close to a factor of 2 [Roelof and Sibeck, 1993], so our coverage corresponds to $+1\sigma$ and -2σ levels of dynamic pressure. The σ for IMF B_Z is near 3.5 nT [Roelof and Sibeck, 1993], so we are covering slightly more than $\pm 1\sigma$ of this parameter. The two dimensional parameter space was spanned with linear increments in B_Z of 1.25 nT and geometric

Current Systems : 1.0 nPa
(a) Northward IMF 2.5 nT

Mantle Current Sheet

(-35,20,20)
R_E

Tail Current Sheet

Dayside Magnetopause

Bow Shock
Current Sheet

(b) Southward IMF 2.5 nT

(17,0,20)R_E
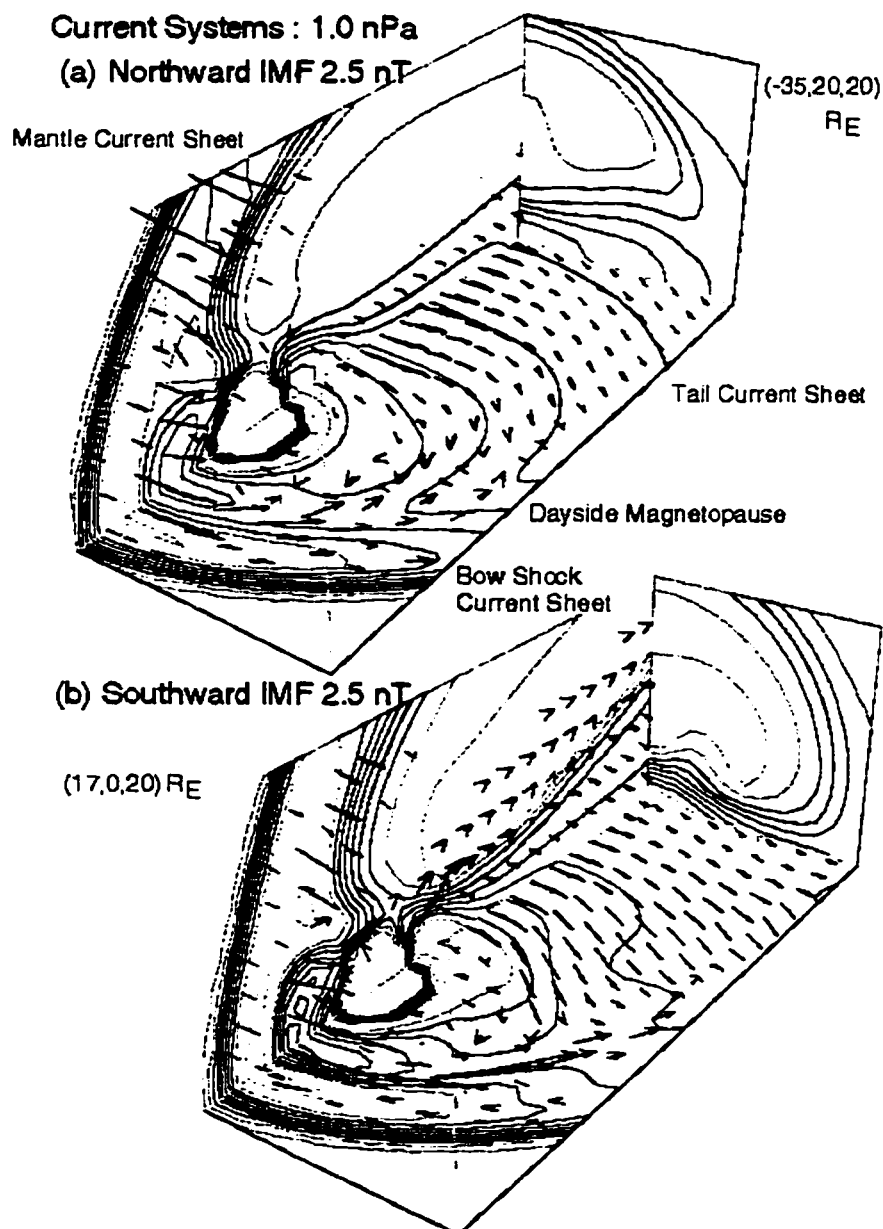
Figure 4.1: Closeup perspective view of global MHD simulations for a dynamic pressure of 1.0 nPa and (a) northward IMF B_Z of +2.5 nT and (b) southward IMF B_Z of -2.5 nT. This closeup ranges from +17 to -35 R_E in X, 0 to 20 R_E in both Y and Z, much smaller than the actual simulation gridspace. Contours show thermal pressure in the noon-midnight plane, equatorial plane, and cross-tail plane at $X = -15R_E$, but displayed at $X = -35R_E$. The pressure contours are scaled by their square root values to give a greater range to the plot contour values to highlight details. The arrows show the electric current vector in the noon-midnight plane and equatorial planes.

Plasma Flow : 1.0 nPa
(a) Northward IMF 2.5 nT

(-35,0,20) R$_E$

(17,20,0)
R$_E$

(b) Southward IMF 2.5 nT

(-35,0,20) R$_E$

(17,20,0)
R$_E$

Figure 4.2: Another closeup perspective view of global MHD simulations showing plasma flow for the same solar wind conditions shown in Figure 4.1. The closeup of the simulation box has the same dimensions as before, but is viewed from a different angle. Contours are again the square root of the thermal pressure in each of the three planes. Arrows show the plasma bulk velocity vector in the noon-midnight plane and equatorial planes.

increases in P_D by a factor of 2.

4.3.2 Magnetic field line mapping

The magnetosphere in our simulations is totally closed for the moderately large north-ward IMF B_Z cases presented here, similar to that produced in *Fedder and Lyon* [1995] with northward IMF for several hours or that produced by *Ogino et al.* [1992] (Figure 1.12). Although the magnetosphere is stable for stronger northward IMF, the tail steadily shrinks (as in the simulations of *Usadi et al.* [1993]) and a steady-state magnetopause was not obtained. The X line (located near 20 R_E) in the simulations increased in width with southward IMF, reaching across the entire magnetosphere for the moderately large southward IMF cases presented here. For larger values of southward IMF B_Z, reconnection in the tail was vigorous, leading to the continual formation and expulsion of plasmoids down the magnetotail. Again, with this contin-uously changing magnetospheric configuration, a suitable steady-state position of the magnetopause could not be measured. For dynamic pressures between these upper and lower IMF thresholds quasi-steady state solutions amenable to accurate mag-netopause measurement were obtained. These upper and lower thresholds are near ±2.5 nT for low pressures of 0.5 n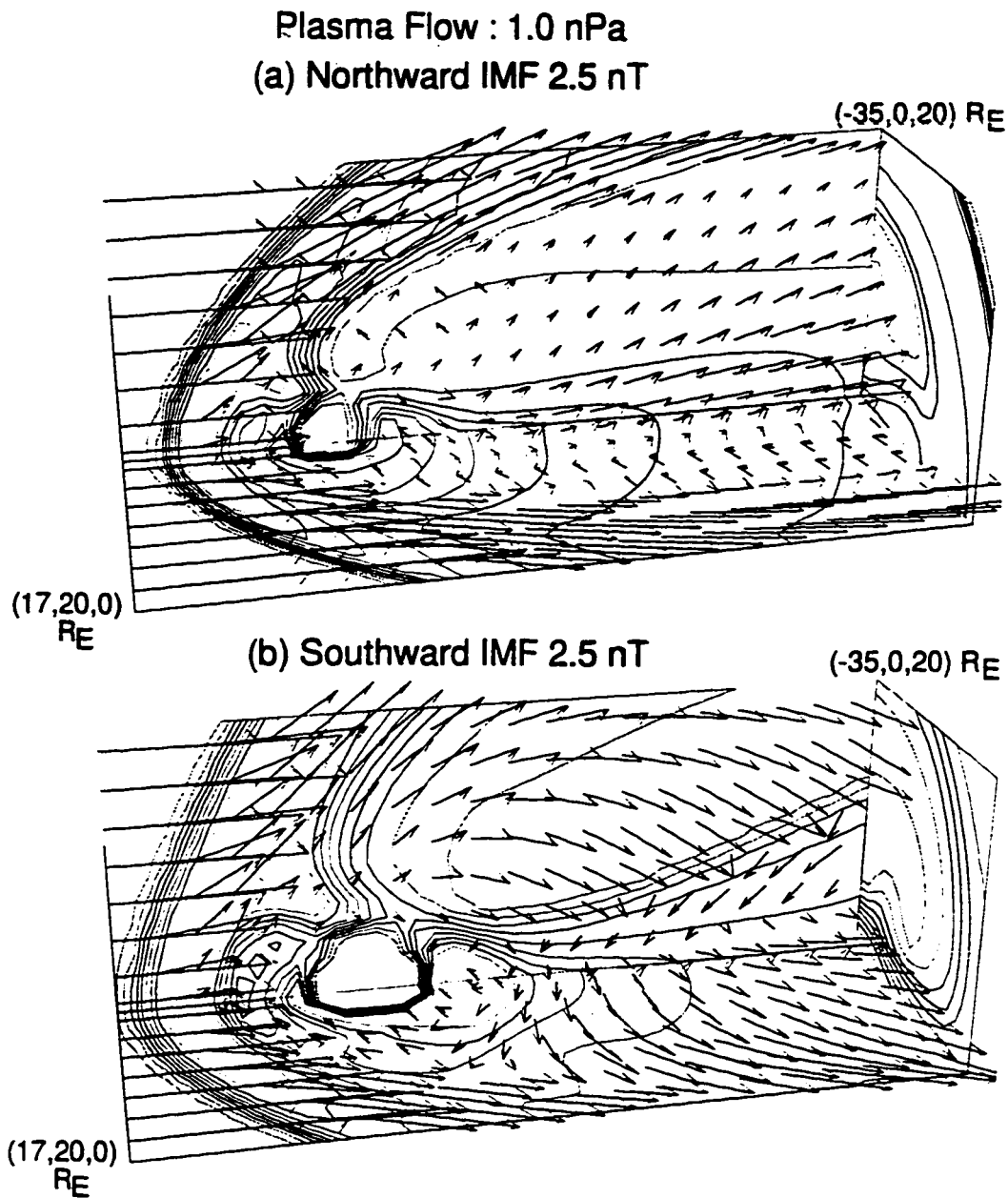Pa. The magnitudes of both thresholds increase with dynamic pressure up to about ±5 nT for high dynamic pressures of 4 nPa.

Figure 4.3 shows magnetic field line mapping for three cases in this stable solution parameter region at a dynamic pressure of 1.0 nPa with IMF B_Z set to +2.5 nT (Figure 4.3a), no IMF or 0 nT (Figure 4.3b), and -2.5 nT (Figure 4.3c). Magnetic field lines are mapped from regularly spaced points in the equatorial plane. Lines which strike the inner boundary are closed. Open geomagnetic field lines anchored in the polar cap do not intersect the equatorial plane in a symmetric simulation such as this and so are missed by such mapping. Vertical lines in front of the bow shock show IMF field lines in the solar wind while those in the magnetosheath are also connected to the solar wind. Many such lines are seen for the northward IMF case (Figure 4.3a) and lesser numbers can seen for the other two cases. Most of the field lines are in the magnetotail are closed for northward IMF, and the number of closed lines decreases as IMF B_Z decreases. A narrow region of field lines not connected to the Earth are seen in the noon-midnight plane in Figure 4.3a indicating that the magnetosphere is not quite closed, which also indicates the presence of a narrow neutral line only a

few R_E wide. These unconnected lines may connect to the solar wind or possibly to themselves forming a magnetic island or plasmoid as was seen in the 2-D simulations shown in Chapter 3. For no IMF (Figure 4.3b) the region of unconnected lines has widened considerably, but closed lines still are seen on the flanks down to -60 R_E. The half width of the neutral line is about 12 R_E, roughly half the total tail width, while for -2.5 nT (Figure 4.3c) the neutral line stretches almost entirely across the magnetotail. Closed field lines are not seen tailward of $X = -20R_E$ and are limited to the region nearer the Earth. Interestingly, the position of the neutral line on the X axis is nearly the same for all three cases and the difference in the number of closed field lines in the magnetotail is governed chiefly by the width of the neutral line.

Open magnetic field lines can be studied by tracing lines outward from the high latitudes on the surface of the Earth. Closed field lines reach the equatorial plane in a symmetric simulation, while open lines do not. This mapping method will miss solar wind field lines unconnected to the Earth. Figure 4.4 shows magnetic field lines mapped from the Earth for the northward IMF case shown in Figure 4.3a. Field lines traced from increasingly higher latitudes reach the equatorial plane further from the Earth at all longitudes. A single open field line can be seen in Figure 4.4a at the midnight longitude reaching past -73 R_E under which lie the unconnected (solar wind) field lines seen in Figure 4.3a. Field lines traced from the noon longitude close on the dayside for latitudes of 80° and below (Figure 4.4a to c), but map instead to the tail from a latitude of 84°. This indicates that the longitude of the magnetic cusp (where the mapping changes discontinuously) lies between 80° and 84° for this case. The number of open field lines increases with latitude, so that several can be seen in Figure 4.4d. At still higher latitudes (not shown) most of the magnetic field lines were found to be open. Such mapping of open field can indicate the size and shape of the polar cap and the amount of open magnetic flux can be quantified.

Figure 4.5 shows magnetic field lines mapped from the Earth for the southward IMF case shown in Figure 4.3c, where all the simulation conditions except IMF B_Z were identical. Many more open field lines can be seen relative to the northward IMF case (Figure 4.4), as expected from the vigorous reconnection that occurs in the simulations along the dayside equatorial magnetopause creating a large amount of open magnetic flux and flaring the magnetotail. Again the number of open field lines increases with latitude until all of the field lines are open at a latitude of 77°. This

(a) Northward IMF 2.5 nT

(-60,0,0) R$_E$

(20,-30,0) R$_E$

(b) 0 IMF

(c) Southward IMF 2.5 nT, 77 Latitude
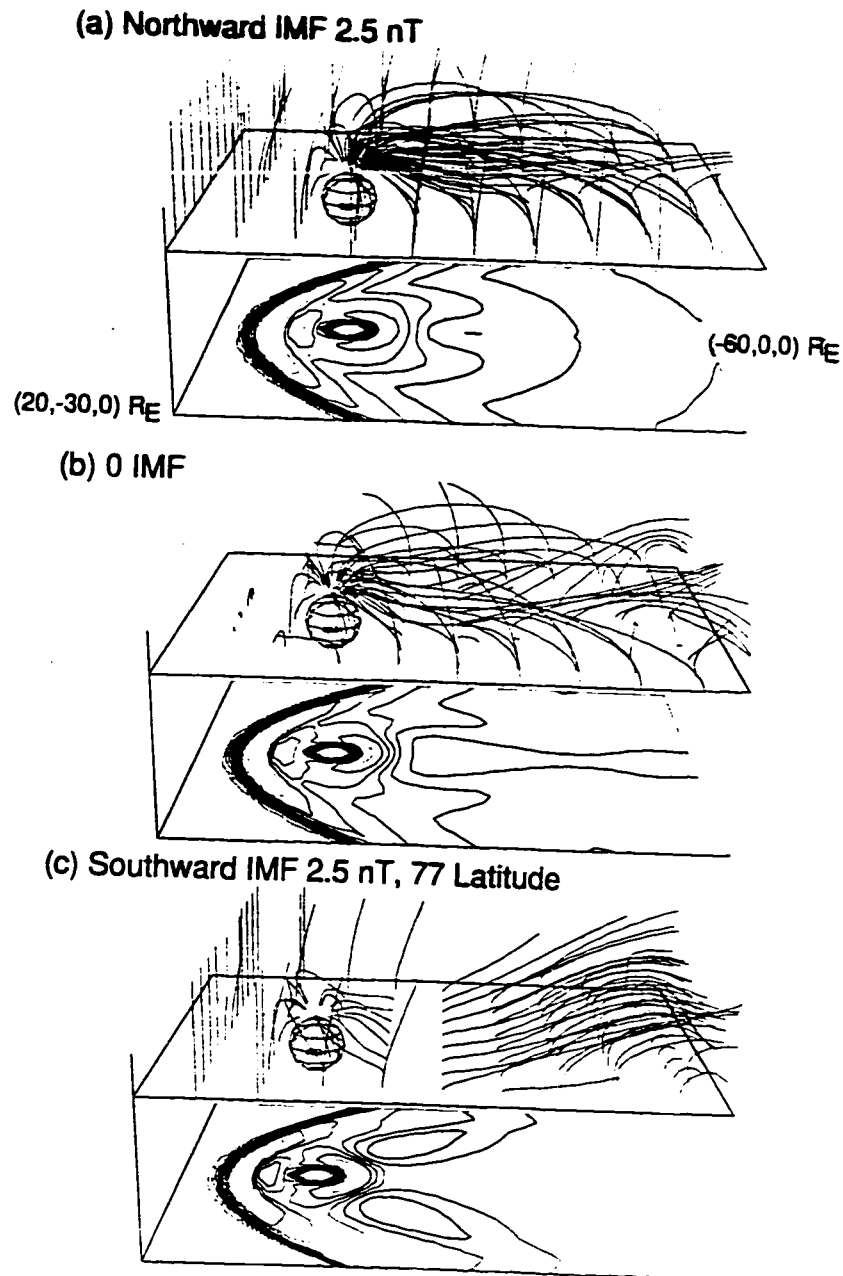
Figure 4.3: Magnetic field line mapping is shown for a dynamic pressure of 1.0 nPa with varying IMF B_Z set to (a) +2.5 nT, (b) 0 nT, and (c) -2.5 nT. The portion of the simulation box shown is larger than in Figures 4.1 and 4.2, ranging from +20 to -60 R_E in X and 0 to 30 R_E in Y. The top portion of each plot shows the mapping of magnetic field lines traced from the equatorial plane. The sphere in the top panel (circle in the bottom panel) indicates the 4.2 R_E radius of the inner boundary of the simulation. Contours of the square root of the plasma thermal pressure in the equatorial plane are shown in the lower portion of each plot.

Solar Wind Dynamic Pressure : 1.0 nPa, 2.5 nT

(20,36,36) (a) 70 Latitude

(20,36,36) (b) 75 Latitude

(20,36,36) (c) 80 Latitude

(20,36,36) (d) 84 Latitude

(20,36,0)

(-73,36,0)

Figure 4.4: Mapped magnetic field lines in global MHD simulations for the northward IMF case shown in Figure 4.3a. Field lines are traced from the surface of the Earth at latitudes of (a) 70°, (b) 75°, (c) 80°, and (d) 84°. The portion of the simulation box shown is still bigger than previously shown, ranging from +20 to -73 R_E in X and 0 to 36 R_E in Y and Z. Contours again show the square root of the plasma pressure in the equatorial plane. A pressure trough (heavy dashed line) is marked by the sharp turn in the pressure contours and is seen to lie near the footpoints of the highest latitude field lines in (d).

indicates the polar cap for this southward IMF case is considerably larger than the northward IMF case and contains several times more magnetic flux. The latitude of the magnetic cusp lies below 77° and has moved equatorward by several degrees relative to the northward IMF case (Figure 4.4). This trend is consistent with empirical results of *Burch* [1972, 1973], who measured the cusp longitude through the precipitation of low energy particles. This equatorward movement of the cusp as IMF B_Z decreased was also seen in Chapter 3 using the 2-D global model (but for southward IMF only).

Most of the magnetic field lines mapped from a latitude of 66° reach the equatorial plane close to the Earth (Figure 4.5a), but a single field line mapped from the midnight longitude travels very deep into the tail to about 65 R_E. This field line actually travels around the region of magnetic field lines unconnected to the Earth seen in Figure 4.3c, as do several other lines near midnight traced from 66° (Figure 4.5b). This indicates that these unconnected field lines lying between -20 and -60 R_E close upon themselves and form a plasmoid. Several truly open field lines are seen to originate from a latitude of 68° (Figure 4.5b), but from longitudes away from midnight. These open lines and those traveling around the plasmoid originate from latitudes statistically associated with the auroral oval near midnight (64° to 72°) [*Feldstein*, 1973]. They also get close to the neutral line lying near -20 R_E, indicating that magnetic reconnection in the magnetotail may be closely connected with nightside auroral currents, as was seen with the 2-D model of Chapter 3. The present 3-D model generates field-aligned currents with a pattern (not shown) that resembles that shown in Figure 1.13. The quantitative study of field-aligned currents and magnetotail reconnection, as well as polar cap size and the cusp position, was not performed for this dissertation, but these possible projects are discussed more in Chapter 5.

4.4 The MHD Magnetopause

4.4.1 Measuring the magnetopause position

The magnetopause in the measured simulations was stationary when quasi-steady state equilibrium solutions were reached. Although the grid spacing used in these simulations was fairly large ($0.84R_E$), the variations due to the solar wind were large enough that systematic variations could be measured from one case to the next. The

Solar Wind Dynamic Pressure : 1.0 nPa, 2.5 nT

(20,36,36) (a) 66 Latitude

(20,36,36) (b) 68 Latitude

(20,36,36)

(c) 77 Latitude

(20,36,36)

(d) 81 Latitude

(20,36,0)

(-73,36,0)

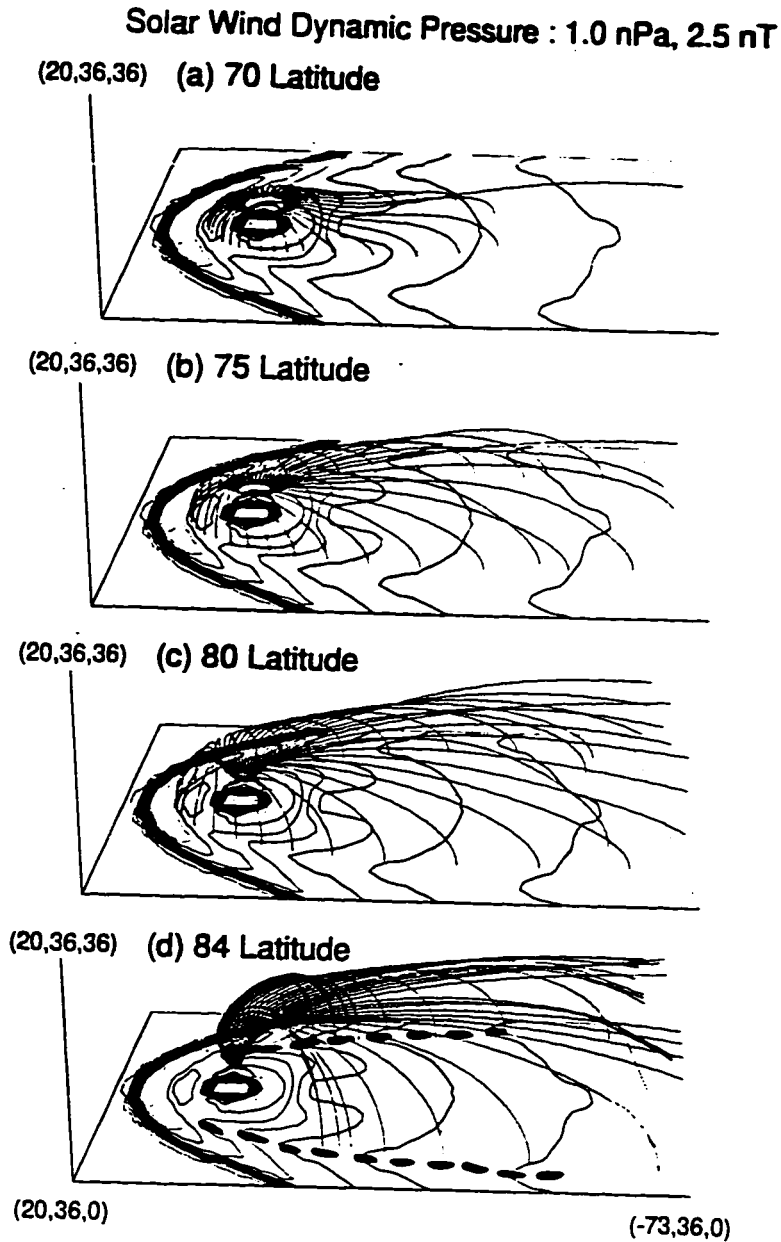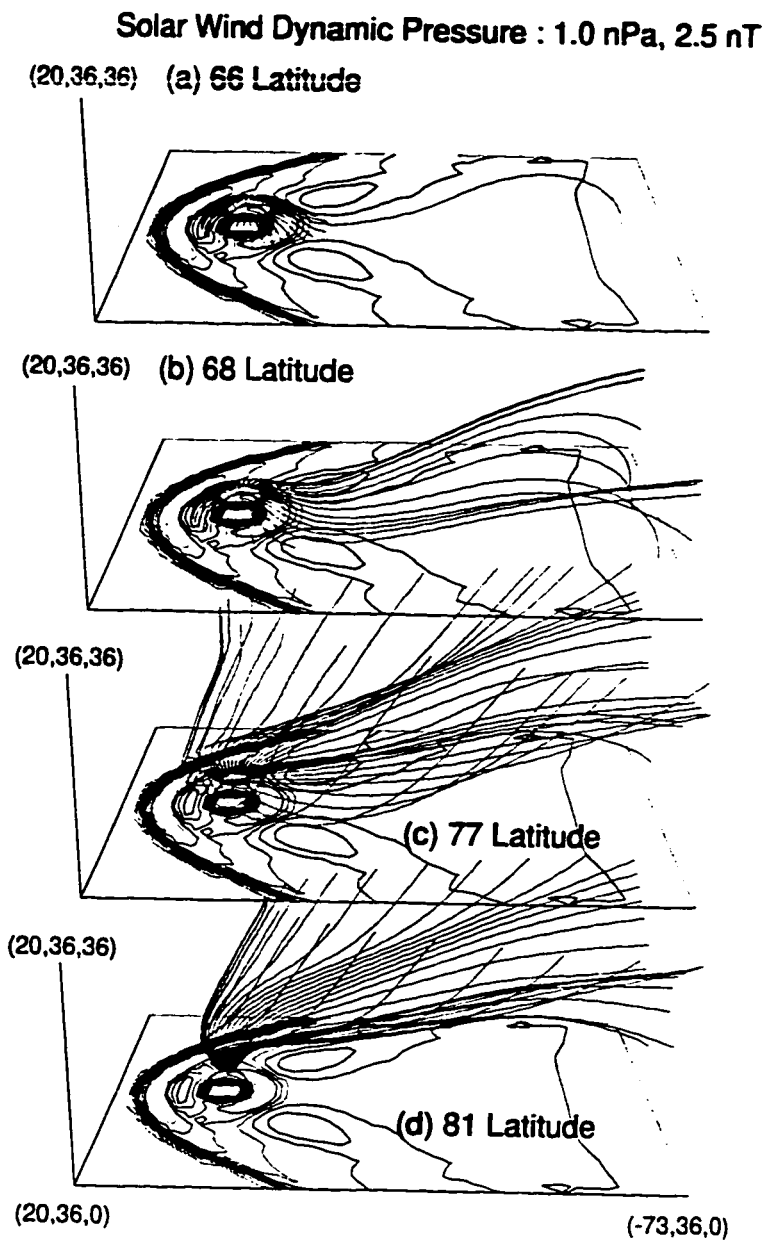Figure 4.5: Mapped magnetic field lines in global MHD simulations for the southward IMF case shown in Figure 4.3c. The style is the same as Figure 4.4, except the field lines are traced from the surface of the Earth at latitudes of (a) 66°, (b) 68°, (c) 77°, and (d) 81°.

magnetopause was measured at the subsolar point, and at $X = 0$, -10, -20, and -40 R_E in both the noon-midnight and the equatorial planes. Measurements at $X = +7.5R_E$ were also made in the equatorial plane for some low pressure cases.

A combination of three diagnostics (magnetopause current intensity, plasma thermal pressure, and mapping of magnetic field lines) was needed to properly identify the magnetopause in these positions for all solar wind combinations studied. Although the Chapman-Ferraro current layer is several grid spaces wide in our fluid simulations, the peak current is well defined near the subsolar point. This peak in the Chapman-Ferraro current layer was found to coincide closely with the last closed magnetic field line on the dayside near the subsolar point, giving a good indication of the magnetopause position. Furthermore, a steep gradient in thermal pressure from the stagnation point in the magnetosheath to just inside the magnetosphere overlapped both the current peak and the outer limit of closed field line mapping. The region of high thermal pressure in the nose of the magnetosheath indicates the stagnation point and can be seen to lie just outside the closed field lines traced from 80° in Figure 4.4c. A pressure minimum within the magnetosphere lies just inside these field lines, creating a steep pressure gradient (across 5 contour line levels) centered on the subsolar magnetopause. The stagnation point and pressure minimum are more sharply outlined in Figure 4.5, where the pressure gradient traverses 7 contour lines. This consistency of all three types of magnetopause diagnostics facilitated interpolation between gridpoints, giving a measurement accuracy down to half a gridspace (0.4 R_E).

In the noon-midnight meridian plane, the peak of the Chapman-Ferraro current matched up with the gradient in pressure between the magnetosheath and magnetosphere (seen in Figures 4.1 and 4.2), providing unambiguous identification of the magnetopause. Mapping from high latitudes does not clearly mark an open magnetopause, since it is often difficult to differentiate between those field lines strictly within the lobes and those that enter the magnetosheath at large distances down the tail, especially when IMF is southward (see Figure 4.5). The mapping of magnetic field lines only clearly delineates the magnetopause in the noon-midnight meridian for a totally closed magnetosphere, as in Figure 1.12. This situation did not exist for almost all the simulations being measured (a few cases were just barely closed), and so mapping was not used as a diagnostic for measurements in the noon-midnight

meridian.

Although the current layer and pressure gradient both have a thickness of 5 or more gridspaces (or several R_E) in the simulations, the peak of the current layer can be easily determined and provides a measurement down to one gridspace. Figure 4.6 shows a cross-section of the tail at $X = -20R_E$ taken from a symmetric simulation with no dipole tilt or IMF. The left panel shows a contour plot of B_X, which clearly outlines the magnetotail lobes. Flux toward the Earth in the northern lobe has positive B_X values, while flux away from the Earth in the southern lobe has negative B_X values. The interior of the lobes is fairly uniform (consistent with observations, Chapter 1) with most of the gradient occurring near the outer edge. The transition from positive to negative at the equatorial plane marks the neutral sheet position.

The right panel of Figure 4.6 shows a contour plot of electric current magnitude, which clearly shows the theta pattern expected for the magnetosphere (Chapter 1, Figure 1.8). The cross-tail current sheet is centered around the equatorial plane while the return current is clearly seen and is most distinct near the noon-midnight meridian plane. Both current sheets have a thickness of only about 5 gridspaces, but the cross-tail current is more heavily concentrated. The peak of the current layer in the noon-midnight meridian represents the magnetopause position and was the primary diagnostic used in the noon-midnight meridian plane. The center of this current layer can be seen to match up well with the center of the outer gradient in B_X. The cross-tail current bifurcates and merges with the return current to create the theta, but it can be seen that this merging is spread out over large distances in the simulation. Thus, the magnitude of the electric current by itself was inadequate to diagnose the magnetopause position in the nightside equatorial plane.

Magnetic field line mapping and thermal pressure contours were used instead in the equatorial plane, since they provided a better indication of the magnetopause position. A trough in plasma pressure (a local minimum) can be seen in the contours of Figure 4.4, with the center of the trough marked by a sharp angle in the contour lines. This pressure trough lies between the higher pressures in the plasma sheet and the magnetosheath and roughly corresponds to the outer edge of the plasma sheet. This pressure trough coincides well with the limit of closed magnetic field lines in these cases, as can be seen in Figure 4.4. The pressure trough also can be seen for moderate southward IMF values (Figure 4.5), but this feature disappears for strongly
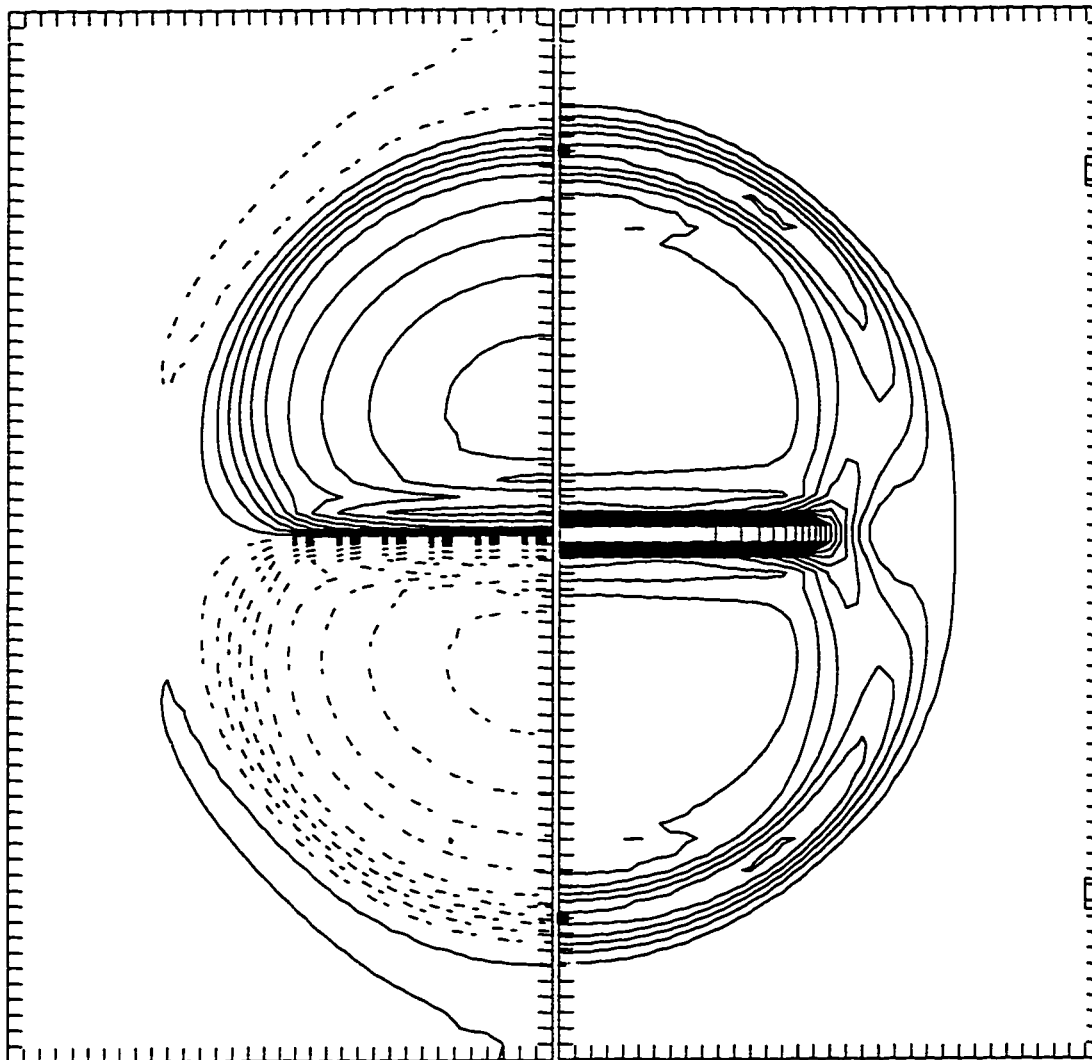
Figure 4.6: Magnetotail lobes and current in cross-tail plane at $X = -20R_E$. The left side is a contour plot of B_X, which clearly outlines the magnetotail lobes. Solid lines show positive B_X, dashed lines negative B_X. The right side is a contour plot of electric current magnitude, which clearly shows the theta pattern. The peak of the current layer in the noon-midnight meridian is marked with a large dot and represents the magnetopause position. The bifurcation of the current in the equatorial plane prevents easy identification of the magnetopause with the current.

southward IMF cases, which were found to be unstable and expel plasmoids down the tail in a cyclical manner similar to the behavior seen in the 2-D model of Chapter 3. This plasmoid expulsion also flushes plasma out of the plasma sheet and presumably prevents thermal pressures within the plasma sheet from building up to the levels necessary to produce a discernable trough.

While the trough is less distinct for southward IMF than northward IMF (compare Figure 4.3a to Figure 4.3c), it can still be recognized by the sudden change in the direction of the contours. The pressure trough was found to provide a simple and relatively accurate indicator of the magnetopause on the nightside equatorial plane from $X = -10R_E$ tailward for all the simulation cases measured. Using these 2-D pressure plots provided an automatic method to measure the magnetopause, since finding the outer limit of closed magnetic field lines requires mapping from many positions. At the terminator ($X = 0$) in the equatorial plane, however, the mapping of magnetic field lines indicated that the trough, which extends a bit past $X = 0$ in Figure 4.4, lies somewhat inside the outer limit of mapped field lines. Thus magnetic field line mapping provided the only reliable indication of the magnetopause position at the equatorial terminator. The measurement errors for these points is estimated to be about one gridspace (0.84 R_E).

4.4.2   The subsolar distance

A contour plot of the measured subsolar distances from our simulations is shown in Figure 4.7a. The circles indicate the quasi-steady state simulations which could be used to construct a predictive model, while the asterisks indicate simulations which did not provide accurate measurements and hence were ignored for the predictive model. Our simulations produced less variation with B_Z at high pressure cases (4 nPa), allowing us to obtain these measurements (marked with an X over the circle) by interpolation. The measured subsolar distance varies from 8.9 to 14.4 R_E over the parameter space of our model, with a mean subsolar distance of 10.3 R_E for the average solar wind conditions of ~ 2 nPa and ~ 0 IMF B_Z. This median subsolar distance matches those reported for the empirical models at these solar wind conditions well; RS93 has 10.8 R_E and PR95 gives 10.4 R_E. Our subsolar point varies somewhat more over the parameter space of our model (5.5 R_E) than RS93 (4.8 R_E) or PR95 (4.6 R_E). Scaling the mean subsolar values of *Fairfield* [1971] and *Holzer and*

Slavin [1978] by the average solar wind dynamic pressure for the observation period [*Fairfield*, 1995] gives 10.7 and 10.4 R_E, respectively. Thus, our subsolar distance at this average condition agrees with all these empirical values to within 0.5 R_E, a little more than our measurement error. This range also covers expected variations due to other factors, e.g. dipole tilt (0.3 R_E) estimated by *Schield* [1969], which are missing from our idealized set of simulations.

The contour lines in Figure 4.7 indicate that subsolar distance depends strongly on both dynamic pressure and B_Z over the entire range of the simulations. The slope of the lines is roughly the same for northward and southward IMF, indicating a uniform increase in subsolar distance with B_Z that does not change much with IMF polarity. This contrasts with PR95 for northward IMF, in which subsolar distance is independent of B_Z for northward IMF, but is similar for southward IMF where subsolar distance varies linearly with B_Z. The shape of the contour lines in the approximate solar-wind $\pm 1\sigma$ region of the model (1 to 4 nPa, -3.75 to +3.75 nT) is remarkably like that in RS93 (their Figure 16) in this region, indicating the qualitative similarity of our simulation results with RS93. The spacing between lines increases with pressure indicating that the variation is stronger at low pressures, also consistent with RS93. We emphasize that the variation of the subsolar distance in these models is inferred, while our subsolar distances are direct measurements from our simulations.

Similar changes in subsolar distance for both northward and southward IMF is unexpected, since reconnection at the magnetopause qualitatively differs with IMF polarity in our simulations. Higher reconnection rates for southward IMF along a wide neutral line are accompanied by stronger convection to the dayside in our quasi-steady-state solutions, while lower reconnection rates (past the cusp) and weaker convection occur for northward IMF. We cannot directly measure reconnection rates in our simulation, but only the combined effects of reconnection and convection. The net result is a linear rate of magnetic flux erosion (or buildup) of the dayside magnetosphere with B_Z at a fixed dynamic pressure (Section 4.10). Our steady-state solutions require about an hour to evolve, consistent with the timescales needed to change near-Earth convection patterns [*Coroniti and Kennel*, 1973], and generate field-aligned and tail current systems due to a change in IMF B_Z [*Maltsev and Lyatsky*, 1975; *Maezawa*, 1975]. This is much longer than the Alfvén travel times (5 to 10 minutes) across the near-Earth magnetosphere, the appropriate timescale for
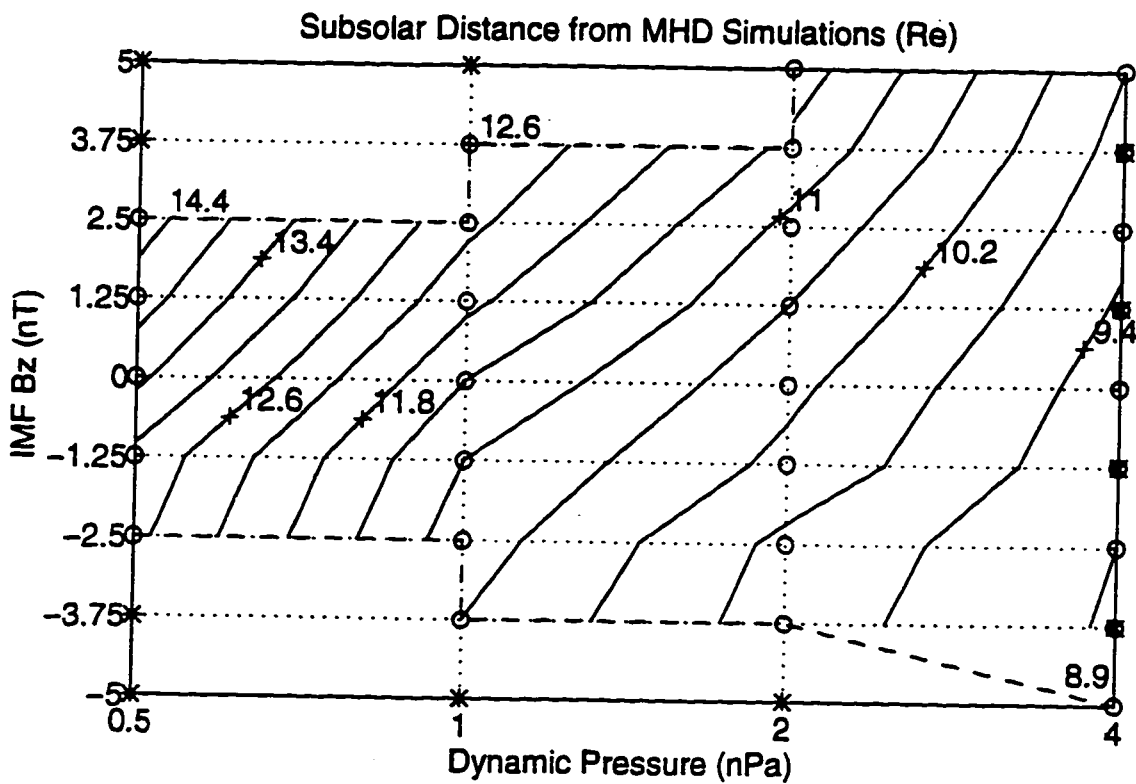
Figure 4.7: The measured subsolar distances from the simulations as a function of dynamic pressure and IMF B_Z. Open circles indicate simulations with a steady magnetopause that were used to construct the predictive magnetopause model. Asterisks represent unsteady cases not suitable for measurement.

reconfiguration due to dynamic pressure changes. Our magnetospheric configurations depend on the integration of B_Z over periods of about an hour, consistent with integration times needed to model expansion and contraction of the dayside magnetosphere due to flux erosion [*Holzer and Slavin*, 1978] and predict the position of the cusp [*Burch*, 1973].

4.4.3 The cusp

Signatures of the cusp are seen in all three indicators of the magnetopause: electric current, plasma pressure, and magnetic field line mapping. The diamagnetic current sheets in the simulations exhibit complex geometry, with currents of very low magnitude circulating around the cusp. The dawnward mantle current sheet can either overlap the duskward low-latitude current sheet or be separated by a gap. In preliminary runs of our model incorporating dipole tilt (discussed in Chapter 5), the degree of this current sheet overlap or separation varies considerably with tilt. The envelope of closed magnetic field line shows a rather small cusp, with a limited latitudinal width of only about 1°. The wedge seen in contours of thermal pressure straddles closed field lines, indicating a much larger cusp. To produce a mathematically simple surface (e.g., an ellipse), the indentation of the magnetopause surface near the cusp was ignored in the present work. This curve overestimates the magnetopause distance near the meridian plane sunward of the cusp, up to $\sim 1R_E$ in some instances. The resulting errors when averaged over a large area are much lower, however, much less than those of the least squares fits (0.7 R_E, next section) and the data bases ($\sim 1R_E$ on the dayside), justifying the neglect of the cusp in our magnetopause surface. Incorporating the cusp indentation into the magnetopause surface would presumably reduce model errors on the dayside, but has been left for future model refinement.

4.5 A Simple Model for the Magnetopause

4.5.1 Fitting a model to the magnetopause surface

To produce a simple magnetopause curve in each plane that fit the simulations well enough to be useful and accurate, we used ellipses, as in the empirical models. *Roelof and Sibeck* [1993] had three independent ellipse parameters that could be fit by least

124

squares, namely

$$AX^2 + BX + C + \rho^2 = 0, \qquad (4.1)$$

where X is the distance along the Earth-sun line and ρ is the axial distance. The ellipsoids used by *Petrinec and Russell* [1993a] were constrained to have their focus at the center of the earth and the eccentricity was fixed for either northward or southward IMF, giving them essentially only one dimensional freedom for fitting of each polarity. This allows only scaling with P_D to be independently studied and forces the curvature of the ellipse to be fixed, preventing the independent study of flaring due to B_Z.

Because our subsolar point is well determined in our simulations, the fitted ellipse is forced through it and a least squares fit is then made using the remaining points. Fixing the subsolar distance also permits connecting the polar and equatorial magnetopause curves smoothly to produce a fully three-dimensional surface. This leaves two free parameters to deal with the effects of P_D and B_Z, and gives

$$f(X_1, X_2) = BX_1 + CX_2 = B(\frac{X^2}{R_{SS}} - X) + C(\frac{X^2}{R_{SS}^2} - 1) = -\rho^2, \qquad (4.2)$$

a form which guarantees that the axial distance is zero at the subsolar point, $X = R_{SS}$, and determines the third ellipse parameter, $A = -B/R_{SS} - C/R_{SS}^2$.

Our magnetopause curves avoid some drawbacks seen in the empirical models. The hybrid model of *Petrinec and Russell* [1993, 1995a] joins separate dayside and nightside models at $X = 0$, producing a non-physical discontinuity in the slope. An ellipse may curve back toward the tail axis in a non-physical manner, as seen in some the ellipses in *Roelof and Sibeck* [1993] at large magnitudes of IMF B_Z. Since the expected curvature of the dayside magnetopause is very high, but very low in the tail, least squares fits heavily weighted to the dayside and lacking enough points on the nightside may produce ellipses that curve back toward the axis in the tail. We prevented this curvature problem by including measurements of the magnetopause at $X = -40R_E$, but this slightly increased the rms error of the fits on the dayside.

We performed a least squares fit of $f(X_1, X_2) = -\rho^2$ in each plane with equal weighting of the data points at $X = 0$, -10, -20, -40 R_E (and $+7.5R_E$, if applicable). Producing a predictive model required interpolating the curve parameters not only by P_D and B_Z, but also by the clock angle of the observation position, $\arctan(Y/Z)$. The fitting parameters (A, B, and C) were converted to three physical parameters that

vary smoothly to ensure good interpolation. Besides the subsolar distance R_{SS}, these are the flank distance R_D, defined as the axial distance at $X = 0$, and the flaring angle α, the angle that the tangent to the curve has at $X = 0$ relative to the X axis. Solving for the two free parameters gives $R_D = \sqrt{-C}$ and $\alpha = \arctan(B/2R_D)$. Figure 4.8 shows the resulting simple model used to represent the 3-D shape of the magnetopause.

4.5.2 The predictive magnetopause model

The results of the least squares fitting to the measurements from the steady-state simulations are shown in Figures 4.9 and 4.10, and together with Figure 4.7 constitute a predictive model for which a predicted magnetopause position can be easily calculated. The three physical parameters (R_{SS}, R_D, α) are linearly interpolated in P_D and B_Z for each plane, and then interpolated by clock angle. The resulting parameters describe an ellipse in the plane containing the the observation point and the earth-sun line, and given X predicts an axial distance ρ to the magnetopause (Figure 4.8).

The flank distances for the meridian plane (Figure 4.9a) and the equatorial plane (Figure 4.9b) are again presented as contour plots, but these are fitted values rather than direct measurements. Combining the curve fitting errors (0.7 R_E in each plane) with measurement errors (0.84 R_E) gives a total error of 1.1 R_E, ignoring additional systematic errors from variables absent in our simulations. The steep slopes indicate that both distances depend more strongly on pressure than B_Z. The polar flank distance is seen to decrease as B_Z becomes more northward, while the equatorial flank distance increases with B_Z at about the same rate. This relative change in the polar distance is consistent with the meridian plane fits of *Formisano et al.* [1979] for north and south IMF.

Thus, the dawn-dusk cross-section is elongated (shortened) in Z for southward (northward) IMF, but shortened (elongated) in Y. Due to these opposing trends, the average of the measured polar and equatorial flank distances (Figure 4.11) is very nearly independent of B_Z over most of parameter space, as indicated by the very vertical contour lines. This result is consistent with PR95, in which flank distance is independent of B_Z and scales only with pressure, and also with the $\pm 1\sigma$ region of RS93 (their Figure 12) for which the contour lines are fairly vertical. Like the subsolar
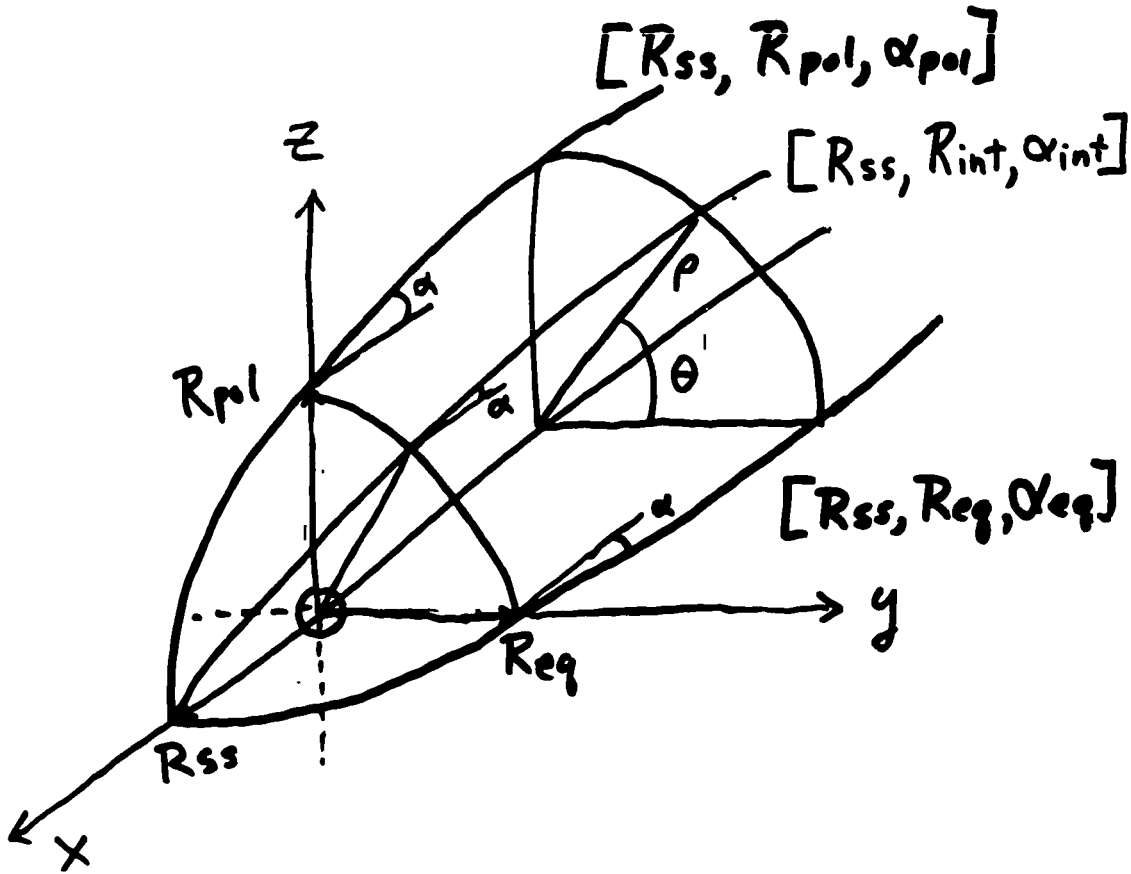
Figure 4.8: A diagram of the simple mathematical model used to approximate the 3-D shape of the magnetopause. The magnetopause is described by an ellipse in the noon-midnight meridian and equatorial planes, which are specified by three physical physical parameters: subsolar distance, R_{SS}; flank distance, R_{POL} or R_{EQ}; and the flaring angle, α_{POL} or α_{EQ}. These physical parameters are calculated for a given solar wind dynamic pressure P_D and IMF B_Z from interpolation of ellipses fitted to the global MHD simulations at discrete values. Values of these physical parameters are then interpolated for an arbitrarily postioned observation point using the clock angle θ around the magnetosphere axis X. This gives an ellipse specified by by R_{SS}, R_{INT}, and α_{INT}, which describes the magnetopause cross-section through the observation point. When the X value of the observation point is specified, an axial distance ρ to the magnetopause is determined.
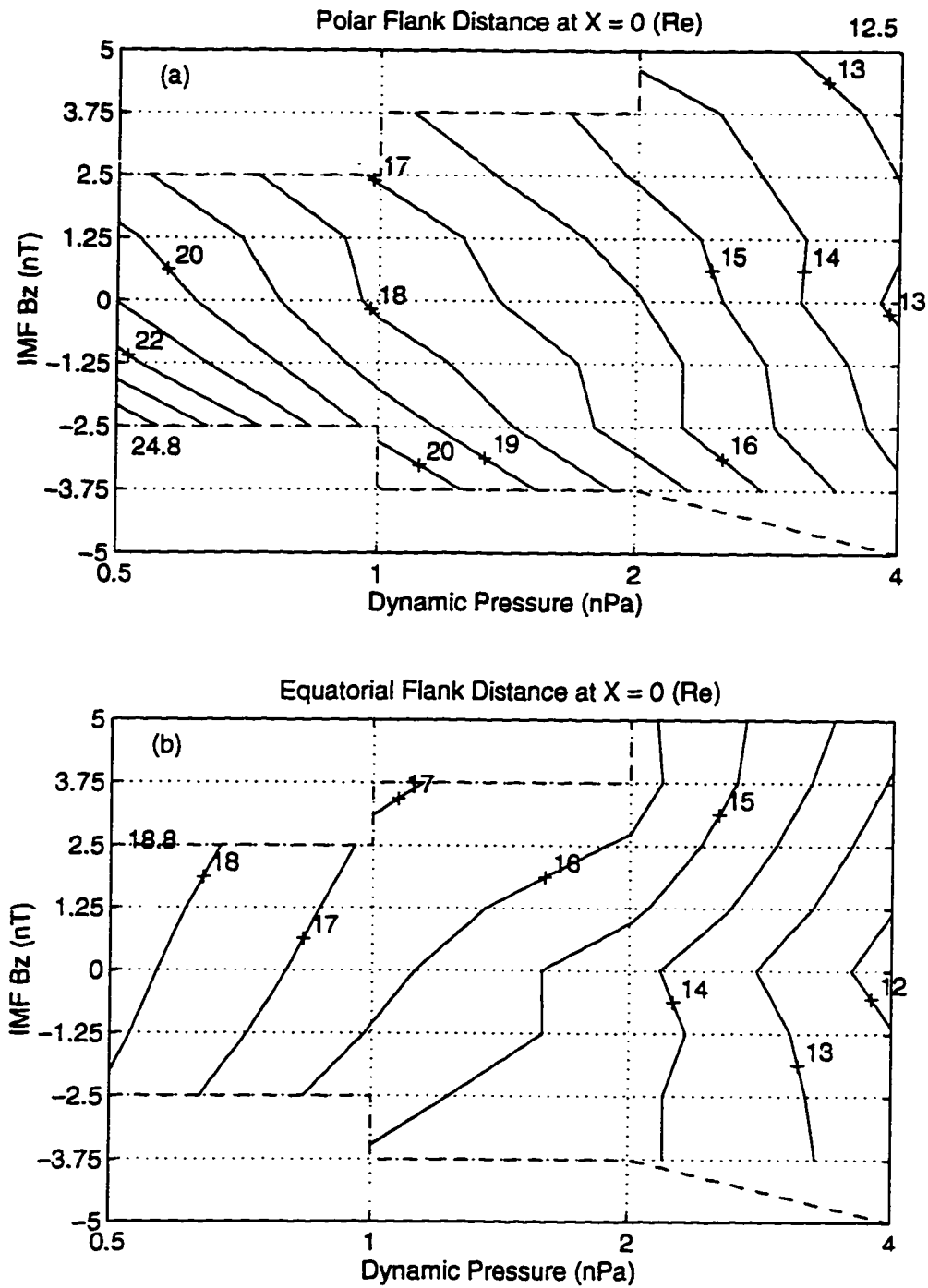
Figure 4.9: The flank distances (axial distance to the magnetopause at $X = 0$) from the fitted predictive model as a function of P_D and IMF B_Z in (a) the noon-midnight plane and (b) the equatorial plane.
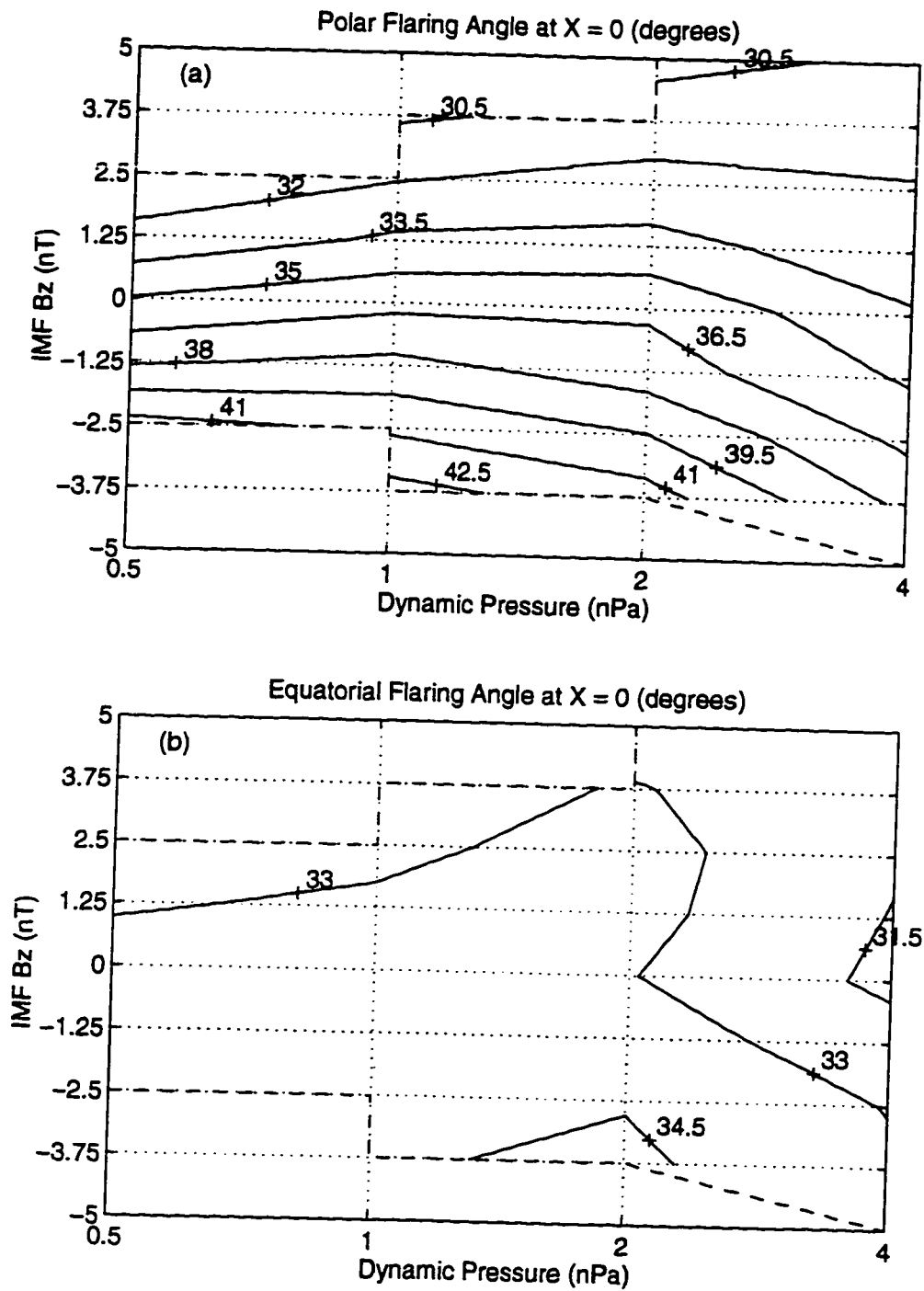
Figure 4.10: The flaring angles (slope of line tangent to the magnetopause at $X = 0$) from the fitted predictive model as a function of P_D and IMF B_Z in (a) the noon-midnight plane and (b) the equatorial plane.

variation, the polarity of the IMF does not seem to produce much of a qualitative difference in these distances, except for southward IMF at low pressures. These contour lines are no longer vertical due to the very strong flaring in the meridian plane for these conditions. A similar trend is seen in RS93 in the same regions of parameter space.

The measured polar and the equatorial flank distances are nearly equal for zero IMF (within a few tenths of an R_E, except for the lowest pressure case). This is because cross-sections of the magnetopause in the dawn-dusk plane (not shown) are nearly circular in our simulations for zero IMF. Our model magnetopause for zero IMF is not as circular in the dawn-dusk plane as our simulations due to fitting errors. The fitted polar flank distance is consistently larger than the measured value, while the fitted equatorial flank distance is consistently less than the measured values. These differences arise from approximating the magnetopause in these planes by an ellipse to 40 R_E in the tail.

If we average the measured flank distances over the $\pm 1\sigma$ solar wind range, we get a mean equatorial radius of 15.2 R_E and a mean polar radius of 15.3 R_E. A similar averaging gives 14.8 R_E for both RS93 and PR95. The mean equatorial flank distance from *Fairfield* [1971] is 15.8 R_E when scaled to 2 nPa. *Formisano et al.* [1979] found a mean flank radius of 15.0 R_E, both for unnormalized fits using all crossings and for fits normalized to dynamic pressure when scaled to 2 nPa. Thus, our mean value agrees with all of these within the range of measurement errors (0.8 R_E).

The mean equatorial (meridian) plane axial distance measured in our simulations at $X = -20R_E$ is 22.5 (25.6) R_E. Our average tail radius at 20 R_E (24.0 R_E) agrees quite well with PR96 (23.5 R_E), and is a bit larger than RS93 (22.7 R_E) and the magnetotail model of *Howe and Binsack* [1972] (22.5 R_E). The increase in mean tail radius from $X = 0$ to -20 R_E is quite similar in all three models (58% for our model, 54% for RS93, and 59% for PR96). The increase in the meridian plane of our simulations is 68%, but only 48% in the equatorial plane, indicating asymmetry of the magnetotail on average.

This asymmetry is reflected in the flaring angles for the meridian plane (Figure 4.10a) and equatorial plane (Figure 4.10b). The fairly horizontal lines in Figure 4.10a show that flaring angle in the meridian plane depends strongly on B_Z and only weakly on pressure. The decrease in α with B_Z shows that the meridian plane
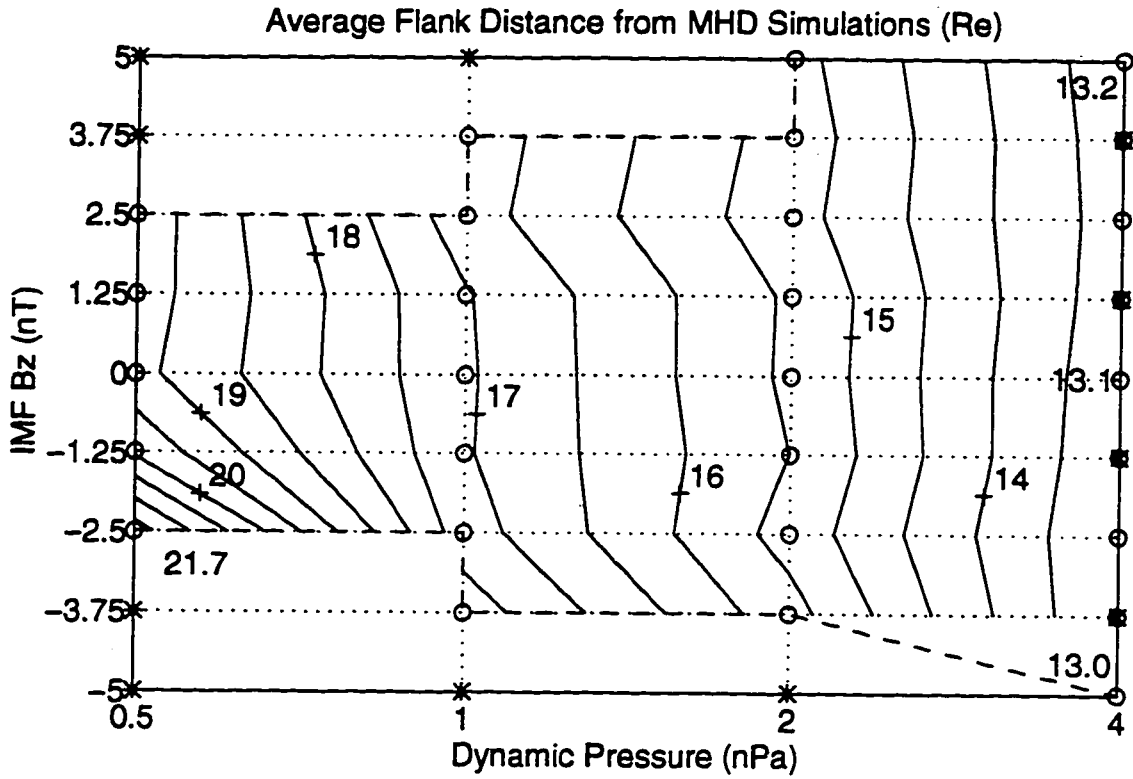
Figure 4.11: The average flank distance at $X = 0$, given by the average of the measured polar and equatorial flank distances from the simulations, in the style of Figure 4.7.

magnetopause shape changes for both southward and northward IMF, but for any given B_Z the shape varies only slightly with pressure (approximately self-similar scaling). The range in flaring angles is quite large (over $\sim 12°$) over the parameter space of the model; this produces a large spread in the north/south magnetotail dimension, as we shall see in Section 4.5. Flaring angle varies less with B_Z as pressure increases, so magnetotail flaring is stronger at low pressures, and suppressed by high pressures, a trend seen in RS93 in an average sense. Conversely, α in the equatorial plane (Figure 4.9b) varies much less than in the meridian plane. The flaring angle decreases slightly as either pressure or B_Z increases, with a range of only $\sim 3°$ over the entire parameter space. This is consistent with the nearly constant magnetopause shape for all solar wind conditions near the equatorial plane inferred by *Holzer and Slavin* [1978].

The average flaring angle (not shown) also depends strongly on B_Z but the gradients are only about half as much as in the meridian plane. The uniform change in average flaring angle for both north and south IMF is similar to RS93 (fairly horizontal lines in $\pm 1\sigma$ range of their Figure 13), but unlike PR96 whose magnetotail flaring angle changes less with northward IMF. The average flaring angle (as well as those in the meridian and equatorial planes) does not show any obvious qualitative difference due to IMF polarity, other than a small decrease in gradient as B_Z increases. The strong flaring in the meridian plane is due to flux transfer driven by magnetic reconnection, both for northward and southward IMF, while the very weak flaring in the equatorial plane results from little or no flux transfer. A more detailed analysis of the variation of the subsolar and flank distances and flaring angles with P_D and B_Z is given later (sections 9 and 10).

4.6 The 3-D Shape of the Magnetopause

Figure 4.12 shows magnetopause position as a function of X produced by our model for northward IMF (+2.5 nT), southward IMF (-3.75 nT), and no IMF at the average solar wind dynamic pressure (2 nPa). The solid (dashed) curve shows the elliptical fits in the noon-midnight meridian (equatorial) plane with the simulation measurements designated by an X (+). For the northward IMF case (Figure 4.12a), the ellipses in the meridian and equatorial planes are seen to be very similar. Our model magnetopause is nearly axisymmetric magnetopause at all four dynamic pressures when IMF $B_Z =$

+2.5 nT, with 1-2 R_E differences in the axial tail distances or less.

For southward IMF (Figure 4.12b), however, the meridian plane ellipse is very strongly flared, i.e. the distance exceeds the equatorial distance by 3 to 9 R_E on the nightside. This flaring for southward IMF is even stronger for lower dynamic pressure in our simulations, where the difference between axial distances can exceed 10 R_E (not shown). Flared configurations are seen in our model for southward IMF up to 1.25 nT northward, with the degree of flaring increasing for IMF more southward. Even the case with no IMF (Figure 4.12c) shows some flaring ($\sim 3R_E$ tailward of -10 R_E), but much less than that in Figure 4.12b. The measured polar and equatorial distances, however, are almost the same at $X = 0$ for zero IMF (see Section 4.5). Flaring, as shown by the simulation measurements, is limited to the nightside for zero IMF, although the fitted magnetopause curves indicate some flaring even on the dayside.

If we reexamine the measurements that produced the nearly symmetric curves in Figure 4.12a, we see that while the polar and equatorial measurements in the tail (-10, -20, and -40 R_E) are very similar, this is not true at $X = 0$. At this position, the polar distance (X) is actually about 2 R_E less than the equatorial distance (+), a phenomenon we shall call "anti-flaring" (or flattening). When IMF B_Z reaches +5 nT (not shown), this anti-flaring extends into the tail as well, with the equatorial distance exceeding the meridian distance from $X = 0$ to -40 R_E. Conversely, for southward IMF (Figure 4.12b), the meridian plane distance exceeds the equatorial distance everywhere on the nightside, even at $X = 0$ by over 2 R_E.

On the dayside these relations between equatorial and meridian plane distances are reversed due to the magnetic cusp. Our simulations display a prominent cusp, typically producing indentations of 1-2 R_E, reminiscent of magnetopause surfaces in older physical models [e.g., *Mead and Beard*, 1964]. Since distances at the terminator are nearly equal at zero IMF, meridian plane distances are significantly smaller than equatorial distances sunward of the cusp in our simulations. The dayside magnetopause, then, is anti-flared (or oblate) for zero IMF and more so for northward IMF. Equatorial and meridian plane distances sunward of the cusp are most nearly equal in our simulations for moderate southward IMF.

Cross-sections of the magnetotail perpendicular to the Earth-Sun line ($Y - Z$ planes) are most nearly circular close to 2.5 nT (not shown), being anti-flared (flat-

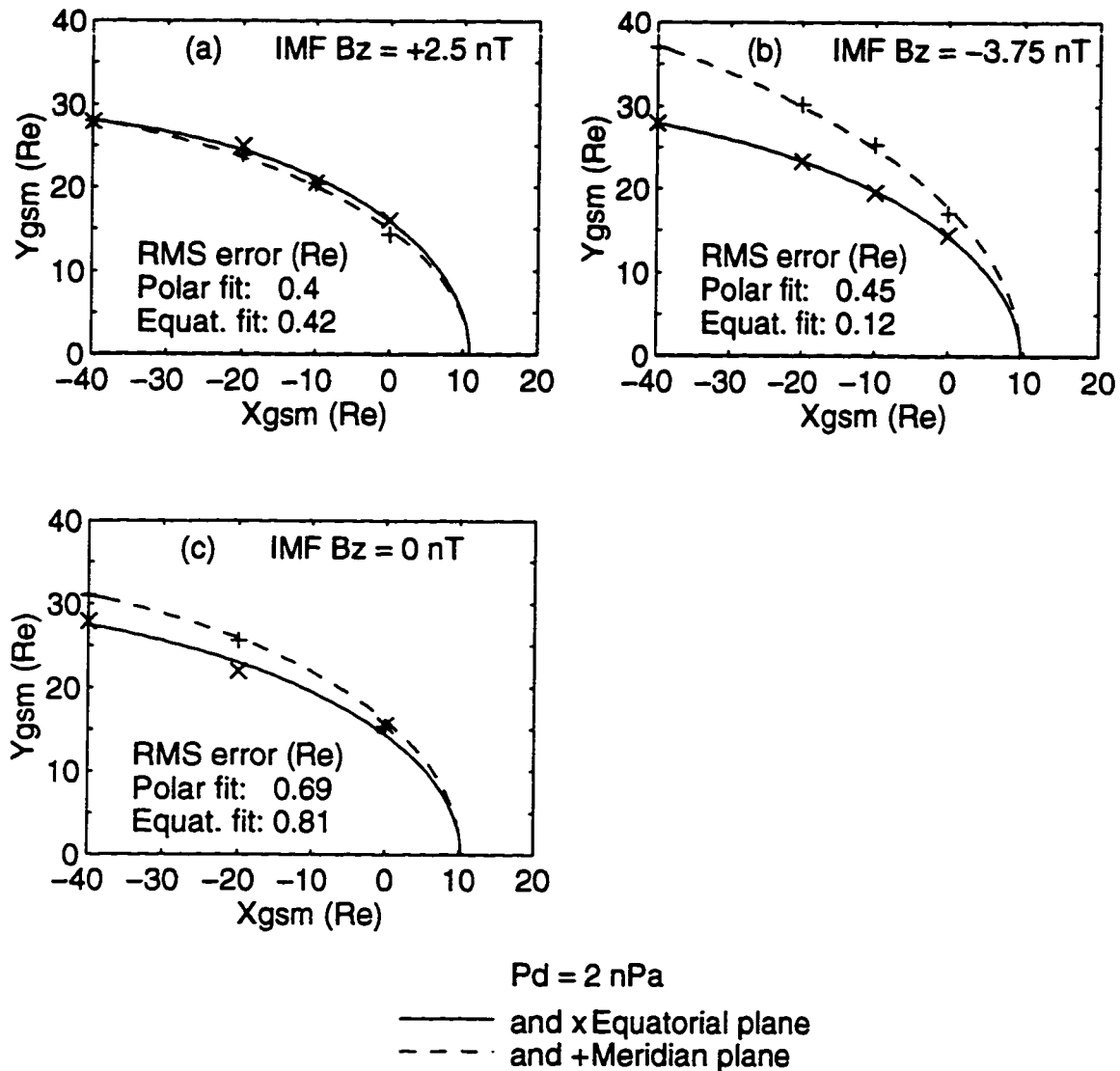Figure 4.12: Fitted magnetopause cross-sections in both the noon-midnight meridian plane (dashed line) and the equatorial plane (solid line) at a dynamic pressure of 2 nPa for different values of IMF B_z: (a) northward IMF (+2.5 nT), (b) southward IMF (-3.75 nT), and (c) no IMF. Measurements from the simulation in the noon-midnight plane (X) and the equatorial plane (+) are also displayed, along with the errors for each fit.

tened) for more northward IMF and flared (elongated) below this threshold. Magneto-sphere cross-sections from global MHD simulations of *Walker et al.* [1990] performed for no IMF with no dipole tilt show a moderate flaring at $X = -15, -30, -45R_E$ (their Figure 6a) very similar to our corresponding simulations. When averaged over solar wind conditions, this would produce an overall asymmetry of the magnetopause between 10 to 40 R_E. This net flaring in the middle tail is consistent with the results of *Meng et al.* [1981], who inferred a net flaring of $\sim 23\%$ between 30 and 40 R_E, and contrary to the results of *Ohtani and Kokubun* [1990], who found a net flattening of $\sim 17\%$ in the same region. It also disagrees with *Hammond et al.* [1994], who found very little asymmetry at $X = -25R_E$ (flaring of $\sim 2\%$) for low dipole tilt angles ($< 5°$).

The lack of net asymmetry in the dawn-dusk plane (circular cross-section for zero IMF) is consistent with *Formisano et al.* [1979], who found that the average equatorial distance exceeds the average polar distance by $2 - 3\%$ at most. Numerical estimates of magnetopause asymmetry at the terminator and along the tail axis are given is Section 4.11. Cross-sections on the dayside tend to be elongated in the Y direction and are most nearly circular for southward IMF. This net asymmetry of the dayside magnetosphere agrees with the results of *Sibeck et al.* [1991], who performed separate elliptical fits using points near the equatorial plane ($-5 < Z < +5R_E$) and the meridian plane ($-5 < Y < +5R_E$). These fits indicate an oblate magnetopause shape on the dayside, with roughly equal equatorial and meridian distances at $X = -10R_E$. The average equatorial distances exceeds the average meridian distance sunward of this point, by an average of 8\% between $X = -5$ and $+7$ R_E.

A strong signature of dayside asymmetry in ISEE magnetopause crossings has been found by *Petrinec and Russell* [1995b] during periods of northward IMF when the dayside portion of our simulations is most oblate. *Petrinec and Russell* [1995b] studied the average distance to the subosolar magnetopause inferred for observation points using their dayside magnetopause model (PR95), which is constructed from measurements near the equatorial plane. After normalizing to the dynamic pressure, this standoff distance is not constant as might be expected from an axisymmetric magnetopause without a significant indentation near the cusp. Rather this inferred distance depends in a systematic way on the dipole tilt and the latitude of the observation point, being maximum for points close the equatorial plane when dipole

tilt is near zero, and decreasing with the sum of latitude of the observation point and the dipole tilt, a parameter which indicates the distance from the magnetic cusp. Since the subsolar distance inferred with their elliptical magnetopause model for observations near the cusp is about 1 R_E less than for observations near the equatorial plane, they attributed this difference in distances to the magnetic cusp. This difference was also shown to be generally consistent with the meridian plane magnetopause curve of a pressure balance model [*Spreiter and Briggs*, 1961] with a prominent cusp indentation.

By examining high-latitude magnetopause crossings identified in HAWKEYE data, *Zhou and Russell* [1995] produced average magnetopause ellipses on the dayside (Figure 4.13) near the equatorial plane, the meridian or polar plane, and at mid-latitudes for both northward and southward IMF. Again these curves indicate that equatorial distances exceed polar distances on average on the dayside. The equatorial ellipses are from the model of *Petrinec and Russell* [1993a], while the meridian plane ellipse was obtained by processing high-latitude HAWKEYE data with the methodology of that model. The average ellipses for southward IMF are nearly axisymmetric, but show a small degree of flaring, with meridian distances exceeding equatorial distances by only a few tenths of an R_E. The average ellipses for northward IMF show considerable anti-flaring, however, with the equatorial distances exceeding the meridian distances everywhere on the dayside and by almost 2 R_E at the terminator. This 2 R_E difference matches that measured in our model for +2.5 nT (Figure 4.12a). These results are consistent with the increase of dayside oblateness in our simulations as B_Z increases.

This trend in the ratio of meridian to equatorial distances along the X axis is similar to that seen in 3-D magnetopause surfaces of older physical models [*Midgely and Davis*, 1963; *Mead and Beard*, 1964; *Olson*, 1969; *Choe et al.*, 1973]. These surfaces are also characterized by pressure balance, in this case of vacuum dipole magnetic field pressure against solar wind dynamic pressure. The meridian to equatorial distance ratio for the zero dipole tilt magnetopause surface of *Olson* [1969] is as low as 0.73 near the cusp and increases monotonically tailward of the cusp reaching a value of 1.09 deep in the tail. This ratio is less than unity (0.84) at the terminator, with equal meridian and equatorial distances at $\sim 20R_E$ in the tail, a somewhat more flattened shape than that in our MHD simulations for zero IMF. We can characterize these
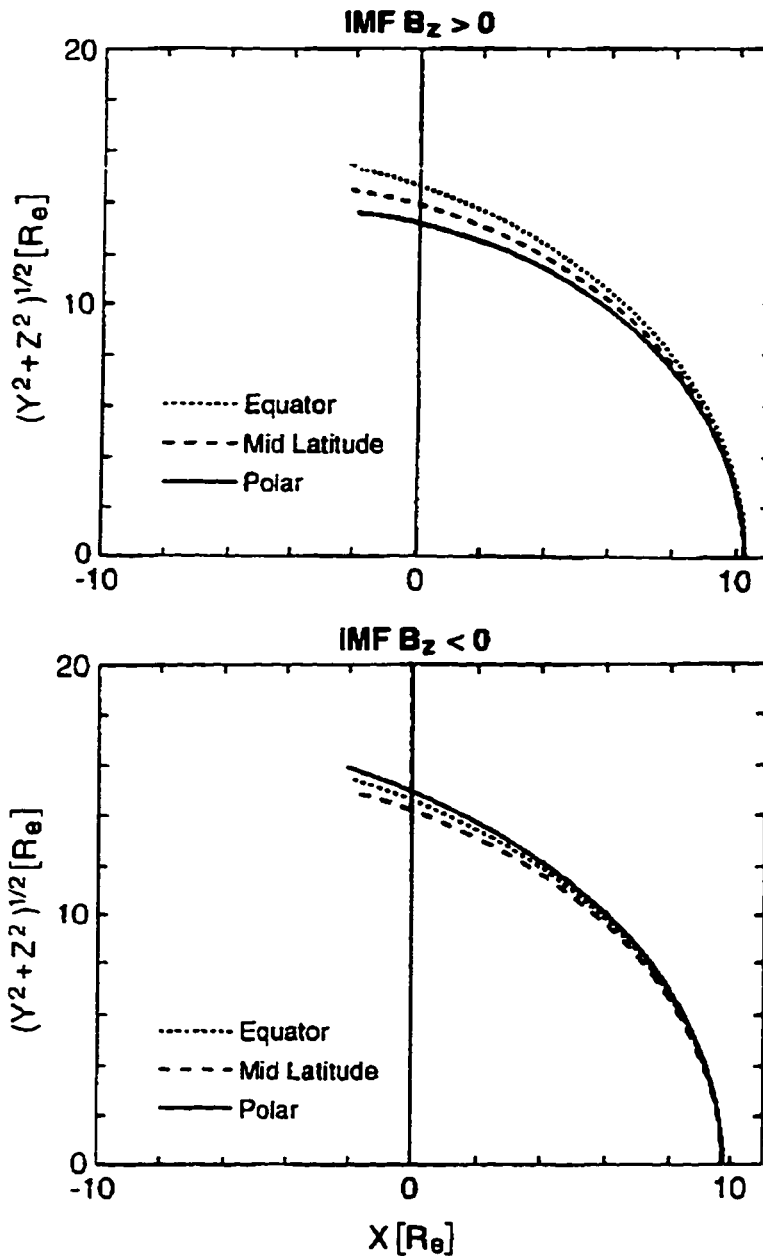
Figure 4.13: Average cross-sections of the dayside magnetopause near the noon-midnight meridian or polar plane (solid line), the equatorial plane (dotted line), and at mid-latitudes (dashed line) for northward IMF (upper panel) and southward IMF (lower panel). The magnetopause curves were determined with high-latitude satellite observations from HAWKEYE using the ellipse fitting procedure of *Petrinec et al.* [1991]. Data points were sorted by clock angle θ (measured from the north): polar plane ($\theta < 22.5°$), mid-latitudes ($22.5° < \theta < 67.5°$), and equatorial plane using the results of *Petrinec et al.* [1991]. [Taken from *Zhou and Russell*, 1995].

models (which do not incorporate IMF or magnetospheric plasma) as anti-flared on the dayside and near-Earth tail, and slightly flared deep in the tail. Like our global simulations, these models exhibit a basic asymmetry of the magnetopause surface that is lacking in the present axisymmetric empirical magnetopause models.

4.7 Families of Magnetopause Ellipses

We plot families of magnetopause ellipses to show their systematic variation with B_Z and P_D. Figure 4.14 shows the parametric variation of the model ellipses in the meridian plane for 3 B_Z values (-2.5, 0, +2.5 nT) at each of the 4 values of P_D. There is considerable flaring on the nightside in these meridian plane magnetopause ellipses, stronger for lower dynamic pressures. To gauge the degree of flaring in the tail, we study the variation of the axial distance at $X = -20R_E$. At the lowest pressure of 0.5 nPa (Figure 4.14a), the axial distance at this position varies between ~ 28 to $\sim 37R_E$ as B_Z ranges between ± 2.5 nT. This spread of distances in the tail (9 R_E, as marked) decreases strongly with pressure to less than 3 R_E at the highest pressure (Figure 4.14d). As we shall see shortly, this degree of flaring is substantially more than in the axisymmetric empirical models. We also see that all of the ellipses intersect near a spot on the dayside (approximately at the position of the cusp) which we shall call the "crossover point".

Corresponding magnetopause ellipses in the equatorial plane show very different qualitative behavior (Figure 4.15). These ellipses do not intersect anywhere, but rather are nearly parallel with one another. Thus, there is no crossover point and flaring is essentially absent in the equatorial plane. These ellipses are approximately self-similar, especially on the dayside, even for variations in B_Z. The variations in distance due to IMF B_Z are relatively small, only about 1 or 2 R_E. In fact, the southward IMF cases have slightly smaller flank distances than the northward IMF cases at generally all values of X. This may be due to high latitude reconnection in the northward IMF simulations, in which nightside magnetic flux is transferred to the dayside and then convected laterally to the flanks, producing slightly larger axial distances.

The average ellipses (calculated for a clock angle of 45°) of our model also show flaring (Figure 4.16), but to much less a degree than the meridian plane ellipses (Figure 4.14). At the lowest pressure (Figure 4.16a) the axial distance at $X = -20R_E$
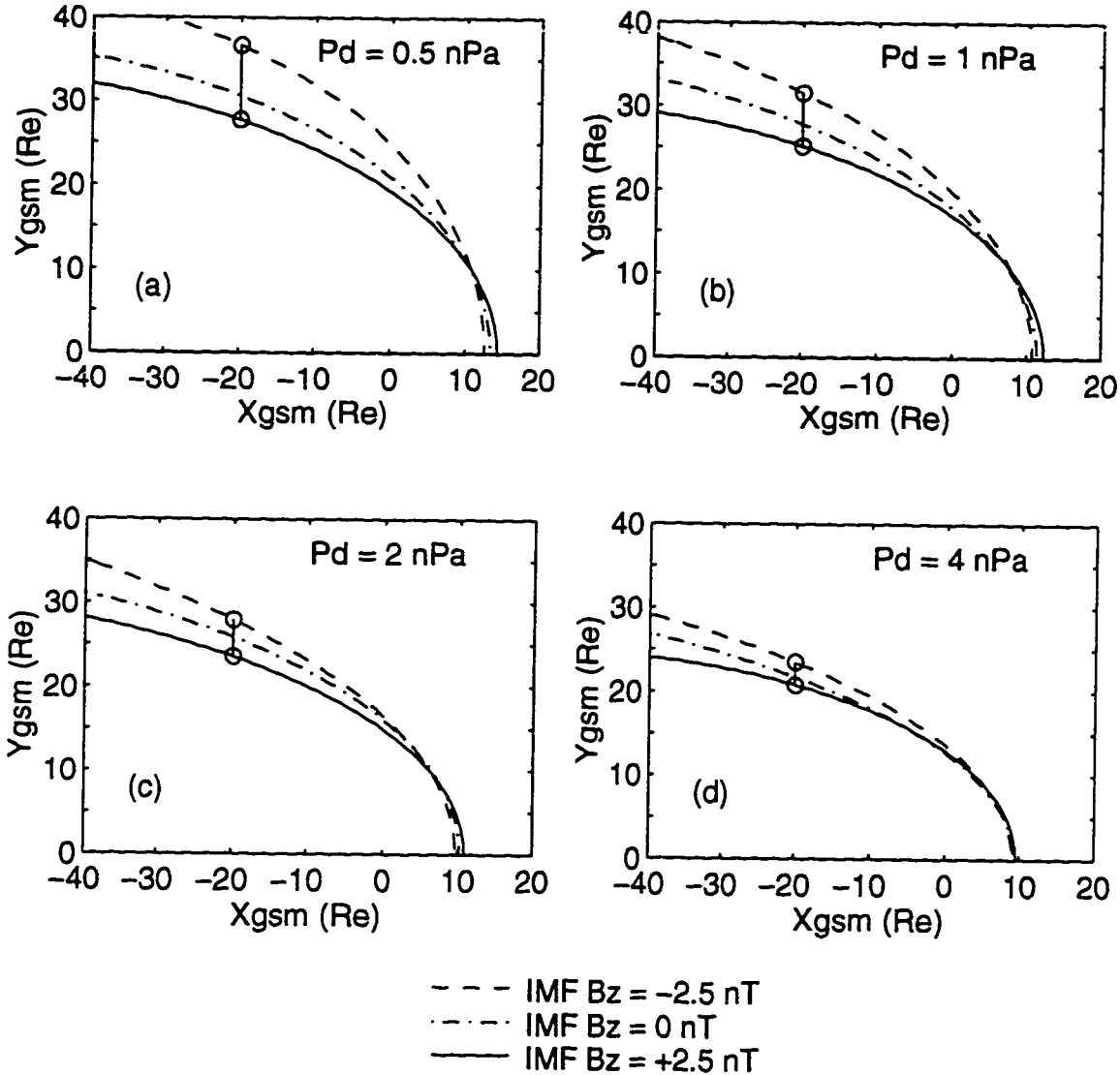
Figure 4.14: Families of fitted magnetopause ellipses in the noon-midnight meridian plane. These are for dynamic pressure of (a) 0.5 nPa, (b) 1.0 nPa, (c) 2.0 nPa, (d) and 4.0 nPa. Each line is a different value of IMF B_Z: -2.5 nT (dotted), no IMF (dot dash), add + 2.5 nT (solid). The vertical bar shows the spread of axial distances at $X = -20$ due to the variation of B_Z.
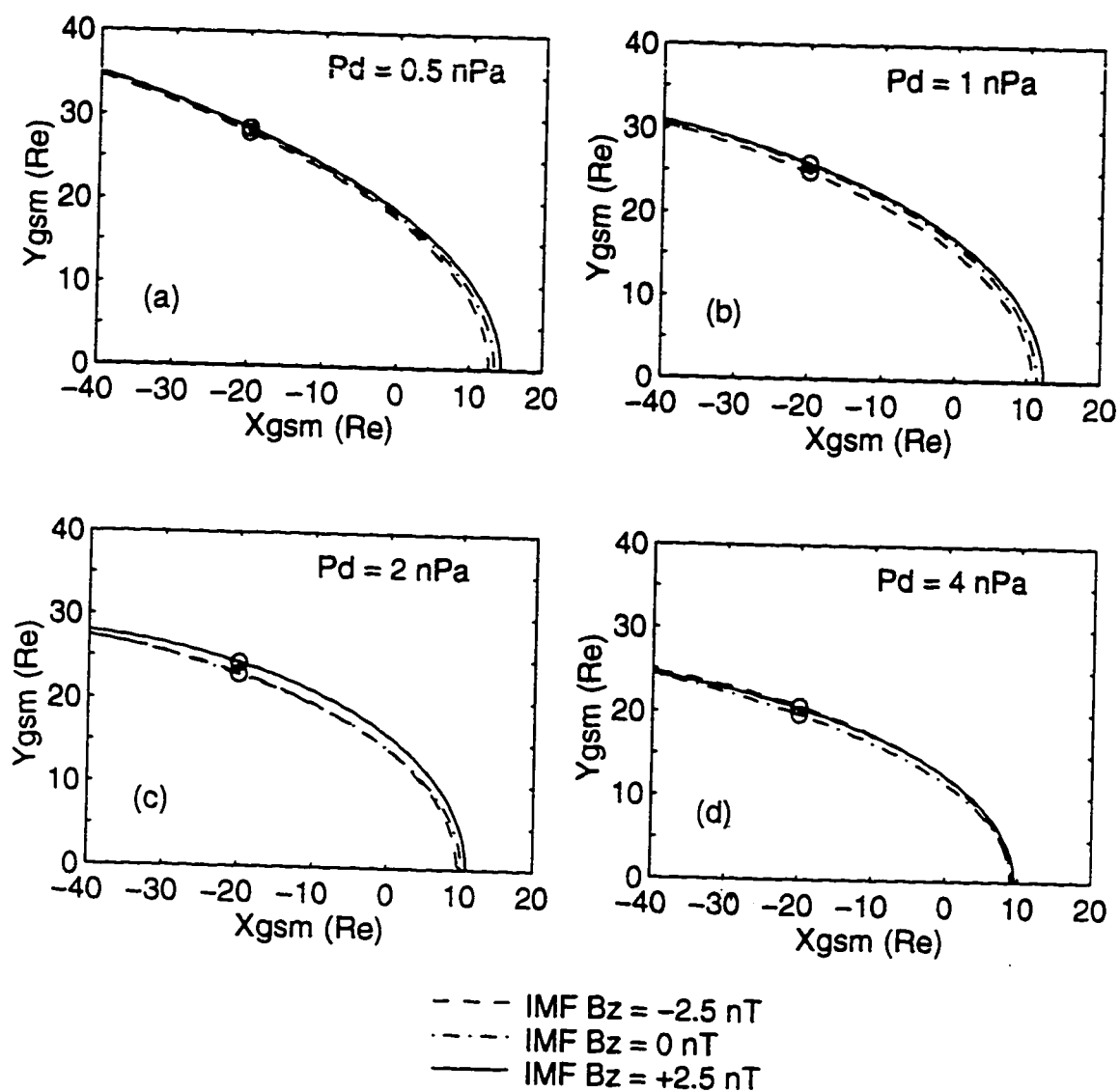
Figure 4.15: Families of magnetopause ellipses in the equatorial plane, in the style of Figure 4.14.

now ranges from ~ 28 to $\sim 32 R_E$. The (marked) spread of axial distance ranges from about ~ 4 to $\sim 1 R_E$ as pressure decreases, roughly half the range in the meridian plane. There is also a well-defined crossover point, but comparing each case with Figure 4.14, we see that the crossover points are consistently at a smaller value of X and a larger axial distance, moving from well on the dayside to just inside the nightside as pressure increases.

We compare these parametric plots to those presented in Figure 4.17, which were produced with the *Roelof and Sibeck* [1993] model. Since RS93 is axisymmetric, it is best compared with the average ellipses of our model. RS93 exhibits both flaring and a well-defined crossover point in these curves. The spread of axial distances for B_Z between -2.5 to +2.5 nT at 20 R_E in tail decreases from about 4 R_E to 1 R_E for the same pressures in RS93 (Figures 4.17b to 4.17e), the same spread as in Figure 4.16. The crossover points are in roughly the same positions, at axial distances greater than 10 R_E, moving from well on the dayside at the lowest pressure to a position in the near nightside at 4.0 nPa. Thus the qualitative behavior of the average ellipses in our model is very similar to those of RS93 and show the same amount of flaring in the tail, even though our ellipses in the meridian and equatorial planes look quite different than RS93.

We also compare our model with PR96, which was not derived directly from magnetopause measurements, but by MHD force balance between lobe and solar wind measurements. The flaring of the PR96 magnetotail (and hence axial distance) changes more for southward IMF than northward IMF. The corresponding spread of distances due to IMF B_Z shown in Figure 5 of *Petrinec and Russell* [1996a] decreases from about 2 to 0.5 R_E as pressure increases, about half the increase in magnetotail flaring seen in RS93 and our model. The weaker magnetotail flaring for northward IMF in PR96 may explain this factor of two difference. The crossover point cannot be compared, as it is constrained to lie at the $X = 0$ in PR95/PR96.

Now we examine the variations in magnetotail size due to pressure changes. Figure 4.18 shows the same average plane curves plotted in Figure 4.16 sorted by each IMF B_Z rather than pressure. We see the systematic effects of compression at each value of IMF B_Z, which produces roughly self-similar families of ellipses, the most so for +2.5 nT. These curves correspond to the outer four curves from RS93, shown in Figure 4.17g to 4.17i. Those curves are very self-similar for zero IMF (Figure 4.17h),
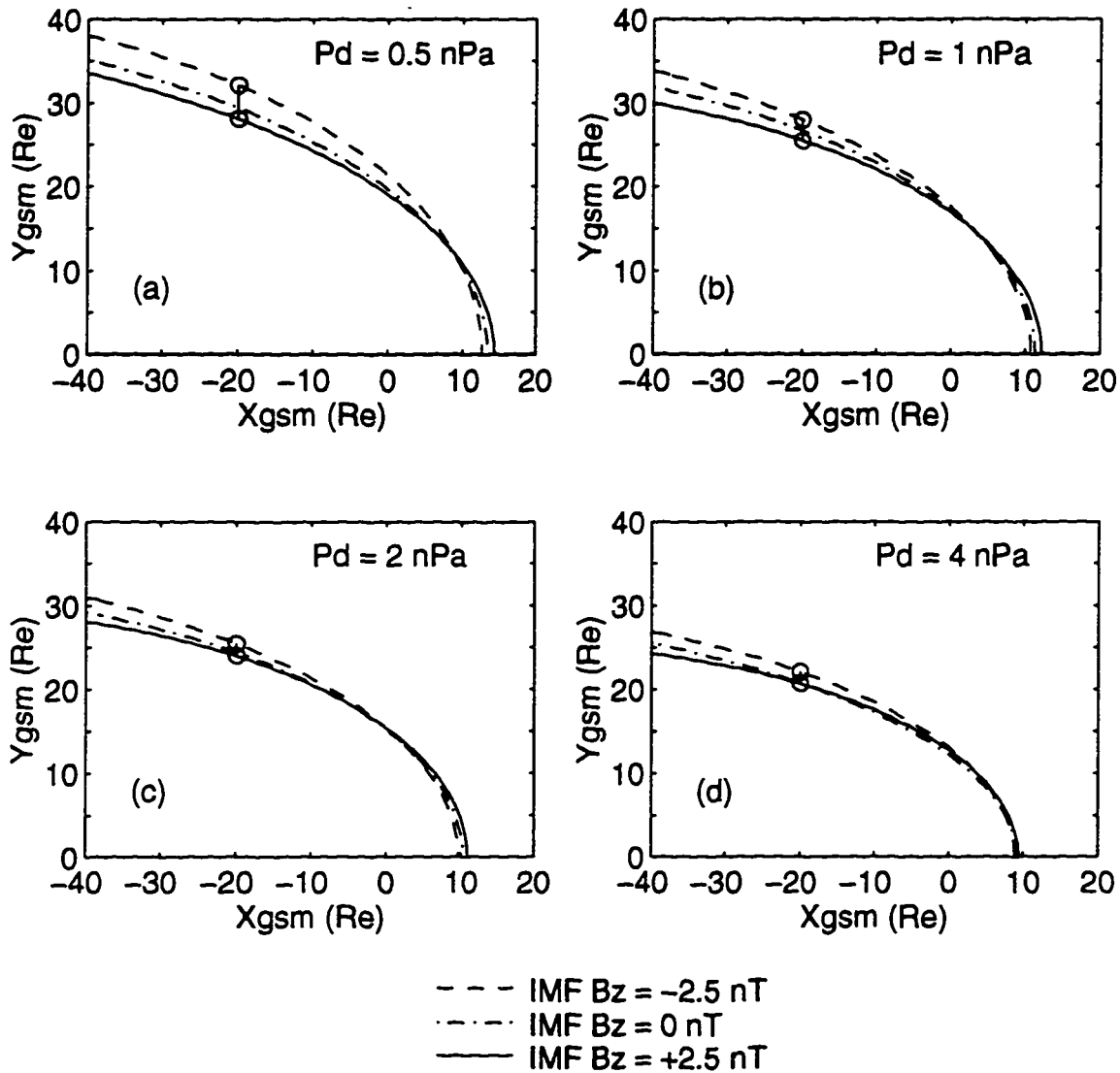
Figure 4.16: Families of average magnetopause ellipses, interpolated for a clock angle of 45°, in the style of Figure 4.14.
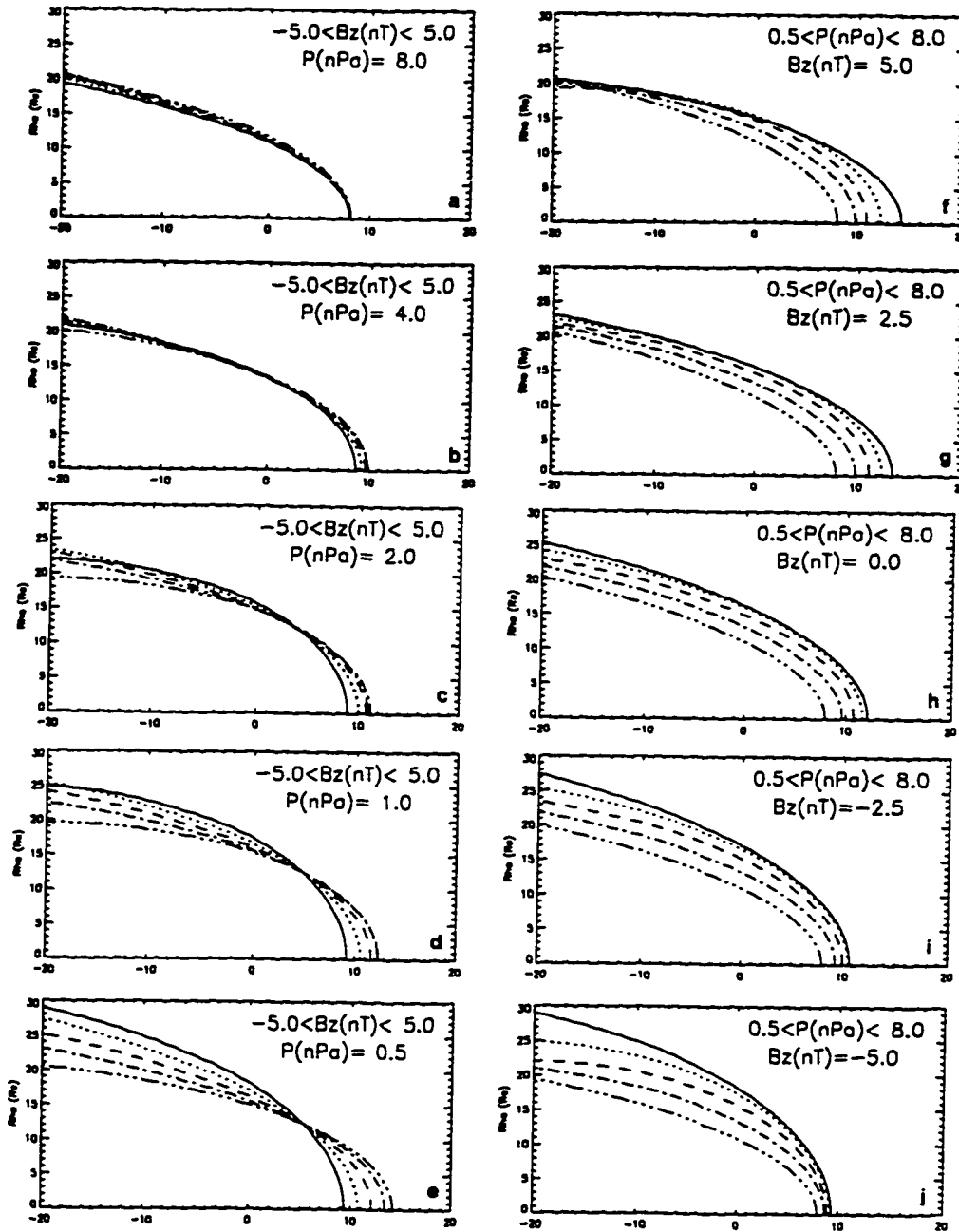
Figure 4.17: Families of average magnetopause ellipses from the model of *Roelof and Sibeck* [1993]. (a)-(e) Families of ellipses in left panels are sorted by dynamic pressure (P) with each curve for different IMF B_Z values [-5.0 nT, solid line; -2.5 nT, dotted; 0 nT, dashed; +2.5 nT, dash-dot; +5.0 nT, dash-dot-dot-dot]. (f)-(j) The ellipses shown in the right panels are the same, but they are arranged in families of IMF B_Z, with each curve for different dynamic pressures [0.5 nPa, solid; 1 nPa, dotted; 2 nPa, dashed; 4 nPa, dash-dot; 8 nPa, dash-dot-dot-dot]. The X axis reaches to -20 R_E and the range of dynamic pressures and IMF B_Z is greater than in th MHD based model. [Taken from corrections of *Roelof and Sibeck*, 1994].

but they converge in the tail for northward IMF (Figures 4.17f, 4.17g) and diverge for southward IMF (Figures 4.17i, 4.17j).

We again measure the spread of tail distances at 20 R_E in the tail as pressure ranges from 0.5 to 4 nPa at each IMF value (again marked). Our model's spread is 10 R_E (-2.5 nT), 9 R_E (0 nT), and 8 R_E (+2.5 nT), showing little difference with B_Z. The corresponding spreads of RS93 are 5, 3, and 2 R_E, respectively, while PR96 gives $\sim 13R_E$ for all three IMF levels. The range of our model is closer to, but somewhat less than, PR96. The difference with RS93 is a factor of two for southward IMF to a factor of 4 for northward IMF. Even if we perform the comparison over the $\pm 1\sigma$ range of the RS93 model, the domain of quantitative validity [*Roelof and Sibeck*, 1993], the difference is still at least a factor of two for all three IMF levels. This different variation with pressure keeps our families of ellipses more self-similar across the spectrum of IMF than in RS93.

To put these differences in perspective, all three models produce similar average magnetopause curves (not shown) for northward IMF(+3.75 nT) and high pressure (4 nPa), with all three curves agreeing within 2 R_E from the subsolar point to $x = -40R_E$. These curves diverge in the tail as B_Z becomes southward, and especially as pressure decreases. Within the $\pm 1\sigma$ solar wind range, the largest divergence of the magnetotail curves is seen at low pressure (1 nPa), where the axial distance at $X = -20R_E$ given by RS93 and PR96 can differ by 3 to 5 R_E between ± 3.75 nT, values larger than claimed model errors. Our model magnetotail generally falls between these models for most cases with significant divergence, but tends to be closer to PR96 at the lowest pressures (not shown).

4.8 Testing the Model with Observations

4.8.1 Magnetopause crossing databases

The magnetopause data sets are briefly discussed, before they are used to compare our predictive model against the empirical models. The *Roelof and Sibeck* data set used to generate the RS93 model is correlated with solar wind dynamic pressure and IMF B_Z using hourly averages. This data set was compiled by *Sibeck et al.* [1991] and consists of 1821 magnetopause crossings by about 15 different spacecraft over a period of about 30 years. Simultaneous solar wind measurements for both solar wind
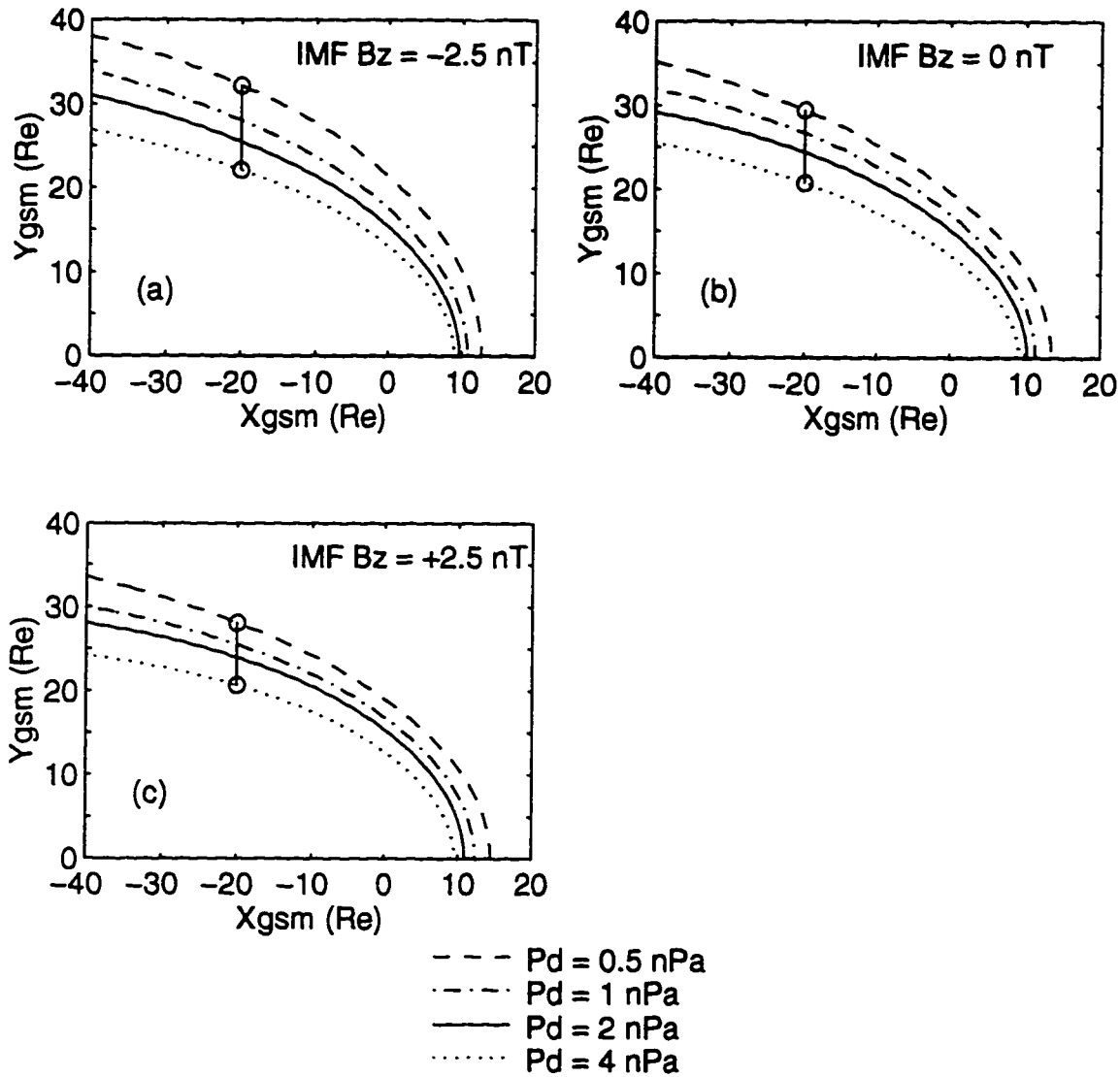
Figure 4.18: The average magnetopause ellipses of Figure 4.16, now plotted for the IMF B_Z levels of (a) -2.5 nT, (b) 0 nT, and (c) +2.5 nT. Each line is for a different value of dynamic pressure: 0.5 nPa (dashed), 1 nPa (dash-dot), 2 nPa (solid), and 4 nPa (dotted).

parameters were available for 797 of these crossings. The data points reach to 37 R_E in the tail and contain a large number of high latitude points, giving good coverage at all clock angles.

The *Petrinec and Russell* data set used to develop the PR95 model is correlated with solar wind using 5 minute averages. This data set was compiled by *Song et al.* [1988] and contains 1147 magnetopause crossings by ISEE 1 and 2 over a period of about 9 years. The measurements do not reach as deep into the tail, only to about 10 R_E in the X direction. The points are also constrained by the ISEE orbits to lie near the equatorial plane, so there is no coverage at high latitudes. Simultaneous solar wind measurements for both solar wind parameters were available for 504 points, again slightly less than half of the total, like the *Roelof and Sibeck* data set.

The average spacecraft positions in the *Roelof and Sibeck* data set are measured in geocentric solar ecliptic (GSE) coordinates, but the associated IMF B_Z value are in geocentric solar magnetospheric (GSM) coordinates. Both the average spacecraft positions and the IMF B_Z values are measured in GSM coordinates in the *Petrinec and Russell* data set. The simulation box can be closely associated with GSM coordinates, so using GSE values will introduce more error, especially when the dipole tilt angle is large, the situation for which these coordinates systems most differ. This is one possible cause for less scatter in the *Petrinec and Russell* data points, which we shall see has only about half of the scatter of the *Roelof and Sibeck* data points. The *Petrinec and Russell* data was also from fewer instruments on fewer orbits, and the magnetopause is identified in the data by fewer observers, each of which may introduce some bias into the data when determining an average magnetopause position. The scatter due to surface waves also is larger on the nightside than the dayside and increases in amplitude with distance down the tail [*Holzer and Slavin*, 1978], so the inclusion of more points deep in the tail can also explain the higher scatter of the *Roelof and Sibeck* data points.

A 5-minute time interval is better to study magnetopause variations due to pressure [*Sibeck*, 1995], but *Sibeck et al.* [1991] felt one hour was better for studying effects due to IMF B_Z. Thus the *Petrinec and Russell* data set may follow dynamic pressure variations better than the *Roelof and Sibeck* data set, but the situation may be reversed for IMF B_Z variations.

146

4.8.2 Model comparisons

Using these data sets, we computed the distance to the magnetopause predicted by our model, the RS93 model, and the hybrid PR95/PR96 model for the observation points falling in several bins of P_D and B_z, and studied the differences between the predicted and observed distances for each model. Unlike the calculations with the axisymmetric empirical models, the axial distances of our model are calculated also using the clock angle of the observed crossing. This comparison was performed against both the *Roelof and Sibeck* data set and the *Petrinec and Russell* data set.

The errors calculated for all three models in each of several solar wind bins are tabulated in Table 4.1 for the *Roelof and Sibeck* data set and Table 4.2 for the *Petrinec and Russell* data set. Plots for each of these bins, showing observation points and each of the models errors, are presented in Appendix A. By inspection, there is not much difference in error among all the models from one bin to another for either data set. Thus, we can conclude that all three models are about equally accurate, regardless of which data set they are tested against. Since all the models have low values for the average error, they have similar values for rms errors, due mostly to the scatter of the observation points (see plots in Appendix A).

Since our simulations (and hence the predictive magnetopause model) had zero dipole tilt, we expect our model errors to decrease if using only crossings during times of low tilt. Errors calculated with our model when tilt angle magnitude is less than 10° are also listed in the bottom row of Tables 4.1 and 4.2, and the rms values are seen to decrease by 10%. Errors for RS93 also decreased when tested in this manner, while those from PR95/PR96 changed little. These results indicate that incorporating dipole tilt (and other variables) may significantly reduce predictive errors of our magnetopause model.

4.9 Variation with Dynamic Pressure

We now examine parametric variation of magnetopause size (subsolar distance, flank and tail radii) with dynamic pressure. The distance to the magnetopause R_i at a dynamic pressure P_D is conventionally scaled with a power law,

$$R_i(P_D) = R_i^{ref}(P_D/P_D^{ref})^{n_i} \qquad (4.3)$$

Table 4.1: Model Errors Using the *Roelof and Sibeck* Data Set.

Dynamic Pressure (nPa)	IMF B_Z (nT)	Number of Points	Average Errors (R_E)			RMS Errors (R_E)		
			RS93	PR95 PR96	MHD	RS93	PR95 PR96	MHD
0.5 to 1	-2.5 to 2.5	51	-0.08	-1.57	-1.45	1.69	2.57	2.48
1 to 2	-3.75 to 0	125	0.37	-0.05	-0.45	1.80	1.83	2.35
1 to 2	0 to +3.75	125	0.28	-0.23	-0.37	1.70	1.94	2.06
2 to 4	-3.75 to 0	117	0.06	0.46	0.05	1.89	2.01	1.81
2 to 4	0 to +3.75	119	-0.04	0.10	-0.02	1.77	1.78	1.85
All bins, all tilts		537	0.15	-0.10	-0.33	1.78	1.97	2.08
| Tilt | < 10°		183	-0.16	-0.39	-0.58	1.64	2.00	1.81

Table 4.2: Model Errors Using the *Petrinec and Russell* Data Set.

Dynamic Pressure (nPa)	IMF B_Z (nT)	Number of Points	Average errors (R_E)			RMS errors (R_E)		
			RS93	PR95 PR96	MHD	RS93	PR95 PR96	MHD
0.5 to 1	-2.5 to 2.5	49	0.63	-0.39	-0.13	1.54	1.30	1.27
1 to 2	-3.75 to 0	87	-.001	-0.32	0.16	0.99	1.05	1.05
1 to 2	0 to +3.75	63	-.001	-0.12	-0.11	0.91	0.81	0.86
2 to 4	-3.75 to 0	52	-0.04	-0.01	0.41	0.89	0.94	1.07
2 to 4	0 to +3.75	61	-0.04	0.08	0.24	0.84	0.83	0.90
All bins, all tilts		312	0.08	-0.16	0.12	1.04	1.00	1.03
| Tilt | < 10°		92	-0.14	-0.20	-.001	0.90	0.94	0.90

where R_t^{ref} is a reference distance, P_D^{ref} a reference dynamic pressure, and n_t the scaling exponent. The scaling exponent for the subsolar distance is expected to lie near $-1/6$ (-0.167), the value determined in the ideal Chapman-Ferraro problem from balancing the magnetic pressure of a vacuum field with the dynamic pressure of incoming plasma lacking an IMF [*Martyn*, 1951; *Sibeck et al.*, 1991]. Departure from this ideal value indicates that the self-similar scaling with dynamic pressure seen in many models (e.g., *Mead and Beard*, 1964) breaks down. It also implies that secondary terms in the Chapman-Ferraro pressure balance equation, such as magnetospheric plasma pressure or magnetosheath magnetic field pressure, may be important in determining the equilibrium position of the magnetopause.

This ideal exponent is used in PR95, based on separate fits for inferred standoff distances in *Petrinec and Russell* [1993a] for both northward and southward IMF that produced exponents close to this value. Although such a scaling exponent is not reported in *Roelof and Sibeck* [1993], their Figure 17b suggests an exponent greater than $-1/6$ over most of their parameter space, except for moderately large northward IMF. The scaling exponent calculated with the subsolar distances of RS93 has an average value of about -0.13 over the $\pm 1\sigma$ range of their model.

Our subsolar distance follows a power law with P_D with an exponent that agrees with PR95 better than RS93 (Table 4.3). Besides increasing the subsolar distance, the additional plasma pressure at the inner model boundary (artificial ring current) increases the variation of the subsolar distance with pressure. The average of this exponent over the entire range of our model is -0.18, meaning that our subsolar distance varies slightly more with pressure than the ideal case (or PR95), while the RS93 subsolar distance varies less. The value of the exponent (and its variation) depends on the exact form of the pressurization used in the simulations, but is generally a bit less than the ideal value. It lies closest to $-1/6$ for southward IMF and is smaller for northward IMF. Like our model, the exponent in RS93 is lower for southward IMF than northward IMF (Table 4.3), decreasing monotonically with B_Z, but RS93 does so at higher rate. While the exponent of PR95 does not vary with B_Z, a difference was found in fits of *Petrinec and Russell* [1993a]. The exponent was slightly lower for northward IMF (-0.14) and higher for southward IMF (-0.19), with an overall average very close to the ideal value. If these values are taken to be significant, this implies the scaling exponent may increase with B_Z, opposite the trend of RS93 and

Table 4.3: Dynamic Pressure Scaling Exponents.

Model	Subsolar Distance	Trend with B_Z	Flank Distance	Trend with B_Z	Tail Radius
MHD	-0.18	Decreasing	-0.20	Increasing	-0.17
RS93	-0.13	Decreasing	-0.14	Increasing	-0.07
PR95/PR96	-0.17	Increasing?	-0.17	None	-0.22

our model (Table 4.3).

We have also analyzed flank distances using measured values (Figure 4.11) to avoid fitting errors. The average flank distance scaling exponent is -0.20 over the range of our simulations, the exponent estimated from RS93 over $\pm 1\sigma$ range is -0.14, while PR95 again uses -1/6 (Table 4.3). The relative differences in the exponents are quite similar to those at the subsolar point. The flank distance scaling exponent from our simulations, however, lies closest to -1/6 for northward IMF and is smaller for southward IMF, opposite the trend seen for the subsolar distance. The RS93 scaling exponent is closest to -1/6 for southward IMF, and greater for northward IMF, also opposite of the trend for the RS93 subsolar scaling exponent. The trends for the flank exponent is the same for RS93 and our model, as the exponent in both models increases monotonically with B_Z at about the same rate, while PR95 shows no variation (Table 4.3).

A different ideal scaling exponent of -1/4 (-0.25) is expected theoretically deeper in the tail if magnetotail flux is assumed to be constant and lobe magnetic pressure is balanced by magnetosheath pressure, but may not be realized in the near-Earth tail where the lobe magnetic field strength falls off rapidly with X [Petrinec and Russell, 1993b]. The exponent calculated with the PR96 magnetotail model averaged over $\pm 1\sigma$ solar wind range is -0.22, showing a tendency to approach -1/4. This result agrees very well with the exponent $(-0.225 \pm .025)$ found by Lui [1986] from analyzing IMP 6 crossings of the magnetopause between 15 and 20 R_E in the tail correlated with simultaneous solar wind measurements. On the other hand, the average (measured) tail radius at $X = -20 R_E$ of our simulations scales with an exponent -0.17 (Table 4.3), shows no tendency to approach -1/4. Unlike the subsolar

and flank distance, the average value of this exponent in the tail remains very close to the ideal Chapman-Ferraro exponent (-1/6). This difference in exponents accounts for the somewhat larger variations in tail radius with pressure when PR96 is compared with our model. The average RS93 exponent (-0.07) reflects much less variation with pressure than our model over the $\pm 1\sigma$ solar wind range (see Section 4.7).

4.10 Variation with IMF B_Z

We now examine the variation of magnetopause size and shape with B_Z, and find a linear relationship with B_Z for most quantities. Figure 4.19a shows the variation of subsolar distance with B_Z plotted at each pressure level. Each curve is roughly linear, but the slope decreases as pressure increases, as in RS93. Both models also have the same gradient ($\sim 0.24 R_E$ / nT) at the average dynamic pressure of 2 nPa. The average gradient in RS93, however, decreases more strongly with P_D over the range of our model (from 0.55 to 0.12 R_E / nT) than does our model (0.34 to .09 R_E / nT) . The reduced slope at higher pressure is close to that estimated by *Rufenach et al.* [1989] for geosynchronous magnetopause crossings (.08 R_E / nT) at much higher pressures.

When we average these values over the $\pm 1\sigma$ range of pressure (1, 2, and 4 nPa), and perform a linear regression with B_Z (Table 4.4), the resulting curve is linear (Figure 4.19b) with a correlation coefficient of 0.99. Independent fits for northward and southward IMF would produce little difference in slopes, indicating a very uniform gradient with B_Z across both IMF polarities. This curve agrees quite well with PR95 for southward IMF, but diverges for northward IMF. The overall range of RS93 agrees with our model giving about the same average slope.

The variations of the pressure-averaged fitted flaring angle with B_Z in the meridian, equatorial and average planes are all roughly linear (Figure 4.20 and Table 4.4). The slopes are quite different, reflecting the strong flaring in the meridian plane, but very little flaring in the equatorial plane. The curves intersect near $B_Z = 2$ nT, where the uniform flaring angle produces a roughly axisymmetric magnetotail. Independent fits for north and south IMF would produce little change in the slope in the meridian plane, but in the equatorial plane separate fits would produce a somewhat steeper slope for southward IMF and a flatter slope for northward IMF.

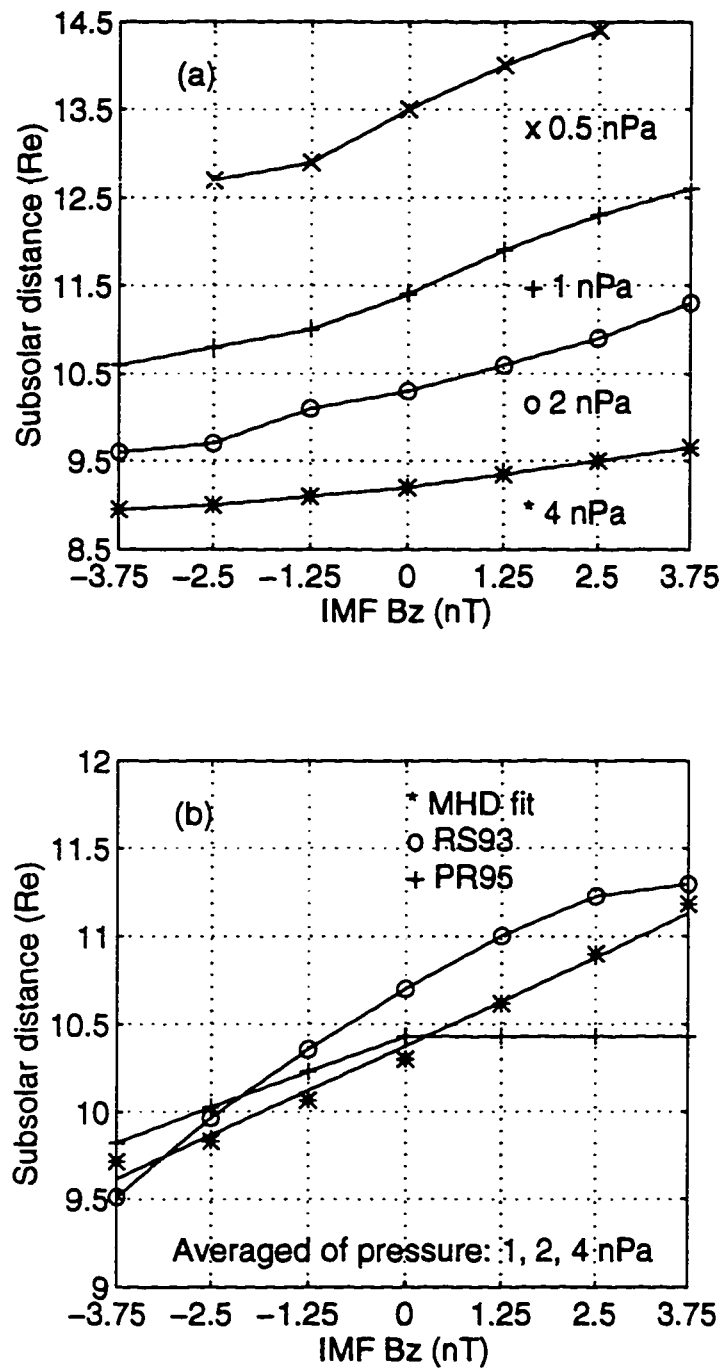The flaring angle from RS93 is $\sim 2°$ less than in our model all across B_Z, with a re-

Figure 4.19: (a) Subsolar distance measured in the MHD simulations are plotted versus IMF B_Z at each of 4 pressure levels. (b) Subsolar distance from MHD simulations averaged over dynamic pressures of 1, 2, and 4 nPa (*) with linear fit. Subsolar distances averaged over the same pressures are shown for the RS93 model (o) and the PR95 model (+).

Table 4.4: Linear Fits with IMF B_Z.

| Quantity	Plane	Intercept at $B_Z = 0$	Slope	Percent Change per nT	Correlation Coeff.
Measured Distances (R_E)		R_E	R_E / nT	%	
Subsolar		10.38	+0.20	+1.95	0.994
Flank ($X = 0$)	Average	15.21	-.0067	-0.28	0.810
Flank ($X = 0$)	Polar	15.25	-0.33	-2.16	0.991
Flank ($X = 0$)	Equatorial	15.16	+0.24	+1.61	0.995
Tail ($X = -20$)	Average	24.02	-0.38	-1.60	0.912
Tail ($X = -20$)	Meridian	25.56	-0.96	-3.82	0.984
Tail ($X = -20$)	Equatorial	22.47	+0.21	+0.93	0.774
Fitted Flaring Angle (deg.) at $X = 0$		deg.	deg. / nT	%	
Flaring Angle	Average	34.3	-0.78	-2.26	0.994
Flaring Angle	Polar	35.5	-1.32	-3.72	0.997
Flaring Angle	Equatorial	33.1	-0.23	-0.70	0.951
Ratios of Distances			nT^{-1}	%	
Flank Subsolar Ratio	Average	1.468	-.032	-2.15	0.998
Flank Subsolar Ratio	Polar	1.476	-.059	-3.97	0.999
Flank Subsolar Ratio	Equatorial	1.460	-.0046	-0.31	0.903
Merid. Equat. Ratio	$X = 0$	1.010	-.052	-3.67	0.998
Merid. Equat. Ratio	$X = -20$	1.141	-.037	-4.56	0.999
Merid. Equat. Ratio	$X = -40$	1.081	-.047	-4.35	0.972
Products of Distances (R_E^2)		R_E^2	R_E^2 / nT	%	
Dayside projection	Average	159.2	2.70	1.70	0.976
Dayside projection	Equatorial	159.1	5.78	3.64	0.994
Dayside projection	Meridian	159.3	-0.38	-0.24	0.495
Tail cross-section	Dawn-dusk	733	-4.67	-0.69	0.844
Tail cross-section	$X = -20$	1816	-52.8	-2.90	0.911
Tail cross-section	$X = -40$	2690	-120	-4.45	0.975
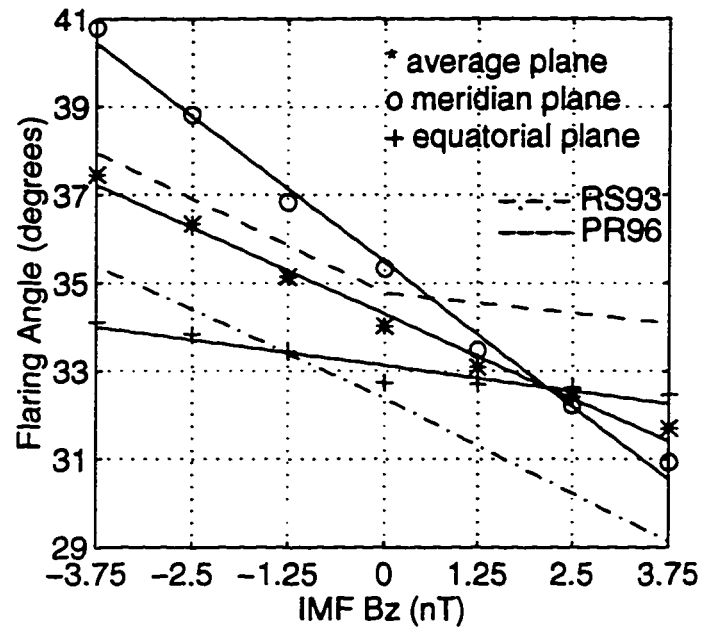
Figure 4.20: The flaring angle at $X = 0$ averaged over dynamic pressure and plotted against B_Z. Solid lines show linear fits to values from predictive magnetopause model in noon-midnight meridian plane (o), equatorial plane (+), and at a clock angle of 45°, the average plane (*). The averaged flaring angle from RS93 (dash-dot line) and PR96 (dashed line) are also shown.

markably similar slope. PR96 and our model are in excellent agreement for southward IMF, but diverge somewhat for northward IMF due to different slopes. Some of the difference with RS93 may be due to curve fitting. Our model was constructed using mostly nightside measurements, which produces a larger α to capture tail flaring but creates slightly larger errors on dayside from the lower resulting curvature. RS93 was constructed using many more dayside measurements, which gives a higher dayside curvature but causes the magnetotail to curve back toward the axis where there are relatively few measurements. The PR96 model is calculated by another method and the curve has a different mathematical form, so this agreement for southward IMF is a good indicator of that the variation of flaring angle with B_Z is well estimated by all models for southward IMF.

Figure 4.21a shows the variation of the measured polar, equatorial, and average flank distances with B_Z. We see that the variations in both the meridian and equatorial planes is close to linear for both north and south IMF (Table 4.4). The measured points in these planes indicate very little difference in the rate of change with B_Z for both IMF polarities, while the approximate independence from B_Z of the average flank distance (Section 4.6) is indicated by a slope an order of magnitude less. The flank distance averaged over pressure for RS93 and PR95 are slightly smaller than our average value. Both our average flank distance and that of RS93 show a slight decrease as B_Z increases, while PR95 is specified to be independent of B_Z.

Figure 4.21b shows axial distances measured in the simulations at $X = -20R_E$. Unlike the roughly equal slopes in Figure 4.21a, the slope in the meridian plane is much larger than that in the equatorial plane (Table 4.4). This means that the average tail radius at 20 R_E decreases significantly with B_Z instead of being nearly independent of B_Z as at the terminator. The curves intersect near $B_Z = 2.5$ nT indicating a roughly circular magnetopause cross-section at this position in the magnetotail for this IMF. The measured values indicate that separate fits for north and south IMF would produce somewhat different slopes. The average tail radius at 20 R_E from RS93 and PR96 are close, but generally a bit less than our average radius. A decrease with B_Z is seen in our model, RS93, and PR96 for southward IMF. The rate of decrease for northward IMF is smaller in our model and PR96 and somewhat larger in RS93.
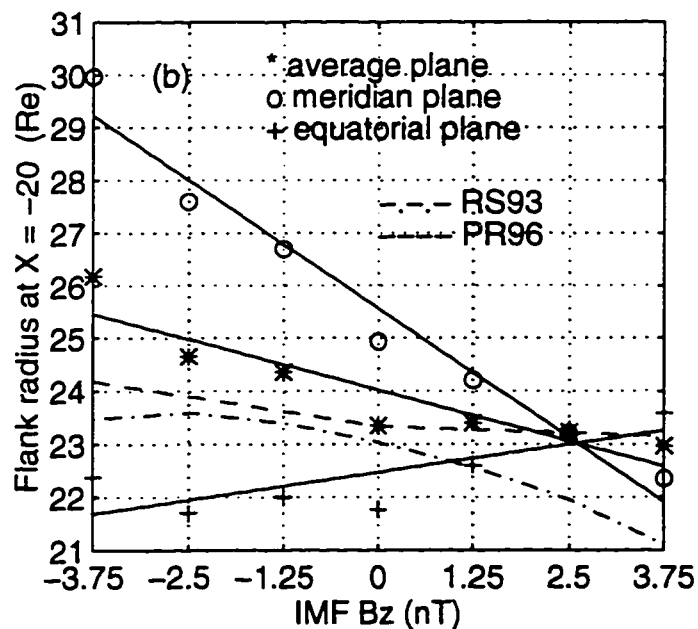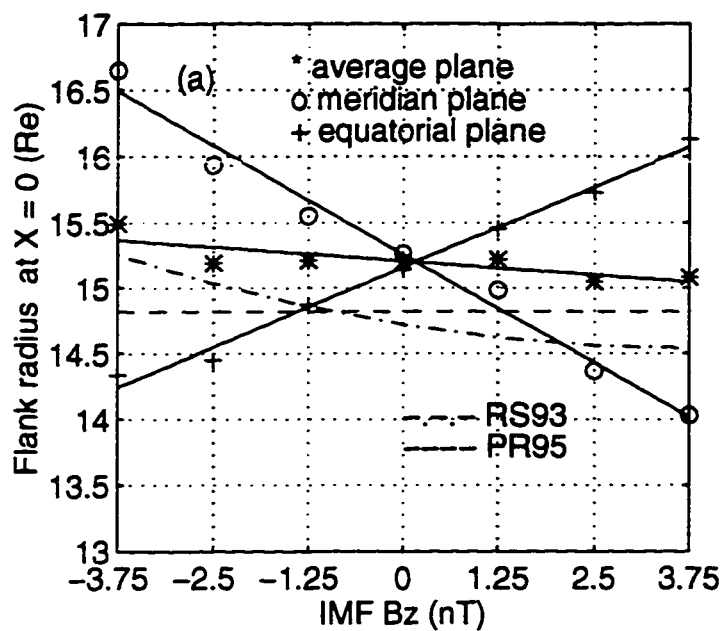
Figure 4.21: (a) Flank distance measured in MHD simulations at $X = 0$ averaged over dynamic pressure and plotted against B_Z. MHD simulation results are compared with empirical models, in the style of Figure 4.20. (b) Same, except at $X = -20R_E$.

4.11 Signatures of Asymmetry

We now investigate how these B_Z variations in subsolar, flank and tail distances produce changes in the shape and size of the magnetopause on both the dayside and nightside. Since both the subsolar distance and average flank distance scale with pressure in about the same way, their ratio is essentially independent of dynamic pressure. Since the flank to subsolar ratio ($R_{flank}/R_{subsolar}$) depends only on B_Z, it is an ideal parameter for studying changes in shape produced by the action of IMF B_Z (flaring). Figure 4.22a shows the linear variation with B_Z of the flank to subsolar ratio in the meridian, equatorial and average planes. Strong flaring in the meridian plane causes the ratio range from 1.70 to 1.26. In the equatorial plane, where there is almost no flaring, the ratio is very uniform (near 1.46). This ratio is close to that derived from conic fits using only points near the equatorial plane (~ 1.4) by both *Fairfield* [1971] and *Holzer and Slavin* [1978]. The flank to subsolar ratio for the average ellipse varies significantly with B_Z, however, between 1.35 and 1.59.

The average ratio calculated from PR95 is a bit less than our average ratio for southward IMF, but has a similar slope. Conversely, the slopes are different for northward IMF, but the average values are more similar. Our ratio averaged over B_Z (1.47) is very close to the average (1.46) of ratios for north (1.50) and south (1.42) IMF from the original fits in *Petrinec et al.* [1991]. The flank to subsolar ratio calculated with RS93 varies a bit more than our model (from 1.29 to 1.60), and has a steeper slope for southward IMF, overall matching our model about as well as PR95.

The area of the dayside magnetosphere projected onto a plane including the X axis can be studied using the product of the subsolar and flank distance, i.e. $Area = kR_{subsolar}R_{flank}$, where the proportionality constant k depends on the exact shape of the projected dayside magnetopause. We could use the elliptical cross-sections of our least squares fits, but using measured values from the simulations avoids fitting errors that may obscure the trends with B_Z. We again see linear variations with B_Z in the projected dayside areas in the equatorial, meridian, and average planes, as indicated by the product of subsolar and flank distances (Figure 4.22b, Table 4.4). The strongest variation with B_Z is now in the equatorial plane, while there is very little change with B_Z in the projected area in the meridian plane (neglecting the indentation from the cusp). This indicates that flaring in the meridian planes by draping of magnetic field lines over the pole operates in such a way as to

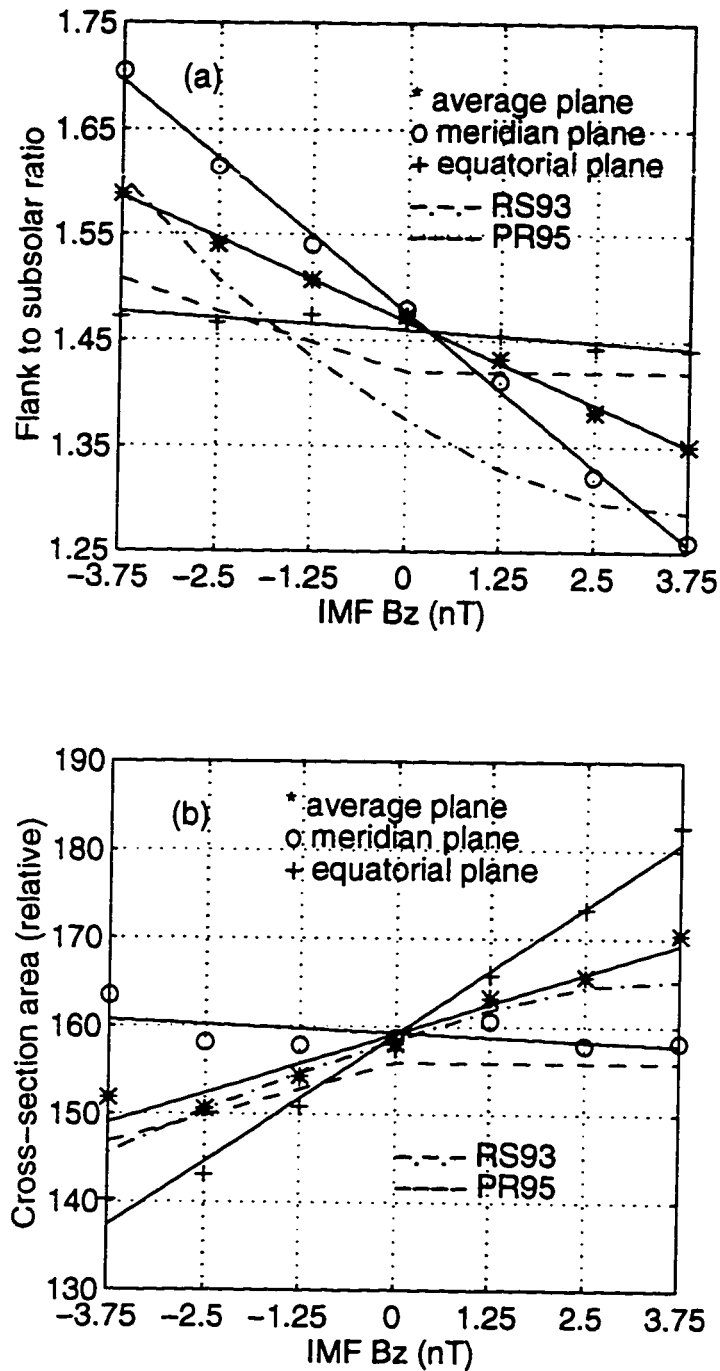Figure 4.22: Shape and area parameters for dayside magnetopause. (a) Ratio of flank $(X = 0)$ to subsolar distances averaged over dynamic pressure and plotted against B_Z, in the style of Figure 4.20. (b) The projected area of the dayside magnetopause, estimated by the product of the flank $(X = 0)$ and subsolar distances, averaged over dynamic pressure and plotted against B_Z, in the style of Figure 4.20.

roughly conserve the projected dayside area at a fixed dynamic pressure. This approximate independence from B_Z of the projected meridian area is also manifested by the limited movement of the crossover point in the families of meridian plane ellipses (Figure 4.14). The projected dayside area in the average plane of our model matches that of RS93 quite well for both northward and southward IMF, and matches PR95 very well for southward IMF, but diverges somewhat for northward IMF.

Changes in the projected dayside equatorial area for a fixed pressure are proportional to changes in the dayside magnetic flux, since the magnetic field magnitude at the magnetopause changes little [*Holzer and Slavin*, 1978]. Our linear variation in equatorial area indicates that magnetic flux erosion (or enhancement) on the dayside is proportional to B_Z with the same proportionality constant for northward and southward IMF. This result is generally consistent with those of *Holzer and Slavin* [1978], who found both expansions and contractions of the dayside magnetosphere of about the same magnitude from flux erosion, observable when scaling distances by dynamic pressure. Dayside expansion was linearly related to the time-integrated AL index, which is believed to indicate net flux return to the dayside and which typically declines to low values an hour or more after IMF B_Z becomes positive [*Holzer and Slavin*, 1978]. They also found only a loose correlation, however, between the amount of contraction on the dayside with the reconnected magnetic flux. The latter was estimated by the applied flux [*Levy et al.*, 1964], a time integral involving negative B_Z which is believed to indicate the amount of dayside magnetic reconnection and flux transfer to the magnetotail [*Burch*, 1974]. They attributed this discrepancy to flux returning to the dayside, since the reconnected flux (measured by applied flux) may significantly exceed the net eroded flux (as gauged by the scaled magnetopause crossings) [*Holzer and Slavin*, 1978].

The fractional change of the subsolar distance with B_Z is close to that for the equatorial (polar) distance with the same (opposite) sign (Table 4.4), leading to the rough conservation of magnetopause shape (projected area) in the equatorial (meridian) plane. Likewise, cross-sectional area is also almost conserved in the dawn-dusk plane (Figure 4.23a) by fractional changes in the polar and equatorial flank distances of similar magnitudes with the opposite signs (Figure 4.22a). Further down the tail, however, the fractional rates of change are much different in magnitude (Figure 4.21b), resulting in a significant change in tail cross-sectional area with B_Z (Figure 4.23a).

Besides agreeing with the empirical models, this decrease in area is also generally consistent with the study of *Maezawa* [1975], who found that the average magnetotail radius increased (decreased) by similar amounts during the period 1-2 hours before (after) the expansion phase onset of a magnetospheric substorm, although substorm phases are not necessarily correlated with B_Z in a simple way. This decrease in area (and hence magnetic flux) with B_Z is expected for southward IMF, which produces net dayside flux erosion and increases flux in the magnetotail. The linear decrease for northward IMF may be due more to changes in net convection of flux to the dayside than to magnetic reconnection past the cusp, which is limited to a rather narrow width in Y and presumably transfers much less flux than dayside reconnection with a wide reconnection zone.

The ratio of the axial distances in the meridian plane to the equatorial plane also indicates net asymmetry. Figure 4.23b shows this ratio at three positions (0, 20, and 40 R_E in the tail). At the terminator the ratio varies linearly with B_Z in such way that the net asymmetry is only $\sim 1\%$, consistent with the results of *Formisano et al.* [1979]. Deeper in the tail, however, the relationship is still roughly linear, but there is a net asymmetry of $\sim 14\%$ at 20 R_E. This asymmetry decreases somewhat, to $\sim 8\%$ at 40 R_E, but the linear fit is not as good, presumably due to scatter in the measurements at this position. This net asymmetry is a bit weaker than that indicated by the results of *Meng et al.* [1980] ($\sim 23\%$), but much stronger than the results of *Hammond et al.* [1994] ($\sim 2\%$) using data where the magnitude of dipole tilt was less than $5°$.

4.12 Summary and Conclusions

We have developed a predictive magnetopause model based on the magnetopause self-consistently produced in 3-D global MHD simulations for different combinations of dynamic pressure and IMF B_Z. A hot plasma population simulates the effects of the ring current and is needed to accurately predict the subsolar magnetopause position. Three diagnostics (current magnitude, magnetic field line mapping, and thermal pressure), were needed to unambiguously identify the magnetopause at all positions in the noon-midnight and equatorial planes. The magnetopause in each plane is fitted by least squares to an ellipse described by three physical parameters: the subsolar point, the flank distance and the flaring angle (both at $X = 0$). Inter-
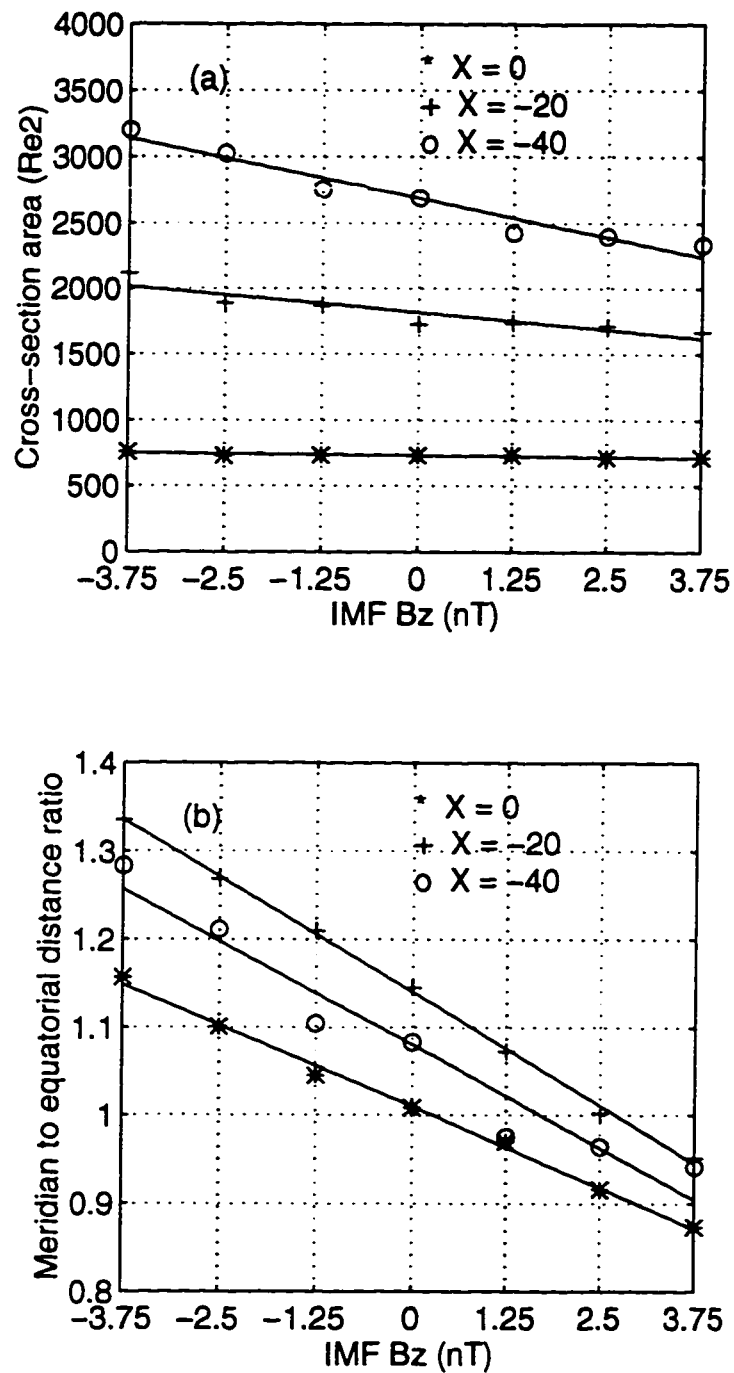
Figure 4.23: Shape and area parameters for magnetotail. (a) The cross-sectional area of the MHD simulation magnetotail, averaged over dynamic pressure and plotted against B_Z. (b) The ratio of the distance to the magnetopause in the meridian plane to the distance in the equatorial plane. Linear fits of the area to B_Z are shown at $X = 0$ (*), at $X = -20$ (+), and at $X = -40$ (o).

polation by clock angle gives a fully 3-D, non-axisymmetric magnetopause surface to 40 R_E in the tail for a given dynamic pressure and IMF B_Z.

Our model is inherently asymmetric. Our meridian plane ellipses are very flared due to magnetic flux erosion while the equatorial ellipses show no flaring. The magnetotail surface departs the most from axial symmetry for southward IMF B_Z and is most nearly axisymmetric for moderate northward IMF of 2.5 nT. Unlike the magnetotail, approximately circular cross-sections are seen at the terminator when IMF B_Z is near zero while the dayside is most symmetric for southward IMF. These characteristic asymmetries for the dayside, tail, and terminator are consistent with a number of empirical studies. They can be explained by the linear variation with B_Z of the subsolar, flank and tail distances in the meridian and equatorial planes for both northward and southward IMF, variations driven changes in both the magnetic reconnection rate and the return of flux to the dayside by convection. Magnetopause shape is roughly conserved in the dayside equatorial plane for changes in B_Z, while projected magnetopause area is conserved in the dayside meridian plane. Cross-sectional area is conserved in the dawn-dusk plane but not in the tail, so that the average tail radius is approximately independent of B_Z only at the terminator. The mean meridian distance exceeds the mean equatorial distance in the tail by as much as 14%, but they are nearly equal at the terminator.

Despite this strong asymmetry, our magnetopause model when averaged agrees with the empirical models to a remarkable degree. Our average ellipses, interpolated for a clock angle of 45°, flare in the tail with B_Z about as much as those in RS93 and twice as much as PR96. Variations with dynamic pressure on the dayside and nightside follow a power law with an exponent near -1/6 or slightly smaller, and are closer to those in PR95/PR96 than RS93. Our subsolar point moves linearly for both northward and southward IMF, agreeing both qualitatively and quantitatively with RS93 for all IMF, but with PR95 only for southward IMF. Averages of the flaring angle, flank and tail radius, flank to subsolar ratio, and cross-sectional area also vary linearly with B_Z and generally are in good agreement with the empirical models.

Our global simulation based model is roughly as accurate as the empirical models, in both average and rms errors. The steady state solutions used to construct the model do not display large amplitude transient magnetopause motions that may result from pressure pulses, flux transfer events (FTE's), and plasma instabilities (e.g., Kelvin-

162

Helmholtz). Nonetheless, when tested against data bases containing large numbers of magnetopause crossings, the model was able to predict the position to within about 1 R_E on the dayside and about 2 R_E on the nightside. The ideal conditions of the simulation also lack dipole tilt, IMF B_Y and B_X, and other variables which are always present in the data sets and may systematically affect magnetopause shape. Some of these variables can be easily incorporated into our global magnetospheric simulations, forming the basis for further parametric studies on their effects on the magnetopause and refinement of the present predictive magnetopause model.

Chapter 5

CONCLUSIONS AND FUTURE WORK

5.1 Summary and Conclusions

The previous two chapters have given examples of quantitative magnetospheric modeling studies using global magnetospheric models. Chapter 3 presented a 2-D study of magnetic field line mapping and auroral currents in the noon-midnight meridian using a modified fluid approximation. This study demonstrated that although the neutral line in the magnetotail may at times lie as close as 13 R_E, the long term average position exceeds 40 R_E. Chapter 4 presented a 3-D study that produced a predictive magnetopause model and was used to study the average three-dimensional shape of the magnetopause. The 3-D study was able to demonstrate the asymmetry of the magnetopause on average and quantify how this shape departs from axisymmetry with IMF B_z. These are new applications of the global magnetospheric models, while previous applications of global models over the last decade have mostly concentrated on qualitative studies of the magnetosphere.

The studies presented here used both the standard MHD description of the plasma (Chapter 4) and a modified fluid approximation that describes some kinetic effects missing in MHD (Chapter 3). This MPD formulation was able to produce additional field-aligned currents in the noon-midnight meridian present in observations [*Potemra*, 1994], but absent from MHD models. As described in Chapter 1, the magnetosphere quite often does not obey the physical conditions necessary for the MHD approximation: plasma pressure is generally not isotropic in collisionless regions, and the Hall and pressure gradient terms in the generalized Ohm's law are often not negligible. The study of space plasmas with formulations other than MHD is critical for understanding the magnetosphere, because the plasma so often is not well described by MHD and non-MHD effects should be widespread, even on the large space and time scales of MHD. The MPD formulation was only possible because it is requires only a third more computer memory than the equivalent MHD simulation. However, as computation performance increases in the future, more sophisticated formulations

that include kinetic effects will become possible.

Both studies employed comparisons with empirical models, which were critical for establishing confidence in the modeling. This included the T89M magnetic field model [*Tsyganenko*, 1989] in Chapter 3 and the RS93 [*Roelof and Sibeck*, 1993] and PR95/PR96 [*Petrinec and Russell*, 1995b, 1996] magnetopause models in Chapter 4. Some aspects of the modeling which did not agree well with the observations, e.g. the magnetopause shape produced by the 2-D simulation, were subsequently discounted because they could not pass this important test. Likewise, the good agreement of the average magnetopause with the empirical models meant further studies of asymmetry were not moot exercises. This led to simple behavior with IMF B_Z being discovered in the simulations, which is credible for two reasons, (1) because it agrees with specific results of previous empirical studies that do not assume axisymmetry and (2) because when averaged the magnetopause model generally reproduces empirical model results.

Both of these studies also employed new methods for analyzing the output of the global models. Time-averaging over a relatively long time interval (3 hours) was used in the 2-D study, and was found to provide a better comparison with ensemble-averaged spacecraft data. This methodology could also be applied to 3-D studies with the extra advantage that the properties peculiar to 2-D models (such as the 2-D dipole and lack of divergence in the noon-midnight meridian plane) would be absent. This should make the comparison with data even better, although the comparison showed the 2-D model was better than might be expected. The new methodology in the 3-D study was the derivation of a predictive magnetopause model with a mathematically simple form similar to the empirical models, in which average model measurements took the place of actual spacecraft observations. The successful comparison with empirical models and the demonstration that the predictive model was as accurate as the empirical models validates this methodology. In addition, the idealized conditions of the simulation make it possible for simulation-based models to go beyond empirical models. The formulation of new and different ways to study the output of global simulations is a critical part of extracting additional information from these simulations.

5.2 Improvements to These Studies

Here we present ideas for further work on the studies presented in Chapter 3 and 4. The 2-D model provided a stepping stone to the subsequent 3-D modeling. Possible future 2-D studies, which permit much smaller grid spacing, include high resolution simulations of the magnetosphere, which have been done for specific regions of the magnetosphere [*Wei et al.*, 1990; *Shi et al.*, 1991]. These models also provide a good means to test the effects of incorporating different kinds of physics into the simulations, such as different formulations for plasma resistivity.

An obvious extension is to use the new methodology in 3-D models, both the MPD formulation and the time averaging methodology. Such a static average magnetospheric configuration averaged over a longer timescale performed with a 3-D model should provide a better comparison with the 3-D empirical models and ensemble-averages data. Static averages of the tail current and other magnetic field features could be compared to that given by empirical models such as T89M or the newer T95 [*Tsyganenko*, 1989, 1995a]. Magnetic field line mapping comparisons of a 3-D model with T89M and Reduced Tail T89M have already been performed by *Winglee* [1995], but these are done with "snapshots" not time-averaged configurations. The average B_Z values at different positions in the tail and the location of the neutral line could be compared to ensemble averaged data, such as *Fairfield* [1986]. Three-dimensional simulations using the modified fluid approximation have been conducted by *Winglee* [1995] and *Winglee et al.* [1996], and represent an important attempt to go beyond the MHD description of the magnetosphere. MPD is found to produce additional field-aligned currents in these studies that supplement the MHD field-aligned currents.

The magnetopause model presented in Chapter 4 could be refined with further work (1) to extend the model range, (2) to extend the number of predictive variables, and (3) to make improvements in the derived predictive model, with all but the first generally decreasing rms errors. The parametric range of the model could be extended by running additional cases to cover a larger fraction of the solar wind conditions. The model used for the simulations in Chapter 4, however, did not provide steady-state solutions at larger southward and northward IMF values, making such an extension difficult. Higher dynamic pressure runs at 8 nPa with -5 nT $\leq B_Z \leq +5$ nT would be the most likely simulations to provide steady-state solutions.

The rms errors can possibly be decreased significantly by adding more solar wind and terrestrial variables to the list of predictive model parameters. In particular, dipole tilt would be expected to produce changes in magnetopause position of $1-2R_E$ in the tail, and so its inclusion would likely reduce the rms errors of the predictive model. As shown in Chapter 4, the use of magnetopause crossings with tilt angle magnitudes less than $10°$ reduced rms errors in position by about 10%. Dipole tilt has been added to the simulation model and some preliminary results were presented in *Elsen and Winglee* [1995].

Figure 5.1 plots the magnitude of the electrical current for cross-tail cuts at $X = -20R_E$ with no tilt and a tilt of $20°$. The cross-tail current sheet is now diplaced upward (north) about 3 R_E and is warped in the Y direction. The northern magnetopause is displaced upward in the noon-midnight meridianby about 1 R_E, but the southern magnetopause is displaced by twice as much. The movement of the magnetopause in the noon-midnight meridian was found to be in general quantitative agreement with two other studies incorporating tilt, i.e. the empirical model of *Hammond et al.* [1994] and the theoretical calculations of pressure balance surfaces using relaxation methods by *Sotirelis* [1995]. The lobes are no longer symmetric in shape, but are also distorted. However, they have approximately the same cross-sectional area since they contain the same amount of magnetic flux. Due to the bifurcation of current it is even more difficult to estimate the magnetopause position in the equatorial plane when dipole tilt is present. The pressure trough is no longer easily imaged in two dimensions, as in Chapter 4, because it is also warped and mcuh of it lies outside the equatorial plane. This makes it more difficult to use pressure contours as a diagnostic of the magnetopause near the nightside equatorial plane, so that the limit of closed magnetic field may be the only reliable indicator of magnetopause position.

Other variables, such as IMF B_Y or density could also be added to the parameter set, but the minor potential improvements to the magnetopause model might not be worth the computational effort that results from a large increase in the number of simulated cases from an expansion of the parameter set. However, simulations varying only one variable while all others are kept constant could still gauge the effect of that variable on the magnetopause, even if the magnetopause model was not refined by that variable's inclusion.

Improvements can be made to the magnetopause fitting procedure, including (1)
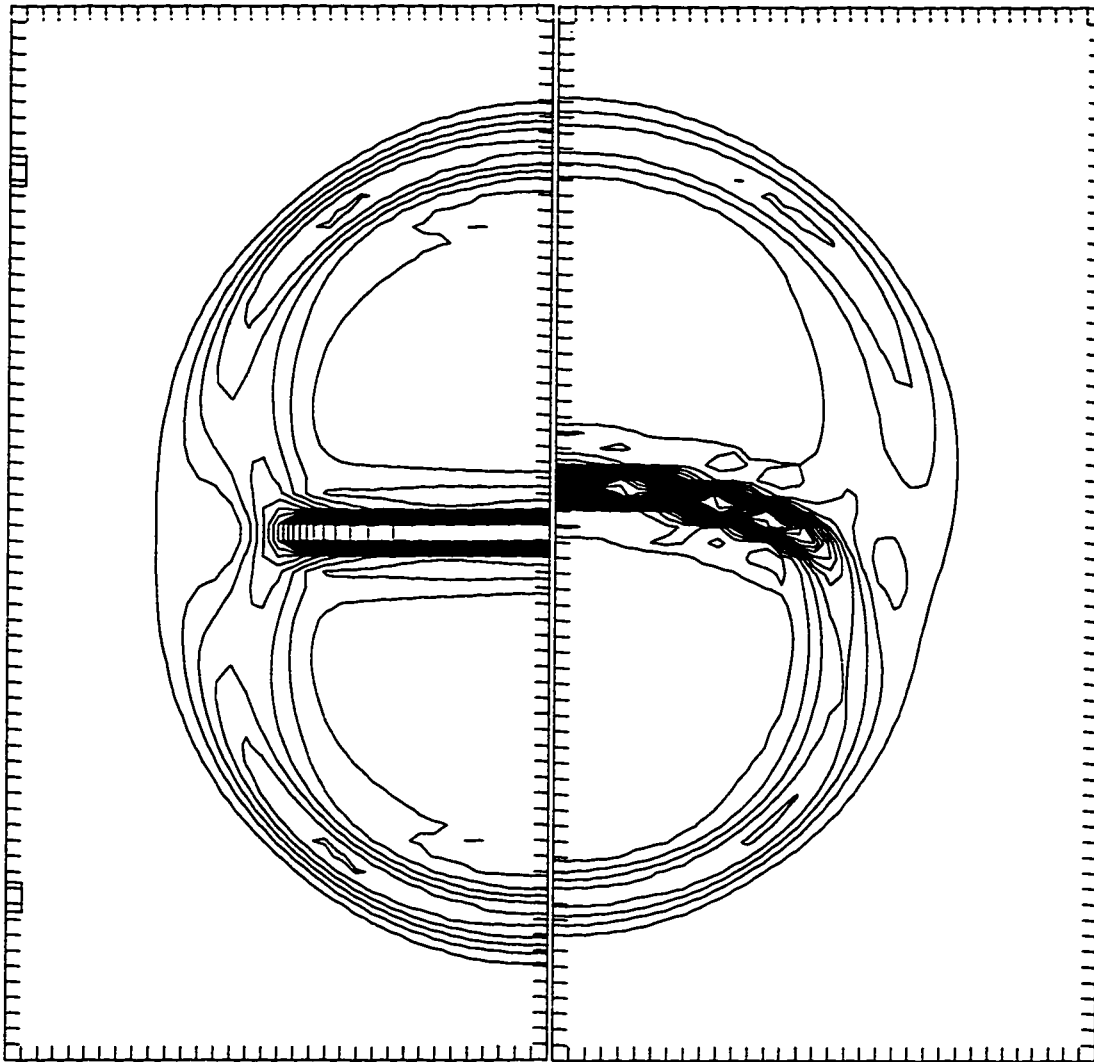
Figure 5.1: Cross-section of magnetotail shown by electric current at $X = -20R_E$ with and without dipole tilt. The tick marks indicate grid spacing, set to 1.0 R_E. The solar wind dynamic pressure is set to 2.0 nPa and there is no IMF. The left panel shows the magnitude of electric current when dipole tilt was set to zero, as in Figure 4.6. The right panel shows the current for a dipole tilt angle of 20°. The cross-tail current sheet and return current outline the magnetotail lobes.

improving on the elliptical approximation, (2) incorporating the cusp, (3) improving measurements from the simulations. A curve other than an ellipse might provide a better fit to magnetopause surface produced in the simulations. The magnetopause surface produced in the simulations was much more curved on the dayside than the nightside, so separate dayside and nightside curves that were still continuous might provide a better fit to the simulations and possibly reduce errors. The cusp was also ignored to produce our smooth magnetopause surface, but this can produce errors of $\sim 1R_E$ at high latitude locations [*Petrinec and Russell*, 1995b]. The cusp indentation may be more easily approximated as a localized perturbation to the magnetopause surface rather than fitting to a more complicated mathematical expression to describe the magnetopause surface. Magnetopause measurements were made with a ruler on contour plots of the simulation, a method that is both laborious and prone to measurement bias. Magnetopause diagnostics (such as current, field line mapping, and pressure trough) can be improved so that the magnetopause measurements are automated, both saving labor and reducing bias.

5.3 Improvements in the Global Simulations

5.3.1 Numerical improvements

There are also a variety of numerical improvements that can be made to the global simulations, but resulting improvements to the magnetopause model would probably be relatively minor, since the predictive model is already fairly accurate. Potential improvements in numerical methods include (1) using non-uniform gridspacing, (2) implementing other numerical algorithms, and (3) guaranteeing the zero divergence of the magnetic field. Although these are currently areas of active numerical research, and potentially may produce significant improvements in global magnetospheric simulations, these methods were not investigated for this dissertation and so will only be discussed briefly.

Reducing the total number of gridpoints with non-uniform gridspacing can give higher resolution in the simulations in regions where desired (e.g., the magnetopause or tail current sheet) by using large gridspacing at places where not needed, e.g. in the solar wind and magnetosheath portions of the simulation. Non-uniform gridding has been implemented in the *Fedder and Lyon* [1987] model with cylindrical geometry,

in the *Raeder* [1994] model with Cartesian geometry, and has also recently been implemented the *Winglee* model used for the simulations of Chapter 4 with a Cartesian geometry.

Two new global models presently under development use "adaptive" gridding, a non-uniform gridspacing that is not fixed, but dynamically changes according to numerical criteria, automatically producing finer gridding in regions where it is most needed. The model of *Spicer et al.* [1996] uses tetrahedral cells, any of which can be split into four more tetrahedra by bisecting each leg of the tetrahedron [see *Zalesak et al.*, 1993]. Resolution of 0.1 R_E is achieved in critical regions such as the magnetopause and the tail current sheet through successive splitting, while the total number of gridpoints is similar to that in other global models which can only achieve a resolution of 0.5 to 1.0 R_E. The model of *Gombosi et al.* [1995] uses cubic cells, which when bisected produce eight more cubes and can also be split *ad infinitum* [see *De Zeeuw and Powell*, 1992]. Unlike the time-dependent models dicsussed in this simulation, this is actually a steady-state global model, but the gridspacing is refined through successive iterations. Non-uniform gridspacing is discussed in several texts on numerical methods.

A numerical algorithm less diffusive than two-step Lax-Wendroff could also be implemented in the model, but the improvements might prove to be rather modest. Thinner shock fronts and current sheets may be resolved, but the reconnection rate (which depends on numerical noise) may not be significantly affected, so that there may not be large changes in the global magnetospheric configuration. As discussed in Chapter 2, most of these algorithms will be slower and require more memory than Lax-Wendroff, their implementation could take a considerable effort, and they might not be as robust. Many suitable algorithms are available in a vast published literature, many of which are given in texts such as *Press et al.* [1986] and *Richtmyer and Morton* [1967]. For example, the Runge-Kutta-Gill method used by *Watanabe and Sato* [1990] would be straightforward to implement.

Another improvement to the simulations concerns the small numerical errors that result from finite differencing methods that sometimes can make the magnetic field violate $\nabla \cdot \mathbf{B} = 0$. Unlike diffusiveness, this is a numerical problem peculiar to MHD and other magnetic fluid simulations. A non-zero divergence of $\mathbf{B}$ not only violates Maxwell's equations, but can produce an anomalous force parallel to the magnetic

field as well [*Brackbill and Barnes*, 1980]. This anomalous force can be large if the conservative form of the momentum equation is used involving the divergence of the Maxwell stress tensor (see Chapter 2), but is not as large if the nonconservative form involving $\mathbf{J} \times \mathbf{B}$ is used, so that the resulting errors are usually small enough to be tolerated [*Ramshaw* [1983]. The global simulation methodology begins with a dipole field, which identically satisfies the initial condition $\nabla \cdot \mathbf{B} = 0$. Additional magnetic field generated by the induction equation has a solenoidal form, so that the total field should have no divergence as it evolves in time, but in practice numerical errors create a finite amount of divergence in the magnetic field and can grow as the simulation evolves in time.

Various numerical methods have been developed which try to minimize this error, but many of these methods can be computationally expensive in terms of the reduction in errors they produce [*Evans and Hawley*, 1987 and references therein]. These methods include: (1) using the vector potential $\mathbf{A}$ in place of the magnetic field $\mathbf{B}$ in the MHD equations, so that $\mathbf{B} = \nabla \times \mathbf{A}$ is automatically solenoidal, a method which has been developed by [*Dorfi*, 1986]; (2) "divergence cleaning" which involves solving Poisson's equation to find a scalar potential over the simulation gridspace that exactly cancels out the divergence error [*Ramshaw*, 1983], a method that is very computationally intensive; (3) a far simpler method that roughly cancels out errors using an artificial source term $-(\nabla \cdot \mathbf{B})\mathbf{V}$ in the electromagnetic induction equation [*Schmidt-Voigt*, 1989]; and (4) the "constrained transport" (CT) method developed by *Evans and Hawley* [1987], a promising method that is not computationally intensive and does not introduce artificial (non-physical) numerical terms, as in methods (2) and (3). The CT method has been implemented in the models of *Raeder* and *Fedder and Lyon*, but a critical review of this method is not available in the literature. The MHD fluid variables (momentum, energy, and mass density) are treated by standard methods, but the magnetic field generated through the induction equation is treated differently, by a method that guarantees that $\nabla \cdot \mathbf{B} = 0$ to machine roundoff error. The change in magnetic flux through each face of a finite-difference cell is instead calculated by summing the EMF around the closed contour given by the the edges of the cell. Although noticeable divergence errors were encountered in the 2-D simulations of Chapter 3, none of the above methods were used in the simulations performed for this dissertation, generally leading to the presence of small

finite divergence in the simulations which do not significantly affect the results.

We now discuss improvements in the physics of the global modeling. This includes (1) replacing the conducting shell inner boundary with a more sophisticated ionospheric model, (2) simulating the ring current, and (3) improving the plasmaspheric model.

5.3.2 Ionospheric models

The ionosphere was simulated with a conducting shell in both the 2-D and 3-D simulations performed for this dissertation, as was described in Chapter 2. The effective resistance of the ionosphere, which is mostly numerical in the conducting shell method, provides a load in which electrical currents can to dissipate energy in the ionospheric plasma from electrical currents, such as field-aligned currents generated in the global models outside of 3 R_E. Replacing the conducting shell approximation for the ionosphere with a physically more realistic ionospheric model is an improvement that has been implemented in global models [*Fedder and Lyon*, 1987; *Raeder et al.*, 1995]. This coupling of the ionosphere to the magnetosphere can possibly have a global influence on magnetospheric dynamics, especially in the magnetotail. While changing the model ionosphere would probably have relatively little affect on the position of the magnetopause, as determined in Chapter 4, it could have a significant effect some model features, e.g. the magnitude of field-aligned currents and the position of the neutral line in the magnetotail.

Fedder and Lyon [1987] terminated their MHD calculations near 3 R_E, as in previous modeling, but this inner boundary was coupled to a separate ionospheric model to help determine the inner boundary conditions. This method maps the field-aligned current generated by the MHD model down to a 2-D ionospheric model at 1R_E, which describes the ionosphere through a 2-D grid over the polar caps with a height-integrated conductance tensor [*Kamide and Matsushita*, 1979]. Such an ionospheric model may include a large number of variables as input, including empirical parameters, e.g. as in the ionospheric model of *Rasmussen and Schunk* [1987] that accounts for ionization by several independent sources (solar EUV radiation, precipitating electrons associated with upward field-aligned currents, and diffuse electron precipitation). This means that the global magnetospheric models with this or other auxiliary models (e.g., ring current or plasmasphere) imposed are no longer strictly

self-consistent.

The ionosphere is treated statically in this method, since the ionosphere has a response time many orders of magnitude less than the magnetosphere and will rapidly reach a steady state condition for a given field-aligned current input in much less than the MHD time step of ~ 1 sec [Kelley, 1989]. Approximating the ionosphere at each time step as a steady state means the electrostatic potential consistent with the conductivity model and the incoming field-aligned current distribution is a solution to Poisson's equation, which must be determined at each time step. Once determined, this potential is then mapped back out to the boundary, and by setting $V_\perp$, the plasma velocity perpendicular to **B**, a convective electric field equal to the magnitude of the mapped ionospheric electric field is imposed at this boundary. As the simulation evolves in time, the MHD inner boundary and the ionospheric model will reach states that are consistent with each other.

While the original simulation [Fedder and Lyon, 1987] used a spatially uniform, scalar conductance constant in time to model the ionosphere, some later simulations use a ionospheric conductivity tensor which varies spatially and in some cases temporally [e.g., Fedder et al., 1995b]. This ionospheric model is also used in their other published simulations [Fedder and Lyon, 1995; Fedder et al., 1991, 1995a; Slinker et al., 1995; Chen et al., 1995]. A similar ionospheric model has also recently been integrated into another global MHD model [Raeder, 1994; Raeder et al., 1995; Berchem et al., 1995; Frank et al., 1995], which uses much the same numerical methodology, but has a different conductivity model. Although the original implementation of Fedder and Lyon [1987] treated magnetic field lines as equipotentials, a non-zero electric potential drop along the field line can also be imposed between the ionosphere and inner boundary, so that the electric field at the inner boundary is modified relative to the ionosphere, e.g. using an empirical model.

Except for the determination of $V_\perp$, the boundary conditions used in the method of Fedder and Lyon [1987] are essentially the same as those described in Chapter 2 for the conducting shell method. (**B** is just set to the dipole value with no magnetic perturbation at the boundary, while the ionospheric model provides no additional information about plasma density and temperature at the inner boundary.) The parallel velocity component $V_\parallel$, which cannot be determined by this method, is still set to zero in the method of Fedder and Lyon [1987], and would require further

modeling for its determination. A non-zero value for this component, however, may be useful for simulating substorms since the plasma sheet after substorm recovery often contains significant amounts of plasma of ionospheric origin, indicative of mass flow up magnetic field lines [*Waite et al.*, 1985; *Moore et al.*, 1986; *Chappell et al.*, 1987].

5.3.3 Plasmasphere and ring current

The increased mass density used near the inner boundary in the simulations of Chapter 4 slows the Alfvén speed to plasmaspheric values while zeroing out velocity screens out the dawn-dusk electric field much the way the plasmasphere does. The inner boundary conditions are thus effectively simulating as the plasmasphere as well as the ionosphere. Enhanced plasma pressurization that varies with latitude was also used, a method that crudely simulates the ring current by accounting for the extra thermal energy of a tenuous hot plasma population. This addition was found to push the magnetopause out to observed distances, and during code development we also found it suppresses magnetic reconnection in the tail, two effects expected of the ring current. The density and pressure enhancements to the conducting shell ionosphere are the first steps toward creating independent plasmasphere and ring current models separate from the ionosphere model. Although an ionospheric model has been incorporated into the *Fedder and Lyon* and *Raeder* models, these models at the present time have not added separate ring current or plasmasphere models. For example, the empirical plasmasphere model of *Gallagher et al.* [1988] could be used to construct a possible plasmasphere model that could be integrated into the global simulations. The Gallagher model of the plasmasphere supplies plasma density and temperature for L shell and K_p, which could be converted to latitude and solar wind conditions, respectively.

The lack of a ring current is probably the most significant discrepancy in the global models [*Pulkkinen et al.*, 1995], which means the near-Earth current profile is significantly underestimated, unlike the empirical models. Likewise, the pressure gradient is observed on average to monotonically decrease from a few R_E [*Spence et al.*, 1989], but contrary to these observations, the global models have a tendency to produce a pressure maximum between 5 and 10 R_E that is probably related to the missing ring current. The lack of a ring current affects magnetospheric mapping and

means that a global simulations cannot at present be used to simulate a geomagnetic storm.

Plasma pressurization at the inner model boundary, as used in the Chapter 4 study, overcomes these deficiencies to some extent and also helps increase the subsolar distance in the simulations to their values inferred from observations. This pressurization is not self-consistently produced within the model, but is imposed, and is still a very crude way to represent the ring current. Unfortunately, the ring current is not easily incorporated into a single fluid model in a self-consistent way.

One possible method would be to introduce a large number of particles into appropriate regions of the model and allow them to drift in the model electric and magnetic fields, something that already has been done using a static snapshot of the magnetosphere simulation [*Richard et al.*, 1994]. In those studies, however, only the kinetic effects on these particles are studied and not the fields produced by particles. To simulate a ring current the electric current produced by these drifting particles could be fed back into the simulation and its effect on the global magnetic field and plasma could be studied. The number of particles, however, would have to be limited to tens of thousands by computational constraints so the current would have to be scaled up by an arbitrary factor so that such a simulation is no longer entirely self-consistent either.

A suite of auxiliary empirical models provides a way to input more data into a global model than just using the solar wind data, so that the model can be tailored with such input that attempts to simulate the concurrent state of the ionosphere, plasmasphere, and ring current. Successful incorporation of such models should improve the realism of the global magnetospheric models, since the states of the ionosphere, plasmasphere, and ring current may also depend on terrestrial variables and the recent history of the magnetosphere lacking in the solar wind time history. Such a method may be useful for "event studies" which attempt to produce the global magnetospheric configuration at a particular time (Section 1.5), producing results that would be expected to match spacecraft data better.

5.4 Future Work with Quantitative Modeling

This section presents suggestions for future quantitative modeling using global magnetospheric simulations.

5.4.1 Bow shock and magnetosheath

The 3-D shape of the bow shock self-consistently generated by a global MHD model is an obvious candidate for another quantitative study. The bow shock shape has been approximated by conic sections fitted to spacecraft measurements, both axisymmetric [*Slavin and Holzer*, 1981] and fully 3-D with no assumed symmetry [*Formisano*, 1979]. These models can provide useful empirical benchmarks for a possible study, in addition to databases of individual bow shock crossings. While dynamic pressure would not be expected to produce asymmetry, following the gasdynamic simulations of *Spreiter et al.* [1966], asymmetry of the bow shock shape could very likely result from the directionality of the IMF. The average IMF direction will differ on the dawn and dusk flanks of the bow shock, in accordance with the Parker spiral. The magnetic field will tend to be parallel to the bow shock surface normal on the dawn side forming a "quasi-parallel shock" while it will tend to be perpendicular on the dusk side (a "quasi-perpendicular shock"). The properties of shock waves are known to be strongly affected by this condition, which may produce a large asymmetry in global bow shock shape on average. The mean bow shock standoff distance should also be sensitive to other parameters, such as the polytropic index γ, the Mach number, and plasma beta of the solar wind.

The IMF may also produce asymmetries in the magnetosheath which could influence the aberration direction of the magnetospheric tail by increasing the mean magnetosheath width on one flank and decreasing it on the other. This has the potential of producing a strong asymmetry in global magnetosheath flow patterns. The draping of magnetic field lines in the magnetosheath over the magnetosphere would also be expected to vary between the dawn and dusk flanks, which may then produce asymmetry in the pattern of reconnection on the dayside magnetopause. This may lead to magnetic flux piling up preferentially on one side, which could change the global shape of the magnetosphere and also affect the aberration angle of the magnetotail. Such an effect was predicted by *Walters* [1964], but has not been observed in the magnetosphere, although *Hundhausen et al.* [1968] reported a difference in the average magnetosheath plasma flow directions between the dawn and dusk flanks of about 8°. Interestingly, the 3-D bow shock surfaces of *Formisano* [1979] also were aberrated by 8°, about twice the observed aberration angle of the magnetotail, a difference which *Formisano* [1979] attributed to magnetic effects.

5.4.2 Magnetic cusp

The magnetic cusp can be mapped down to the surface of the Earth with dipole field lines even if the inner boundary is set at a much larger radius. Results from 3-D codes could be compared with empirical results, obtained mostly through the observation of low energy particles at low altitudes [e.g., *Burch*, 1968; *Frank and Ackerson*, 1971]. The position of the cusp is a sensitive indicator of magnetic topology and its correct prediction by a global model would be a generally useful tool for magnetospheric studies and for interpreting particle data.

Changes in dynamic pressure are expected to produce little change in the mapped position in the ionosphere [*Maltsev and Lyatsky*, 1975], in accordance with the self-similar scaling of the dayside magnetopause with dynamic pressure [*Sibeck et al.*, 1991]. The mapped latitude of the cusp, however, is expected to decrease with IMF B_Z, and is consistent with changes due to large scale field-aligned current systems [*Maltsev and Lyatsky*, 1975; *Tsyganenko and Sibeck*, 1994]. Such behavior is also seen in the empirical model of *Burch* [1973]. Such qualitative behavior was also seen in the 2-D model of Chapter 3, but the quantitative comparisons were limited due to the 2-D nature of the simulation.

The influence of other variables on the cusp position is also significant. The IMF B_Y component is expected to shift the cusp out of the noon-midnight meridian, with a positive B_Y (pointing toward dusk) expected to shift the cusp toward dusk. Dipole tilt shifts the cusp sunward in the summer hemisphere and tailward in the winter hemisphere [*Burch*, 1972]. The IMF B_X component has a similar effect in each hemisphere, so it can be thought of as artificial tilt.

5.4.3 Neutral sheet and tail cross-section

The neutral sheet that separates the lobes of the magnetotail is warped by dipole tilt [*Russell and Brody*, 1967; *Fairfield and Ness*, 1970]. This includes hinging in the X direction at the transition from the inner magnetosphere centered around the dipole axis to the magnetotail aligned with the solar wind flow direction. This curvature is maximum in the noon-midnight meridian and decreases in the dawn and dusk directions, producing a warping in the Y direction. Predicting the distance of a spacecraft from the warped neutral sheet is a generally useful tool for magnetospheric studies. Simple empirical models of the neutral sheet dependence on tilt based on

spacecraft data have been given by *Fairfield* [1980] and *Gosling et al.* [1986]. The current sheet can be seen to warp in this manner in Figure 5.1. The neutral sheet cross-section in $Y - Z$ planes are easily discerned in a global simulation by the line where $B_X = 0$ (clearly seen in Figure 4.6). Similar to the method used in Chapter 4, these measurements could be fitted to a simple curve, e.g. a parabola or ellipse, to produce a predictive model for the neutral sheet. This model could be compared to the empirical models and/or databases of magnetic field measurements close to the magnetotail equatorial plane, again in the method of Chapter 4. Such a predictive model for the neutral sheet could also easily mated with the predictive magnetopause model presented in Chapter 4.

The IMF B_Z component produces additional asymmetry, as we have seen, and could influence the degree of warping. Unlike the models, which lack an IMF B_Z dependence, the global models could easily study the effects of both tilt and IMF B_Z, and so have the potential to exceed empirical models, which like the magnetopause models, are limited by the amount of data. Cross-sections of the magnetotail are elongated by dipole tilt, with this elongation described by the empirical model of *Hammond et al.* [1994]. We have also found a similar elongation of this cross-section that depends on IMF B_Z in Chapter 4. The total elongation produced by a combination of dipole tilt and IMF B_Z could be parametrically studied, which when averaged over B_Z could be compared to the model of *Hammond et al.* [1994].

IMF B_Y produces a twisting of the magnetotail and the neutral sheet also, an effect predicted from theoretical work by *Cowley* [1981] which is seen both in observations [*Sibeck et al.*, 1985] and the global simulations [*Ogino et al.*, 1986]. IMF B_y will also affect the position of the dayside magnetic neutral line, causing it to rotate out of the equatorial plane as seen for exactly southward IMF, thus affecting the magnetic flux transfer between dayside and nightside. Rotation of the neutral line is seen is the global MHD simulations [*Fedder et al.*, 1995a]. Reconnection in the northern dayside in the afternoon sector puts magnetic flux on the dawnside of the northern magnetotail, for example, moving the position of the cusp to the afternoon. The symmetry between dawn and dusk hemispheres is lost when IMF B_Y is non-zero, and possibly there are significant differences in the dawn and dusk magnetopause positions. Although twisting can drastically affect the mapping of magnetic field lines, the twisting of an approximately cylindrical tail (as for northward IMF) will

produce rather small effects. When the magnetotail is highly flared, as for southward IMF, twisting of the tail by IMF B_Y may produce significant perturbations to the magnetopause distance. Further magnetospheric twisting and asymmetry is provided by IMF B_X, which produces twisting relative to the Y axis, rather than the X axis by IMF B_Y. If both IMF B_Z and dipole tilt (and possibly even B_Y and B_X) were included in a series of simulations, a predictive model exceeding *Hammond et al.* [1994] and other empirical models could possibly be constructed.

An extreme case of magnetotail reconfiguration is predicted to occur when dipole tilt becomes unrealistically large, i.e. greater than $\sim 60°$. Although such values of tilt do not occur at present since the magnitude of the tilt angle is always less than 35°, they may have occurred in the past, especially during magnetic reversals. The warping of the current sheet becomes so extreme at these tilt angles that it is predicted to wrap around and connect to itself, becoming a cylinder in the limit of 90° when the magnetic moment is aligned with the Sun-Earth line [*Siscoe*, 1970]. The magnetic cusp in this limiting case is at the subsolar point, and the dawn-dusk electric field of the magnetotail and cross-tail current and plasma sheet near the equatorial plane are absent, changes which will totally alter magnetospheric dynamics. Such a global magnetospheric configuration was produced during development work for the simulations (not shown) and has been produced previously by global models [*Wu*, 1984; *Walker et al.*, 1989]. The magnetospheres of Uranus and Neptune also have very high tilt angles [*Ness et al.*, 1986, 1989], and so can be modeled by such means. Global models provide a powerful tool to study theoretical predictions for situations such as these in which few or no observations are available.

5.4.4   X line position and shape

The X line position and shape is very sensitive to the components of the IMF, especially B_Z. The X line is found to be present in our simulations when IMF is zero and also for small values of positive IMF B_Z [*Elsen and Winglee*, 1995]. The X line position along the X axis was found to be close to 20 R_E for all cases studied, while IMF B_Z mainly had the effect of varying the width of the neutral line in the Y direction. Again this change in width was roughly linear between threshold values of IMF B_Z, above which the magnetosphere was totally closed and below which the neutral line stretched all the way to the magnetopause with a very dynamic magnetotail.

The neutral position will also be affected by IMF B_Y and dipole tilt, but the neutral line will no longer be restricted to the equatorial plane and will acquire a 3-D shape. Not only is this harder to visualize, but the simple diagnostic of finding where B_Z changes sign in the equatorial plane is no longer adequate.

5.4.5   Field-aligned currents

Many global models have produced field-aligned current patterns [e.g., *Ogino*, 1986; *Fedder and Lyon*, 1995], but they have not been quantitatively tested. The integrated Region 1 current both in longitudinal sectors and the total amount could be calculated for different IMF conditions and compared with empirical results [*Iijima and Potemra*, 1976a, 1976b, 1978; *Potemra*, 1994]. The relative contributions from MHD and MPD could also be studied, again by sector and in total. The total integrated field-aligned current could also compared to other changes in the magnetosphere, such as the shift in cusp latitude or the change in subsolar distance, both of which are expected to have linear relationships from crude analytical estimates [*Maltsev and Lyatsky*, 1975].

Other current systems, such as the Region 0 and 2 currents that are poleward and equatorward of the Region 1 systems, respectively, can also be studied and compared with empirical results. While Region 1 currents are quite strong in global MHD simulations, the Region 2 current systems are much weaker, contrary to observations which show similar integrated magnitudes for both current systems [*Iijima and Potemra*, 1976b]. The Region 2 currents are believed to map to the partial ring current [*Potemra*, 1994], whose strong underestimate may account for the weakness of this current system in global MHD models.

5.4.6   Anisostropic MHD

Space plasmas, being collisionless, are generally anisotropic, as discussed in Chapter 1. Anisotropic MHD can be formulated, but requires two energy equations when the pressure tensor is gyrotropic. The increase in thermal pressure associated with Joule heating must be arbitrarily divided between perpendicular and parallel pressures [*Hesse and Birn*, 1992]. Nevertheless, the effect of anisotropic pressure on the various aspects of the magnetospheric configuration, such as the position of the neutral line and the magnitude of field-aligned currents, could be parametrically studied. Any change in the magnetic reconnection rate would also affect flux erosion rate and may

lead to differences in the average magnetopause size and shape. Anisotropic MHD could also be compared to MPD, and possibly even a modified fluid approximation that incorporates both effects could be formulated.

BIBLIOGRAPHY

Akasofu, S.-I., The development of the auroral substorm, *Planet. Space Sci.*, *12*, 273-282, 1964.

Akasofu, S.-I., A. T. Y. Lui, C.-I. Meng, and M. Haurwitz, The need for a three-dimensional analysis of magnetic fields in the magnetotail during substorms, *Geophys. Res. Lett.*, *5*, 283-286, 1978.

Alfvén, H., Existence of electromagnetic-hydromagnetic waves, *Nature*, *150*, 405, 1942.

Alfvén, H., *Ark. f. Mat. Astr. Fys.*, *29A*, no. 11, 1943.

Alfvén, H., On the theory of comet tails, *Tellus*, *9*, 92-96, 1957.

Anderson, K. A., and Lin, R. P., Observations of interplanetary field lines in the magnetotail, *J. Geophys. Res.*, *74*, 3953, 1969.

Anger, C. D., T. Fancott, J. McNally, and H. S. Kerr, ISIS-II scanning auroral photometer, *Appl. Opt.*, *12*, 1753-1766, 1973.

Arnoldy, R. L., Auroral particle precipitation and Birkeland currents, *Rev. Geophys. Space Phys.*, *12*, 217-231, 1974.

Ashour-Abdalla, M., J. Berchem, J. Büchner, and L. M. Zelenyi, Shaping of the magnetotail from the mantle: Global and local structuring, *J. Geophys. Res.*, *98*, 5651-5676, 1993.

Aubry, M. P., C. T. Russell, and M. G. Kivelson, Inward motion of the magnetopause before a substorm, *J. Geophys. Res.*, *75*, 7018-7031, 1970.

Aubry, M. P., M. G. Kivelson, and C. T. Russell, Motion and structure of the magnetopause, *J. Geophys. Res.*, *75*, 1673-1696, 1971.

Axford, W. I., The interaction between the solar wind and the earth's magneto-sphere, *J. Geophys. Res.*, *67*, 3791-3796, 1962.

Axford, W. I., and C. O. Hines, A unifying theory of high-latitude geophysical phenomena and geomagnetic storms, *Can. J. Phys.*, *39*, 1433-1464, 1961.

Axford, W. I., H. E. Petschek, and G. L. Siscoe, Tail of the magnetosphere, *J. Geophys. Res.*, *70*, 1231-1236, 1965.

Bame, S. J., J. R. Asbridge, H. E. Felthauser, E. W. Hones, Jr., and I. B. Strong, Characteristics of the plasma sheet in the Earth's magnetotail, *J. Geophys. Res.*, *72*, 113-129, 1967.

Bame, S. J., A. J. Hundhausen, J. R. Asbridge, and I. B. Strong, Solar wind ion composition, *Phys. Rev. Lett.*, *20*, 393, 1968.

Beard, D. B., The interaction of the terrestrial magnetic field with the solar corpuscular radiation, *J. Geophys. Res.*, *65*, 3559-3568, 1960.

Behannon, K. W., Mapping of the earth's bow shock and magnetic tail by Explorer 33, *J. Geophys. Res.*, *73*, 907-930, 1968.

Behannon, K. W., Geometry of the geomagnetic tail, *J. Geophys. Res.*, *75*, 743-753, 1970.

Belcher, J. W., H. S. Bridge, F. Bagenal, B. Coppi, O. Divers, A. Eviatar, G. S. Gordon Jr., A. J. Lazarus, R. L. McNutt Jr., K. W. Ogilvie, J. D. Richardson, G. L. Siscoe, E. C. Sittler Jr., J. T. Steinberg, J. D. Sullivan, A. Szabo, L. Villanueva, and V. M. Vasyliunas, Plasma observations near Neptune: Initial results from Voyager 2, *Science*, *246*, 1478-1483, 1989.

Berchem, J., and C. T. Russell, The thickness of the magnetopause current layer: ISEE 1 and 2 observations, *J. Geophys. Res.*, *87*, 2108-2114, 1982.

Berchem, J., J. Raeder, and M. Ashour-Abdalla, Reconnection at the magnetospheric boundary: Results from global magnetohydrodynamic simulations, in

Physics of the Magnetopause, Geophys. Monogr. Ser., vol. 90, edited by P. Song, B. U. Ö. Sonnerup, and M. F. Thomsen, pp. 205-213, AGU, Washington, D. C., 1995a.

Berchem, J., J. Raeder, and M. Ashour-Abdalla, Magnetic flux ropes at the high-latitude magnetopause, *Geophys. Res. Lett., 22*, 1189-1192, 1995b.

Biermann, L., Kometenschweife und solare Korpuscularsthrahlung, *Z. Astrophys., 29*, 274-286, 1951.

Biermann, L., Solar corpuscular radiation and the interplanetary gas, *Observatory, 77*, 109-110, 1957.

Birn, J., and E. W. Hones Jr., Three-dimensional computer modeling of dynamic reconnection in the geomagnetic tail, *J. Geophys. Res., 86*, 6802-6808, 1981.

Boris, J. P., and D. L. Book, Flux-corrected transport, 1.SHASTA, a fluid transport algorithm that works, *J. Comput. Phys., 11*, 38, 1973.

Boyd, T. J. M., and J. J. Sanderson, *Plasma Dynamics*, 348 pp., Barnes Noble, New York, 1969.

Brackbill, J. U., and D. C. Barnes, The effect of non-zero div B on the numerical solutions of the magnetohydrodynamic equations, *J. Comp. Phys., 35*, 426-430, 1980.

Brecht, S. H., Global simulations using MHD codes: A few points to consider before you try one, *Space Sci. Rev., 42*, 169-185, 1985.

Brecht, S. H., J. G. Lyon, J. A. Fedder, and K. Hain, A simulation study of east-west IMF effects on the the magnetosphere, *Geophys. Res. Lett., 8*, 397-400, 1981.

Brecht, S. H., J. G. Lyon, J. A. Fedder, and K. Hain, A time-dependent three-dimensional simulation of the Earth's magnetosphere: Reconnection events, *J. Geophys. Res., 87*, 6098-6108, 1982.

Bridge, H. S., J. W. Belcher, A. J. Lazarus, J. D. Sullivan, R. L. McNutt Jr., F. Bagenal, J. D. Scudder, E. C. Sittler Jr., G. L. Siscoe, V. M. Vasyliunas, C. K. Goertz, and C. M. Yeates, Plasma observations near Jupiter: Initial results from Voyager 1, *Science, 204*, 987-991, 1979a.

Bridge, H. S., J. W. Belcher, A. J. Lazarus, J. D. Sullivan, F. Bagenal, R. L. McNutt Jr., K. W. Ogilvie, J. D. Scudder, E. C. Sittler Jr., V. M. Vasyliunas, and C. K. Goertz, Plasma observations near Jupiter: Initial results from Voyager 2, *Science, 206*, 972-976, 1979b.

Bridge, H. S., J. W. Belcher, B. Coppi, A. J. Lazarus, R. L. McNutt Jr., S. Olbert, J. D. Richardson, M. R. Sands, R. S. Selesnick, J. D. Sullivan, R. E. Hartle, K. W. Ogilvie, E. C. Sittler Jr., F. Bagenal, R. S. Wolff, V. M. Vasyliunas, G. L. Siscoe, C. K. Goertz, and A. Eviatar, Plasma observations near Uranus: Initial results from Voyager 2, *Science, 233*, 89-93, 1986.

Burch, J. L., Low-energy electron fluxes at latitudes above the auroral zone, *J. Geophys. Res., 73*, 3585-3591, 1968.

Burch, J. L., Precipitation of low-energy electrons at high latitudes: Effects of interplanetary magnetic field and dipole tilt angle, *J. Geophys. Res., 77*, 6696-6707, 1972.

Burch, J. L., Rate of erosion of dayside magnetic flux based on a quantitative study of the dependence of polar cusp latitude on the interplanetary magnetic field, *Radio Sci., 8*, 955, 1973.

Burch, J. L., Observations of interactions between interplanetary and geomagnetic fields, *Rev. Geophys. Space Phys., 12*, 363-378, 1974.

Cahill, L. J., and Amazeen, P. G., The boundary of the the geomagnetic field, *J. Geophys. Res., 68*, 1835-1843, 1963.

Carpenter, D. L., Whistler evidence of a 'knee' in the magnetospheric ionization density profile, *J. Geophys. Res., 68*, 1675-1682, 1963.

Carrington, R. C., Description of a singular appearance seen in the Sun on September 1, 1859, *Mon. Not. R. Astron. Soc., 20*, 13, 1860.

Chapman, S., Some phenomena of the upper atmosphere, *Proc. R. Soc. London, A, 132*, 353-374, 1931.

Chapman, S., The electric conductivity of the ionosphere: A review, *Nuovo Cimento, 5*, Suppl., 1385-1412, 1956.

Chapman, S., Notes on the solar corona and the terrestrial atmosphere, *Smithsonian Inst. Publ. Contribs. to Astrophysics, 2*, 1-12, 1957.

Chapman, S., and J. Bartels, *Geomagnetism* (2 vols.), Oxford Univ. Press, New York, 1940.

Chapman, S., and V. C. A. Ferraro, A new theory of magnetic storms, *Nature, 126*, 129-130, 1930.

Chapman, S., and V. C. A. Ferraro, A new theory of magnetic storms, I. The initial phase, *Terr. Magn. Atmosph. Elec., 36*, 77-97 and 171-186, 1931; *37*, 147-156 and 421-429, 1932.

Chapman, S., and V. C. A. Ferraro, A new theory of magnetic storms, II. The main phase, *Terr. Magn. Atmosph. Elec., 38*, 79-96, 1933.

Chapman, S., and V. C. A. Ferraro, The theory of the first phase of a geomagnetic storm, *Terr. Magn. Atmosph. Elec., 45*, 245-268, 1940.

Chappell, C. R., K. K. Harris, and G. W. Sharp, A study of the influence of magnetic activity on the location of the plasmapause as measured by OGO 5, *J. Geophys. Res., 75*, 50-56, 1970.

Chappell, C. R., T. E. Moore, and J. H. Waite Jr., The ionosphere as a fully adequate source of plasma for the Earth's magnetosphere, *J. Geophys. Res., 92*, 5896-5910, 1987.

186

Chen, J., S. P. Slinker, J. A. Fedder, and J. G. Lyon, Simulation of geomagnetic storms during the passage of magnetic clouds, *Geophys. Res. Lett.*, *22*, 1749-1752, 1995.

Chen, S.-H., M. G. Kivelson, J. T. Gosling, R. J. Walker, and A. J. Lazarus, Anomalous aspects of magnetosheath flow and of the shape and oscillations of the magnetopause during an interval of strong northward interplanetary magnetic field, *J. Geophys. Res.*, *98*, 5727-5742, 1993.

Choe, J. Y., D. B. Beard, and E. C. Sullivan, Precise calculation of the magnetosphere surface for a tilted dipole, *Planet. Space Sci.*, *21*, 485-498, 1973.

Coleman, P. J., Jr., Characteristics of the region of interaction between the interplanetary plasma and the geomagnetic field, *J. Geophys. Res.*, *69*, 3051-3076, 1964.

Coroniti, F. V., and C. F. Kennel, Changes in magnetospheric configuration during the substorm growth phase, *J. Geophys. Res.*, *77*, 3361-3370, 1972.

Coroniti, F. V., and C. F. Kennel, Can the ionosphere regulate magnetospheric convection?, *J. Geophys. Res.*, *78*, 2837-2851, 1973.

Coroniti, F. V., L. A. Frank, D. J. Williams, R. P. Lepping, F. L. Scarf, S. M. Krimigis, and G. Gloeckler, Variability of plasma sheet dynamics, *J. Geophys. Res.*, *85*, 2957-2977, 1980.

Courant, R., K. O. Friedrichs, and H. Lewy, Über die partiellen Differenzengleichungen der mathematischen Physik, *Math. Ann.*, *100*, 32, 1928.

Cowley, S. W. H., Magnetic asymmetries associated with the y-component of the IMF, *Planet. Space Sci.*, *29*, 79-96, 1981.

Crooker, N. U., T. E. Eastman, and G. S. Stiles, Observations of plasma depletion in the magnetosheath at the dayside magnetopause, *J. Geophys. Res.*, *82*, 869-874, 1979.

Dessler, A. J., Length of the magnetospheric tail, *J. Geophys. Res.*, *69*, 3913-3918, 1964.

Dessler, A. J., and E. N. Parker, Hydromagnetic theory of geomagnetic storms, *J. Geophys. Res.*, *64*, 2239-2259, 1959.

DeZeeuw, D. L., and K. G. Powell, An adaptively-refined Cartesian mesh solver for the Euler equations, *J. Comput. Phys.*, *104*, 55, 1992.

Donovan, E. F., G. Rostoker, and C. Y. Huang, Regions of negative B_z in the Tsyganenko 1989 model neutral sheet, *J. Geophys. Res.*, *97*, 8697-8700, 1992.

Dorfi, E. A., Numerical methods for astrophysical plasmas, *Comp. Phys. Commun.*, *43*, 1-15, 1986.

Dryer, M., and G. R. Heckman, On the hypersonic analogue as applied to planetary interaction with the solar plasma, *Plan. Space Sci.*, *15*, 515-546, 1967.

Dungey, J. W., Electrodynamics of the outer atmosphere, Pennsylvania State University Ionosphere Research Laboratory Report 69, 1954; brief version in *Proceedings of the Ionosphere Conference*, pp. 229-236, The Physical Society of London, 1955.

Dungey, J. W., Interplanetary magnetic field and auroral zone, *Phys. Rev. Lett.*, *6*, 47-48, 1961.

Dungey, J. W., The structure of the exosphere or adventures in velocity space, in Geophysics: The Earth's Environment, edited by C. DeWitt, J. Hieblot, and A. Lebeau, p. 503, Gordon and Breach, New York, 1963.

Eastman, T. E., L. A. Frank, W. K. Peterson, and W. Lennartson, The plasma sheet boundary layer, *J. Geophys. Res.*, *89*, 1553-1572, 1984.

Elphinstone, R. D., D. Hearn, J. S. Murphree, and L. L. Cogger, Mapping using the Tsyganenko long magnetosphere model and its relationship to Viking auroral images, *J. Geophys. Res.*, *96*, 1467-1480, 1991.

Elsen, R. K., and R. M. Winglee, Mapping of the auroral field lines and currents as a function of magnetospheric activity, *IAGA conference, IUGG XXI General Assembly, Abstracts Week B*, paper GAB41L-7, p. B161, Boulder, CO, July 1995.

Elsen, R. K., and R. M. Winglee, Mapping of magnetic field lines and auroral currents in the noon-midnight meridian, *J. Geophys. Res., 101*, 13,239-13,253, 1996a.

Elsen, R. K., and R. M. Winglee, The average shape of the magnetopause: A comparison of 3-D global MHD and empirical models, manuscript submitted to *J. Geophys. Res.*, 1996b.

Evans, C. R., and J. F. Hawley, Simulation of magnetohydrodynamic flows: A constrained transport method, *Ap. J., 332*, 659-677, 1988.

Fairfield, D. H., The ordered magnetic field of the magnetosheath, *J. Geophys. Res., 72*, 5865-5877, 1967.

Fairfield, D. H., Average magnetic field configuration of the outer magnetosphere, *J. Geophys. Res., 73*, 7329-7338, 1968.

Fairfield, D. H., Average and unusual locations of the Earth's magnetopause and bow shock, *J. Geophys. Res., 76*, 6700-6716, 1971.

Fairfield, D. H., Magnetic fields of the magnetosheath, *Rev. Geophys. Space Phys., 14*, 117-134, 1976.

Fairfield, D. H., On the average configuration of the geomagnetic tail, *J. Geophys. Res., 84*, 1950-1958, 1979a.

Fairfield, D. H., Global aspects of the Earth's magnetopause, in *Magnetospheric Boundary Layers, European Space Agency Spec. Publ.*, edited by B. Battrick, ESA SP-148, pp. 5-13, 1979b.

Fairfield, D. H., A statistical determination of the shape and position of the geomagnetic neutral sheet, *J. Geophys. Res., 85*, 775-780, 1980.

Fairfield, D. H., The magnetic field of the equatorial magnetotail from 10 to 40 R_E, *J. Geophys. Res.*, *91*, 4238-4244, 1986.

Fairfield, D. H., Solar wind control of the size and shape of the magnetosphere, *J. Geomag. Geoelectr.*, *43, Suppl.*, 117-127, 1991.

Fairfield, D. H., On the structure of the distant magnetotail: ISEE 3, *J. Geophys. Res.*, *97*, 1403-1410, 1992.

Fairfield, D. H., Observations of the shape and location of the magnetopause: A Review, in *Physics of the Magnetopause, Geophys. Monogr. Ser.*, vol. 90, edited by P. Song, B. U. Ö. Sonnerup, and M. F. Thomsen, pp. 53-60, AGU, Washington, D. C., 1995.

Fairfield, D. H., and N. F. Ness, Configuration of the geomagnetic tail during substorms, *J. Geophys. Res.*, *75*, 7032-7047, 1970.

Fedder, J. A., and J. G. Lyon, The solar wind-magnetosphere-ionosphere current-voltage relationship, *Geophys. Res. Lett.*, *14*, 880-883, 1987.

Fedder, J. A., and J. G. Lyon, The Earth's magnetosphere is 165 R_E long: Self-consistent currents, convection, magnetospheric structure, and processes for northward interplanetary magnetic field, *J. Geophys. Res.*, *100*, 3623-3635, 1995.

Fedder, J. A., C. M. Mobarry, and J. G. Lyon, Reconnection voltage as a function of IMF clock angle, *Geophys. Res. Lett.*, *18*, 1047-1050, 1991.

Fedder, J. A., J. G. Lyon, S. P. Slinker, and C. M. Mobarry, Topological structure of the magnetotail as a function of IMF direction, *J. Geophys. Res.*, *100*, 3613-3621, 1995a.

Fedder, J. A., S. P. Slinker, J. G. Lyon, and R. D. Elphinstone, Global numerical simulation of the growth phase and the expansion onset for a substorm observed by Viking, *J. Geophys. Res.*, *100*, 19,083-19,093, 1995b.

Feldman, W. C., J. R. Asbridge, S. J. Bame, and J. T. Gosling, Plasma and magnetic fields from the Sun, in *The Solar Output and Its Variations*, edited by O. R. White, p. 351, Colo. Assoc. Univ. Press, Boulder, Colo., 1977.

Feldstein, Y. I., Auroral oval, *J. Geophys. Res.*, *78*, 1210-1213, 1973.

Formisano, V., Orientation and shape of the Earth's bow shock in three dimensions, *Planet. Space Sci.*, *27*, 1151-1161, 1979.

Formisano, V., V. Domingo, and K.-P. Wenzel, The three-dimensional shape of the magnetopause, *Planet. Space Sci.*, *27*, 1137-1149, 1979.

Frank, L. A., On the extraterrestrial ring current during geomagnetic storms, *J. Geophys. Res.*, *72*, 3753-3767, 1967.

Frank, L. A., and K. L. Ackerson, Observations of charged particle precipitation into the auroral zone, *J. Geophys. Res.*, *76*, 3612-3643, 1971.

Frank, L. A., J. D. Craven, K. L. Ackerson, M. R. English, R. H. Eather, and R. L. Carovillano, Global auroral imaging instrumentation for the Dynamics Explorer mission, *Space Sci. Instr.*, *5*, 369-393, 1981.

Frank, L. A., M. Ashour-Abdalla, J. Berchem, J. Raeder, W. R. Paterson, S. Kokubun, T. Yamamoto, R. P. Lepping, F. V. Coroniti, D. H. Fairfield, and K. L. Ackerson, Observations of plasmas and magnetic fields in Earth's distant magnetotail: Comparison with a global MHD model, *J. Geophys. Res.*, *100*, 19,177-19,190, 1995.

Friedman, H., *Sun and Earth, Scientific American Library*, no. 15, 251 pp., W. H. Freeman, New York, 1986.

Friis-Christensen, E., and K. Lassen, Large-scale distribution of auroras and field-aligned currents, in *Auroral Physics*, edited by C.-I. Meng, M. J. Rycroft, and L. A. Frank, pp. 369-381, Cambridge Univ. Press, New York, 1991.

Fukunishi, H., Y. Takahashi, T. Nagatsuma, T. Mukai, and S. Machida, Latitudinal structures of nightside field-aligned currents and their relationships to the plasma sheet regions, *J. Geophys. Res.*, *98*, 11,235-11,255, 1993.

Gallagher, D. L., P. D. Craven, and R. H. Comfort, An empirical model of the Earth's plasmasphere, *Adv. Space Res.*, *8*, 15, 1988.

Gold, T., Motion in the magnetosphere, *J. Geophys. Res.*, *64*, 1219-24, 1959.

Gombosi, T. I., D. L. De Zeeuw, and K. G. Powell, A new solution adaptive 3-D MHD model of the magnetosphere: First results and their validation, *IAGA conference, IUGG XXI General Assembly, Abstracts Week B*, paper GAB41K-10, p. B160, Boulder, CO, July 1995.

Gonzalez, W. D., J. A. Joselyn, Y. Kamide, H. W. Kroehl, G. Rostoker, B. T. Tsurutani, and V. M. Vasyliunas, What is a geomagnetic storm?, *J. Geophys. Res.*, *99*, 5771-5792, 1994.

Gosling, J. T., D. J. McComas, M. F. Thomsen, and S. J. Bame, The warped neutral sheet and plasma sheet in the near-Earth geomagnetic tail, *J. Geophys. Res.*, *91*, 7093-7099, 1986.

Gosling, J. T., M. F. Thomsen, S. J. Bame, T. G. Onsager, and C. T. Russell, The electron edge of the low latitude boundary layer during accelerated flow events, *Geophys. Res. Lett.*, *17*, 1833, 1990.

Grad, H., and P. N. Hu, Neutral point in the geomagnetic field, *Phys. Fluids*, *9*, 1610-1611, 1966.

Hamlin, D. A., R. Karplus, R. C. Vik, and K. M. Watson, Mirror and azimuthal drift frequencies for geomagnetically trapped particles, *J. Geophys. Res.*, *66*, 1-4, 1961.

Hammond, C. M., M. G. Kivelson, and R. J. Walker, Imaging the effect of dipole tilt on magnetotail boundaries, *J. Geophys. Res.*, *99*, 6079-6092, 1994.

Heppner, J. P., and N. C. Maynard, Empirical high-latitude electric field models, *J. Geophys. Res.*, *92*, 4467-4489, 1987.

Heppner, J. P., N. F. Ness, S. S. Scearce, and T. L. Skillman, Explorer 10 magnetic field measurements, *J. Geophys. Res.*, *68*, 1-46, 1963.

Hesse, M., and J. Birn, Plasmoid evolution in an extended magnetotail, *J. Geophys. Res.*, *96*, 5683-5696, 1991.

Hesse, M., and J. Birn, MHD modeling of magnetotail instability with anisotropic pressure, *J. Geophys. Res.*, *97*, 10,643-10,654, 1992.

Holzer, R. E., and J. A. Slavin, Magnetic flux transfer associated with expansions and contractions of the dayside magnetosphere, *J. Geophys. Res.*, *83*, 3831-3839, 1978.

Hones, E. W., Jr., Plasma sheet behavior during substorms, in *Magnetic Reconnection in Space and Laboratory Plasmas, Geophys. Monogr. Ser.*, vol. 30, edited by E. W. Hones Jr., pp. 178-184, AGU, Washington, D. C., 1984.

Howe, H. C., Jr., and J. H. Binsack, Explorer 33 and 35 plasma observations of magnetosheath flow, *J. Geophys. Res.*, *77*, 3334-3344, 1972.

Huang, C. Y., and L. A. Frank, Magnitude of B_Z in the neutral sheet of the magnetotail, *J. Geophys. Res.*, *99*, 73-82, 1994.

Huang, C. Y., and L. A. Frank, A statistical survey of the central plasma sheet, *J. Geophys. Res.*, *99*, 83-95, 1994.

Huang, C. Y., G. Rostoker, and L. A. Frank, The plasma sheet magnetic field during varying phases of geomagnetic activity (abstract), *Eos Trans. AGU, 71(46)*, Fall Meet. Suppl., 1545, 1990.

Huang, C. Y., G. Rostoker, and L. A. Frank, The magnetic field in the neutral sheet of the magnetotail (abstract), *Eos Trans. AGU, 72(17)*, Spring Meet. Suppl., 243, 1991.

Hundhausen, A. J., Composition and dynamics of the solar wind, *Rev. Geophys. Space Phys.*, *8*, 729-811, 1970.

Hundhausen, A. J., J. R. Asbridge, S. J. Bame, H. E. Gilbert, and I. B. Strong, Vela 3 satellite observations of solar wind ions: A preliminary report, *J. Geophys. Res.*, *72*, 87-100, 1967.

Hundhausen, A. J., S. J. Bame, and J. R. Asbridge, Plasma flow pattern in the Earth's magnetosheath, *J. Geophys. Res.*, *74*, 2799-2806, 1969.

Iijima, T., and T. A. Potemra, The amplitude distribution of field aligned currents at northern high latitude observed by TRIAD, *J. Geophys. Res.*, *81*, 2165-2174, 1976a.

Iijima, T., and T. A. Potemra, Field aligned currents in the dayside cusp observed by TRIAD, *J. Geophys. Res.*, *81*, 5971-5979, 1976b.

Iijima, T., and T. A. Potemra, Large scale characteristics of field-aligned currents associated with substorms, *J. Geophys. Res.*, *83*, 599-615, 1978.

Intriligator, D. S., J. H. Wolfe, D. D. McKibbin, and H. R. Collard, Preliminary comparison of solar wind plasma observations in the geomagnetic wake at 1000 and 500 Earth radii, *Planet. Space Sci.*, *17*, 321, 1969.

Intriligator, D. S., H. R. Collard, J. D. Mihalov, O. L. Vaisberg, and J. H. Wolfe, Evidence for Earth magnetospheric tail associated phenomena at 3100 R_E, *Geophys. Res. Lett.*, *6*, 585-588, 1979.

Johnson, F. S., The gross character of the geomagnetic field in the solar wind, *J. Geophys. Res.*, *65*, 3049-3053, 1960.

Johnson, F. S., (ed.), Satellite Environment Handbook, Stanford Univ. Press, Stanford, CA, 1961.

Kageyama, A., K. Watanabe, and T. Sato, Global simulation of the magnetosphere with a long tail: No interplanetary magnetic field, *J. Geophys. Res.*, *97*, 3929-3943, 1992.

194

Kamide, Y. The auroral electrojets: Relative importance of ionospheric conductivities and electric fields, in *Auroral Physics*, edited by C.-I. Meng, M. J. Rycroft, and L. A. Frank, pp. 385-398, Cambridge Univ. Press, New York, 1991.

Kamide, Y., and S. Matsushita, Simulation studies of ionospheric electric fields and currents in relation to field aligned currents, 1. Quiet periods, *J. Geophys. Res.*, *84*, 4083-4098, 1979.

Kan, J. R., Developing a global model of magnetospheric substorms, *Eos Trans. AGU*, *71*, 1083 and 1086-1087, 1990.

Kaufmann, R. L., and A. Konradi, Explorer 12 magnetopause observations: Large-scale nonuniform motion, *J. Geophys. Res.*, *74*, 3609-3627, 1969.

Kaymaz, Z., G. L. Siscoe, J. G. Luhmann, J. A. Fedder, and J. G. Lyon, Interplanetary magnetic field control of the magnetotail field: IMP 8 data and MHD model compared, *J. Geophys. Res.*, *100*, 17,163-17,172, 1995.

Kelley, M. C., *The Earth's Ionosphere: Plasma Physics and Electrodynamics*, *Internat. Geophys. Ser.*, vol. 43, 484 pp., Academic Press, San Diego, 1989.

Kellogg, P. J., Flow of plasma around the earth, *J. Geophys. Res.*, *67*, 3805-3811, 1962.

Khurana, K. K., R. J. Walker, and T. Ogino, Magnetospheric convection in the presence of interplanetary magnetic field B_y: A conceptual model and simulations, *J. Geophys. Res.*, *101*, 4907-4916, 1995.

Kivelson, M. G., and C. T. Russell, *Introduction to Space Physics*, 568 pp., Cambridge Univ. Press, New York, 1995.

Krall, N. A., and A. W. Trivelpiece, *Principles of Plasma Physics*, 674 pp., San Francisco Press, San Francisco, CA, 1986.

Krimigis, S. M., T. P. Armstrong, W. I. Axford, C. O. Bostrom, C. Y. Fan, G. Gloeckler, L. J. Lanzerotti, J. F. Carbury, E. P, Keath, R. D. Zwickl, and D. C.

Hamilton, Low energy charged particle environment at Jupiter: A first look, *Science*, *204*, 998-1003, 1979a.

Krimigis, S. M., T. P. Armstrong, W. I. Axford, C. O. Bostrom, C. Y. Fan, G. Gloeckler, L. J. Lanzerotti, J. F. Carbury, E. P, Keath, R. D. Zwickl, and D. C. Hamilton, Hot plasma environment at Jupiter: Voyager 2 results, *Science, 206*, 977-984, 1979b.

Krimigis, S. M., T. P. Armstrong, W. I. Axford, A. F. Cheng, G. Gloeckler, D. C. Hamilton, E. P, Keath, L. J. Lanzerotti, and B. H. Mauk, The magnetosphere of Uranus: Hot plasma and radiation environments, *Science, 233*, 97-102, 1986.

Krimigis, S. M., T. P. Armstrong, W. I. Axford, C. O. Bostrom, A. F. Cheng, G. Gloeckler, D. C. Hamilton, E. P, Keath, L. J. Lanzerotti, B. H. Mauk, and J. A. Van Allen, Hot plasma and energetic particles in Neptune's magnetosphere, *Science, 246*, 1483-1489, 1989.

Landau, L. D., and E. M. Lifshitz, *Fluid Mechanics*, 539 pp., Second edition, Pergamon Press, New York, 1987.

Landau, L. D., E. M. Lifshitz, and L. P. Pitaevskii, *Electrodynamics of Continuous Media*, 460 pp., Second edition, Pergamon Press, New York, 1984.

Lapidus, A., A detached shock calculation by second-order finite differences, *J. Comput. Phys., 2*, 154-175, 1967.

Lax, P. D., Weak solution of nonlinear hyperbolic equations and their numerical computation, *Commun. Pure Appl. Math., 7*, 159, 1954.

Lax, P. D., and B. Wendroff, *Commun. Pure Appl. Math., 13*, 217, 1960.

Lebouef, J. N., T. Tajima, C. F. Kennel, and J. M. Dawson, Global simulations of the time-dependent magnetosphere, *Geophys. Res. Lett., 5*, 609-612, 1978.

Lebouef, J. N., T. Tajima, C. F. Kennel, and J. M. Dawson, Global simulations of the three-dimensional magnetosphere, *Geophys. Res. Lett., 8*, 257-530, 1981.

Ledley, B. G., Magnetopause attitudes during OGO 5 crossings, *J. Geophys. Res.*, *76*, 6736-6742, 1971.

Lepping, R. P., Characteristics of the magnetopauses of the magnetized planets, in *Physics of the Magnetopause, Geophys. Monogr. Ser.*, vol. 90, edited by P. Song, B. U. Ö. Sonnerup, and M. F. Thomsen, pp. 61-70, AGU, Washington, D. C., 1995.

Levy, R. H., H. E. Petschek, and G. L. Siscoe, Aerodynamic aspects of magnetospheric flow, *AIAA J.*, *2*, 2065-2076, 1964.

Luhmann, J. G., The magnetopause counterpart at the weakly magnetized planets: The ionopause, in *Physics of the Magnetopause, Geophys. Monogr. Ser.*, vol. 90, edited by P. Song, B. U. Ö. Sonnerup, and M. F. Thomsen, pp. 71-79, AGU, Washington, D. C., 1995.

Lui, A. T. Y., Solar wind influence on magnetotail configuration and dynamics, in *Solar Wind-Magnetosphere Coupling*, edited by Y. Kamide and J. A. Slavin, pp. 671-690, Terra Press, Baltimore, Md., 1986.

Lyon, J. G., S. H. Brecht, J. A. Fedder, and P. J. Palmadesso, The effect on the Earth's magnetotail from shocks in the solar wind, *Geophys. Res. Lett.*, *7*, 721-724, 1980.

Lyon, J. G., S. H. Brecht, J. D. Huba, J. A. Fedder, and P. J. Palmadesso, Computer simulation of a geomagnetic substorm, *Phys. Rev. Lett.*, *46*, 1038-1041, 1981.

Lyon, J. G., J. A. Fedder, and J. D. Huba, The effect of different resistivity models on magnetotail dynamics, *J. Geophys. Res.*, *91*, 8057-8064, 1986.

Lyons, L. R., and D. J. Williams, *Quantitative Aspects of Magnetospheric Physics*, 231 pp., D. Reidel, Norwell, Mass., 1984.

Maezawa, K., Dependence of the magnetopause position on the southward interplanetary magnetic field, *Planet. Space Sci.*, *22*, 1443-1453, 1974.

Maezawa, K., Magnetotail boundary motion associated with geomagnetic substorms, *J. Geophys. Res.*, *80*, 3543-3548, 1975.

Maltsev, Yu. P., and W. P. Lyatsky, Field-aligned currents and erosion of the dayside magnetosphere, *Planet. Space Sci.*, *23*, 1257-1260, 1975.

Mariani, F., and N. F. Ness, Observations of the geomagnetic tail at 500 Earth radii by Pioneer 8, *J. Geophys. Res.*, *80*, 5633-5641, 1969.

Martyn, D. F., The theory of magnetic storms and auroras, *Nature*, *167*, 92-94, 1951.

Maxwell, J. C., *A Treatise on Electricity and Magnetism*, Cambridge Univ. Press, 1873; Dover ed., New York, 1954.

Maynard, N. C., Space weather prediction, *U. S. Natl. Rep. Int. Union Geod. Geophys. 1991-1994, Rev. Geophys.*, *33*, Suppl., 547-557, 1995.

Mead, G. D., and D. B. Beard, Shape of the geomagnetic field solar wind boundary, *J. Geophys. Res.*, *69*, 1169-1179, 1964.

Mead, G. D. and Fairfield, D. H., A quantitative magnetospheric model derived from spacecraft magnetospheric data, *J. Geophys. Res.*, *80*, 523-534, 1975.

Meng, C.-I., Variation of the magnetopause position with substorm activity, *J. Geophys. Res.*, *75*, 3252-3254, 1970.

Meng, C.-I., A. T. Y. Lui, S. M. Krimigis, S. Ismail, and D. J. Williams, Spatial distribution of energetic particles in the distant magnetotail, *J. Geophys. Res.*, *86*, 5682-5700, 1981.

Mizera, and J. F. Fennel, Satellite observations of polar, magnetotail lobe and interplanetary electrons at low energies, *Rev. Geophys. Space Phys.*, *16*, 147-153, 1978.

Michel, F. C., and A. J. Dessler, Diffusive entry of solar flare particles into the geomagnetic tail, *J. Geophys. Res.*, *75*, 6061-6072, 1970.

Midgely, J. E., and L. Davis Jr., Calculation by a moment technique of the perturbation of the geomagnetic field by the solar wind, *J. Geophys. Res., 68*, 5111-5123, 1963.

Mihalov, J. D., D. S. Colburn, R. G. Currie, and C. P. Sonnett, Configuration and reconnection of the geomagnetic tail, *J. Geophys. Res., 73*, 943-959, 1968.

Moore, T. E., M. Lockwood, J. H. Waite Jr., M. O. Chandler, W. K. Peterson, D. Wiemer, and M. Sugiura, Upwelling O^+ ion source characteristics, *J. Geophys. Res., 91*, 7019-7031, 1986.

Mozer, F. S., Electric field evidence on the viscous interaction at the magnetopause, *Geophys. Res. Lett., 11*, 135-138, 1984.

Ness, N. F., The earth's magnetic tail, *J. Geophys. Res., 70*, 2989-3005, 1965.

Ness, N. F., The geomagnetic tail, *Rev. Geophys. Space Phys., 7*, 97-127, 1969.

Ness, N. F., C. S. Scearce, and J. B. Seek, Initial results of the Imp 1 magnetic field experiment, *J. Geophys. Res., 69*, 3531-3569, 1964.

Ness, N. F., C. S. Scearce, and S. C. Cantarano, Probable observations of the geomagnetic tail at $10^3 R_E$ by Pioneer 7, *J. Geophys. Res., 72*, 3769, 1967.

Ness, N. F., M. H. Acuña, R. P. Lepping, L. F. Burlaga, K. W. Behannon, and F. M. Neubauer, Magnetic field studies at Jupiter by Voyager 1: Preliminary results, *Science, 204*, 982-987, 1979a.

Ness, N. F., M. H. Acuña, R. P. Lepping, L. F. Burlaga, K. W. Behannon, and F. M. Neubauer, Magnetic field studies at Jupiter by Voyager 2: Preliminary results, *Science, 206*, 966-972, 1979b.

Ness, N. F., M. H. Acuña, K. W. Behannon, L. F. Burlaga, J. E. P. Connerney, R. P. Lepping, and F. M. Neubauer, Magnetic fields at Uranus, *Science, 233*, 85-89, 1986.

Ness, N. F., M. H. Acuña, L. F. Burlaga, J. E. P. Connerney, R. P. Lepping, and F. M. Neubauer, Magnetic fields at Neptune, *Science, 246*, 1473-1478, 1989.

Neugebauer, M., and C. W. Snyder, Mariner 2 observations of the solar wind, 1. Average properties, *J. Geophys. Res., 71*, 4469-4484, 1966.

Nicolet, M., The collision frequency of electrons in the ionosphere, *J. Atmos. Terr. Phys., 3*, 200-211, 1953.

Northrop, T. *The Adiabatic Motion of Charged Particles*, Interscience Publishers, New York, 1963.

Ogino, T., A three-dimensional MHD simulation of the interaction of the solar wind with the Earth's magnetosphere: The generation of field-aligned currents, *J. Geophys. Res., 91*, 6791-6806, 1986.

Ogino, T., and R. J. Walker, A magnetohydrodynamic simulation of the bifurcation of tail lobes during intervals with a northward interplanetary magnetic field, *Geophys. Res. Lett., 11*, 1018-1021, 1984.

Ogino, T., R. J. Walker, M. Ashour-Abdalla, and J. M. Dawson, An MHD simulation of B_y dependent magnetospheric convection and field aligned currents during northward IMF, *J. Geophys. Res., 90*, 10,835-10,842, 1985.

Ogino, T., R. J. Walker, M. Ashour-Abdalla, and J. M. Dawson, An MHD simulation of the effects of the interplanetary magnetic field B_y component on the interaction of the solar wind with the Earth's magnetosphere during southward interplanetary magnetic field, *J. Geophys. Res., 91*, 10,029-10,045, 1986.

Ogino, T., R. J. Walker, and M. Ashour-Abdalla, A magnetohydrodynamic simulation of the formation of magnetic flux tubes at the Earth's magnetopause, *Geophys. Res. Lett., 16*, 155-158, 1989.

Ogino, T., R. J. Walker, and M. Ashour-Abdalla, Magnetic flux ropes in 3-dimensional MHD simulations, in *Physics of Magnetic Flux Ropes, Geophys.*

Monogr. Ser., vol. 58, edited by C. T. Russell, E. R. Priest, and L. C. Lee, pp. 669-678, AGU, Washington, D. C., 1990.

Ogino, T., R. J. Walker, and M. Ashour-Abdalla, A global magnetohydrodynamic simulation of the magnetosheath and the magnetosphere when the interplanetary magnetic field is northward, *IEEE Trans. Plasma Sci.*, *20*, 817-828, 1992.

Ogino, T., R. J. Walker, and M. Ashour-Abdalla, A global magnetohydrodynamic simulation of the response of the magnetosphere to a northward turning of the interplanetary magnetic field, *J. Geophys. Res.*, *99*, 11,027-11,042, 1994.

Ogino, T., R. J. Walker, and M. Ashour-Abdalla, An MHD simulation of energy flow in the solar wind, magnetosphere, and ionospheric system: steady convection events, *Adv. Space Res.*, *18*, (8)247-251, 1996.

Ohtani, S., and S. Kokubun, IMP 8 magnetic observations of the high-latitude tail boundary: Location and force balance, *J. Geophys. Res.*, *95*, 20,759-20,769, 1990.

Olbert, S., Summary of experimental results from MIT detector on Imp-1, in *Physics of the Magnetosphere*, edited by R. L. Carovillano, J. F. McClay, and H. R. Radowski, pp. 641-659, D. Reidel, Norwell, Mass., 1968.

Olson, W. P., The shape of the tilted magnetopause, *J. Geophys. Res.*, *74*, 5642-5651, 1969.

Olson, W. P., and K. A. Pfitzer, A quantitative model of the magnetospheric magnetic field, *J. Geophys. Res.*, *79*, 3739-3748, 1974.

Parker, E. N., Newtonian development of the dynamical properties of ionized gases of low density, *Phys. Rev.*, *107*, 924-933, 1957a.

Parker, E. N., Sweet's mechanism for merging magnetic fields in conducting fluids, *J. Geophys. Res.*, *62*, 509-520, 1957b.

Parker, E. N., Interaction of the solar wind with the geomagnetic field, *Phys. Fluids*, *1*, 171-187, 1958a.

Parker, E. N., Dynamics of the interplanetary gas and magnetic fields, *Astrophys. J., 128*, 664-676, 1958b.

Parker, E. N., Extension of the solar corona into interplanetary space, *J. Geophys. Res., 64*, 1675-1681, 1959.

Parker, E. N., Dynamics of the geomagnetic storm, *Space Sci. Rev., 107*, 62-99, 1962.

Parker, E. N., The solar-flare phenomenon and the theory of reconnection and annihilation of magnetic field, *Astrophys. J., Suppl. Ser., 8*, 177, 1963.

Parks, G. K., *Physics of Space Plasmas: An Introduction*, 538 pp., Addison-Wesley, Redwood City, CA, 1991.

Paschmann, G., I. Papamastorakis, W. Baumjohann, N. Sckopke, C. Carlson, B. U. Ö. Sonnerup, and H. Lühr, The magnetopause for large magnetic shear: AMPTE/IRM observations, *J. Geophys. Res., 91*, 11,099-11,115, 1986.

Peredo, M., D. P. Stern, and N.A. Tsyganenko, Are existing magnetospheric models excessively stretched?, *J. Geophys. Res., 98*, 15,343-15,354, 1993.

Petrinec, S. M., and C. T. Russell, External and internal influences on the size of the dayside terrestrial magnetosphere, *Geophys. Res. Lett., 20*, 339-342, 1993a.

Petrinec, S. M., and C. T. Russell, An empirical model of the size and shape of the near-Earth magnetopause, *Geophys. Res. Lett., 20*, 2695-2698, 1993b.

Petrinec, S. M., and C. T. Russell, Comments on "Magnetopause shape as a bivariate function of interplanetary magnetic field B_z and solar wind dynamic pressure" by E. C. Roelof and D. G. Sibeck, *J. Geophys. Res., 100*, 1899-1901, 1995a.

Petrinec, S. M., and C. T. Russell, An examination of the effect of dipole tilt angle and cusp regions on the shape of the dayside magnetopause, *J. Geophys. Res., 100*, 9559-9566, 1995b.

202

Petrinec, S. M., and C. T. Russell, Near-Earth magnetotail shape and size as determined from the magnetopause flaring angle, *J. Geophys. Res.*, *101*, 137-152, 1996a.

Petrinec, S. M., and C. T. Russell, Influencing factors on the shape and size of the dayside magnetopause, *Adv. Space Res.*, *18*, (8)207-211, 1996b.

Petrinec, S. M., and C. T. Russell, Factors controlling the shape and size of the post-terminator magnetopause, *Adv. Space Res.*, *18*, (8)213-216, 1996c.

Petrinec, S. M., P. Song, and C. T. Russell, Solar cycle variations in the size and shape of the magnetopause, *J. Geophys. Res.*, *96*, 7893-7896, 1991.

Petschek, H. E., Magnetic field annihilation, in *The Physics of Solar Flares*, edited by W. N. Hess, NASA SP-50, p. 425, NASA, Washington, DC, 1964.

Piddington, J. H., Geomagnetic storm theory, *J. Geophys. Res.*, *65*, 93-106, 1960.

Potemra, T. A., Sources of large-scale Birkeland currents, in *Physical Signatures of Magnetospheric Boundary Layer Processes*, edited by J. A. Holtet and A. Egeland, pp. 3-27, Kluwer Acad., Norwell, Mass., 1994.

Press, W. H., B. P. Flannery, S. A. Teukolsky, and W. T. Vetterling, *Numerical Recipes: The Art of Scientific Computing*, 818 pp., Cambridge Univ. Press, New York, 1986.

Priest, E. R., and T. G. Forbes, New models for fast steady state magnetic reconnection, *J. Geophys. Res.*, *91*, 5579-5588, 1986.

Pulkkinen, T. I., A study of magnetic field and current configurations in the magnetotail at the time of a substorm onset, *Planet. Space Sci.*, *39*, 833-845, 1991.

Pulkkinen, T. I., D. N. Baker, D. H. Fairfield, R. J. Pellinen, J. S. Murphree, R. D. Elphinstone, R. L. McPherron, J. F. Fennell, R. E. Lopez, and T. Nagai, Modeling the growth phase of a substorm using the Tsyganenko model and multispacecraft observations: CDAW-9, *Geophys. Res. Lett.*, *18*, 1963-1966, 1991.

Pulkkinen, T. I., D. N. Baker, R. J. Walker, J. Raeder, and M. Ashour-Abdalla, Comparison of empirical magnetic field models and global MHD simulations: The near-tail currents, *Geophys. Res. Lett.*, *22*, 675-678, 1995.

Raeder, J., Global MHD simulations of the dynamics of the magnetosphere: Weak and strong solar wind forcing, in *Proceedings of the Second International Conference on Substorms*, edited by J. R. Kan, J. D. Craven, and S.-I. Akasofu, pp. 561-568, Univ. of Alaska Press, Fairbanks, 1994.

Raeder, J., R. J. Walker, and M. Ashour-Abdalla, The structure of the distant geomagnetic tail during long periods of northward IMF, *Geophys. Res. Lett.*, *22*, 349-352, 1995.

Rasmussen, C. E., and R. W. Schunk, Ionospheric convection driven by NBZ currents, *J. Geophys. Res.*, *92*, 4491-4504, 1987.

Ramshaw, J. D., *J. Comput. Phys.*, *52*, 592, 1983.

Richard, R. L., R. J. Walker, and M. Ashour-Abdalla, The population of the magnetosphere by solar wind ions when the interplanetary magnetic field is northward, *Geophys. Res. Lett.*, *21*, 2455-2458, 1994.

Richtmyer, R. D., and K. W. Morton, *Difference Methods for Initial Value Problems*, 2nd ed., Wiley-Interscience, New York, 1967.

Roederer, J. G., Quantitative models of the magnetosphere, *Rev. Geophys. Space Phys.*, *7*, 77-96, 1969.

Roelof, E. C., and D. G. Sibeck, Magnetopause shape as a bivariate function of interplanetary magnetic field B_z and solar wind dynamic pressure, *J. Geophys. Res.*, *98*, 21,421-21,450, 1993.

Roelof, E. C., and D. G. Sibeck, Correction to "Magnetopause shape as a bivariate function of interplanetary magnetic field B_z and solar wind dynamic pressure" by Edmund C. Roelof and David G. Sibeck, *J. Geophys. Res.*, *99*, 8787-8788, 1994.

Roelof, E. C., and D. G. Sibeck, Reply to "Comments on 'Magnetopause shape as a bivariate function of interplanetary magnetic field B_z and solar wind dynamic pressure' by E. C. Roelof and D. G. Sibeck" by S. M. Petrinec and C. T. Russell, *J. Geophys. Res., 100,* 1903-1910, 1995.

Rogers, E. H., D. F. Nelson, and R. C. Savage, Auroral photography from a satellite, *Science, 183,* 951, 1974.

Rosenbauer, H., H. Grunwaldt, M. D. Montgomery, G. Paschmann, and N. Sckopke, HEOS 2 plasma observations in the distant polar magnetosphere: the plasma mantle, *J. Geophys. Res., 80,* 2723-2737, 1975.

Rufenach, C. L., R. F. Martin Jr., and H. H. Sauer, A study of geosynchronous magnetopause crossings, *J. Geophys. Res., 94,* 15,125-15,134, 1989.

Russell, C. T., Geophysical coordinate transformations, *Cosmic Electrodynamics, 2,* 184-196, 1971.

Russell, C. T., The structure of the magnetopause, in *Physics of the Magnetopause, Geophys. Monogr. Ser.,* vol. 90, edited by P. Song, B. U. Ö. Sonnerup, and M. F. Thomsen, pp. 81-98, AGU, Washington, D. C., 1995.

Russell, C. T., and K. I. Brody, Some remarks on the position and shape of the neutral sheet, *J. Geophys. Res., 72,* 6104-6106, 1967.

Russell, C. T., and R. Elphic, ISEE observations of flux transfer events at the dayside magnetopause, *Geophys. Res. Lett., 6,* 33, 1979.

Russell, C. T., and R. L. McPherron, The magnetotail and substorms, *Space Sci. Rev., 11,* 111-122, 1973.

Russell, C. T., C. R. Chappell, M. D. Montgomery, M. Neugebauer, and F. L. Scarf, OGO-5 observations of the polar cusp on November 1, 1968, *J. Geophys. Res., 76,* 6743-6764, 1971.

Schield, M. A., Pressure balance between solar wind and magnetosphere, *J. Geophys. Res.*, *74*, 1275-1286, 1969.

Schindler, K., A theory of the substorm mechanism, *J. Geophys. Res.*, *79*, 2803-2810, 1974.

Schmidt-Voigt, M., *Astr. Astrophys.*, *210*, 433, 1989.

Shi, Y., C. C. Wu, and L. C. Lee, Magnetic field reconnection patterns at the dayside magnetopause: An MHD simulation study, *J. Geophys. Res.*, *96*, 17,627-17,650, 1991.

Sibeck, D. G., Demarcating the magnetopause boundary, *U. S. Natl. Rep. Int. Union Geod. Geophys. 1991-1994, Rev. Geophys.*, *33*, Suppl., 651-655, 1995.

Sibeck, D. G., G. L. Siscoe, J. A. Slavin, E. J. Smith, B. T. Tsurutani, and R. P. Lepping, The distant magnetotail's response to a strong IMF B_Y: Twisting, flattening, and field line bending, *J. Geophys. Res.*, *90*, 4011-4019, 1985.

Sibeck, D. G., G. L. Siscoe, J. A. Slavin, and R. P. Lepping, Major flattening of the distant geomagnetic tail, *J. Geophys. Res.*, *91*, 4223-4237, 1986.

Sibeck, D. G., R. E. Lopez, and E. C. Roelof, Solar wind control of the magnetopause shape, location, and motion, *J. Geophys. Res.*, *96*, 5489-5495, 1991.

Siedentopf, H., A. Behr, and H. Elsässer, Photoelectric observations of the zodiacal light, *Nature*, *171*, 1066-1067, 1953.

Singer, S. F., A new model of magnetic storms and aurorae, *Trans. Am. Geophys. Union*, *38*, 175-190, 1957.

Siscoe, G. L., Two magnetic tails for Uranus, *Planet. Space Sci.*, *19*, 483-490, 1971.

Siscoe, G. L., F. L. Scarf, D. S. Intriligator, J. H. Wolfe, J. H. Binsack, H. S. Bridge, and V. M. Vasyliunas, *J. Geophys. Res.*, *75*, 5319-5330, 1970.

Slavin, J. A., and R. E. Holzer, Solar wind flow about the terrestrial planets, 1. Modeling bow shock position and shape, *J. Geophys. Res.*, *86*, 11,401-11,418, 1981.

Slavin, J. A., E. J. Smith, D. G. Sibeck, D. N. Baker, R. D. Zwickl, and S.-I. Akasofu, An ISEE 3 study of average and substorm conditions in the distant magnetotail, *J. Geophys. Res.*, *90*, 10,875-10,895, 1985.

Slinker, S. P., J. A. Fedder, and J. G. Lyon, Plasmoid formation and evolution in a numerical simulation of a substorm, *Geophys. Res. Lett.*, *22*, 859-862, 1995.

Sod, G. A., A survey of several finite difference methods for systems of nonlinear hyperbolic conservation laws, *J. Comput. Phys.*, *27*, 1-31, 1978.

Song, P., R. C. Elphic, and C. T. Russell, ISEE 1 & 2 observations of the oscillating magnetopause, *Geophys. Res. Lett.*, *15*, 744-747, 1988.

Song, P., C. T. Russell, and C. Y. Huang, Wave properties near the subsolar magnetopause: Pc 1 waves in the sheath transition layer, *J. Geophys. Res.*, *98*, 5907-5923, 1993.

Sonnerup, B. U. Ö., Magnetic field reconnection in a highly conducting incompressible fluid, *J. Plasma Phys.*, *4*, 161, 1970.

Sonnerup, B. U. Ö., Magnetic field reconnection at the magnetopause: An overview, in *Magnetic Reconnection in Space and Laboratory Plasmas, Geophys. Monogr. Ser.*, vol. 30, edited by E. W. Hones Jr., pp. 92-103, AGU, Washington, D. C., 1984.

Sonnett, C. P., D. L. Judge, and J. M. Kelso, A radial rocket survey of the distant geomagnetic field, *J. Geophys. Res.*, *65*, 55-68, 1960.

Sotirelis, T., The shape and field of the magnetopause as determined from pressure balance, paper presented at IAGA meeting, Boulder, Colo., July 1995.

Spence, H. E., M. G. Kivelson, R. J. Walker, and D. J. McComas, Magnetospheric plasma pressures in the midnight meridian: Observations from 2.5 to 35 R_E, *J. Geophys. Res.*, *94*, 5264-5272, 1989.

Spicer, D. S., S. T. Zalesak, R. Löhner, and S. Curtis, Simulation of the magnetosphere with a new three dimensional MHD code and adaptive grid mesh refinement, *Adv. Space Res.*, *18*, (8)252-262, 1996.

Spreiter, J. R., and A. Y. Alksne, Plasma flow around the magnetosphere, *Rev. Geophys. Space Phys.*, *7*, 11-50, 1969.

Spreiter, J. R., and B. R. Briggs, Theoretical determination of the form of the hollow produced in the solar corpuscular stream by interaction with the magnetic dipole field of the Earth, NASA Tech. Rept. R-120, pp. 1-27, 1961.

Spreiter, J. R., and Hyett, B. J., The effect of a uniform external pressure on the boundary of the geomagnetic field in a steady solar wind, *J. Geophys. Res.*, *68*, 1631-1642, 1963.

Spreiter, J. R., A. L. Summers, and A. Y. Alksne, Hydromagnetic flow around the magnetosphere, *Planet. Space Sci.*, *14*, 223-253, 1966.

Spreiter, J. R., A. Y. Alksne, and A. L. Summers, External aerodynamics of the magnetosphere, in *Physics of the Magnetosphere*, edited by R. L. Carovillano, J. F. McClay, and H. R. Radowski, pp. 301-375, D. Reidel, Norwell, Mass., 1968.

Stahara, S. S., R. R. Rachiele, J. R. Spreiter, and J. A. Slavin, A three dimensional gasdynamic model for solar wind flow past nonaxisymmetric magnetospheres: Application to Jupiter and Saturn, *J. Geophys. Res.*, *94*, 13,353-13,365, 1989.

Stern, D. P., Modeling the field of the global magnetopause, in *Physics of the Magnetopause, Geophys. Monogr. Ser.*, vol. 90, edited by P. Song, B. U. Ö. Sonnerup, and M. F. Thomsen, pp. 45-51, AGU, Washington, D. C., 1995.

Stern, D. P., and N. A. Tsyganenko, Uses and limitations of the Tsyganenko magnetic field models, *Eos Trans. AGU*, *73(46)*, 489 and 493-494, 1992.

Storey, L. R. O., An investigation of whistling atmospherics, *Phil. Trans. Roy. Soc.*, A, *246*, 113-141, 1953.

208

Sweet, P. A., The neutral point theory of solar flares, in *Electromagnetic Phenomena in Cosmical Physics*, edited by B. Lehnert, Cambridge Univ. Press, New York, 1958.

Taylor, and E. W. Hones Jr., Adiabatic motion of auroral particles in a model of the electric and magnetic fields surrounding the earth, *J. Geophys. Res.*, *70*, 3605-3628, 1965.

Tsurutani, B. T., D. E. Jones, and D. G. Sibeck, The two-lobe structure of the magnetotail, from x = -60 to -240 R_e, *Geophys. Res. Lett.*, *11*, 1066-1069, 1984.

Tsyganenko, N. A., Global quantitative models of the geomagnetic field in the cislunar magnetosphere for different disturbance levels, *Planet. Space Sci.*, *35*, 1347-1358, 1987.

Tsyganenko, N. A., A magnetospheric magnetic field model with a warped tail current sheet, *Planet. Space Sci.*, *37*, 5-20, 1989.

Tsyganenko, N.A., Quantitative models of the magnetospheric magnetic field: Methods and results, *Space Sci. Rev.*, *54*, 75-186, 1990.

Tsyganenko, N. A., Modeling the Earth's magnetospheric magnetic field confined within a realistic magnetopause, *J. Geophys. Res.*, *100*, 5599-5612, 1995a.

Tsyganenko, N. A. Towards new-generation data-based models of the Earth's distant magnetic field, *SIMPO Newsletter*, vol. 4, no.12, pp. 3-22, Solar-Terrestrial Energy Program (STEP) Simulation Promotion Office, Kyoto University, Kyoto, Japan, 1995b.

Tsyganenko, N. A., and D. G. Sibeck, Concerning flux erosion from the dayside magnetosphere, *J. Geophys. Res.*, *99*, 13,425-13,436, 1994.

Tsyganenko, N. A., and A. V. Usmanov, Determination of the magnetospheric current system parameters and development of experimental geomagnetic field models based on data from IMP and HEOS satellites, *Planet. Space Sci.*, *30*, 985-998, 1982.

Unti, T., and G. Atkinson, Two-dimensional Chapman-Ferraro problem with neutral sheet, 1. The boundary, *J. Geophys. Res.*, *73*, 7319-7327, 1968.

Usadi, A., A. Kageyama, K. Watanabe, and T. Sato, A global simulation of the magnetosphere with a long tail: Southward and northward interplanetary magnetic field, *J. Geophys. Res.*, *98*, 7503-7517, 1993.

Van Allen, J. A., G. H. Ludwig, E. C. Ray, and C. E. McIlwain, Observation of high intensity radiation by satellites, *Jet Propul.*, *28*, 588, 1958.

Vasyliunas, V. M., Theoretical models of magnetic field line merging, *Rev. Geophys. Space Phys.*, *13*, 303-336, 1975.

Voigt, G.-H., K. W. Behannon, and N. F. Ness, Magnetic field and current structures in the magnetosphere of Uranus, *J. Geophys. Res.*, *92*, 15,337-15,346, 1987.

von Neumann, J., and R. D. Richtmyer, *J. Appl. Phys.*, *21*, 232, 1950.

Waite, J. H., Jr., T. Nagai, F. E. Johnson, C. R. Chappell, J. L. Burch, T. L. Killeen, P. B. Hays, G. R. Carignan, W. K. Peterson, and E. G. Shelley, Escape of suprathermal O^+ ions in the polar cap, *J. Geophys. Res.*, *90*, 1619-1630, 1985.

Walén, C., *Ark. f. Mat. Astr. Fys.*, *30A*, no. 15, 1946.

Walker, R. J., and M. Ashour-Abdalla, The magnetosphere in the machine: Large scale theoretical models of the magnetosphere, *U. S. Natl. Rep. Int. Union Geod. Geophys. 1991-1994*, *Rev. Geophys.*, *33*, Suppl., 639-643, 1995.

Walker, R. J., and T. Ogino, Field-aligned currents and magnetospheric convection - A comparison between MHD simulations and observations, in *Modeling Magnetospheric Plasma, Geophys. Monogr. Ser.*, vol. 44, edited by T. E. Moore and J. H. Waite Jr., pp. 39-49, AGU, Washington, D. C., 1988.

Walker, R. J., and T. Ogino, Global magnetohydrodynamic simulations of the magnetosphere, *IEEE Trans. Plasma Sci.*, *17*, 135-149, 1989.

Walker, R. J., and T. Ogino, A global magnetohydrodynamic simulation of the origin and evolution of magnetic flux ropes in the magnetotail, *J. Geomag. Geoelectr.*, *48*, 765-779, 1996.

Walker, R. J., T. Ogino, and M. Ashour-Abdalla, A magnetohydrodynamic simulation of reconnection in the magnetotail during intervals with southward interplanetary magnetic field, in *Magnetotail Physics*, edited by A. T. Y. Lui, pp. 183-190, Johns Hopkins Univ. Press, Baltimore, MD, 1987.

Walker, R. J., T. Ogino, and M. Ashour-Abdalla, Simulating the magnetosphere: The structure of the magnetotail, in *Solar System Plasma Physics, Geophys. Monogr. Ser.*, vol. 54, edited by J. H. Waite Jr., J. L. Burch, and R. L. Moore, pp. 61-68, AGU, Washington, D. C., 1989.

Walker, R. J., T. Ogino, J. Raeder, and M. Ashour-Abdalla, A global magnetohydrodynamic simulation of the magnetosphere when the interplanetary magnetic field is southward: The onset of magnetotail reconnection, *J. Geophys. Res.*, *98*, 17,235-17,249, 1993.

Walters, G. K., Effect of oblique interplanetary magnetic field on the shape and behavior of the magnetosphere, *J. Geophys. Res.*, *69*, 1769-1783, 1964.

Watanabe, K., and T. Sato, Global simulation of the solar wind-magnetosphere interaction: The importance of its numerical validity, *J. Geophys. Res.*, *95*, 75-88, 1990.

Watanabe, K., A. Kageyama, and T. Sato, Global simulations of magnetic substorms, *Plasma Phys. Controlled Fusion*, *34*, 2031-2037, 1992.

Wei, C. G., L. C. Lee, and A. L. LaBelle-Hamer, A simulation study of the vortex structure in the low-latitude boundary layer, *J. Geophys. Res.*, *95*, 20,793-20,807, 1990.

Williams, D. J., and G. D. Mead, Nightside magnetosphere configuration as obtained from trapped electrons at 1100 kilometers, *J. Geophys. Res.*, *70*, 3017-3029, 1965.

Winglee, R. M., Non-MHD influences on the magnetospheric current systems, *J. Geophys. Res.*, *99*, 13,437-13,454, 1994.

Winglee, R. M., Regional particle simulations and global two-fluid modeling of the magnetospheric current system, in *Cross-Scale Coupling in Space Plasmas, Geophys. Monogr. Ser.*, vol. 93, edited by J. L. Horwitz, N. Singh, and J. L. Burch, pp. 71-80, AGU, Washington, D. C., 1995.

Winglee, R. M., P. L. Pritchett, P. B. Dusenbery, A. M. Persoon, J. H. Waite Jr., T. E. Moore, J. L. Burch, H. L. Collin, J. A. Slavin, and M. Sugiura, Particle acceleration and wave emissions associated with the formation of auroral cavities and enhancements, *J. Geophys. Res.*, *93*, 14,567-14,590, 1988.

Winglee, R. M., R. M. Skoug, M. P. McCarthy, G. K. Parks, R. P. Lin, K. A. Anderson, C. Carlson, R. Ergun, D. Larson, J. McFadden, R. L. Lepping, A. Szabo, H. Rème, J. Bosqued, C. d'Uston, T. R. Sanderson, and K.-P. Wenzel, Modeling of upstream energetic particle events observed by WIND, *Geophys. Res. Lett.*, *23*, 1227-1230, 1996.

Wolfe, J. H., Pioneer 10, 11 observations of the solar wind interaction with Jupiter, *Abstracts of the XIXth COSPAR Symposium*, paper VII.4.5, p. 444, 1976.

Wolfe, J. H., R. W. Silva, D. D. McKibbin, and R. H. Mason, Preliminary observations of a geomagnetic wake at 1000 Earth radii, *J. Geophys. Res.*, *72*, 4577, 1967.

Wu, C. C., R. J. Walker, and J. M. Dawson, A three-dimensional MHD model of the Earth's magnetosphere, *Geophys. Res. Lett.*, *8*, 523-526, 1981.

Wu, C. C., Shape of the magnetosphere, *Geophys. Res. Lett.*, *10*, 545-548, 1983.

Wu, C. C., The effects of dipole tilt on the structure of the magnetosphere, *J. Geophys. Res.*, *89*, 11,048-11,052, 1984.

Wu, C. C., The effects of northward IMF on the structure of the magnetosphere, *Geophys. Res. Lett.*, *12*, 839-842, 1985.

Zalesak, S. T., D. S. Spicer, R. Löhner, and S. Curtis, in *Spatio-Temporal Analysis for Resolving Plasma Turbulence (START)*, edited by A. Roux, F. Lefeuvre, and D. LeQueau, European Space Agency, ESA WPP-047, p. 315, 1993.

Zhou, X.-W., and C. T. Russell, HAWKEYE observations of the shape of the magnetopause in the vicinity of the polar cap, *Snowmass Online Poster Session*, www address: http://igpp.ucla.edu/gem/snowmass.html, presented at Geospace Environmental Modeling (GEM) conference, Snowmass, Colo., June 1995.

Zmuda, A. J., and J. C. Armstrong, The diurnal flow pattern of field-aligned currents, *J. Geophys. Res.*, *79*, 4611-4619, 1974.

Zmuda, A. J., J. H. Martin, and F. T. Heuring, Transverse magnetic disturbances at 1100 kilometers in the auroral region, *J. Geophys. Res.*, *71*, 5033-5045, 1966.

Zwan, B. J., and Wolf, R. A., Depletion of solar wind plasma near a planetary boundary, *J. Geophys. Res.*, *81*, 1636-1648, 1976.

Appendix A

MODEL COMPARISONS WITH MAGNETOPAUSE CROSSING DATA SETS

This appendix presents plots showing the comparison of the three predictive mag-netopause models discussed in Chapter 4 with two magnetopause crossing data sets. The models are (1) the MHD based model developed in Chapter 4, (2) RS93, the model of *Roelof and Sibeck* [1993], and (3) PR95/PR96, the dayside/nightside models of *Petrinec and Russell* [1995a, 1996a]. All three models predict the magnetopause surface for a given solar wind dynamic pressures P_D and north/south component of the interplanetary magnetic field (IMF B_Z). However, the MHD model predictions also use the clock angle of the observation point, unlike the axisymmetric empirical models. Figures A.1 through A.5 show the results for predictions made with the *Roelof and Sibeck* data set for five different bins of P_D and IMF B_Z. Figures A.6 through A.10 show the results for predictions made with the *Petrinec and Russell* data set for the same 5 solar wind bins.

Four bins cover P_D from 1.0 to 4.0 nPa and IMF B_Z from -3.75 to +3.75 nT, which corresponds roughly to the $\pm 1\sigma$ for both P_D and IMF B_Z. They are divided into low dynamic pressure (1.0 to 2.0 nPa) and high dynamic pressure (2.0 to 4.0 nPa), and also northward IMF and southward IMF. In addition, a fifth bin with even lower dynamic pressures (0.5 to 1.0 nPa) is tested, but the IMF range is less (-2.5 nT to +2.5 nT) and contains both northward and southward IMF. These five bins cover all of the parameter space of the MHD predictive model developed in Chapter 4.

The positions in the *Roelof and Sibeck* data set extend down the tail to almost 40 R_E, are in geocentric solar ecliptic (GSE) coordinates, and contain a substantial number of high latitude measurements. The solar wind values are 1 hour averages. The magnetopause crossings in the *Petrinec and Russell* data set are mostly on the dayside and at low latitudes, but there are some points on the near-Earth nightside. The positions in the *Petrinec and Russell* data set are in aberrated geocentric solar magnetospheric (GSM) coordinates, so we would expect the scatter of points to be

somewhat less than RS93 (in GSE coordinates). The solar wind values are 5 minute averages (See discussion in Section 4.8).

The upper panel of each figure shows with asterisks the observed axial distance and X value for each observation point (mean magnetopause position) falling within that solar wind bin. The curves show representative magnetopause shapes that were generated for each of the models for solar wind conditions at the centroid of the bin. The curves are from the present MHD derived model (solid line), the empirical model *Roelof and Sibeck* [1993] (dot-dash line), and the hybrid empirical models of *Petrinec and Russell* [1995a, 1996a] (dashed line). The pressure centroid is the geometric mean of the minimum and maximum pressures (due to the logarithmic scale used for the pressure bins), while the IMF B_Z centroid is simply a linear average. Note the discontinuity in the slope at $X = 0$ in the hybrid PR95/PR96 model. All of the figures are prepared in the same style, except for the spatial dimensions of the graphs differ for each data set. Figures A.1 through A.5 (*Roelof and Sibeck* data set) cover a larger range of space than Figures A.6 through A.10 (*Petrinec and Russell* data set).

Taking the predicted values for each model, we calculated the errors by comparing each prediction against the observed magnetopause position. The lower panel of each figure shows the signed errors for each model, defined as $R_{observed} - R_{predicted}$. The errors [MHD derived (+), RS93 (X), and PR95/PR96 (o)] are again plotted against X. Note that the errors run between $\pm 8 R_E$ for the *Roelof and Sibeck* data set comparison and between $\pm 4 R_E$ for the *Petrinec and Russell* data set comparison. The true error is a vector normal to the model magnetopause surface, which we estimated using simple approximations. On the nightside (very roughly cylindrical), $R_{predicted}$ was just the axial distance to the magnetopause predicted by each model at the X value and clock angle of the measurement. On the dayside (very roughly spherical), the predicted position was the radial distance to the magnetopause along a line from the center of the Earth to the observation point. Thus, the nightside errors are all axial, while the dayside errors are all radial. This approximation is found to be a very good approximation to the errors, but it produces values slightly larger than those computed with RS93 in *Roelof and Sibeck* [1993], where the error is a vector normal to the model magnetopause surface.

The average errors and root mean square (rms) errors calculated for each model

are listed at the bottom of the figure. A negative average error shows a consistent overestimation of the predicted range. All three models have average errors near zero indicating fairly good fits and similar rms values. The errors on the nightside are typically two to three times larger than those on the dayside ($\sim 1R_E$) for all the models. The calculated errors are governed more by the spread in the data measurements than in differences between the models, which all fit about equally well. Again, all three models have low average errors and similar rms error values. The rms errors are about half as large in this data set ($\leq 1R_E$), mostly because it lacks the measurements deep in the tail that produce large scatter. The error statistics from these model comparisons are tabulated in Tables 4.1 and 4.2.
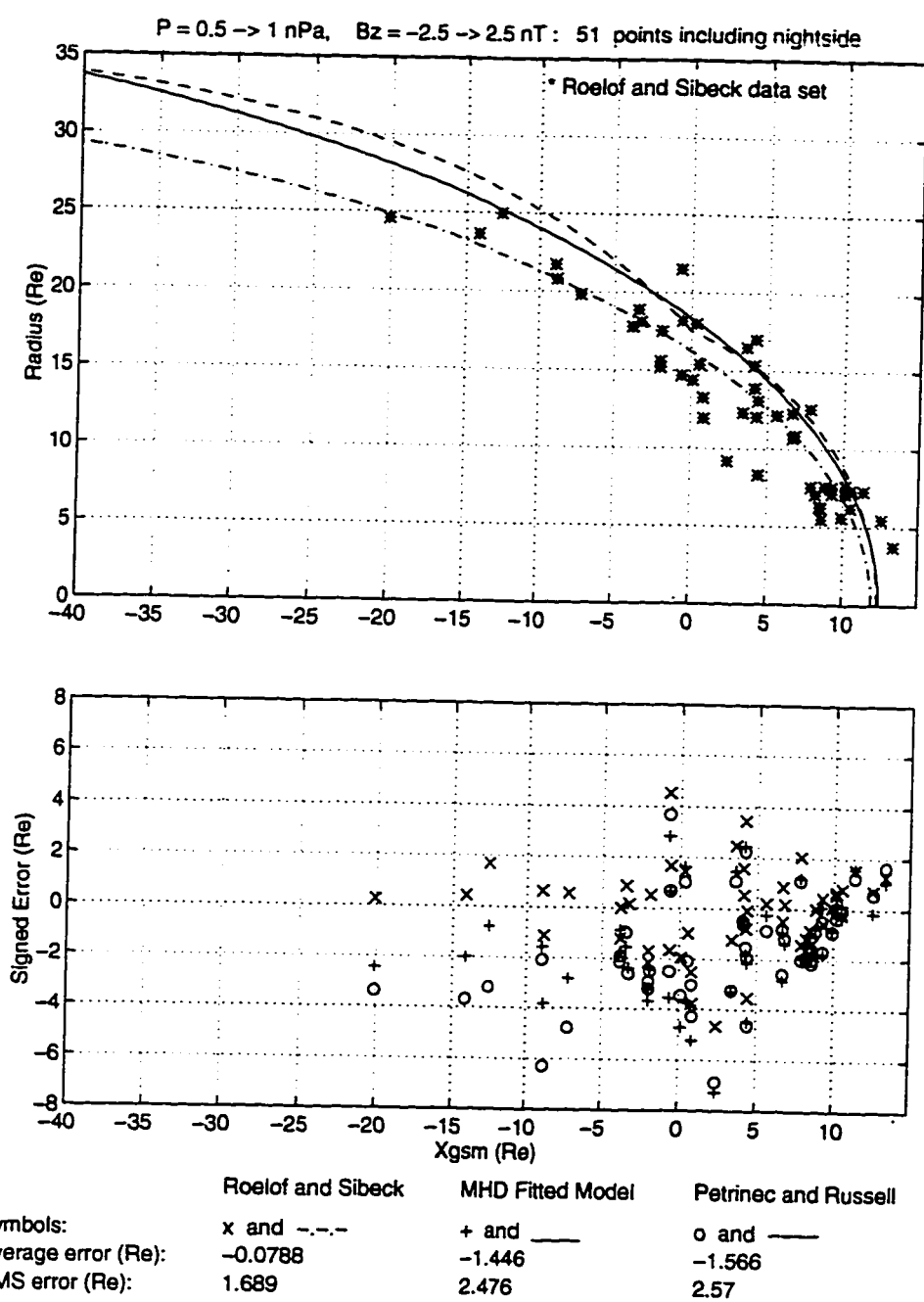
Figure A.1: Magnetopause model comparison using the *Roelof and Sibeck* data set for very low dynamic pressure (0.5 to 1 nPa) and IMF B_Z from -2.5 to +2.5 nT.
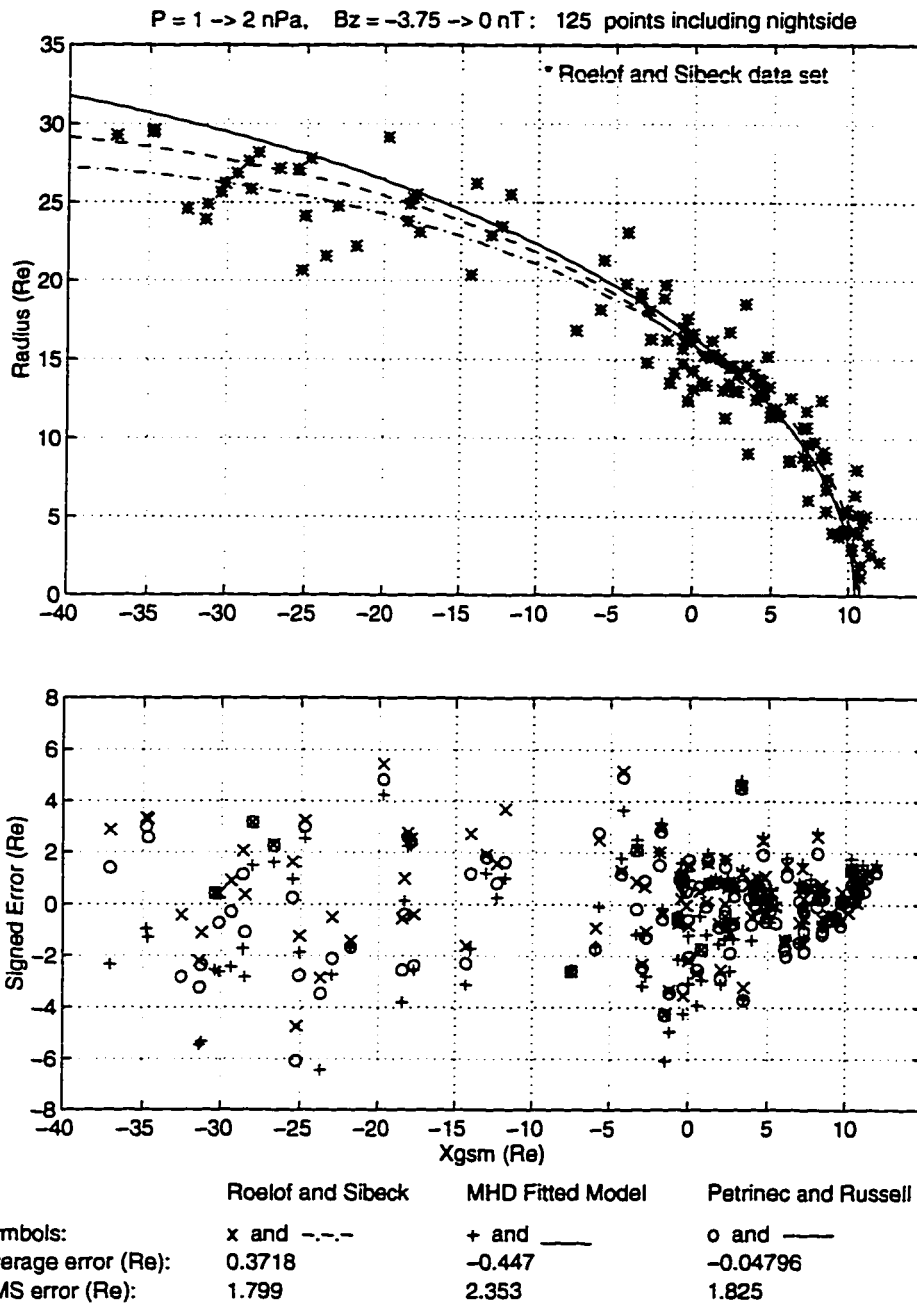
Figure A.2: Magnetopause model comparison using the *Roelof and Sibeck* data set for low dynamic pressure (1 to 2 nPa) and southward IMF B_Z (-3.75 to 0 nT).
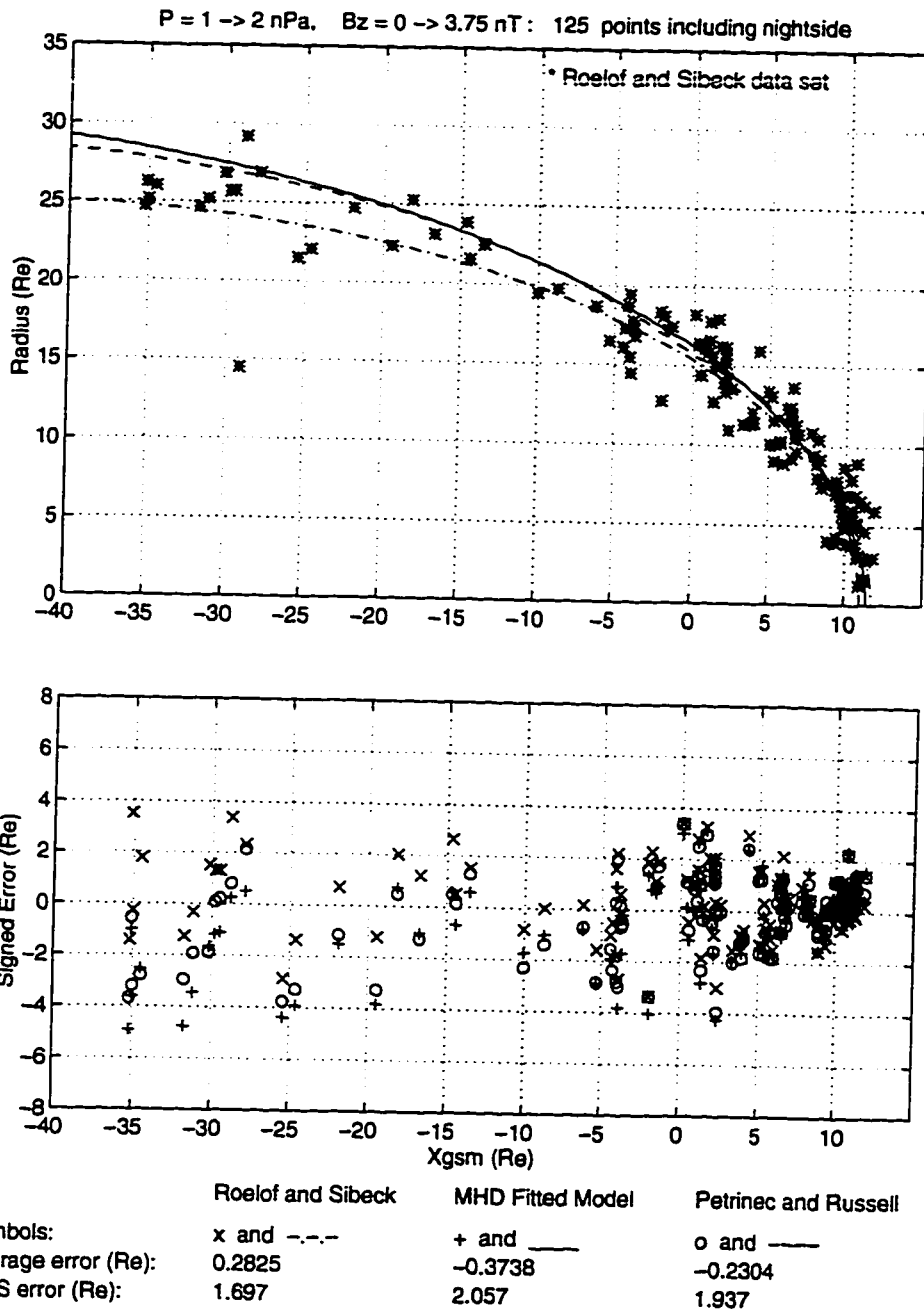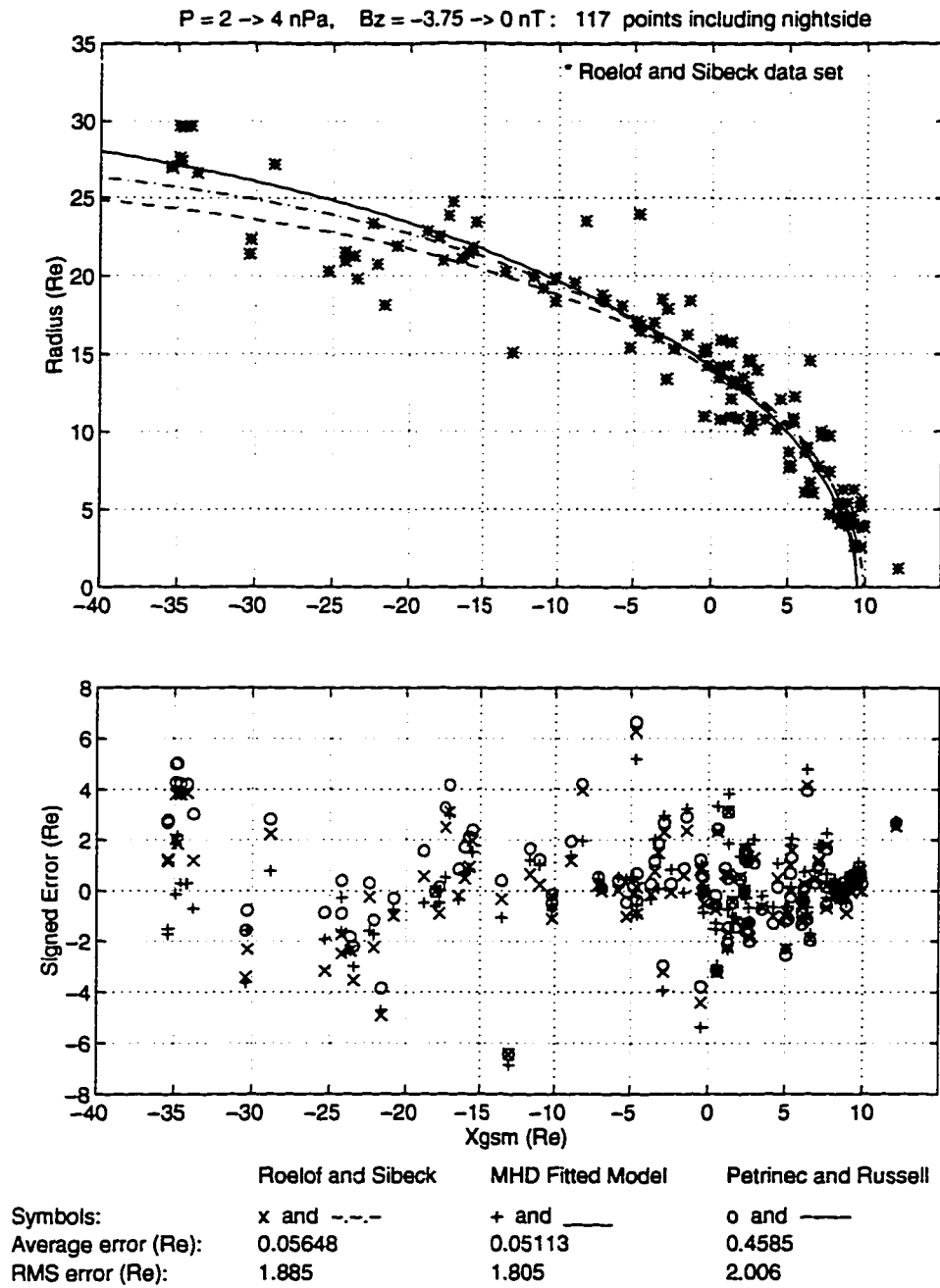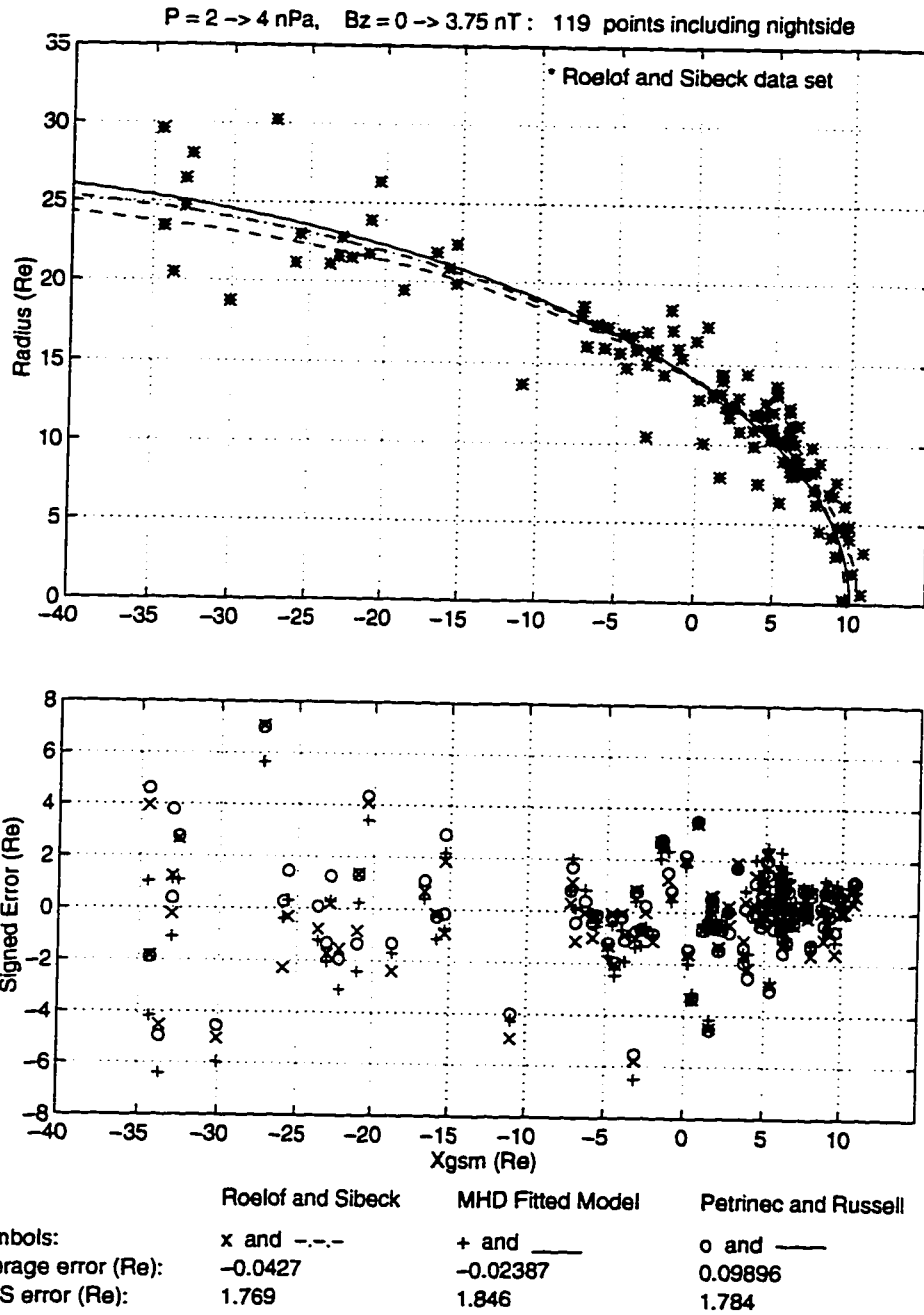
Figure A.3: Magnetopause model comparison using the *Roelof and Sibeck* data set for low dynamic pressure (1 to 2 nPa) and northward IMF B_Z (0 to +3.75 nT).

P = 2 -> 4 nPa,   Bz = -3.75 -> 0 nT :   117 points including nightside

Roelof and Sibeck data set

Radius (Re)

35
30
25
20
15
10
5
0

-40 -35 -30 -25 -20 -15 -10 -5 0 5 10

Signed Error (Re)

8
6
4
2
0
-2
-4
-6
-8

-40 -35 -30 -25 -20 -15 -10 -5 0 5 10

Xgsm (Re)

	Roelof and Sibeck	MHD Fitted Model	Petrinec and Russell
Symbols:	x and -.-.-	+ and ___	o and ——
Average error (Re):	0.05648	0.05113	0.4585
RMS error (Re):	1.885	1.805	2.006

Figure A.4: Magnetopause model comparison using the *Roelof and Sibeck* data set for high dynamic pressure (2 to 4 nPa) and southward IMF B_Z (-3.75 to 0 nT).

Figure A.5: Magnetopause model comparison using the *Roelof and Sibeck* data set for high dynamic pressure (2 to 4 nPa) and northward IMF B_Z (0 to +3.75 nT).
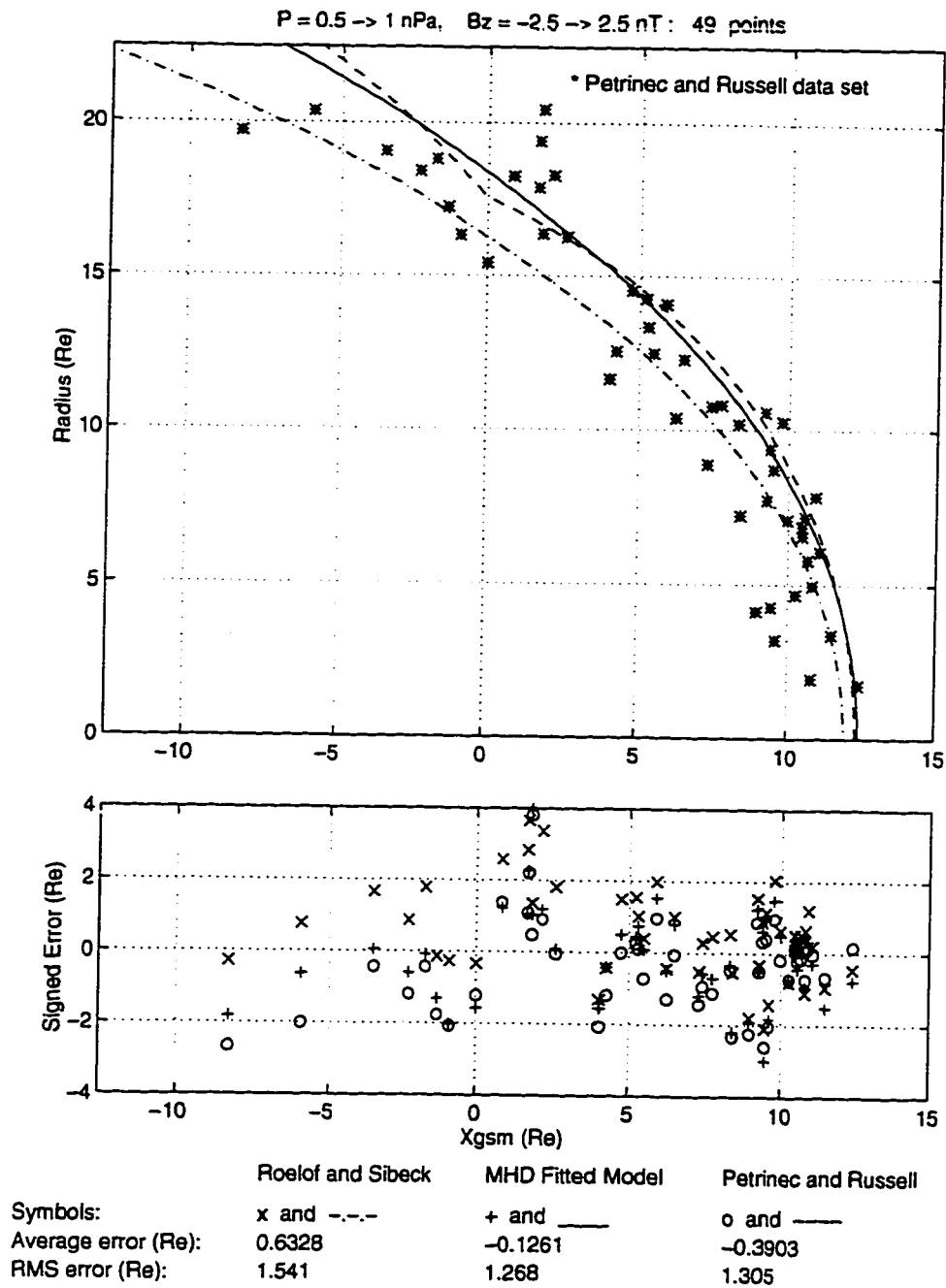
Figure A.6: Magnetopause model comparison using the data set of *Petrinec and Russell* data set for very low dynamic pressure (0.5 to 1 nPa) and IMF B_Z from -2.5 to 2.5 nT.
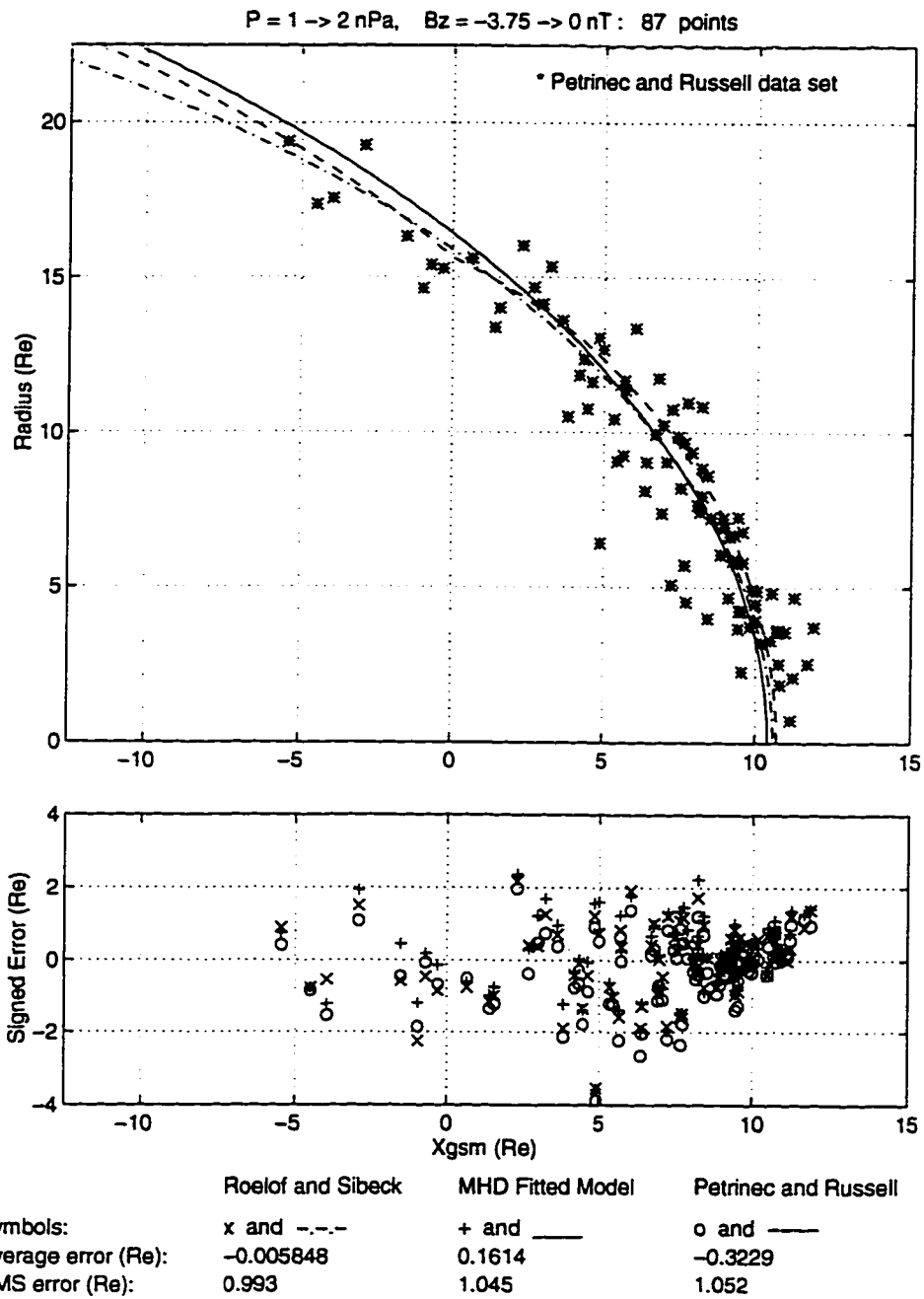
Figure A.7: Magnetopause model comparison using the *Petrinec and Russell* data set for low dynamic pressure (1 to 2 nPa) and southward IMF B_Z (-3.75 to 0 nT).
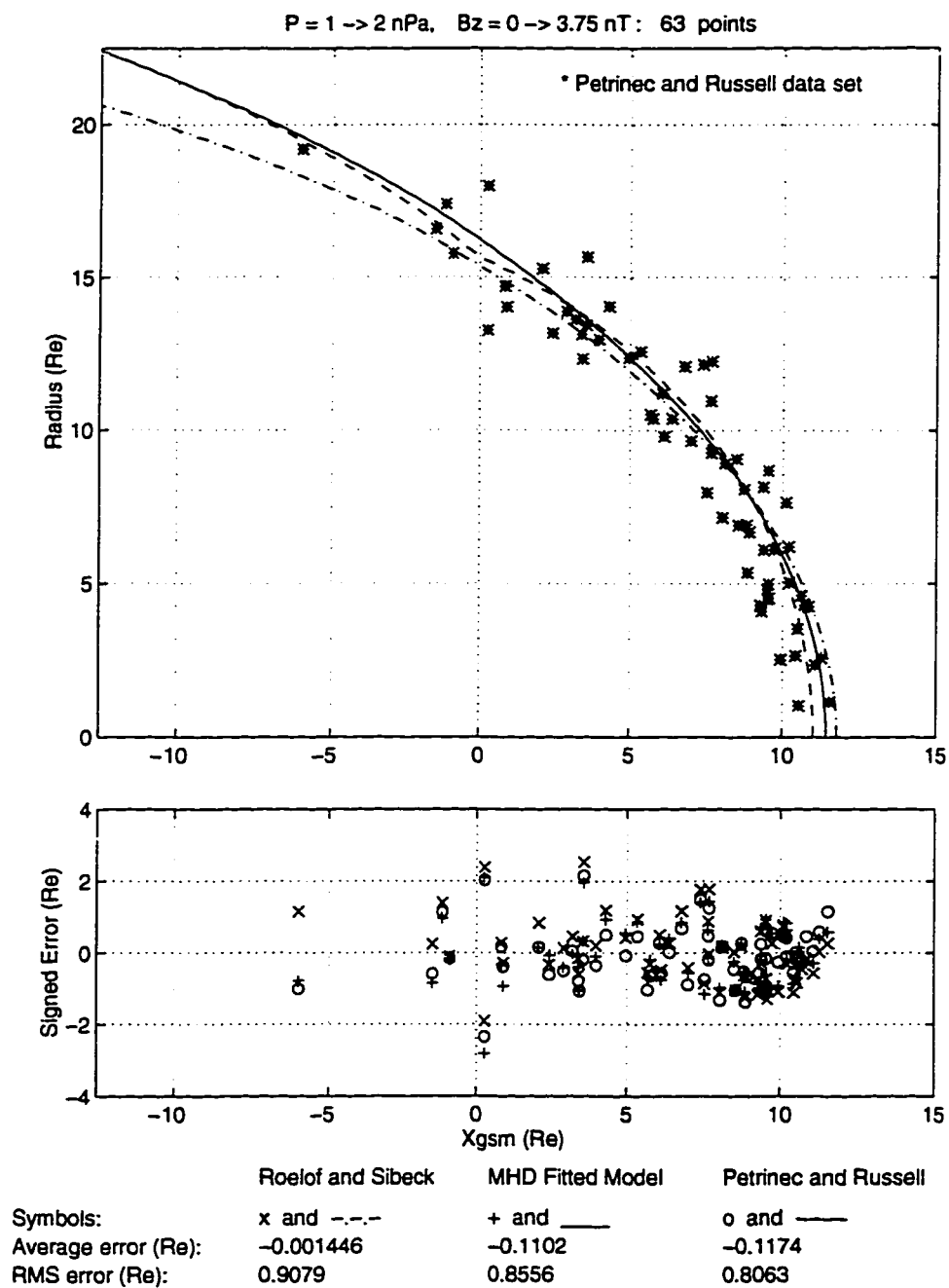
Figure A.8: Magnetopause model comparison using the *Petrinec and Russell* data set for low dynamic pressure (1 to 2 nPa) and northward IMF B_Z (0 to +3.75 nT).
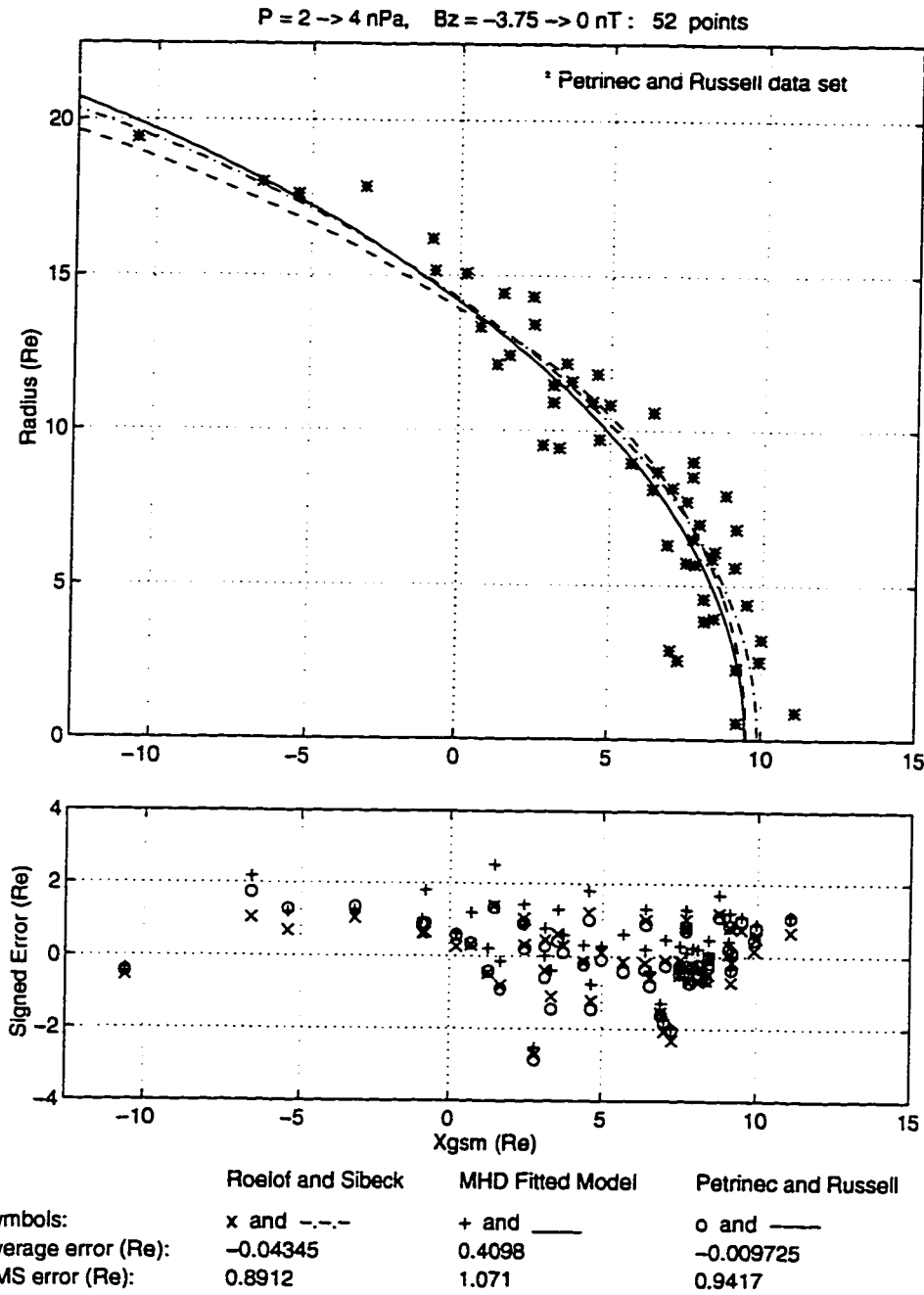
Figure A.9: Magnetopause model comparison using the *Petrinec and Russell* data set for high dynamic pressure (2 to 4 nPa) and southward IMF B_Z (-3.75 to 0 nT).
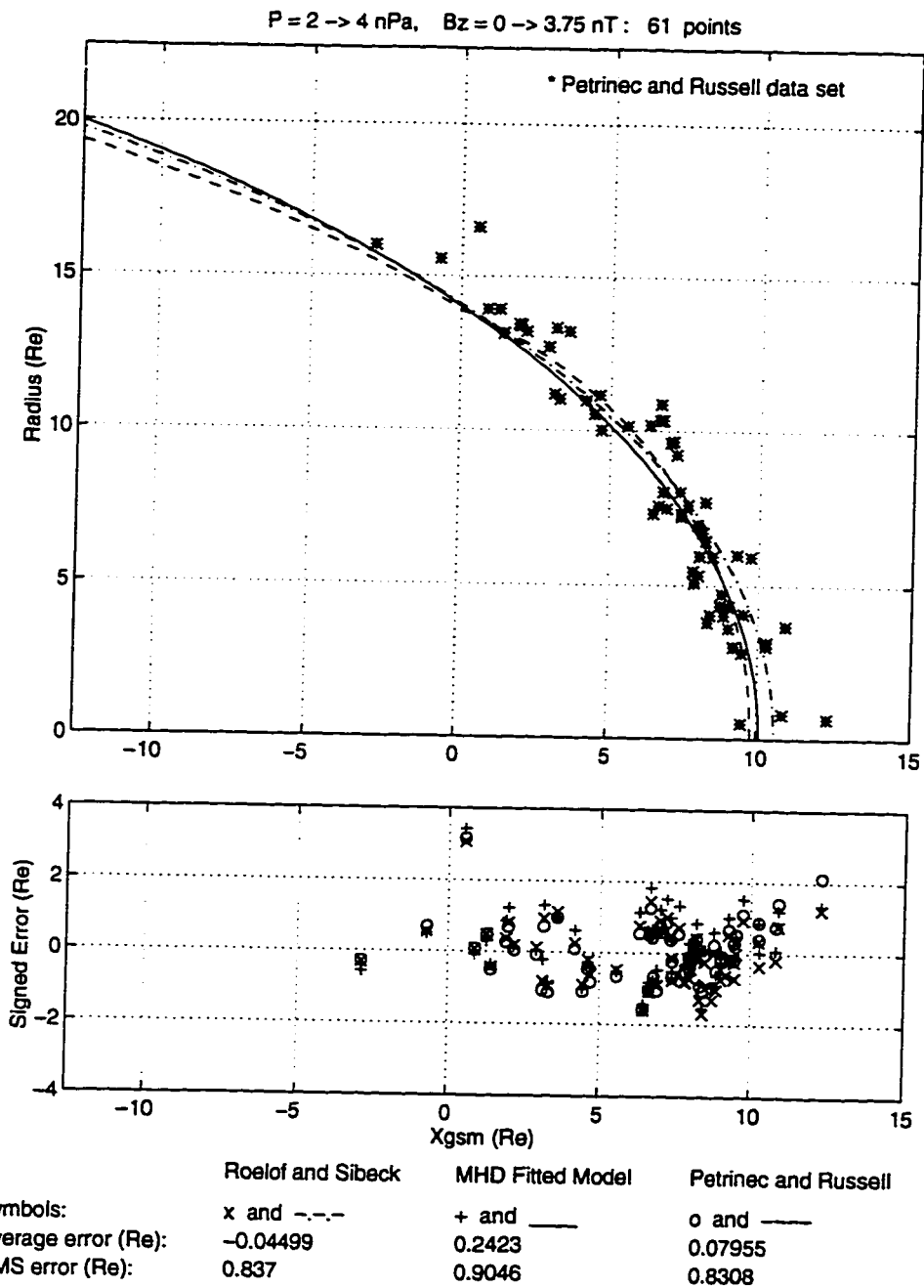
Figure A.10: Magnetopause model comparison using the *Petrinec and Russell* data set for high dynamic pressure (2 to 4 nPa) and northward IMF B_Z (0 to +3.75 nT).

VITA

Ronald Keith Elsen was born in Denver, Colorado on September 9, 1956 to Hans and Louise Elsen. He graduated from Abraham Lincoln High School in Denver in 1974. He received a bachelor's degree in physics from The Colorado College, Colorado Springs, in 1978. He worked in the aerospace industry at Rockwell International from 1978 to 1985 and Boeing Aerospace Company from 1985 to 1991. After taking several courses while employed as an engineer, he entered graduate school full time in January 1992.